Computation of Unsteady Transonic Flowfields Using Shock Capturing and the Linear Perturbation Euler Equations

by

Dana Rae Lindquist

B.S. Cornell University (1986)
S.M. Massachusetts Institute of Technology (1988)

SUBMITTED TO THE DEPARTMENT OF
AERONAUTICS AND ASTRONAUTICS
IN PARTIAL FULFILLMENT OF THE REQUIREMENTS
FOR THE DEGREE OF

Doctor of Philosophy
at the
Massachusetts Institute of Technology

February 1992

Signature of Author ____________
Department of Aeronautics and Astronautics
December 11, 1991

Certified by ____________
Professor Michael B. Giles
Thesis Supervisor, Department of Aeronautics and Astronautics

Certified by ____________
Professor Earll M. Murman
Chairman, Department of Aeronautics and Astronautics

Certified by ____________
Professor Edward F. Crawley
Department of Aeronautics and Astronautics

Certified by ____________
Professor Steven R. Hall
Department of Aeronautics and Astronautics

Accepted by ____________
Professor Harold Y. Wachman
Chairman, Department Graduate Committee

Computation of Unsteady Transonic Flowfields Using Shock Capturing and the Linear Perturbation Euler Equations

by

Dana Rae Lindquist

Submitted to the Department of Aeronautics and Astronautics
on December 11, 1991
in partial fulfillment of the requirements for the degree of
Doctor of Philosophy in Aeronautics and Astronautics

When the fully nonlinear equations are used to compute unsteady flowfields, the computer resources required can be quite extensive. Linear methods in which an unsteady linear perturbation on a full, nonlinear, steady solution is found offer a method to reduce the resources required to find a computational flow solution. Linearized potential methods have been used for smooth flowfields, but their applicability to transonic and rotational flowfields is limited. By using the Euler equations these limitations are eliminated, but the question arises as to how to deal with the shocks computationally. Shock fitting has been used successfully, but shock fitting is not applicable when complicated shock structures exist. A new method is presented which uses the linearized Euler equations with shock capturing to find unsteady flowfields. This new method can be applied to a much larger class of flowfields than either of the previously mentioned linear methods. Analysis is presented which shows the validity of this method, and computational examples on a quasi-one-dimensional duct show how it is applied. The computational results on the model problem show surprising accuracy which should be applicable in more complicated higher-dimensional problems.

Thesis Supervisor: Michael B. Giles,
Associate Professor of Aeronautics and Astronautics

Acknowledgments

Although a thesis represents original work by the author, the influence and guidance of many other people are represented in the end product.

I'd like to start by thanking the members of my committee, Earll Murman, Ed Crawley and Steve Hall. We had some lively discussions about linear methods which contributed to much of the analysis in this thesis. The interest in this project extended beyond the borders of Cambridge. John Dannenhoffer, Kenneth Hall, Bob Ni, and Graham Holmes have continued to take an interest in my work and have supported me through the last few years. Most importantly, I would like to thank my thesis advisor, Mike Giles. I am extremely fortunate to have you for a teacher and a friend. I could not have asked for a better advisor.

The C.F.D. Lab has always been a supportive, friendly environment to work in. This is due to both the professors and students who have been associated with the group throughout the years. Several people have passed through the lab while I've been here, all of whom have played a special part in my M.I.T. experience. I hope the spirit of the lab continues to live on. There are so many people I could mention, but in particular, I would like to thank Dave Darmofal, Peter Schmid and Rich Shapiro for taking a red pen to draft copies of this thesis. Your comments were greatly appreciated.

Finally, I would like to acknowledge the part my family played in this work. My parents, Lois and Norman, have always supported me in whatever endeavors I took on. I thank them for believing in me and being my friends. Although my sister Cristina and I have taken seemingly different paths in life, she has been a role model to me. I appreciate her energy and dedication to being her own person. My family also includes my friend Chris. He's been with me through this whole project, the good times and the bad times, reminding me of what's really important in life. I could not have done it without him.

Research funding for this work was provided by Rolls-Royce PLC under the supervision of Dr. Peter Stow. Additional funding to support my education was provided by the Zonta Amelia Earhart Fellowship and the Air Force Research in Aero Propulsion Technology program. I would like to thank the people who support these programs and institutions.

Contents

List of Figures

List of Tables

Nomenclature

a	constant in the scalar model equation
$\bar{A}_1$	linearization coefficient matrix (Equation (2.29))
$\bar{A}_2$	linearization coefficient matrix (Equation (2.30))
$\mathbf{A}$	constant matrix for boundary condition analysis (Equation (5.36))
c	speed of sound
D	dissipation residual
e	internal energy
E	total energy
F	flux vector (Equation (2.16))
F_E	Euler flux vector (Equations (3.2) and (3.19))
F_V	Viscous flux vector (Equations (3.2) and (3.19))
g	amplification factor
h	height of the duct
H	total enthalpy
k	reduced frequency ($\frac{\omega L}{c}$)
ℓ	lift (Section 2.5)
L	length scale of the domain
M	Mach number
p	pressure
P	pressure vector (Equation (2.16))
q_x	heat conduction
Re	Reynolds number ($\frac{\bar{c}L}{\nu}$)
R	Flux Residual
s	logarithm of the entropy
S	switch for artificial viscosity (Equation 5.12)
t	time
$\mathcal{T}$	time scale
$\mathbf{T}$	matrix of right eigenvectors of $\mathbf{A}$ (Equation 5.38))
U	state vector (Equation 2.16))
U_p	primitive state vector (Equation 5.34))
u	velocity
u_b	boundary velocity
x	independent spatial variable
X	length scale
z	Fourier transform operator

α	coefficients in the Runge-Kutta schemes
γ	specific heat ratio
δ	width of the shock
$\Delta(\,)$	discrete change in a quantity
ϵ_2	second difference artificial viscosity coefficient
ϵ_4	fourth difference artificial viscosity coefficient
κ	conductivity
λ	CFL number
$\mathbf{\Lambda}$	matrix of eigenvalues of **A** (Equation (5.37))
μ	viscosity
ν	kinematic viscosity $(\frac{\mu}{\rho})$
ξ	scaled spatial variable $(\frac{x}{\mu_{ref}})$
ρ	density
τ_{xx}	viscous stress
ϕ	characteristic variables
ψ	flux limiter (Section 5.2)
ω	forcing frequency
$[[\cdot]]$	jump across the shock
$\Re\{\,\}$	real part of a quantity
$\Im\{\,\}$	Imaginary part of a quantity

Superscripts and Subscripts

$\bar{*}$	mean value
$\tilde{*}$	perturbation
$\hat{*}$	complex amplitude perturbation
$\dot{*}$	time derivative
$(\,)^n$	iteration index
$(\,)_D$	downstream of the shock
$(\,)_g$	of the grid
$(\,)_J$	node index
$(\,)_{new}$	new value at the boundary
$(\,)_o$	stagnation quantity
$(\,)_{old}$	old value at the boundary
$(\,)_{pred}$	predicted value at the boundary
$(\,)_s$	of the shock
$(\,)_{spec}$	specified value at the boundary
$(\,)_U$	upstream of the shock
$(\,)_V$	viscous shock region

Chapter 1

Introduction

There has been an increased interest in the computation of unsteady flowfields in recent years, particularly in the turbomachinery field where the flow is inherently unsteady due to the relative motion of blade passages. This interest is partly motivated by the continuing increase in available computing power which makes the computation of unsteady flowfields feasible, but it is also motivated by the need to understand the unsteady flowfields in the development of new engineering designs. The emphasis here is on the small-scale flutter or forced response problems which exist in external aerodynamics as well as turbomachinery. In these problems, the ideal flowfield is steady and undesirable unsteady effects are introduced through induced fluctuations of the body or fluctuations in the ambient fluid (corresponding to the flutter and forced response problems, respectively). The structural response to the aerodynamic forces on a blade determines if a small perturbation in the blade loading will cause the motion of the blade to decay or to amplify and cause fatigue which can eventually lead to failure. Past experience in the field has provided empirical correlations which provide the designer with safe operating zones, but with the present demand for increased performance there is a demand for higher tip speeds, higher blade loadings, increased efficiencies and noise suppression which leads to operating regions where these correlations are invalid. The need clearly exists for computational models of the unsteady flowfield which accurately predict the aerodynamic forces to allow the designer to work in areas where there is no past experience; however, these aerodynamic models must be very efficient so the design process will not bankrupt the designer in terms of either computational cost or time. The goal of this work is to provide a new method for developing these computational aerodynamic models.

The interaction between the aerodynamics and structures is part of the field of aeroelasticity. Fortunately, in most cases it is possible to decouple the structural dynamics from the unsteady aerodynamics, so these two fields can be considered independently. The decoupling occurs since the blade density is so much higher than the density of the surrounding fluid, hence the unsteady aerodynamic forces have an insignificant effect on the blade vibration characteristics. For the forced response problem, the unsteadiness is due to an external source, such as the preceding blade row. Only when calculating the aerodynamic damping on the blade must the actual motion of the blade be considered, since this damping is in direct response to the blade motion. For the flutter problem, the moving blade is the source of the unsteadiness in the flowfield. The structural characteristics of the blade are found before the flowfield calculation is done, so particular frequencies and mode shapes of the blade motion become the input for the aerodynamic calculation. The aerodynamic calculation then determines if energy is transferred from the flowfield to this blade motion or vice versa, or, in other words, if the structural mode is amplified or damped by the flowfield. Flutter occurs when the mode is amplified and, by sweeping through a range of structural modes, the flutter boundary can be determined. As mentioned earlier, the aerodynamic computation is the focus of this work, but more information can be found on the structural problem and the coupling between the aerodynamics and the structures in [3, 10].

The earliest methods for the computation of unsteady flowfields were analytical and have their roots in what is today referred to as classical fluid dynamics. These techniques aim at finding closed form solutions to the unsteady partial differential equations which govern the flow and apply several simplification techniques to make this possible. For example, often the flow is isentropic, incompressible or contains only small perturbations to a uniform flow. From these methods grew the semi-analytical methods which distribute singularities such as sources or vortices along the blade surface and calculate the strength of these singularities as part of the solution procedure, given certain constraints on the system. Many of these solutions are found with the assistance of the computer, but the source of these methods is still mostly analytical. Whitehead [30] provides a good review of these classical analytical methods, many of which provide the backbone of the design methods which are used today.

More recent methods in unsteady and steady fluid dynamics involve forming a grid in the space around the blade or airfoil and solving some governing equations by a finite difference, finite volume, finite element or spectral element method. The rest of the methods described here involve this type of computation. While having greater computational cost than the analytical methods, the additional ability to model geometric and field effects add to the accuracy of these methods. The governing equations used range from the isentropic, irrotational potential equations to the Euler or Navier Stokes equations. As the level of physics involved in the numerical method increases, there is a corresponding increase in the required computational effort.

The Navier-Stokes equations are a coupled set of equations which correspond to the laws of conservation of mass, momentum and energy. By assuming the Reynolds number is sufficiently high and the Prandtl number is order unity, most of the flow can be considered inviscid and non-heat-conducting, so these equations can be reduced to another coupled set of equations called the Euler equations. By further assuming that the flow is both isentropic and irrotational, the Euler equations can be reduced to a single equation which is termed the potential equation. Subsonic or supersonic flow away from boundary layers is generally inviscid, isentropic, and will be irrotational as well if there is no means of introducing vorticity into the flowfield, therefore these flowfields are governed by the potential equations. The addition of a shock introduces an entropy jump into the flowfield and vorticity is produced behind a curved shock. If the shock has any significant strength, these effects must be modeled and the potential equations are no longer valid.

Computational schemes require some special treatment in shock regions. Since there is a pressure jump across a shock, the correct prediction of the location and movement of the shock are important in getting accurate results for the forces on a surface. Two treatments are commonly used: shock fitting and shock capturing. Shock fitting involves applying a shock jump condition at a grid line which is aligned with the shock. The jump condition is derived from the equations and enforces the appropriate conservation laws. Since the shock location is not known before the computation is performed, the grid line which is aligned with the shock must move as part of the computation.

This method produces very crisp shocks, but has the disadvantage that some notion of where the shock will be must exist before the computation starts. The complicated shock structures which are inherent in three-dimensional transonic turbomachinery flows cause current shock fitting schemes to break down. Shock capturing, on the other hand, produces shocks as part of the computation. The shocks are formed in the flowfield by a means similar to the physical means for generating shocks in a viscous flowfield. The location, or even the existence, of a shock no longer must be known before the computation commences, and complicated shock structures appear naturally in the computation. Since the location of shocks is not part of the scheme's data structure, the coding effort is also simplified.

To find an unsteady solution to the governing equations, the time dependent equations are advanced forward in time. If a periodic solution is desired, it is necessary to step through several cycles of the transient solution until the periodic solution is reached. This method requires a significant amount of computer time [12, 1]. The alternative for small scale unsteadiness is to assume that the unsteadiness is a linear perturbation superimposed upon the fully nonlinear steady solution, reducing the computation time for an unsteady flow solution by a factor of ten or more. This is the method used in this thesis.

1.1 Linear Solution Methods

Linear methods superimpose a linear perturbation on a fully nonlinear steady state solution. The steady solution is found independently of the unsteady solution, and the coefficients in the perturbation equation are functions of this steady solution. Since the perturbations are linear, each perturbation is assumed to have a single frequency, and more general solutions are formed by superposition. The complex amplitude of the perturbation is time independent and well known solution methods for time independent equations can be used. The zero frequency perturbation may also be used to find the sensitivity of the solution to some parameter such as outlet pressure or blade geometry.

The first linear perturbation field methods used the isentropic, irrotational potential equations. Verdon and Caspar [29, 7, 28] and Whitehead [31] made pioneering efforts in this field, and their work dominates the literature on these methods. Verdon and Caspar used a finite volume method with shock fitting. Since the flow is isentropic and irrotational, the jump conditions used for the shock fitting only conserve mass and tangential momentum, which makes them appropriate only for weak shock jumps. Whitehead's approach used a finite element method with triangular elements and a shock capturing technique. Again, this method is only appropriate for weak shocks.

In 1974, Ni [23, 24] presented a method which used the isentropic form of the Euler equations for shock free flowfields. This method was applicable to flat plate geometries at zero incident flow angle, so the steady flowfield was uniform. An interesting new idea introduced in this work was to make the perturbation time dependent, march the solution in time until there is no change from one iteration to the next, at which point the time independent perturbation was found. The use of the Euler equations did not receive much attention for another decade, until in 1987 Hall [15, 17] used the Euler equations with shock fitting in a method similar to that of Verdon and Caspar for the potential equations. Hall's results were very encouraging, but, as with all shock fitting methods, the complexity of fitting the shock along a grid line for complicated shock structures was beyond the then current technology, so this method was limited to cases with simple shock structures. This project was motivated by the success of Hall's work, but extends his idea to the use of shock capturing.

1.2 Overview

The focus of this work is to show that shock capturing techniques are applicable to the linear perturbation Euler equations, as well as to discuss the applicability to the full unsteady Euler equations. Chapter 2 describes the governing equations used in this thesis. Chapter 3 looks at the problem analytically and provides the backbone for justifying the use of shock capturing. The approach which will be taken is to examine the unsteady Navier-Stokes equations. These viscous equations provide a reasonable starting place for the analysis, since the artificial viscosity involved in shock capturing mimics the true viscosity. The major difference between artificial viscosity and true viscosity is the magnitude of the viscosity, which in turn governs the width of the shock. The larger the viscosity, the thicker the shock, so instead of a shock on the order of a few mean free paths (as in a true shock), the artificial viscosity produces a shock with the width of a few computational cells. From the unsteady Navier-Stokes equations it will be shown that the actual magnitude of the viscosity does not govern the location or movement of the shock. The linear Navier-Stokes equations produce the correct integrated value of the flow variables independent of the actual viscosity level as well, which means that the lift or moment on the body is accurately predicted by these equations. This analysis then highlights questions involved with the discretization of the shock motion. These computational issues are explored in Chapter 4 by using a constant area duct problem. In particular, it is found that the shock shape in the numerical solution must remain fairly constant as the shock moves. The issues involving a discrete shock shape apply to the fully unsteady solution as well as to the steady state and linear perturbation solutions.

After exploring the analytic issues related to the problem and pointing out important issues which must be addressed, several numerical schemes are developed in Chapter 5. Since the motion of the shock is essentially a one-dimensional problem, a quasi-one-dimensional duct is used. Here, the height of the duct varies, but the flow variables are constant across the duct. First, a finite volume shock capturing scheme is described. This scheme uses two forms of artificial viscosity, as well as flux vector splitting, to capture the shock for both the steady state solution and the perturbation. An extension is made to these methods which allows the grid to move in the computation of the linear perturbation. The prescribed grid movement is added as a linear perturbation about the steady grid location. Since the grid can then be moved with the shock, the moving shock shape maintains its shape, an important requirement pointed out by the analysis in Chapters 3 and 4. A shock fitting scheme is also described which follows the work of Hall [15, 17] and is used for comparison purposes. Results from the computational schemes are presented in Chapter 6, supporting the analytic findings showing that shock capturing is a viable technique for use with the linear equations. Finally, since the motion for using the linear equations is to have a fast computational method, convergence acceleration methods are described in Chapter 7.

Chapter 2

Governing Equations

The work in this thesis is mostly concerned with numerical techniques used to model fundamental features in fluid dynamics. The flow geometry used throughout is a 'quasi-one-dimensional' duct where the height of the duct varies so there are some two-dimensional effects in the flowfield, but the state variables are constant across the duct. In the next sections the governing equations for the quasi-one-dimensional duct will be derived, first as the viscous Navier-Stokes equations which will then be simplified to form the inviscid Euler equations.

2.1 Derivation of the Quasi-One-Dimensional Navier-Stokes Equations

The Navier-Stokes equations are the governing equations of fluid motion and include the effects of viscosity and conductivity. In one dimension they consist of three coupled equations for conservation of mass, momentum and energy. The equations are derived by enforcing the conservation laws in a control volume, producing an integral equation. This integral equation can be manipulated to produce a differential equation which is often easier to conceptualize. Both forms of the equations will be derived in this chapter.

In the case of the quasi-one-dimensional equations, the control volume consists of a piece of duct of varying height where the flow properties ρ, ρu and ρE are constant across the duct as shown in Figure 2.1. The height varies slowly, so strictly speaking, the non-streamwise velocity v (where $v \ll u$) varies linearly across the duct, because the velocity must be tangent to the walls. The walls of the duct are treated as slip surfaces, so the duct can be viewed as a varying height stream tube. For now, the boundaries

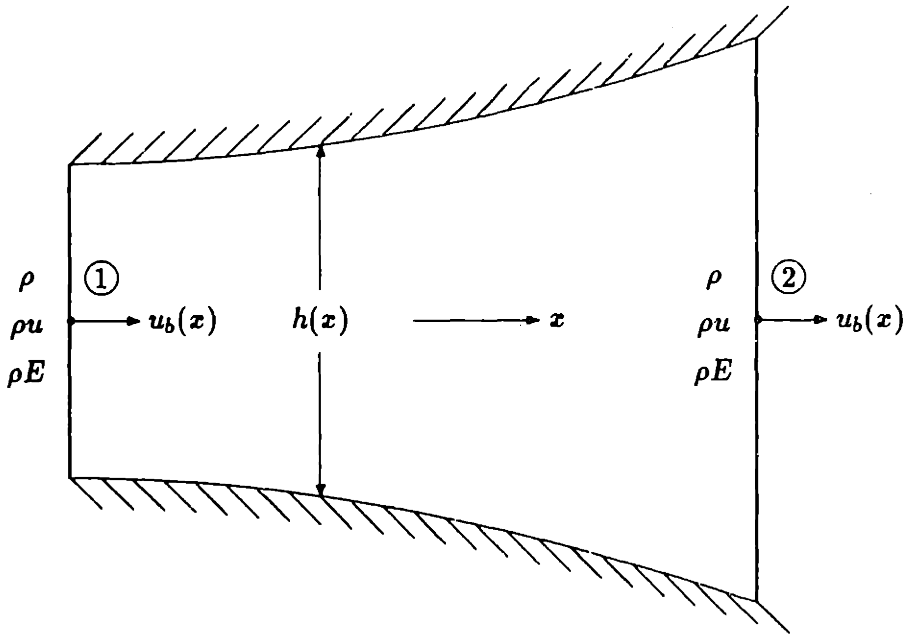

Figure 2.1: Control volume in a quasi one-dimensional duct.

of the control volume are not held fixed, but are allowed to move at some velocity u_b. This added complexity will be used in Section 5.5, where a control volume with moving boundaries is used in the derivation of discrete equations with a moving grid.

2.1.1 Conservation of Mass

If mass is conserved, then all the mass in a control volume must be accounted for. In general this accounting can be stated in words as

$$\begin{aligned}\frac{d}{dt}(\text{mass in control volume}) \;=\;& \\ &(\text{net mass flux entering control volume}) + \qquad (2.1)\\ &(\text{net mass flux swept into control volume by moving boundary}).\end{aligned}$$

This can be put in mathematical terms by considering a general multi-dimensional control volume where $d\mathcal{V}$ represents a small piece of the volume and $d\vec{S}$ is a small piece of the volume surface with its normal vector pointing outward. Equation (2.1) can then be written as

$$\frac{d}{dt}\iint \rho \, d\mathcal{V} = -\oint \rho\vec{V}\cdot d\vec{S} + \oint \rho\vec{u}_b \cdot d\vec{S}. \tag{2.2}$$

However, the control volume for this case is not just any volume, but the special control volume depicted in Figure 2.1. As stated previously, the flow properties ρ, ρu and ρE are assumed constant across the duct. The slight variation in the height of the duct and the assumption that the vertical velocity v varies linearly across the duct remove the higher dimensional dependency from the equations. With this description of the control volume, the following equation can be formed where the subscripts $(\,)_1$ and $(\,)_2$ refer to the two ends of the duct segment.

$$\frac{d}{dt}\int_1^2 \rho h \, dx = -\Big[(\rho u h)_2 - (\rho u h)_1\Big] + \Big[(\rho h u_b)_2 - (\rho h u_b)_1\Big] \tag{2.3}$$

2.1.2 Conservation of Momentum

Conservation of momentum is a statement of Newton's second law which says that the rate of change of momentum is equal to the forces on the object. For a general control volume, this becomes

$$\begin{aligned} &\frac{d}{dt}(\text{momentum in control volume}) \\ &-(\text{net momentum flux entering control volume}) \\ &-(\text{net momentum flux swept into control volume by moving boundary}) \\ &\qquad\qquad = (\text{force on control volume}). \end{aligned} \tag{2.4}$$

It will be assumed that there are no body forces present. Since the flow is viscous, the forces on the control volume are due to pressure and viscous shear. Casting this equation into a form similar to Equation (2.2), one obtains

$$\frac{d}{dt}\iint \rho\vec{V}\, d\mathcal{V} + \oint \rho\vec{V}(\vec{V}\cdot d\vec{S}) - \oint \rho\vec{V}(\vec{u}_b\cdot d\vec{S}) = -\oint p\, d\vec{S} + \oint \tau \cdot d\vec{S}, \tag{2.5}$$

where τ is the shear tensor which in two dimensions is

$$\tau = \begin{bmatrix} \tau_{xx} & \tau_{xy} \\ \tau_{yx} & \tau_{yy} \end{bmatrix}.$$

Again, the more specific equation for the control volume depicted in Figure 2.1 for the quasi one-dimensional duct can be found. The assumptions stated earlier do not allow for the growth of a boundary layer on the edges of the duct, so there is no viscous stress in these areas, yielding

$$\begin{aligned} \frac{d}{dt}\int_1^2 \rho u h\, dx \; + \; \left[(\rho u^2 h)_2 - (\rho u^2 h)_1\right] \; - \; \left[(\rho u h u_b)_2 - (\rho u h u_b)_1\right] \\ = -\left[(ph)_2 - (ph)_1 - \int_1^2 p\, dh\right] + \left[(\tau_{xx} h)_2 - (\tau_{xx} h)_1\right], \end{aligned} \tag{2.6}$$

where

$$\tau_{xx} = \mu \frac{\partial u}{\partial x}.$$

After rearranging some terms, this equation becomes

$$\begin{aligned} \frac{d}{dt}\int_1^2 \rho u h\, dx &= -\left[((\rho u^2 + p)h)_2 - ((\rho u^2 + p)h)_1\right] \\ &\quad - \left[(\tau_{xx} h)_2 - (\tau_{xx} h)_1\right] + \left[(\rho u h u_b)_2 - (\rho u h u_b)_1\right] + \int_1^2 p\, dh. \end{aligned} \tag{2.7}$$

2.1.3 Conservation of Energy

Similarly, the statement that energy is conserved in a control volume can be stated in words as

$$\begin{aligned}&\frac{d}{dt}\,(\text{energy in control volume})\\&-\,(\text{net energy flux entering control volume})\\&-\,(\text{net energy flux swept into control volume by moving boundary})\\&\qquad\qquad = (\text{heat flux added to control volume}) +\\&\qquad\qquad\ (\text{time rate at which work is done on control volume}).\end{aligned}\tag{2.8}$$

The only heat added to the domain is through conduction. The work done on the fluid is through both pressure forces and viscous shear. Again, this equation can be put in mathematical terms:

$$\frac{d}{dt}\iint \rho E\,d\mathcal{V} + \oint \rho E\vec{V}\cdot d\vec{S} - \oint \rho E\vec{u}_b\cdot d\vec{S} = -\oint \vec{q}\cdot d\vec{S} - \oint p\,\vec{V}\cdot d\vec{S} + \oint(\tau\cdot\vec{V})\cdot d\vec{S},\tag{2.9}$$

where E is the total energy per unit mass and $\vec{q}$ is the heat conduction flux. Again, considering the control volume depicted in Figure 2.1 for the quasi one-dimensional duct, this equation becomes

$$\begin{aligned}\frac{d}{dt}\int_1^2 \rho Eh\,dx &+ \Big[(\rho Euh)_2 - (\rho Euh)_1\Big] - \Big[(\rho Ehu_b)_2 - (\rho Ehu_b)_1\Big]\\&= -\Big[(q_xh)_2 - (q_xh)_1\Big] - \Big[(puh)_2 - (puh)_1\Big] + \Big[(u\tau_{xx}h)_2 - (u\tau_{xx}h)_1\Big],\end{aligned}\tag{2.10}$$

where

$$q_x = -\kappa\frac{\partial T}{\partial x}.$$

Introducing, the total enthalpy per unit mass $H = E + \frac{p}{\rho}$ and rearranging some terms gives:

$$\begin{aligned}\frac{d}{dt}\int_1^2 \rho Eh\,dx &= -\Big[(\rho Huh)_2 - (\rho Huh)_1\Big] + \Big[(\rho Ehu_b)_2 - (\rho Ehu_b)_1\Big]\\&\quad - \Big[(q_xh)_2 - (q_xh)_1\Big] + \Big[(u\tau_{xx}h)_2 - (u\tau_{xx}h)_1\Big].\end{aligned}\tag{2.11}$$

2.1.4 Closure

So far three equations have been found in four variables: ρ, u, p and E. For closure one more equation must be found and this comes from the equation of state. For a ideal gas

$$p = \rho R T,$$

where R is a constant for each gas. Also in an ideal gas

$$\begin{aligned} dh &= c_p \, dT \\ de &= c_v \, dT, \end{aligned}$$

where h and e are the enthalpy and internal energy, and the specific heats $c_p = (\frac{\partial h}{\partial T})$ at constant pressure, and $c_v = (\frac{\partial e}{\partial T})$ at constant volume. The ratio of specific heats is often given, for convenience, as

$$\gamma = \frac{c_p}{c_v}.$$

The total energy is the sum of the internal energy and the kinetic energy, and the total enthalpy has a similar contribution.

$$E = e + \frac{1}{2} u^2 \tag{2.12}$$

$$H = h + \frac{1}{2} u^2 \tag{2.13}$$

As stated earlier, the relationship between the total energy and the total enthalpy is known by the definition of enthalpy.

$$H = E + \frac{p}{\rho} \tag{2.14}$$

By assuming c_p and c_v are constant and combining these relationships using some simple algebra, a relationship between the four variables ρ, u, p and E can be found.

$$p = (\gamma-1)(\rho E - \tfrac{1}{2}\rho u^2) \tag{2.15}$$

This is the equation which will be used for closure.

2.1.5 Summary

The three equations for conservation of mass, momentum and energy can be combined into one vector equation. First define the following vectors

$$U = \begin{bmatrix} \rho \\ \rho u \\ \rho E \end{bmatrix}, \quad F = \begin{bmatrix} \rho u \\ \rho u^2 + p \\ \rho u H \end{bmatrix}, \quad F_V = \begin{bmatrix} 0 \\ -\tau_{xx} \\ -u\tau_{xx} + q_x \end{bmatrix}, \quad P = \begin{bmatrix} 0 \\ p \\ 0 \end{bmatrix}. \tag{2.16}$$

Equations (2.3), (2.8) and (2.11) then become the single vector equation

$$\begin{aligned} \frac{d}{dt}\int_1^2 Uh\,dx &= -\Big[(Fh)_2 - (Fh)_1\Big] - \Big[(F_V h)_2 - (F_V h)_1\Big] \\ &\quad + \Big[(Uhu_b)_2 - (Uhu_b)_1\Big] + \int_1^2 P\,dh, \end{aligned} \tag{2.17}$$

which together with Equation (2.15) forms the equation set which will be used for the remainder of this work.

2.2 Differential Equation

At this point the control volume will be assumed to have fixed boundaries and the differential form of Equation (2.17) will be formed. First, with $u_b = 0$, Equation (2.17) becomes

$$\frac{d}{dt}\int_1^2 Uh\,dx = -\Big[(Fh)_2 - (Fh)_1\Big] - \Big[(F_V h)_2 - (F_V h)_1\Big] + \int_1^2 P\,dh. \tag{2.18}$$

Now, instead of leaving $(Fh)_2$ and $(Fh)_1$ as independent variables, they are connected by integrating across the control volume

$$(Fh)_2 = (Fh)_1 + \int_1^2 \frac{\partial (Fh)}{\partial x} dx. \tag{2.19}$$

By linearizing in a small length dx, the small term dh can be written

$$dh = \frac{\partial h}{\partial x} dx. \tag{2.20}$$

Making these substitutions and taking the time derivative $\frac{d}{dt}$ inside the integral, Equation (2.18) becomes

$$\int \frac{\partial}{\partial t}(Uh)\, dx = -\int \frac{\partial (Fh)}{\partial x} dx - \int \frac{\partial (F_V h)}{\partial x} dx + \int P \frac{\partial h}{\partial x} dx. \tag{2.21}$$

Now each term of the equation includes the integral with respect to x over the control volume, so it can be written

$$\int \left[\frac{\partial}{\partial t}(Uh) - \left(-\frac{\partial (Fh)}{\partial x} - \frac{\partial (F_V h)}{\partial x} + P \frac{\partial h}{\partial x} \right) \right] dx = 0. \tag{2.22}$$

Since no particular restrictions have been made on the size of the control volume, the equation must hold for all control volumes, therefore the integrand itself must be zero for any control volume. In this way the differential form of the equation is found to be

$$\frac{\partial}{\partial t}(Uh) = -\frac{\partial (Fh)}{\partial x} - \frac{\partial (F_V h)}{\partial x} + P \frac{\partial h}{\partial x}, \tag{2.23}$$

which holds for all points in the domain.

2.3 Quasi-One-Dimensional Euler Equations

At this point the effects of viscosity and conductivity will be neglected to form the Euler equations. These assumptions are implemented by setting $F_V = 0$.

2.3.1 Steady State Equations

The integral Equation (2.17) and the differential Equation (2.23) are nonlinear. For some initial condition, it is possible to come to a situation where the solution no longer changes with time, or in other words a steady state is reached. At this point, $\frac{\partial}{\partial t} = 0$. The Euler form of the integral equation for the steady state becomes

$$-\left[(\bar{F}h)_2 - (\bar{F}h)_1\right] + \int_1^2 \bar{P}\,dh = 0, \tag{2.24}$$

and the differential equation becomes

$$-\frac{\partial(\bar{F}h)}{\partial x} + \bar{P}\frac{\partial h}{\partial x} = 0. \tag{2.25}$$

An important point is that when this steady state solution exists, whether it is reached by advancing the Euler form of Equation (2.23) from an initial condition to the point where there is no change in time or Equation (2.25) is solved directly, the same solution is found. Computationally, both methods are used to find the steady state. The solution procedures are very different, but the same result is reached. The choice of which procedure is used usually depends on which method requires the least amount of computer resources.

2.3.2 Linear Harmonic Equations

Our interest is in unsteady flowfields. If the perturbations to the flowfield are small, the equations can be linearized. The perturbations will be about the steady state solution discussed in the previous section. One way to simplify the linear perturbation equations is to assume that the input is harmonic and the output at every point in the flowfield is also harmonic with the same frequency but some phase shift. At first this may seem like a severe restriction on the flowfield, but since the perturbations are linear, an arbitrary perturbation can be formed by combining several linear perturbations at different frequencies.

The vector U in Equation (2.16) is termed the state vector, since from it the state of the flowfield at some point is completely defined. All other quantities which are of interest are derived from the three elements of this vector. It was previously stated that the solution is some steady part plus a perturbation, or

$$U(x,t) = \bar{U}(x) + \tilde{U}(x,t). \tag{2.26}$$

The steady state solution, $\bar{U}(x)$, satisfies Equation (2.25) and will be assumed to be known. The perturbation term is assumed small compared to the steady state, so the solution will be linearized about the steady state solution. This allows the steady state and perturbation parts of the nonlinear terms to be separated. By keeping only the first order term of a Taylor expansion:

$$\begin{aligned} F(\bar{U}+\tilde{U}) &= F(\bar{U}) + \frac{\partial F(\bar{U})}{\partial \bar{U}}\tilde{U} + O(\tilde{U}^2) && (2.27)\\ P(\bar{U}+\tilde{U}) &= P(\bar{U}) + \frac{\partial P(\bar{U})}{\partial \bar{U}}\tilde{U} + O(\tilde{U}^2), && (2.28) \end{aligned}$$

where $\frac{\partial F(\bar{U})}{\partial \bar{U}}$ and $\frac{\partial P(\bar{U})}{\partial \bar{U}}$ are matrices which will be termed $\bar{A}_1$ and $\bar{A}_2$ respectively. These matrices are

$$\frac{\partial F(\bar{U})}{\partial \bar{U}} = \bar{A}_1(\bar{U}) = \begin{bmatrix} 0 & 1 & 0 \\ \frac{1}{2}(\gamma-3)u^2 & (3-\gamma)u & \gamma-1 \\ -\gamma E u+(\gamma-1)u^3 & \gamma E-\frac{3}{2}(\gamma-1)u^2 & \gamma u \end{bmatrix} \tag{2.29}$$

$$\frac{\partial P(\bar{U})}{\partial \bar{U}} = \bar{A}_2(\bar{U}) = \begin{bmatrix} 0 & 0 & 0 \\ \frac{1}{2}(\gamma-1)u^2 & -(\gamma-1)u & \gamma-1 \\ 0 & 0 & 0 \end{bmatrix} \qquad (2.30)$$

Substituting Equation (2.26) into the Euler form of Equation (2.17) with fixed boundaries so $u_b = 0$, linearizing about the steady state solution and subtracting off the parts from the equation for the steady state, the following equation results:

$$\frac{d}{dt}\int_1^2 \tilde{U} h \, dx = -\left[(\bar{A}_1 \tilde{U} h)_2 - (\bar{A}_1 \tilde{U} h)_1\right] + \int_1^2 \bar{A}_2 \tilde{U} \, dh. \qquad (2.31)$$

If the process for finding the differential equation from Section 2.2 is repeated, the following differential equation for the perturbation is found:

$$\frac{\partial}{\partial t}(\tilde{U} h) = -\frac{\partial(\bar{A}_1 \tilde{U} h)}{\partial x} + \bar{A}_2 \tilde{U} \frac{\partial h}{\partial x}. \qquad (2.32)$$

As expected, this equation is linear and still dependent on time. Earlier it was said that the flow would be harmonic, and now that assumption is imposed. The time dependency of the perturbation will be harmonic in a single frequency represented by the real part of a complex amplitude multiplied by $e^{i\omega t}$. To make a point later, the magnitude of the perturbation will still contain a dependency on time. The state vector is now

$$U(x,t) = \bar{U}(x) + \Re\{\hat{U}(x,t)\, e^{i\omega t}\}. \qquad (2.33)$$

When this is substituted into Equation (2.32) and the equation is divided through by the common term $e^{i\omega t}$, the following equation results:

$$\frac{\partial}{\partial t}(\hat{U} h) + i\omega \hat{U} h = -\frac{\partial(\bar{A}_1 \hat{U} h)}{\partial x} + \bar{A}_2 \hat{U} \frac{\partial h}{\partial x}. \qquad (2.34)$$

In the previous section the idea of starting with an initial condition and advancing in time until there was no change in the flowfield to a time independent steady state was discussed. If the same concept is used here, Equation (2.34) can be advanced to a 'steady state' where the solution actually satisfies the equation:

$$i\omega\widehat{U}h = -\frac{\partial(\bar{A}_1\widehat{U}h)}{\partial x} + \bar{A}_2\widehat{U}\frac{\partial h}{\partial x}. \tag{2.35}$$

The solution to this equation is what is wanted and in fact, the state vector then becomes

$$U(x,t) = \bar{U}(x) + \Re\{\widehat{U}(x)\,e^{i\omega t}\},$$

where both unknowns $\bar{U}$ and $\widehat{U}$ are only functions of the spatial variable x. This concept was introduced by Ni in 1976 [24]. To find the perturbation variable $\widehat{U}(x)$ either the concept of advancing in time until there is no change in time or the concept of finding the solution directly from Equation (2.35) is used.

2.4 Shock Jump Conditions

Near discontinuities in the flowfield, where the viscous and convection terms balance, are called shocks. The internal structure of a shock is discussed in greater detail in Chapter 3. The discussion here is limited to finding the *weak solutions* to the Euler equations found from the integral form of these equations. As such, the analysis will start with the Navier-Stokes Equation (2.17)

$$\begin{aligned}\frac{d}{dt}\int_1^2 Uh\,dx &= -\Big[(Fh)_2 - (Fh)_1\Big] - \Big[(F_Vh)_2 - (F_Vh)_1\Big] \\ &\quad + \Big[(Uhu_b)_2 - (Uhu_b)_1\Big] + \int_1^2 P\,dh. \end{aligned} \tag{2.17}$$

The viscous term F_V is higher order compared to F upstream and downstream of the shock. When the control volume in Equation (2.17) encompasses the shock, the viscous term is negligible and can be ignored, thus the jump across the shock is not a function of the viscous term. If the width of the control volume is then taken to zero as the viscosity goes to zero, where the control volume velocity is the shock velocity $\dot{x}_s$, this becomes

$$[[Fh - \dot{x}_s U h]]_i = 0, \tag{2.36}$$

where $[[\cdot]]$ indicates the jump in a quantity. Equation (2.36) is the jump condition for a moving shock and applies at the instantaneous location of the shock, indicated by the subscript i.

For the steady state, the shock does not move, so the jump condition in Equation (2.36) becomes

$$[[Fh]] = 0. \tag{2.37}$$

Since the height of the duct, h, is constant across the shock (the shock has no thickness), it can be removed from this jump condition.

Now it is possible to linearize the unsteady jump condition from Equation (2.36) about both the steady state flow solution and the steady state shock location to get the jump condition for the perturbation equation. As in Equation (2.33), the state vector is $U = \bar{U} + \Re\{\widehat{U}e^{i\omega t}\}$. The shock location will be set to $x_s = \bar{x}_s + \Re\{\widehat{x}_s e^{i\omega t}\}$, so it has a linear harmonic unsteady component as well. The jump condition in Equation (2.36) then becomes

$$[[\bar{F}h + \Re\{\bar{A}_1\widehat{U}h\,e^{i\omega t}\} - \Re\{i\omega\widehat{x}_s\bar{U}h\,e^{i\omega t}\}]]_i = 0, \tag{2.38}$$

where $\bar{A}_1 = \frac{\partial \bar{F}}{\partial \bar{U}}$ as defined in Equation (2.29). This equation must still be applied at the instantaneous shock location, so it is further linearized about the steady shock location.

$$\left[\left[\bar{F}h + \Re\left\{\left(\bar{A}_1\widehat{U}h + \widehat{x}_s\frac{\partial(\bar{F}h)}{\partial x} - \bar{U}h\,i\omega\,\widehat{x}_s\right)e^{i\omega t}\right\}\right]\right] = 0 \tag{2.39}$$

After subtracting off the steady jump condition Equation (2.37) and dividing by $e^{i\omega t}$, the perturbation jump condition becomes

$$\left[\left[\bar{A}_1\widehat{U}h + \widehat{x}_s\frac{\partial(\bar{F}h)}{\partial x} - \bar{U}h\,i\omega\,\widehat{x}_s\right]\right] \;=\; 0. \tag{2.40}$$

There are now two jump conditions for the steady equations and the perturbation equations given in Equations (2.37) and (2.40) respectively.

2.5 Lift Calculation

The previous sections presented the equations which govern the solution to the quasi-one-dimensional duct problem. If the flowfield in question is shock free, the Euler or Navier-Stokes equations are solved for the steady state and the perturbation. Once the solution is found, it is possible to find the integral of the pressure along the duct. Since the vertical force due to the integrated pressure on an airfoil or blade is termed the lift, this term will be used here as well. In general, for a nonlinear flowfield, the lift will be defined as

$$\ell(t) \;=\; \int p(x,t)\,dx. \tag{2.41}$$

Since the flow variables have been defined as a steady state plus a harmonic perturbation, $p(x,t) = \bar{p}(x) + \Re\{\widehat{p}e^{i\omega t}\}$, so likewise the lift is

$$\ell(t) \;=\; \bar{\ell} \;+\; \Re\{\,\widehat{\ell}e^{i\omega t}\,\}, \tag{2.42}$$

where

$$\bar{\ell} \;=\; \int \bar{p}(x)\,dx \tag{2.43}$$

$$\widehat{\ell} \;=\; \int \widehat{p}(x)\,dx. \tag{2.44}$$

If the flow is transonic, then the steady and perturbation lift are calculated from the solution of the Navier-Stokes equations. There is, however, another method for finding the transonic flowfield which must be discussed. The shock jump conditions presented in Section 2.4 can be used in conjunction with the Euler equations to find the Euler solution to the flowfield. The jump conditions become an internal boundary condition in the flowfield, thus the jump conditions become part of the governing equations. From the solution to these equations, the steady shock location, $\bar{x}_s$, and the perturbation shock movement, $\hat{x}_s$, are known along with the flowfield away from the shock. This information is used to find the lift, so the steady and perturbation lift are

$$\bar{\ell} = \int^{\bar{x}_s} \bar{p}(x)\,dx + \int_{\bar{x}_s} \bar{p}(x)\,dx \tag{2.45}$$

$$\hat{\ell} = \int^{\bar{x}_s} \hat{p}(x)\,dx - \hat{x}_s[[\bar{p}]] + \int_{\bar{x}_s} \hat{p}(x)\,dx, \tag{2.46}$$

where the shock location and the perturbation in that location come into the calculation of the lift.

Chapter 3

Analysis of the Navier-Stokes Equations

Before turning to discretization and computational issues associated with modeling an unsteady transonic flowfield, more must be understood about the flowfield to be modeled. In particular, our interest is in unsteady shock motion, so this will be the focus of the analysis presented here. Since viscosity plays an important role in the detailed characteristics of a shock, the analysis will start with the Navier-Stokes equations. The simplest transonic flowfield to study is a shock in a constant area duct, so this flowfield will be examined first. Next, a variable area duct, which has a gradient in the flow upstream and downstream of the shock, will be studied to more realistically represent two and three-dimensional flowfields.

3.1 Shock Motion in a Constant Area Duct

A moving shock in a constant area duct is usually referred to experimentally as a shock-tube and is often used to probe the internal structure of a shock. Here it will be used to isolate and explore the effect of viscosity on a moving shock. An understanding of the analytic solution to the shock-tube problem will point to features of the flowfield which must be modeled.

Since the effect of viscosity is of interest, the viscous form of the equations presented in Chapter 2 are used where the height of the duct, h, is assumed to be unity:

$$\frac{\partial U}{\partial t} + \frac{\partial F_B}{\partial x} + \frac{\partial F_V}{\partial x} = 0, \tag{3.1}$$

where

$$U = \begin{bmatrix} \rho \\ \rho u \\ \rho E \end{bmatrix}, \quad F_B = \begin{bmatrix} \rho u \\ \rho u^2 + p \\ \rho u H \end{bmatrix}, \quad F_V = \begin{bmatrix} 0 \\ -\tau_{xx} \\ -u\tau_{xx} + q_x \end{bmatrix}. \tag{3.2}$$

In the above expression for the viscous flux F_V, τ_{xx} is the viscous stress with viscosity μ and q_x is the heat conduction term with conductivity κ:

$$\begin{aligned} \tau_{xx} &= \mu \frac{\partial u}{\partial x} \\ q_x &= -\kappa \frac{\partial T}{\partial x}, \end{aligned}$$

which causes the viscous term to involve the second derivative of a flow variable.

3.1.1 Steady Shock

The steady solution lends insight to the unsteady problem, therefore it will be examined first. The steady state equations are:

$$\frac{\partial F_B}{\partial x} + \frac{\partial F_V}{\partial x} = 0. \tag{3.3}$$

Integrating these equations from one end of the duct to the other gives

$$\begin{aligned} F_B + F_V &= (F_B + F_V)_{\text{upstream}} \\ &= (F_B + F_V)_{\text{downstream}} \\ &= \text{constant}. \end{aligned} \tag{3.4}$$

For a given constant of integration, it is possible to have a solution where the upstream and downstream states are different and still satisfy Equation (3.4), as well as the obvious trivial solution where the states are the same. Here, the more complicated and interesting case where the states are different is considered. One assumption in the following analysis is that the gradients are zero at the upstream and downstream boundaries:

$$\left(\frac{\partial U}{\partial x}\right)_{\text{upstream}} = \left(\frac{\partial U}{\partial x}\right)_{\text{downstream}} = 0. \tag{3.5}$$

By assuming the gradients are zero, the viscous flux, F_V, in these regions of the duct is also zero. Since the constant in Equation (3.4) which governs the flowfield is now only a function of the Euler fluxes, the magnitude of the viscosity does not govern the nature of the flowfield. What this provides is a flowfield where the solution near the boundaries is inviscid, and the viscous region is restricted to the interior regions of the flowfield.

$$F_E + F_V = (F_E)_{\text{upstream}} = (F_E)_{\text{downstream}} = \text{constant} \tag{3.6}$$

Now, if the equations are rescaled by creating a new variable $\xi = \frac{x}{\mu_{ref}}$, where μ_{ref} is some reference viscosity, the equation in ξ no longer has a dependence on the viscosity μ but only on a non-dimensionalized viscosity $\frac{\mu}{\mu_{ref}}$, which further says that the role of the viscosity is only to scale the viscous region. The role of the conductivity κ is similar to that of the viscosity and now becomes the scaled quantity $\frac{\kappa}{\mu_{ref}}$. Since the role of the conductivity is similar to the role of the viscosity, future references to the viscosity will likewise hold for the conductivity. Equation (3.3) in the new coordinate system is now

$$\frac{\partial F_E}{\partial \xi} + \frac{\partial F_V}{\partial \xi} = 0, \tag{3.7}$$

where now F_V is

$$F_V = \begin{bmatrix} 0 \\ -\tau_{\xi\xi} \\ -u\tau_{\xi\xi} + q_\xi \end{bmatrix}$$

and

$$\tau_{\xi\xi} = \frac{\mu}{\mu_{ref}} \frac{\partial u}{\partial \xi}$$

$$q_\xi = -\frac{\kappa}{\mu_{ref}} \frac{\partial T}{\partial \xi}.$$

An inviscid, or Euler, solution can be found by taking the limits $\frac{\mu}{\mu_{ref}} \to 0$ and $\frac{\kappa}{\mu_{ref}} \to 0$. In this Euler flowfield the flow upstream and downstream are constant and invariant along the duct, so the only possibility is that the two regions are joined by a true discontinuity. The role of the viscosity is merely to provide a smooth form of this discontinuity, and it is the actual level of the viscosity which determines how wide this region is. From Equation (3.6) it can be seen that the jump across the discontinuity, called a shock, is given by

$$(\boldsymbol{F_B})_{\text{upstream}} = (\boldsymbol{F_B})_{\text{downstream}}, \tag{3.8}$$

which can be re-written in a shorthand notation as

$$[[\,\boldsymbol{F_B}\,]] = 0, \tag{3.9}$$

where $[[\cdot]]$ means the jump across the shock. Some computational schemes use this jump condition as an internal boundary condition in the flowfield and model the shock as a true discontinuity; this is referred to as shock fitting.

Since, in the steady case, the viscosity only plays a role in scaling the shock region and not in the determination of the nature of the flowfield away from the shock, the level of viscosity can be changed, yet the overall nature of the solution will remain the same. Computationally, this means the shock region can be modeled with an artificial viscosity which only needs to model the nature of the true viscous terms. This is helpful when computing a discrete solution, since the true viscosity would produce shocks with widths of a few mean free paths which cannot be captured on a larger computational grid where we require shocks with widths of a few computational cells.

3.1.2 Unsteady Shock

The analysis presented thus far is only for a stationary shock. What happens if the shock moves? Does the level of the viscosity again only play the role of scaling the width of the shock region? These are important questions which must be addressed when we consider unsteady flowfields. To model the flowfield computationally, the role of the viscosity must be known. It would be nice to be able to use the artificial viscosity model for unsteady flowfields as well as for steady flowfields.

The analysis starts with the unsteady equations:

$$\frac{\partial U}{\partial t} + \frac{\partial F_E}{\partial x} + \frac{\partial F_V}{\partial x} = 0. \qquad (3.1)$$

As before, these equations can be integrated along the duct, but now there is a time derivative term:

$$\frac{d}{dt}\int U\,dx + (F_E + F_V)_{\text{downstream}} - (F_E + F_V)_{\text{upstream}} = 0. \qquad (3.10)$$

Once again, the gradients at the upstream and downstream boundaries are assumed to be zero, so the viscous flux there is also zero. There exists an unsteady solution where the flow variables at the upstream and downstream boundaries are constant, as in the steady case. For given upstream and downstream conditions, the integrated equation is now

$$\begin{aligned}\frac{d}{dt}\int U\,dx &= -\Big((F_E)_{\text{downstream}} - (F_E)_{\text{upstream}}\Big)\\ &= \text{constant}. \qquad (3.11)\end{aligned}$$

What happens to this equation when time is advanced from 0 to $\mathcal{T}$? The time derivative can now be written in terms of the solution at time 0 and $\mathcal{T}$.

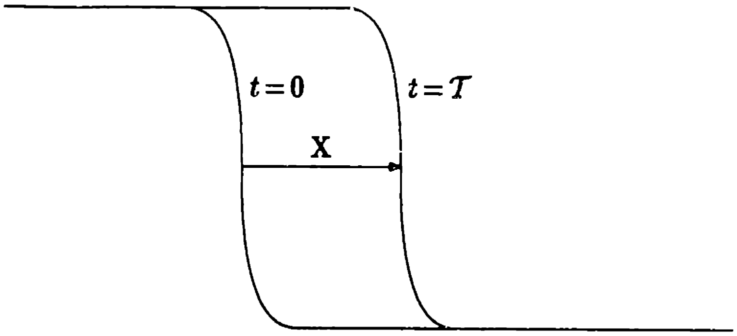

Figure 3.1: Displacement of a shock in an unsteady shock-tube.

$$\int U(x,\mathcal{T})\,dx \;-\; \int U(x,0)\,dx \;=\; -\mathcal{T}\Big((F_B)_{\text{downstream}} \;-\; (F_B)_{\text{upstream}}\Big) \qquad (3.12)$$

The only solution to this equation is a constant moving flowfield which is, in fact, a steady state flowfield moving at some velocity. In the time from 0 to $\mathcal{T}$, the steady flowfield has moved some distance X, as shown in Figure 3.1, which as an equation can be written

$$U(x,\mathcal{T}) \;=\; U(x-X,0), \qquad (3.13)$$

where the shock is moving at velocity

$$\dot{x}_s \;=\; \frac{X}{\mathcal{T}} \;=\; \text{constant}. \qquad (3.14)$$

Putting this information together gives

$$\dot{x}_s\Big(U_{\text{downstream}} - U_{\text{upstream}}\Big) \;=\; \Big((F_B)_{\text{downstream}} \;-\; (F_B)_{\text{upstream}}\Big), \qquad (3.15)$$

which in the notation earlier for the jump across the shock is

$$[[\,F_B - \dot{x}_s U\,]] \;=\; 0, \qquad (3.16)$$

where the shock velocity is

$$\dot{x}_s = \frac{[[F_B]]}{[[U]]}, \tag{3.17}$$

which is not a function of the viscosity. Equation (3.16) is the same unsteady jump condition discussed in Section 2.4. As in the steady case, the magnitude of the viscosity only plays a role in scaling the shock region so it is possible to use artificial viscosity to computationally model the moving shock.

3.2 Variable Area Duct

In the previous section, several issues concerning the shock-tube, or true one-dimensional duct, problem were investigated. In particular, it was found that the viscosity only plays the role of scaling the viscous shock region in both the steady and unsteady cases. But to more accurately model the real problems in which shocks are encountered, the case where the flow upstream and downstream of the shock varies will be discussed. The shock position and strength are now clearly dependent on the viscosity because the gradients away from the shock region are no longer zero. But how strong is this dependence? Is it part of a higher order effect that can be neglected? These are the questions which will be answered in this section.

3.2.1 Dominant Terms

For the time being, consider the quasi-one-dimensional problem discussed in Chapter 2 whose governing differential equation is given in Equation (2.23). The flowfield will be unsteady and transonic with the unsteadiness imposed at the boundaries. A transonic region is divided into three subregions; the region upstream of the shock, the viscous region around the shock, and the region downstream of the shock. The state vector in each of these regions will be called U_U, U_V, and U_D respectively. The shock's location is again marked by x_s which is a function of time. Each of these regions is shown in

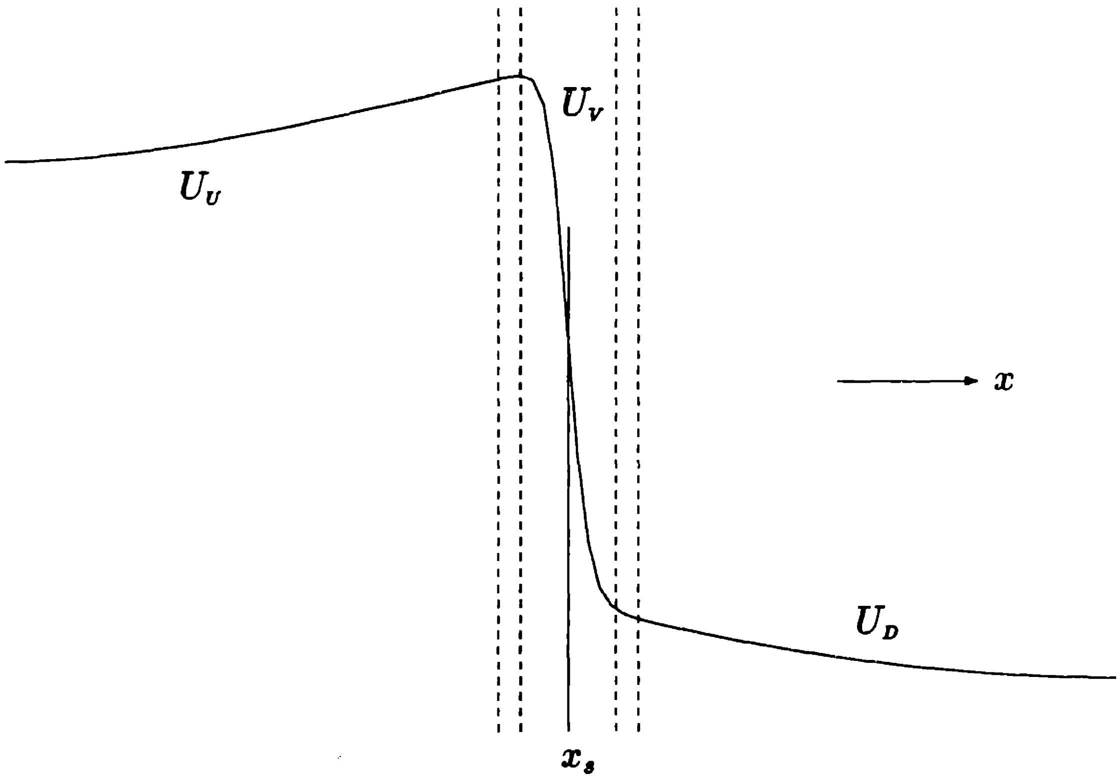

Figure 3.2: Regions around a shock for analysis.

Figure 3.2. There exists an overlap region between the viscous region and the upstream and downstream solutions indicated by the dashed lines which will be mentioned later. For now, let each region be considered in turn.

The equations are written in conservation form with the flux vector divided into two terms, one which represents the Euler terms and the other the viscous terms. The unsteady Navier-Stokes equations are written

$$\frac{\partial(Uh)}{\partial t} + \frac{\partial(F_E h)}{\partial x} + \frac{\partial(F_V h)}{\partial x} - P\frac{\partial h}{\partial x} = 0, \tag{3.18}$$

where

$$U=\begin{bmatrix}\rho\\ \rho u\\ \rho E\end{bmatrix},\quad F_E=\begin{bmatrix}\rho u\\ \rho u^2+p\\ \rho uH\end{bmatrix},\quad F_V=\begin{bmatrix}0\\ -\tau_{xx}\\ -u\tau_{xx}+q_x\end{bmatrix},\quad P=\begin{bmatrix}0\\ p\\ 0\end{bmatrix}. \tag{3.19}$$

As before, in the expression for the viscous flux F_V, τ_{xx} is the viscous stress with viscosity μ and q_x is the heat conduction term with conductivity κ,

$$\begin{aligned}\tau_{xx} &= \mu\frac{\partial u}{\partial x}\\ q_x &= -\kappa\frac{\partial T}{\partial x},\end{aligned}$$

which both cause the viscous term to involve the second derivative of a flow variable.

First consider the equations for the steady state regions away from the shock represented by U_U and U_D. In the momentum equation, let the velocity u go as $\bar{U}$ and vary over a length L, a characteristic length scale for the geometry. The steady convection speed is $\bar{c}$ and the kinematic viscosity ν is μ/ρ. Given these parameters, each term of the equation is scaled:

$$\begin{tikzcd}
\frac{\partial(F_E h)}{\partial x} \arrow[d] & + & \frac{\partial(F_V h)}{\partial x} \arrow[d] & - & P\frac{\partial h}{\partial x} \arrow[d] \\
\bar{c}\frac{\bar{U}h}{L} & & \nu\frac{\bar{U}h}{L^2} = \frac{1}{Re}\left(\bar{c}\frac{\bar{U}h}{L}\right) & & \bar{c}\frac{\bar{U}h}{L}
\end{tikzcd} \tag{3.20}$$

For high Reynolds number ($Re=\frac{\bar{c}L}{\nu}$), the second term is much smaller than the first and third terms, therefore the steady solution in the region away from the shock is dominated by the Euler fluxes. Now, if an unsteadiness is added where the scale of the unsteadiness is given by ω, let the difference in the velocity u from the steady state go as $\tilde{U}$. Again, each term in the equation is scaled:

$$\begin{tikzcd}
\frac{\partial(Uh)}{\partial t} \arrow[d] & + & \frac{\partial(F_B h)}{\partial x} \arrow[d] & + & \frac{\partial(F_V h)}{\partial x} \arrow[d] & - & P\frac{\partial h}{\partial x} \arrow[d] \\
\begin{array}{c} \tilde{U}h\omega = \\ k\left(\bar{c}\frac{\tilde{U}h}{L}\right) \end{array} & & \bar{c}\frac{\tilde{U}h}{L} & & \begin{array}{c} \nu\frac{\tilde{U}h}{L^2} = \\ \frac{1}{Re}\left(\bar{c}\frac{\tilde{U}h}{L}\right) \end{array} & & \bar{c}\frac{\tilde{U}h}{L}
\end{tikzcd} \tag{3.21}$$

For reduced frequency ($k = \frac{\omega L}{\bar{c}}$) of order 1 (which is the region of interest in turbomachinery) the first, second and fourth terms balance. This is actually true for $k \ll O(Re)$. As in the steady equation, for high Reynolds number the third term is much smaller than the other terms. From this it is clear that, to leading order, U_U and U_D are represented by the Euler solution, where the viscous term is neglected in both the steady and the unsteady solution. This is similar to the shock-tube problem where the flow outside the shock region is inviscid and should come as no surprise.

Next, consider the viscous shock region represented by U_V. Again the analysis starts with the steady equation. Let u go as $\bar{U}$ as before, but now $\bar{U}$ varies over the length δ, the shock width. The kinematic viscosity ν is as defined before, as is the steady convection speed $\bar{c}$. Each term in the steady equation is scaled in turn:

$$\begin{tikzcd}
\frac{\partial(F_B h)}{\partial x} \arrow[d] & + & \frac{\partial(F_V h)}{\partial x} \arrow[d] & - & P\frac{\partial h}{\partial x} \arrow[d] \\
\begin{array}{c} \bar{c}\frac{\bar{U}h}{\delta} = \\ \bar{c}\frac{\bar{U}h}{L}\frac{L}{\delta} \end{array} & & \begin{array}{c} \nu\frac{\bar{U}h}{\delta^2} = \\ \frac{L}{\delta}\frac{1}{Re}\left(\bar{c}\frac{\bar{U}h}{L}\frac{L}{\delta}\right) \end{array} & & \begin{array}{c} \bar{c}\frac{\bar{U}h}{\delta} = \\ \bar{c}\frac{\bar{U}h}{L}\frac{L}{\delta} \end{array}
\end{tikzcd} \tag{3.22}$$

The shock is defined as the region in which these terms balance which, implies that $\frac{\delta}{L} = O(Re^{-1})$. All the terms are necessary to find the steady solution in the shock region. Next, consider the shock region where the flow is unsteady. In this case the shock will move, so the frame of reference is changed to one moving with the shock, where the new spatial variable is $X = x - x_s(t)$. The shock velocity is given by the time rate of change of x_s. To change frames of reference, the time derivative $\frac{\partial}{\partial t}$ is replaced by $\frac{\partial}{\partial t} - \dot{x}_s \frac{\partial}{\partial X}$, and the spatial derivative $\frac{\partial}{\partial x}$ is replaced by $\frac{\partial}{\partial X}$. Now, let the change in u from the steady state solution $\bar{U}$ go as $\tilde{U}$, which again varies over the length δ, the shock width. The shock moves some distance $\tilde{x}_s$ from its steady location. The scale of the unsteadiness is given by the same ω as before, as is the kinematic viscosity ν. The steady convection speed $\bar{c}$ is also the same. The changes from steady state of each term of the governing equations can be scaled:

$$\begin{tikzcd}
\frac{\partial(Uh)}{\partial t} \arrow[d] & - & \dot{x}_s \frac{\partial(Uh)}{\partial X} \arrow[d] & + & \frac{\partial(F_B h)}{\partial X} \arrow[d] & + & \frac{\partial(F_V h)}{\partial X} \arrow[d] & - & P\frac{\partial h}{\partial X} \arrow[d] \\
\begin{array}{c} \tilde{U} h \omega = \\ k\left(\bar{c}\frac{\tilde{U}h}{L}\right) \end{array} & & \omega \tilde{x}_s \frac{\tilde{U}h}{\delta} & & \begin{array}{c} \bar{c}\frac{\tilde{U}h}{\delta} = \\ \frac{L}{\delta}\left(\bar{c}\frac{\tilde{U}h}{L}\right) \\ = Re\left(\bar{c}\frac{\tilde{U}h}{L}\right) \end{array} & & \begin{array}{c} \nu \frac{\tilde{U}h}{\delta^2} = \\ \left(\frac{L}{\delta}\frac{1}{Re}\right)\frac{L}{\delta}\left(\bar{c}\frac{\tilde{U}h}{L}\right) \\ = Re\left(\bar{c}\frac{\tilde{U}h}{L}\right) \end{array} & & \begin{array}{c} \bar{c}\frac{\tilde{U}h}{\delta} = \\ \frac{L}{\delta}\left(\bar{c}\frac{\tilde{U}h}{L}\right) \\ = Re\left(\bar{c}\frac{\tilde{U}h}{L}\right) \end{array}
\end{tikzcd} \tag{3.23}$$

From the steady case it was found that $\frac{\delta}{L} = O(Re^{-1})$, so as before the last three terms balance. ω and $\bar{c}$ are the same as before, but for $k \ll O(Re)$, the first term is much smaller than the last three, and can be neglected with respect to the other terms. From this it is argued that the leading order term of the unsteady shock shape U_V is quasi-steady. At any instant in time, the shape of the shock is a steady function given the boundary conditions upstream and downstream of this region, similar to the true one-dimensional moving shock.

Again, like the shock-tube problem in Section 3.1, a coordinate transformation can be made such that $\xi = \frac{X}{\mu_{ref}}$, which is merely a scaling of the shock region. This transformation renders the equations unchanged except the parameter μ is replaced by the non-dimensional $\frac{\mu}{\mu_{ref}}$. This again implies that the shock width is a function of the viscosity, but the shape of the shock is not.

What has been learned is that, as with the steady flowfield, the region away from the shock is not governed by the full Navier-Stokes equations, but the inviscid Euler equations. In the shock region the shape of the shock is governed by the boundary conditions on the shock region, but the viscosity only governs the width. Other than the unsteady boundary conditions, the shock region has no temporal dependence, but is a quasi-steady function of the upstream and downstream solutions.

3.2.2 Estimation of Errors in the Leading Order Term

In the previous section, the leading order term of the solution was found for each of the three regions: U_U, U_V and U_D. An argument was made for neglecting certain terms of the equations in favor of others. In this section the error in the solution imposed by neglecting these terms will be estimated.

In the regions away from the shock the viscous term $\frac{\partial F_V}{\partial x}$ was neglected in Equation (3.18), and only the convection and unsteady terms were kept. The region upstream of the shock has a leading order solution given by U_U which then satisfies the equation

$$\frac{\partial(U_U h)}{\partial t} + \frac{\partial(F_B(U_U)h)}{\partial x} - P(U_U)\frac{\partial h}{\partial x} = 0. \tag{3.24}$$

The solution of the full Equation (3.18) is now taken to be the leading order term plus a correction $U = U_U(1+\epsilon_U)$. To find the next order perturbation, the convection term is compared to the leading order term from the previously neglected viscous term. From Equation (3.20) and (3.21) the following scaling results:

$$\bar{c}\frac{U_U h \epsilon_U}{L} \sim \nu\frac{U_U h}{L^2}. \tag{3.25}$$

This balance, considering $Re = \frac{\bar{c}L}{\nu}$, shows that $\epsilon_U = O(\frac{1}{Re})$. Clearly, the same holds for U_D.

A similar analysis can be performed for the unsteady viscous region where the first order solution is given by U_V. The term $\frac{\partial U}{\partial t}$ was neglected in Equation (3.23). In the frame of reference moving with the shock, the leading order solution U_V satisfies the equation

$$-\dot{x}_s \frac{\partial(Uh)}{\partial X} + \frac{\partial(F_B h)}{\partial X} + \frac{\partial(F_V h)}{\partial X} - P\frac{\partial h}{\partial X} = 0. \qquad (3.26)$$

As before, a correction term is added to the leading order term such that $\tilde{U} = \tilde{U}_V(1+\epsilon_V)$. The leading order contribution which was previously neglected from the unsteady term is compared to the next order perturbation for the viscous term. The following scaling results:

$$\tilde{U}_V h k \frac{\bar{c}}{L} \sim \nu \frac{\tilde{U}_V h \epsilon_V}{\delta^2} = \tilde{U}_V h \epsilon_V \frac{\bar{c}}{L} Re. \qquad (3.27)$$

This balance shows that $\epsilon_U = O(\frac{k}{Re})$. For $k \ll O(Re)$, which is the case considered here, the next order correction for all terms in the solution is much less than $O(1)$. In conclusion, the solution, given the approximations presented here, is in error by a contribution of $O(\frac{1}{Re})$ away from the shock and $\ll O(1)$ in the shock region, which are both negligibly small for large Reynolds numbers.

3.2.3 Matching The Euler And Shock Regions

The three regions described above are joined together using asymptotic matching principles [27, pages 64-68]. In the viscous equations for U_V, the second derivative terms are multiplied by the small parameter μ. The scaling described above is performed so that $\xi = \frac{x-x_s}{\mu}$. In this transformed coordinate system, the leading order solution $U_V(\xi)$ can be found. The matching between U_U and U_V is performed as follows:

1. Take a one term expansion of U_U and write this in terms of the shock variable ξ, then take the limit as the small parameter $\mu \rightarrow 0$ and the shock variable ξ is held fixed. This can be performed using a two-term Taylor series about the shock location x_s.

$$\begin{aligned} U &= \lim_{\mu\to 0} U_U(\xi) \\ &= \lim_{\mu\to 0}\left(U_U(x_s) + (x - x_s)\frac{\partial U_U}{\partial x}(x_s)\right) \\ &= \lim_{\mu\to 0}\left(U_U(x_s) + \mu\,\xi\,\frac{\partial U_U}{\partial x}(x_s)\right) \\ &= U_U(x_s) \end{aligned}$$

2. Take a one-term expansion of U_V and transform from the shock variable ξ into the Euler variable x, and again take the limit as $\mu \to 0$ and the Euler variable x is held fixed. Note that for the matching with U_U, $x < x_s$.

$$\begin{aligned} U &= \lim_{\mu\to 0} U_V(\xi) \\ &= \lim_{\mu\to 0} U_V\left(\frac{x - x_s}{\mu}\right) \\ &= U_V(-\infty) \qquad \text{for} \quad x < x_s \end{aligned}$$

3. These two limits are equated to get the matching condition

$$U_U(x_s) \;=\; U_V(-\infty).$$

The matching between U_D and U_V clearly produces the similar result

$$U_D(x_s) \;=\; U_V(\infty).$$

A composite solution for the whole region will be defined as [27, pages 94-97]

$$U_C = \begin{cases} U_U + U_V - U_U(x_s) & \text{for} \quad x < x_s \\ U_D + U_V - U_D(x_s) & \text{for} \quad x > x_s, \end{cases}$$

which displays several desirable traits. In the Euler region, the term $U_U(x_s)$ balances the term U_V due to the matching condition, so what remains is the Euler solution. In the shock region the same term balances the Euler solution leaving U_V. The solution is clearly continuous at $x = x_s$, although the derivative with respect to x is not. What results is a first-order solution which is valid for the whole region and is continuous. The error in this first-order solution $\ll O(1)$ for $Re^{-1} \ll O(1)$.

3.2.4 Lift Calculation

For many calculations it is important to know the unsteady forces on the moving blade due to the unsteady fluid motion to determine if the fluid causes the flutter mode to amplify or decay. Model the flow as a steady flow with an unsteady perturbation so that in one dimension the unsteady state vector becomes $U(x,t) = \bar{U}(x) + \tilde{U}(x,t)$. Does the viscous flowfield just discussed conform to this assumption? This question will be answered by determining if the lift perturbation, $\tilde{l}$, in the shock region is linear with the forcing perturbation when the flow away from the shock is in the linear regime.

The lift perturbation as described in Section 2.5 is the integral of the unsteady pressure perturbation given by $\tilde{l} = \int \tilde{p}\, dx$. In Figure 3.3, four possibilities for the lift perturbation with a perturbation shock movement $\tilde{x}_s(t)$ are shown. In each case the question of linearity between the lift perturbation and the shock movement is discussed.

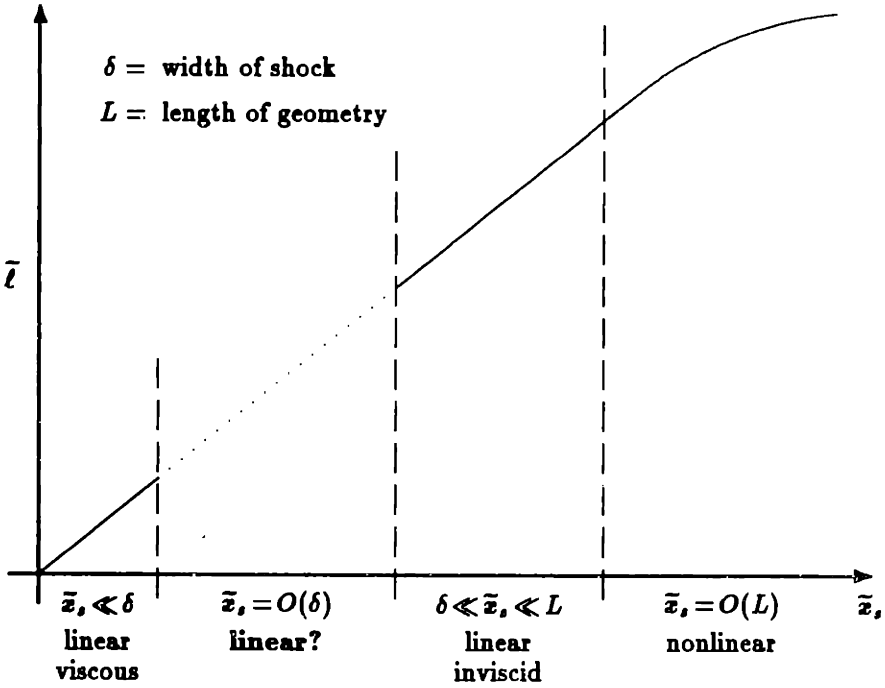

Figure 3.3: Lift perturbation for different levels of shock movement.

$\tilde{x}_s \ll \delta$: In this region the shock movement is much smaller than the width of the shock. An example is given in the first case of Figure 3.4. The shock moves, but the strength of the shock remains nearly constant. To leading order, the lift perturbation due to the movement of the shock is just minus the strength of the shock times the movement of the shock, so the lift perturbation is clearly linear with the shock movement. This case is what would be considered 'linear viscous' since the effect of unsteadiness is small and the effect of viscosity is large, and represents a solution of the linear Navier-Stokes equations.

$\delta \ll \tilde{x}_s \ll L$: In this region, the lift perturbation can also be shown to be linear. This is the third case in Figure 3.4. The change in the shape of the shock is negligible compared to the area over which the shock traveled, so the lift perturbation due to the movement of the shock is again minus the strength of the shock times the movement of the shock, the same linear function found before. The lift perturbation from influences other than the shock movement is linear by definition since the rest of the flowfield is linear. This can essentially be considered as the inviscid limit for the shock and will be called 'linear inviscid', and represents a solution of the linear Euler equations.

$\tilde{x}_s = O(L)$: When the shock movement is on the same order as the length scale of the geometry, the rest of the flowfield will probably be in the nonlinear regime, so in this region the lift perturbation is not linear with the shock movement.

What remains is the region where the shock movement is of the same order as the shock width ($\tilde{x}_s = O(\delta)$). This case is more complicated than the previous three cases and makes use of the scaling analysis presented earlier in this chapter. In particular:

1. The viscosity only determines the scaling of the shock shape.
2. The shock shape itself is a quasi-steady function of $U_U(x_s)$ and $U_D(x_s)$, the Euler solution at the shock.

As shown in the middle case of Figure 3.4, when the shock moves some $\tilde{x}_s$, the contribution to the lift can be divided into two parts, one due to the movement of the shock and the other due to the change in strength of the shock. The contribution to the

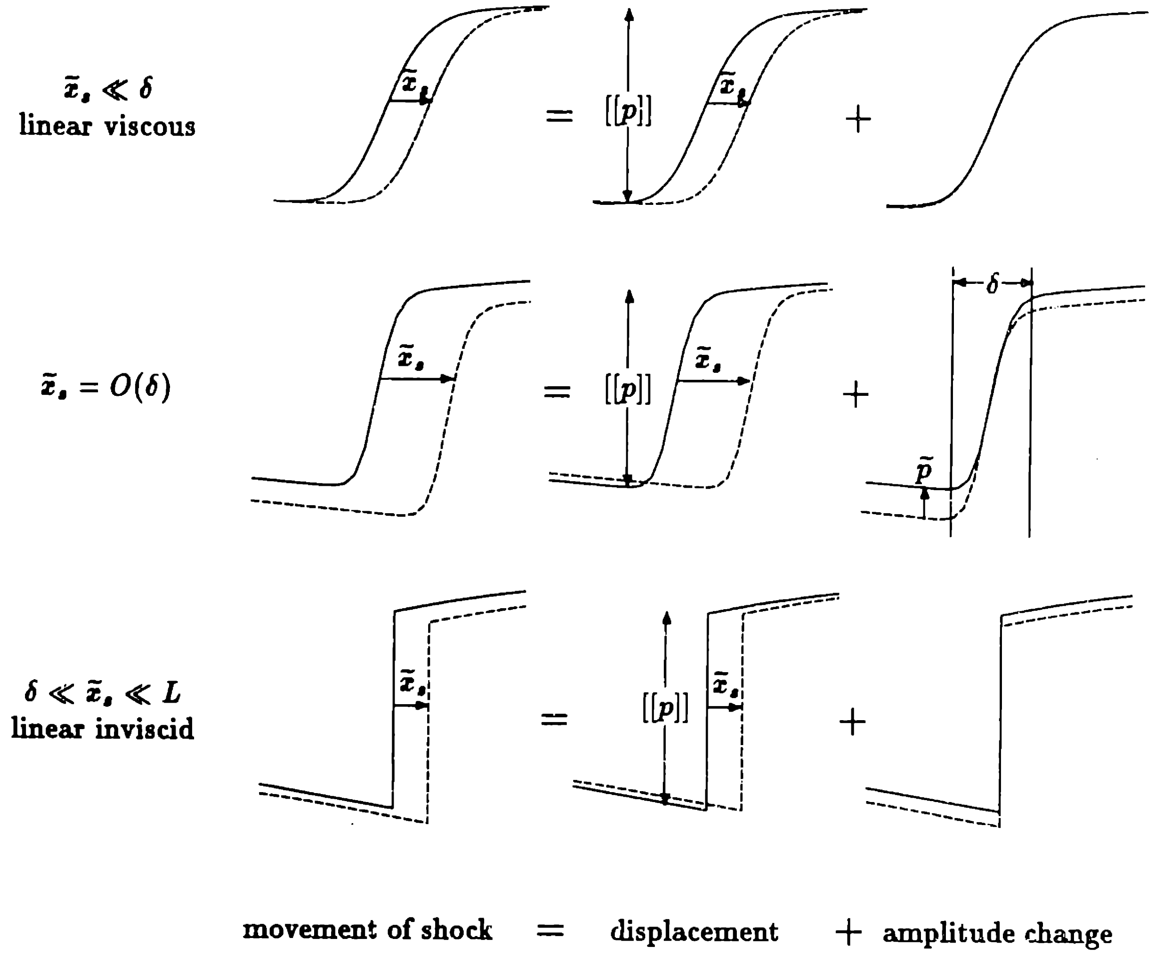

Figure 3.4: Shock movement for various relative levels of shock width and shock motion. To leading order the change in integrated lift $\tilde{\ell} = -[[p]]\tilde{x}_s$ in all cases.

lift perturbation from the shock movement is as before, minus the change in strength of the shock times the shock movement. Here, there is also a contribution from the amplitude change of the shock. Since the shock shape is a quasi-steady function of the flow upstream and downstream of the shock and the steady shock shapes are similar, the two unsteady shock shapes in this figure are also similar. Therefore, the contribution from the amplitude change goes like the pressure perturbation on the upstream or downstream sides of the shock times the width of the shock. This is a higher order effect compared to the contribution from the movement of the shock since, away from the shock, the pressure perturbations are small as is the shock width. This case really draws the linear viscous and linear inviscid cases together. Considering the limit of this case where the viscosity decreases to zero, the width of the shock decreases and the linear inviscid case is reached. In the limit as unsteadiness goes to zero, the linear viscous case is reached. The conclusion is that the unsteady lift of a transonic flow has a lift distribution which is linear in the forcing perturbation, and the linear function is the same as for the two previous cases, $\tilde{l} = -[[p]]\tilde{x}_s$. As long as the portion of the flowfield away from the shock is in the linear regime, the shock portion will be as well. Therefore, if either a linear viscous solution from the linear Navier-Stokes equations or a linear inviscid solution from the linear Euler equations is found, due to linearity the solution in the intermediate region is known as well.

As discussed in the shock-tube problem, it has become common practice to model a flowfield computationally with the Euler equations and use an artificial viscosity to 'capture' the shock. For a small, unsteady perturbation of the flowfield, shock capturing with the linear Euler equations is similar to the linear viscous case presented above, where the movement of the shock is much smaller than the width of the shock. When shock fitting is used, the shock has no thickness, so shock fitting is similar to the linear inviscid case. The important point is that whether shock fitting or capturing is used, there is still the same linear relationship between the shock motion $\tilde{x}_s$ and the lift perturbation $\tilde{l}$. To find the solution in the region between the linear viscous and linear inviscid regions, either solution can be found for the lift perturbation. This is the basis for the computational schemes used here.

3.3 Linear Perturbation Equations

Another method of examining the information just presented is in the frame of reference of the perturbation equations themselves. It was just shown that the perturbation in lift is linear with the movement of the shock. Here it will be shown that this information can be found in the perturbation equations by showing that the perturbation shock jump conditions Equation (2.40) can be derived from the perturbation equations.

This analysis will start with the nonlinear, unsteady differential Equation (2.23) for the quasi-one-dimensional duct. The viscous term F_V will be modeled by an artificial viscosity term which simulates the true viscosity. The coefficient for this simulated viscosity will be ϵ.

$$\frac{\partial(Uh)}{\partial t} + \frac{\partial(Fh)}{\partial x} - P\frac{\partial h}{\partial x} = \epsilon\frac{\partial^2(Uh)}{\partial x^2} \tag{3.28}$$

The addition of the simulated viscosity term must be made to the linear perturbation equation as well. A slightly different version of the perturbation equation than was derived in Chapter 2 will be used for this analysis, where now the constant matrices will be left as derivatives in the equation.

$$i\omega\widehat{U}h + \frac{\partial}{\partial x}\left(\frac{\partial(\bar{F}h)}{\partial(\bar{U}h)}\widehat{U}h\right) - \frac{\partial\bar{P}}{\partial(\bar{U}h)}\widehat{U}h\frac{\partial h}{\partial x} = \epsilon\frac{\partial^2(\widehat{U}h)}{\partial x^2} \tag{3.29}$$

In Section 3.2.4, it was shown that to leading order the shock motion is a pure translation of the shock profile. This shock profile translation is represented by

$$\widehat{U}h = -\widehat{x}_s\frac{\partial(\bar{U}h)}{\partial x}, \tag{3.30}$$

which can be shown to be a solution to the perturbation Equation (3.29) where $\widehat{x}_s$ is the constant shock movement. To show this, Equation (3.30) is substituted into Equation (3.29).

$$\begin{aligned}
i\omega\widehat{U}h + \frac{\partial}{\partial x}\left(\frac{\partial(\bar{F}h)}{\partial(\bar{U}h)}\widehat{U}h\right) - \frac{\partial\bar{P}}{\partial(\bar{U}h)}\widehat{U}h\frac{\partial h}{\partial x} &= \epsilon\frac{\partial^2(\widehat{U}h)}{\partial x^2}\\
-i\omega\widehat{x}_s\frac{\partial(\bar{U}h)}{\partial x} - \frac{\partial}{\partial x}\left(\frac{\partial(\bar{F}h)}{\partial(\bar{U}h)}\widehat{x}_s\frac{\partial(\bar{U}h)}{\partial x}\right) + \frac{\partial\bar{P}}{\partial(\bar{U}h)}\widehat{x}_s\frac{\partial(\bar{U}h)}{\partial x}\frac{\partial h}{\partial x} &\overset{?}{=} -\epsilon\frac{\partial^2(\widehat{x}_s\frac{\partial(\bar{U}h)}{\partial x})}{\partial x^2}\\
-i\omega\frac{\partial(\bar{U}h)}{\partial x} - \frac{\partial}{\partial x}\left(\frac{\partial(\bar{F}h)}{\partial x}\right) + \frac{\partial\bar{P}}{\partial x}\frac{\partial h}{\partial x} &\overset{?}{=} -\epsilon\frac{\partial^3(\bar{U}h)}{\partial x^3}\\
\frac{\partial}{\partial x}\left(-i\omega\bar{U}h\right) - \frac{\partial}{\partial x}\left(\frac{\partial(\bar{F}h)}{\partial x} - \bar{P}\frac{\partial h}{\partial x} - \epsilon\frac{\partial^2(\bar{U}h)}{\partial x^2}\right) &\overset{?}{=} \bar{P}\frac{\partial^2 h}{\partial x^2}
\end{aligned} \tag{3.31}$$

This equation includes the equation for the steady state solution which is identically zero. The rest of the terms in this equation can be shown to be higher order than these terms. First, consider a balance of the terms $\frac{\partial}{\partial x}\left(-i\omega\bar{U}h\right)$ and $\frac{\partial}{\partial x}\left(\frac{\partial(\bar{F}h)}{\partial x}\right)$. Let the state vector $\bar{U}$ vary over the shock width δ and define the reduced frequency $k = \frac{\omega L}{\bar{c}}$, where L is some geometric length scale for the problem.

$$\begin{tikzcd}
-i\omega\bar{U}h \arrow[r, Leftrightarrow] \arrow[d] & \frac{\partial(\bar{F}h)}{\partial x} \arrow[d] \\
\omega\bar{U}h \arrow[d] & \frac{\bar{c}\bar{U}h}{\delta} \arrow[d] \\
k\frac{\bar{c}\bar{U}h}{L} & \frac{\bar{c}\bar{U}h}{\delta}
\end{tikzcd}$$

Since $\frac{L}{\delta} = Re$ and $k \ll O(Re)$, clearly the first term is higher order than the second term. Now check the balance of the terms:

$$\frac{\partial}{\partial x}\left(\hat{x}_s\frac{\partial(\bar{F}h)}{\partial x}\right) = \hat{x}_s\left(\bar{F}\frac{\partial^2 h}{\partial x^2} + 2\frac{\partial\bar{F}}{\partial x}\frac{\partial h}{\partial x} + h\frac{\partial^2\bar{F}}{\partial x^2}\right) \iff \hat{x}_s\bar{P}\frac{\partial^2 h}{\partial x^2}.$$

$\bar{F}$ and $\bar{P}$ are similar, as are any higher derivatives of these functions. In the shock these higher derivatives are not negligible. If the height of the duct, h, is slowly varying, than derivatives higher than the first derivative are negligible when compared to the constant and linear term. It can be seen that the first term given above is much larger than the second term since $\frac{\partial^2 h}{\partial x^2} \ll \frac{\partial^2\bar{F}}{\partial x^2}$. Neglecting these higher order terms, Equation (3.31) is now

$$\underbrace{\frac{\partial}{\partial x}\left(\frac{\partial(\bar{F}h)}{\partial x} - \bar{P}\frac{\partial h}{\partial x} - \epsilon\frac{\partial^2(\bar{U}h)}{\partial x^2}\right)}_{\text{equation for steady state} = 0} = 0,$$

which is identically true, so Equation (3.30) does indeed provide a solution to the perturbation Equation (3.29).

This solution will now be used to derive the jump conditions from the perturbation equation. First, each term of the perturbation equation is examined in turn.

$$\underbrace{i\omega\hat{U}h}_{1} + \underbrace{\frac{\partial}{\partial x}\left(\frac{\partial(\bar{F}h)}{\partial(\bar{U}h)}\hat{U}h\right)}_{2} - \underbrace{\frac{\partial\bar{P}}{\partial(\bar{U}h)}\hat{U}h\frac{\partial h}{\partial x}}_{3} = \underbrace{\epsilon\frac{\partial}{\partial x}\left(h\frac{\partial\hat{U}}{\partial x}\right)}_{4}$$

$$1)\qquad i\omega\hat{U}h = -i\omega\hat{x}_s\frac{\partial\bar{U}h}{\partial x}$$

$$= \frac{\partial}{\partial x}\left[-i\omega\hat{x}_s\bar{U}h\right]$$

$$2)\qquad \frac{\partial}{\partial x}\left(\frac{\partial(\bar{F}h)}{\partial(\bar{U}h)}\hat{U}h\right)$$

$$3)\qquad -\frac{\partial\bar{P}}{\partial(\bar{U}h)}\hat{U}h\frac{\partial h}{\partial x} = \frac{\partial\bar{P}}{\partial(\bar{U}h)}\hat{x}_s\frac{\partial\bar{U}h}{\partial x}\frac{\partial h}{\partial x}$$

$$= \hat{x}_s\frac{\partial\bar{P}}{\partial x}\frac{\partial h}{\partial x}$$

$$= \hat{x}_s\frac{\partial}{\partial x}\left(\bar{P}\frac{\partial h}{\partial x}\right) - \hat{x}_s\bar{P}\frac{\partial^2 h}{\partial x^2}$$

$$= \frac{\partial}{\partial x}\left[\hat{x}_s\frac{\partial(\bar{F}h)}{\partial x}\right] - \hat{x}_s\bar{P}\frac{\partial^2 h}{\partial x^2}$$

$$4)\qquad \epsilon\frac{\partial^2(\hat{U}h)}{\partial x^2} = -\epsilon\hat{x}_s\frac{\partial^3(\bar{U}h)}{\partial x^3}$$

$$= -\frac{\partial}{\partial x}\left[\hat{x}_s\epsilon\frac{\partial^2(\bar{U}h)}{\partial x^2}\right]$$

Putting these manipulated terms together gives

$$\frac{\partial}{\partial x}\left[-i\omega\hat{x}_s\bar{U}h + \frac{\partial(\bar{F}h)}{\partial(\bar{U}h)}\hat{U}h + \hat{x}_s\frac{\partial(\bar{F}h)}{\partial x} + \hat{x}_s\epsilon\frac{\partial^2(\bar{U}h)}{\partial x^2}\right] - \hat{x}_s\bar{P}\frac{\partial^2 h}{\partial x^2} = 0.$$

As discussed before, the last term is of higher order and can be neglected. The simulated viscosity terms away from the shock are negligible, so integrating over the shock gives

$$\left[\left[-i\omega\hat{x}_s\bar{U}h + \frac{\partial(\bar{F}h)}{\partial(\bar{U}h)}\hat{U}h + \hat{x}_s\frac{\partial(\bar{F}h)}{\partial x}\right]\right] = 0,$$

which is the same jump condition shown in Equation (2.40) found by linearizing the unsteady shock jump conditions.

It should be noted that a naive approach to finding the perturbation shock jump conditions from the perturbation equations can yield an incorrect result. Starting with the integral Equation (2.31) with the addition of the moving control volume term where $u_b = i\omega\,\widehat{x}_s$ gives

$$i\omega\int_1^2 \widehat{U} h\, dx \;=\; -\Big[(\bar{A}_1\widehat{U}h)_2 - (\bar{A}_1\widehat{U}h)_1\Big] + \Big[(i\omega\widehat{x}_s\bar{U}h)_2 - (i\omega\widehat{x}_s\bar{U}h)_1\Big] \;+\; \int_1^2 \bar{A}_2\widehat{U}\, dh\,. \tag{3.32}$$

If the integration interval is then taken to zero, it would be possible to think the resulting jump condition would be

$$[[\,\bar{A}_1\widehat{U}h - \bar{U}h\,i\omega\,\widehat{x}_s\,]] \;=\; 0, \tag{3.33}$$

which is incorrect. This was a mistake which was made by earlier researchers in this field [20], convincing them that using the perturbation equations with shock capturing would be impossible.

3.4 Conclusions

The shock-tube problem discussed in Section 3.1 showed that the location and movement of the shock are independent of the viscosity, which only governs the width of the shock profile. Next, in Section 3.2, it was shown that to leading order this is true for a variable area duct as well. Finally, the question of linearity was addressed, and it was found that the perturbation in lift is linear with the movement of the shock to leading order in the linear viscous and linear inviscid regions as well as the region in between. If the linear relationship is the same, than either solution can be found and linear scaling provides the solution for the other regions. Shock fitting represents the linear inviscid solution. For shock capturing the linear viscous solution is found. If there is a linear relationship between the shock movement and the lift perturbation, then it is possible to use the perturbation equations to find the unsteady perturbation directly.

Chapter 4

Computational Issues in Modeling the Euler Equations

Chapter 3 looked at the analytic issues associated with a moving shock, emphasizing the need to understand the flowfield before a computational model can be developed. In this chapter, computational issues will be addressed to ensure that the numerical solution is consistent with this analysis. Again, the discussion starts with the constant area duct since it provides a simple model of a flowfield in which the shock motion can be examined. Next, the issues which were found to be important in the constant area duct problem will be investigated in a variable area duct problem.

4.1 Constant Area Duct

In Section 3.1, the analytical solution to the shock-tube problem was discussed. It was found that, for both the steady solution and the unsteady solution, the viscosity only plays the role of scaling the shock region and not in the location or strength of the shock. Here, this knowledge will be used to model the shock computationally using artificial viscosity.

The computational methods used here will store the flow variables at discrete locations, or nodes, and use linear interpolation to find the values between the nodes. Aside from the usual concerns associated with numerical schemes, such as stability or accuracy, there are concerns in this problem associated with the shock region. If the shock is modeled as a highly stretched viscous region, the shape of the shock will still only be captured in a few cells. As a shock moves, the location of the shock in the discrete

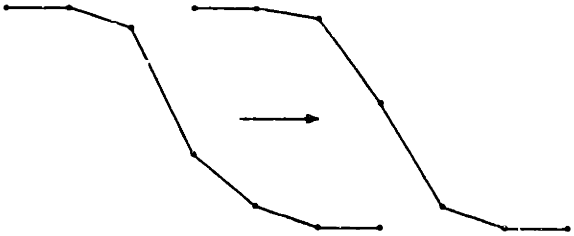

Figure 4.1: Change in the discrete shock shape as the shock moves.

approximation lands at a different place with respect to the computational nodes. By only knowing the solution at the nodes, the discrete shape of the moving shock will be different depending on its location with respect to the nodes as shown in Figure 4.1. What kind of error does this cause? The analytical solution is a true translation of the shock profile. Does the error due to the changing shock shape diminish in the integral of the quantity? As discussed earlier, the integrated solution is of interest since the integrated pressure represents the force on the surface, and would correspond to lift or drag in a multi dimensional application.

The first computational scheme which will be discussed uses the Euler equations and artificial viscosity, a term similar to the true viscous terms, to model the shock region. This is a nonlinear scheme with finite volume spatial discretization, constant grid spacing and a four-stage Runge-Kutta method to advance the solution in time. When artificial viscosity is used to capture the shock, the shock is smeared over several cells; the exact nature of the shock is dependent on the level of the coefficient.

The analytical version of the governing equation with an added artificial viscosity term is

$$\frac{\partial U}{\partial t} = -\left(\frac{\partial F_s}{\partial x} + \epsilon \frac{\partial}{\partial x}\left(\Delta x \frac{\partial U}{\partial x}\right)\right) = -R(U), \qquad (4.1)$$

where ϵ is the artificial viscosity coefficient. The term Δx is a measure of the grid spacing and is added to the equation to make the width of the shock proportional to the grid spacing. This term intentionally has a second derivative, as in the true viscosity terms, to model the nature of true viscosity.

The discretization in time is a four-stage Runge-Kutta scheme which will be written

$$\begin{aligned}
U^{(0)} &= U(t_n) \\
U^{(1)} &= U^{(0)} - \alpha_1 \Delta t \, R(U^{(0)}) \\
U^{(2)} &= U^{(0)} - \alpha_2 \Delta t \, R(U^{(1)}) \\
U^{(3)} &= U^{(0)} - \alpha_3 \Delta t \, R(U^{(2)}) \\
U^{(4)} &= U^{(0)} - \alpha_4 \Delta t \, R(U^{(3)}) \\
U(t_{n+1}) &= U^{(4)}
\end{aligned} \tag{4.2}$$

where

$$\alpha_1 = \tfrac{1}{4}, \qquad \alpha_2 = \tfrac{1}{3}, \qquad \alpha_3 = \tfrac{1}{2}, \qquad \alpha_4 = 1.$$

Each time through Equation (4.2) the solution is advanced forward by some time Δt, whose magnitude is limited due to stability considerations. The term $R(U)$ is a discrete representation of $\frac{\partial F_x}{\partial x}$ plus the artificial viscosity and is called the residual. In this case

$$R(U)_J = \frac{F_{J+\frac{1}{2}} - F_{J-\frac{1}{2}}}{\Delta x_J} - \epsilon \frac{(U_{J+1} - U_J) - (U_J - U_{J-1})}{\Delta x_J}, \tag{4.3}$$

where

$$F_{J+\frac{1}{2}} = \tfrac{1}{2}(F_{J+1} + F_J) \qquad F_{J-\frac{1}{2}} = \tfrac{1}{2}(F_J + F_{J-1}).$$

Figure 4.2 shows a representative shock shape for this kind of scheme. The shock region covers about eight cells in this case and produces a smooth transition between the upstream and downstream states.

Another important aspect of this scheme is that it is conservative. Conservation is a way of stating that Equation (3.11) holds regardless of what the control volume is when the analytical equations are modeled computationally. In other words, the flowfield becomes fully governed by the boundary conditions. In devising the numerical scheme, the control volume may be a single cell. For the case which will be discussed here, the control volume will be the computational space composed of several cells. In

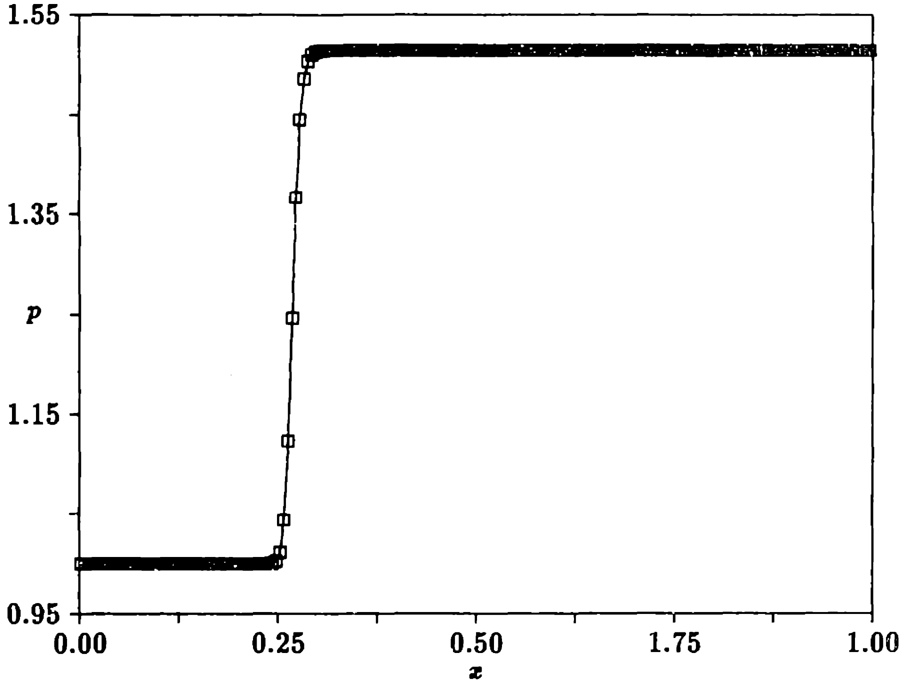

Figure 4.2: Pressure for relative inlet Mach number 1.2 shock with shock speed 0.1 and artificial viscosity coefficient 0.075.

a computational space where the index J represents the computational nodes and goes from 1 to $J_{\max}$, Equation (3.11) becomes

$$\sum_{1}^{J_{\max}} \left(\frac{\partial U}{\partial t}\right)_J \Delta x = -\sum_{1}^{J_{\max}} R(U)_J \Delta x = F_1 - F_{J_{\max}}. \tag{4.4}$$

Now, to determine if a scheme satisfies this equation, it is merely a matter of putting in the values for the residual from Equation (4.3). Here the boundary nodes are excluded from the summation, since boundary conditions provide a method for setting the values at these nodes.

$$\begin{aligned} \sum_{2}^{J_{\max}-1} R(U)_J \Delta x &= -\sum_{2}^{J_{\max}-1} \left\{ F_{J+\frac{1}{2}} - F_{J-\frac{1}{2}} - \epsilon\left[(U_{J+1} - U_J) - (U_J - U_{J-1}) \right] \right\} \\ &= -F_{J_{\max}-\frac{1}{2}} + F_{1+\frac{1}{2}} + \epsilon\left[(U_{J_{\max}} - U_{J_{\max}-1}) - (U_2 - U_1) \right] \end{aligned} \tag{4.5}$$

The important thing to notice is that the sum is only a function of the fluxes at the boundary cells. This is similar to the analytical result stated previously which said the flowfield is governed solely by the boundary conditions. Cancellation of the fluxes in the interior is the basis for this result.

There are computational methods which do not capture the shock with artificial viscosity, but rely on conservation to make the rest of the flowfield independent of the internal shape of the shock region. One such method which will be described here is similar to the one already described, but uses van Leer flux vector splitting [26]. The flux vector split scheme produces a nice crisp shock with two nodes in the shock, one each supersonic and subsonic. Upwinded differences are used such that the residual is now

$$R(U)_J = \frac{F_{J+\frac{1}{2}} - F_{J-\frac{1}{2}}}{\Delta x_J}, \tag{4.6}$$

where

$$F_{J+\frac{1}{2}} = F^+(U_J) + F^-(U_{J+1}) \qquad F_{J-\frac{1}{2}} = F^+(U_{J-1}) + F^-(U_J).$$

The fluxes F^+ and F^- are the upwinded fluxes which, depending on the local Mach number, are found from:

$M < 1$:

$$F^{\pm} = \begin{bmatrix} f_1^{\pm} \\ f_1^{\pm} \frac{[(\gamma-1)u \pm 2c]}{\gamma} \\ f_1^{\pm} \frac{[(\gamma-1)u \pm 2c]^2}{2(\gamma^2-1)} \end{bmatrix} \qquad \text{where} \qquad f_1^{\pm} = \pm\tfrac{1}{4}\rho c(1 \pm M)^2$$

$M > 1$:

$$F^+ = \begin{bmatrix} \rho u \\ \rho u^2 + p \\ \rho u H \end{bmatrix}, \qquad F^- = \begin{bmatrix} 0 \\ 0 \\ 0 \end{bmatrix}$$

One important feature of these upwind fluxes is that $F^+ + F^- = F$. The representative shock shape for the flux vector split scheme is shown in Figure 4.3.

It can be shown, as in the previous scheme, that the flux vector split scheme is conservative. The internal structure of the shock is merely a function of the scheme, similar

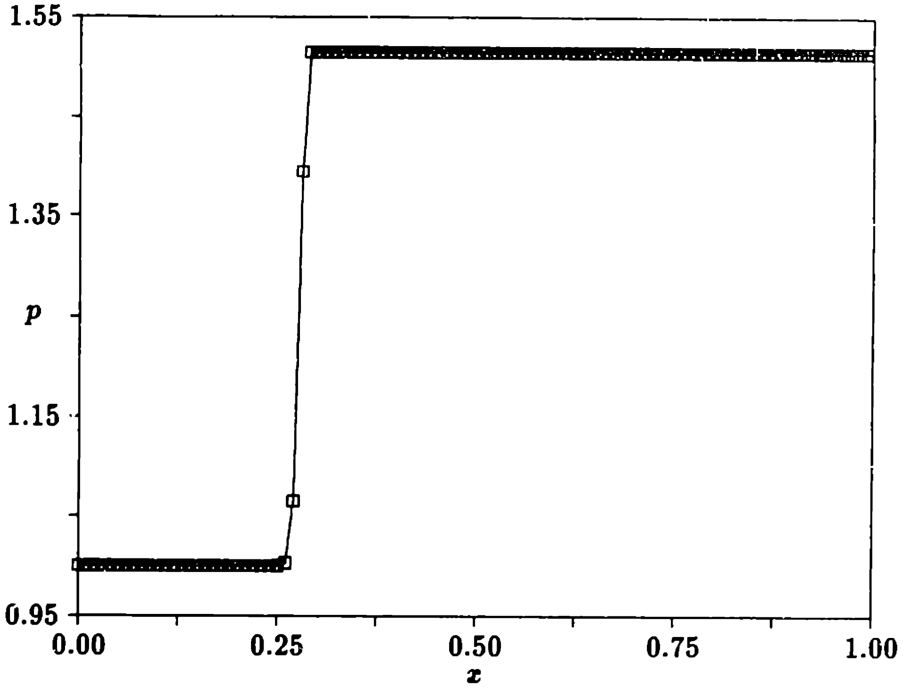

Figure 4.3: Pressure for relative inlet Mach number 1.2 shock with shock speed 0.1 for flux vector split scheme.

to the artificial viscosity scheme where the internal structure of the shock is a function of the artificial viscosity.

4.1.1 Computational Results

Since the two numerical schemes presented here are conservative, we are guaranteed that the overall solution follows the exact solution. But what is the effect of changing shock shape due to discretization as the shock moves? If the discrete shock is smooth enough, then this effect should be small because the shock shape is well resolved regardless of its location relative to the grid. Using artificial viscosity the shock is smeared out and keeps a similar profile from one iteration to the next. The scheme which produces the most crisp shocks is flux vector splitting, which forces only two points to be in the shock, and therefore has a more radically changing shock shape. This scheme should have a larger error due to discretization, and in fact represents a worst case for shock capturing schemes.

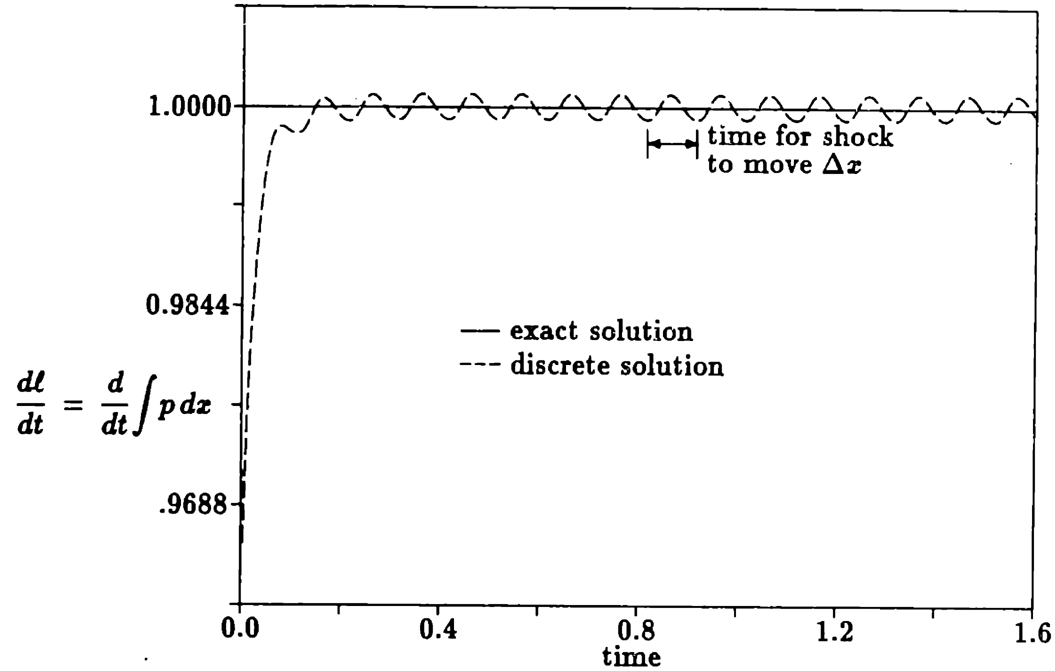

Figure 4.4: Time rate of change of integrated pressure normalized by the exact solution vs. time for relative inlet Mach number 1.2 shock with shock speed 0.1 for the flux vector split scheme.

To quantify the effects of discretization on the solution, the results are presented as the difference in the integral over the whole domain from one timestep to the next. The shock-tube problem has an exact solution given in Equation (3.11), which is only a function of the boundary values, to which the discrete value can be compared. For the conserved quantities in the state vector ρ, ρu and ρE, the difference in the integral should be a constant in the computational results (by the definition of conservation). Any other quantities may waver about the exact solution, but as the shock moves over several cells, will track with the exact solution since they are a function of these conserved quantities. As an example, the computational rate of change in integrated pressure normalized by the exact solution is shown in Figure 4.4 as a function of time for the flux vector split scheme. This is the same case for which the shock profile is shown in Figure 4.3. For small time, the shock shape is settling into its natural shape. As time progresses the function takes the shape of a periodic oscillation about the exact solution. The period of the oscillation is the time for the shock to move one computational cell. Roberts [25] found that this error can cause entropy waves to appear in the solution away from the shock. These waves have been seen in some of the cases run for this thesis as well.

To illustrate the effects of shock shape, both schemes were run for a range of Mach numbers. The rate of change of the integral of some quantity over the domain ($\frac{d}{dt}\int(\star)dx$) was found for several quantities. The effect of shock speed and CFL number were investigated, but the results were found to have a weak dependence on these parameters. The percent deviation from the exact solution (or error) as shown in Figure 4.4 was then computed, and is shown in Tables 4.1 to 4.6 and illustrated graphically in Figure 4.5. The conserved quantities, ρ, ρu and ρE, are not shown since they do not have a perturbation about the exact value, which is as it should be for a conservative scheme. It can be seen that when artificial viscosity is used, the shape of the shock is better preserved from one iteration to the next than it is in the flux vector split schemes, so the magnitude of the error is reduced. With the artificial viscosity scheme, as the coefficient is increased there are more nodes in the shock, and again the shape of the shock is better preserved, so the error is reduced. As the Mach number increases, the magnitude of the jump over the shock increases, and the error likewise increases. In most cases the error is quite small, particularly for the pressure integral.

4.1.2 Discussion of Computational Results

The results shown in the previous section are quite remarkable. For moderate relative Mach numbers, especially when artificial viscosity is used, the error due to the changing shock shape is much less than one percent. In this section the reason for this small error will be explored.

One method for analyzing the effect of the discretization on the governing equations is to produce the modified form of the analytical differential equation which is actually being solved computationally. The modified equation should have terms which include the grid spacing Δx and approach zero as the grid spacing is reduced to zero, producing the analytical equation in this limit. The Taylor series representation used to form the modified equation is only valid for a smooth function, so one limitation of the analysis

integrated quantity	magnitude of error	exact value	percent error
ρ	none	-0.03416	0.%
ρu	none	-0.00342	0.%
ρE	none	-0.10284	0.%
u	1.5564e-4	0.03615	0.43049%
M	2.2603e-4	0.03628	0.62308%
ρu^2	2.5670e-4	0.05099	0.50342%
p	5.1863e-5	-0.05133	0.10103%

Table 4.1: Errors due to the changing shock shape for flux vector split scheme with $M_{rel} = 1.2$.

integrated quantity	magnitude of error	exact value	percent error
ρ	none	-0.16667	0.%
ρu	none	-0.01667	0.%
ρE	none	-0.70083	0.%
u	3.7522e-3	0.14790	2.5370%
M	5.2626e-3	0.14421	3.6492%
ρu^2	1.5403e-2	0.34833	4.4220%
p	3.0760e-3	-0.35000	0.8789%

Table 4.2: Errors due to the changing shock shape for flux vector split scheme with $M_{rel} = 2.0$.

integrated quantity	magnitude of error	exact value	percent error
ρ	none	-0.35714	0.%
ρu	none	-0.03571	0.%
ρE	none	-3.50180	0.%
u	1.2981e-2	0.36975	3.5108%
M	9.7999e-2	0.36075	27.1651%
ρu^2	1.4097e-1	1.74643	8.0717%
p	2.8196e-2	-1.75000	1.6112%

Table 4.3: Errors due to the changing shock shape for flux vector split scheme with $M_{rel} = 4.0$.

integrated quantity	magnitude of error	exact value	percent error
ρ	none	-0.03416	0.%
ρu	none	-0.00342	0.%
ρE	none	-0.10284	0.%
u	1.3738e-5	0.03615	0.03800%
M	2.1255e-5	0.03628	0.05859%
ρu^2	1.9450e-5	0.05099	0.03815%
p	3.8910e-6	-0.05133	0.00758%

Table 4.4: Errors due to the changing shock shape for artificial viscosity coefficient $\epsilon = 0.075$ with $M_{rel} = 1.2$.

integrated quantity	magnitude of error	exact value	percent error
ρ	none	-0.16667	0.%
ρu	none	-0.01667	0.%
ρE	none	-0.70083	0.%
u	9.8373e-4	0.14790	0.6651%
M	4.4097e-3	0.14421	3.0578%
ρu^2	3.7018e-3	0.34833	1.0627%
p	6.4416e-4	-0.35000	0.1840%

Table 4.5: Errors due to the changing shock shape for artificial viscosity coefficient $\epsilon = 0.075$ with $M_{rel} = 2.0$.

integrated quantity	magnitude of error	exact value	percent error
ρ	none	-0.16667	0.%
ρu	none	-0.01667	0.%
ρE	none	-0.70083	0.%
u	2.2064e-4	0.14790	0.14918%
M	1.1591e-3	0.14421	0.80377%
ρu^2	7.0762e-4	0.34833	0.20314%
p	1.5561e-4	-0.35000	0.04446%

Table 4.6: Errors due to the changing shock shape for artificial viscosity coefficient $\epsilon = 0.1$ with $M_{rel} = 2.0$.

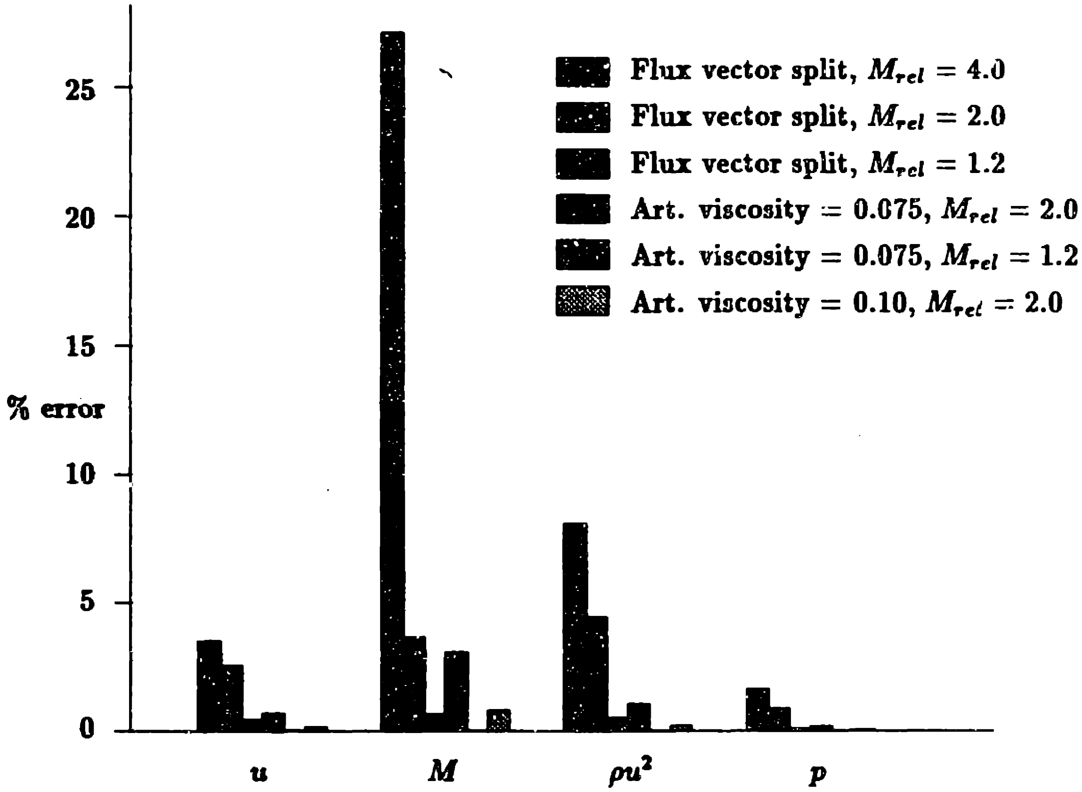

Figure 4.5: For various schemes, the percent error in $\frac{d}{dt}\int(\star)dx$ from the exact solution for the quantities u, M, ρu^2 and p. The data for this graph is given in Tables 4.1 to 4.6.

is that the flowfield must be reasonably smooth; in other words, the analysis is only valid for the scheme which uses artificial viscosity. Forming the Taylor series for U and F at nodes $J+1$ and $J-1$ gives:

$$\begin{aligned}
U_{J+1} &= U_J + \Delta x\left(\frac{\partial U}{\partial x}\right)_J + \tfrac{1}{2}\Delta x^2\left(\frac{\partial^2 U}{\partial x^2}\right)_J + \tfrac{1}{6}\Delta x^3\left(\frac{\partial^3 U}{\partial x^3}\right)_J + \tfrac{1}{24}\Delta x^4\left(\frac{\partial^4 U}{\partial x^4}\right)_J + \cdots \\
U_{J-1} &= U_J - \Delta x\left(\frac{\partial U}{\partial x}\right)_J + \tfrac{1}{2}\Delta x^2\left(\frac{\partial^2 U}{\partial x^2}\right)_J - \tfrac{1}{6}\Delta x^3\left(\frac{\partial^3 U}{\partial x^3}\right)_J + \tfrac{1}{24}\Delta x^4\left(\frac{\partial^4 U}{\partial x^4}\right)_J - \cdots \\
F_{J+1} &= F_J + \Delta x\left(\frac{\partial F}{\partial x}\right)_J + \tfrac{1}{2}\Delta x^2\left(\frac{\partial^2 F}{\partial x^2}\right)_J + \tfrac{1}{6}\Delta x^3\left(\frac{\partial^3 F}{\partial x^3}\right)_J + \tfrac{1}{24}\Delta x^4\left(\frac{\partial^4 F}{\partial x^4}\right)_J + \cdots \\
F_{J-1} &= F_J - \Delta x\left(\frac{\partial F}{\partial x}\right)_J + \tfrac{1}{2}\Delta x^2\left(\frac{\partial^2 F}{\partial x^2}\right)_J - \tfrac{1}{6}\Delta x^3\left(\frac{\partial^3 F}{\partial x^3}\right)_J + \tfrac{1}{24}\Delta x^4\left(\frac{\partial^4 F}{\partial x^4}\right)_J - \cdots
\end{aligned}$$

Placing these functions into Equation (4.3), the discrete equation for the artificial viscosity scheme, and assuming Δx is constant gives:

$$\begin{aligned}
R(U)_J &= \frac{F_{J+\frac{1}{2}} - F_{J-\frac{1}{2}}}{\Delta x_J} - \epsilon\frac{(U_{J+1} - U_J) - (U_J - U_{J-1})}{\Delta x_J} \\
&= \frac{1}{2}\,\frac{F_{J+1} - F_{J-1}}{\Delta x_J} - \epsilon\frac{U_{J+1} - 2U_J + U_{J-1}}{\Delta x_J} \\
&= \frac{1}{2\,\Delta x}\Bigg[F_J + \Delta x\left(\frac{\partial F}{\partial x}\right)_J + \tfrac{1}{2}\Delta x^2\left(\frac{\partial^2 F}{\partial x^2}\right)_J + \tfrac{1}{6}\Delta x^3\left(\frac{\partial^3 F}{\partial x^3}\right)_J + \tfrac{1}{24}\Delta x^4\left(\frac{\partial^4 F}{\partial x^4}\right)_J + \cdots \\
&\qquad - F_J + \Delta x\left(\frac{\partial F}{\partial x}\right)_J - \tfrac{1}{2}\Delta x^2\left(\frac{\partial^2 F}{\partial x^2}\right)_J + \tfrac{1}{6}\Delta x^3\left(\frac{\partial^3 F}{\partial x^3}\right)_J - \tfrac{1}{24}\Delta x^4\left(\frac{\partial^4 F}{\partial x^4}\right)_J + \cdots\Bigg] \\
&\quad -\epsilon\frac{1}{\Delta x}\Bigg[U_J + \Delta x\left(\frac{\partial U}{\partial x}\right)_J + \tfrac{1}{2}\Delta x^2\left(\frac{\partial^2 U}{\partial x^2}\right)_J + \tfrac{1}{6}\Delta x^3\left(\frac{\partial^3 U}{\partial x^3}\right)_J + \tfrac{1}{24}\Delta x^4\left(\frac{\partial^4 U}{\partial x^4}\right)_J + \cdots \\
&\qquad - 2\,U_J \\
&\qquad + U_J - \Delta x\left(\frac{\partial U}{\partial x}\right)_J + \tfrac{1}{2}\Delta x^2\left(\frac{\partial^2 U}{\partial x^2}\right)_J - \tfrac{1}{6}\Delta x^3\left(\frac{\partial^3 U}{\partial x^3}\right)_J + \tfrac{1}{24}\Delta x^4\left(\frac{\partial^4 U}{\partial x^4}\right)_J - \cdots\Bigg] \\
&= \left[\frac{\partial F}{\partial x} - \epsilon\frac{\partial}{\partial x}\left(\Delta x\frac{\partial U}{\partial x}\right)\right]_J + \left[\tfrac{1}{6}\Delta x^2\left(\frac{\partial^3 F}{\partial x^3}\right) - \tfrac{\epsilon}{12}\Delta x^3\left(\frac{\partial^4 U}{\partial x^4}\right) + \cdots\right]_J
\end{aligned}$$

The first bracketed expression in this equation is the analytical expression which is modeled. The second expression is an infinite series in increasing powers of Δx and is the truncation error for the equation, the error induced in the discrete formulation of the analytical equation. One very important point is that in the limit as Δx goes to zero, the truncation error also goes to zero and the original equation is obtained.

Now look at the truncation error term in more detail. Since the mesh spacing Δx is constant, this term can be rewritten as

$$\frac{\partial^2}{\partial x^2}\left(\frac{1}{6}\Delta x^2\left(\frac{\partial F}{\partial x}\right) - \frac{\epsilon}{12}\Delta x^3\left(\frac{\partial^2 U}{\partial x^2}\right) + \cdots\right),$$

which is zero away from the shock region. This term acts similarly to the viscosity term in the analytical equation, and only contributes to the shape of the shock. What this shows is that the effect of the truncation error is to add another conservative term which has no effect on the location or strength of the shock. This modified equation analysis contributes to an explanation of why the artificial viscosity scheme has such small errors, since discretization does not introduce global errors into the solution.

Another explanation for why the errors are small can be seen by looking at the trapezoidal integration formula [8, pages 290-301]. Trapezoidal integration of a function is described on the interval $[a, b]$ with grid spacing Δx as

$$\int_a^b f(x)\,dx \approx \hat{T}(\Delta x) = \Delta x\left(\tfrac{1}{2}f_0 + f_1 + f_2 + \cdots + f_{J-1} + \tfrac{1}{2}f_J\right). \tag{4.7}$$

This formula is based on piecewise linear interpolation in the intervals (x_{j-1}, x_j), $j = 1, 2, \ldots, J$ as shown in Figure 4.6.

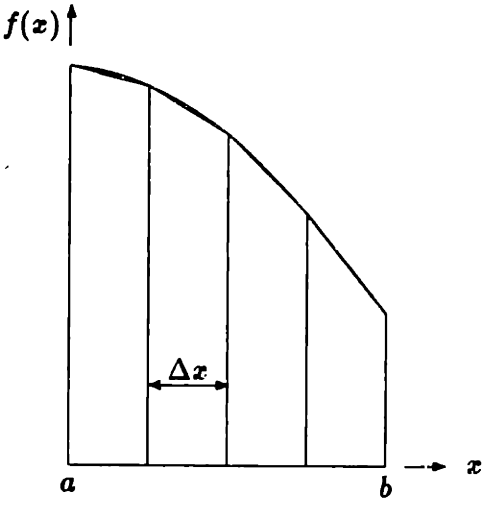

Figure 4.6: Representation of trapezoidal integration.

We are interested in the error associated with trapezoidal integration. For some value of p, this error is defined by the Euler-Maclaurin summation formula:

$$\int_a^b f(x)\,dx \;=\; \hat{T}(\Delta x) \;-\; \sum_{i=1}^{p-2} c_{i+1}(\Delta x)^{i+1}\left(f^{(i)}(b) - f^{(i)}(a)\right) \;-\; \sum_{j=1}^{J} Q_j , \tag{4.8}$$

where

$$\left|\sum_{j=1}^{J} Q_j\right| \;\leq\; |2c_p(\Delta x)^p| \cdot \int_a^b |f^{(p)}(x)|\,dx.$$

Equation (4.8) shows that the first error term in the trapezoidal integration is a function of the derivative of the integrand at the boundaries. In most cases this would be the dominant error, but in the shock-tube case the spatial derivatives of the solution at the boundaries go to zero. This produces the result that the error in the integration approaches zero faster than any power of Δx for a shock of fixed shape. For a shock with artificial viscosity parameter ϵ, $f^{(p)}(x) = O((\epsilon \Delta x)^{-p})$ in the shock region of width $O(\epsilon \Delta x)$, so $|\sum Q| = O(\Delta x\, \epsilon^{1-p})$ and the error essentially goes to zero faster than any power of ϵ^{-1}.

Another very interesting feature of these results is that the integrated pressure, or lift, has a smaller relative error than other non-conserved integrated values. The lift is of more interest than any other integral value, so this is a particularly pleasing result. This result appears to come from the relation between the pressure and the conserved quantity ρE, total energy. The time rate of change of integrated pressure can be written as

$$\frac{d}{dt}\int p\,dx \;=\; (\gamma-1)\left[\frac{d}{dt}\int \rho E\,dx \;-\; \tfrac{1}{2}\frac{d}{dt}\int \rho u^2 dx\right]. \tag{4.9}$$

In the case of a zero width, inviscid shock, this is another statement of the shock jump relations

$$[[p]] \;=\; (\gamma-1)\Big([[\rho E]] \;-\; \tfrac{1}{2}[[\rho u^2]]\Big). \tag{4.10}$$

Manipulating the shock jump relations in Equation (3.16),

$$[[\,\rho u^2 + p - \dot{x}_s \rho u\,]] \;=\; 0 \quad \text{and} \quad [[\,\rho u - \dot{x}_s \rho\,]] \;=\; 0,$$

produces

$$\begin{aligned} [[\,\rho u^2 + p - \dot{x}_s \rho u\,]] &= 0 \\ [[\,p\,]] &= -[[\,\rho u^2\,]] \;+\; \dot{x}_s [[\,\rho u\,]] \\ &= -[[\,\rho u^2\,]] \;+\; \dot{x}_s^2\, [[\,\rho\,]]. \end{aligned}$$

When $\gamma = 1.4$ and the shock speed is small, the second term in Equation (4.10) contributes an amount which is only 20% of the total jump in pressure,

$$\frac{-\frac{1}{2}(\gamma-1)[[\,\rho u^2\,]]}{[[\,p\,]]} \;=\; \tfrac{1}{2}(\gamma-1) - \dot{x}_s^2 \frac{[[\,\rho\,]]}{[[\,p\,]]} \;\approx\; 0.20, \tag{4.11}$$

so the conserved quantity ρE contributes 80% to the rate of change of the integral. Since this larger term does not contribute to the errors, due to conservation, all these errors come from the much smaller $\frac{1}{2}\rho u^2$ contribution.

4.2 Variable Area Duct

In Section 3.2 the leading order relationship between the integrated pressure, or lift, and the location of the shock was shown to be linear. An important point in this analysis is that analytically the shock shape would remain similar as it moved. Here, the effects of discretization on this result will be examined. In particular, since the discrete solution is only known at computational nodes and linear interpolation is used between these nodes, a discrete shock shape does not remain similar as it moves relative to the mesh. As with the constant area duct or shock-tube problem in Section 4.1, the effect of the changing shock shape will be quantified, except now there will be variation in the flowfield upstream and downstream of the shock.

In Section 4.1, the effect of the changing shock shape on an integrated quantity was found to be very small for the shock-tube problem. In essence, the results from the shock-tube problem are directly applicable to the variable area duct (since it is the effect of changing shock shape which is in question) but to justify this statement an example will be presented. The problem will be a quasi-steady, quasi-one-dimensional duct problem with variable exit pressure. The focus will be on the definition of linearity, or that one solution multiplied by some constant is another solution. Here the relationship between the lift and the exit pressure for a transonic duct will be examined. If there is a linear relationship between these variables the following relationship will hold.

$$\hat{l} = \left(\frac{d\bar{l}}{d\bar{p}_{exit}}\right)\hat{p}_{exit} \tag{4.12}$$

The example given here will test the validity of Equation (4.12) for an analytic and a computational problem.

In Figure 4.7, two similar transonic flow solutions are shown for two exit pressures $p_{exit} = 0.4893$ and $p_{exit} = 0.4983$. Since the steady, variable area duct has an exact solution, this is essentially what is plotted here. All that was varied to find these solutions was the exit pressure. A solution with an exit pressure between these two bounds would fall somewhere between these solutions, which in essence form an envelope for a whole set of solutions. In Figure 4.8, the steady lift for these solutions is plotted as a function of exit pressure in this envelope. Notice that the relationship between these variables is nearly linear. When a linear function is subtracted from the steady lift, $\bar{l}$, to create a new variable $\bar{l}'$, it can be seen that the relationship is not exactly linear, but contains some slight nonlinearity. It can now be said that to leading order the relationship between lift and exit pressure follows Equation (4.12), and the flow is linear. This is the result that would be expected given the analysis in Section 3.2. In Figure 4.9, a set of symbols has been added to the plots shown in Figure 4.8. These symbols present results from several computational solutions, where each symbol represents a separate steady calculation. The computational scheme uses second difference artificial viscosity of the type discussed in the previous section with coefficient $\epsilon = 0.1$ (described in more

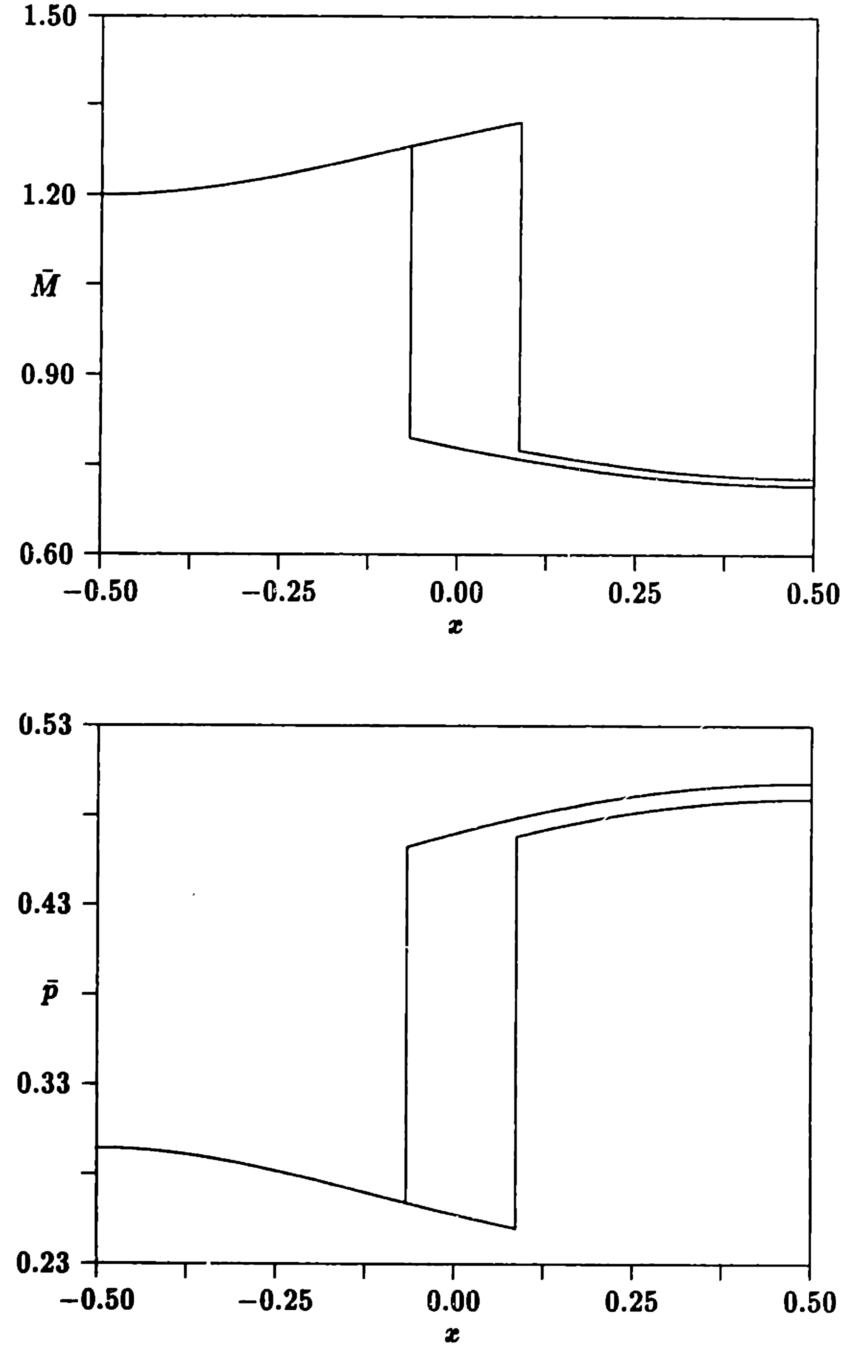

Figure 4.7: Mach number and pressure distribution for two flow solutions defined by two different exit pressures which form an envelope for solutions with exit pressures between these bounds.

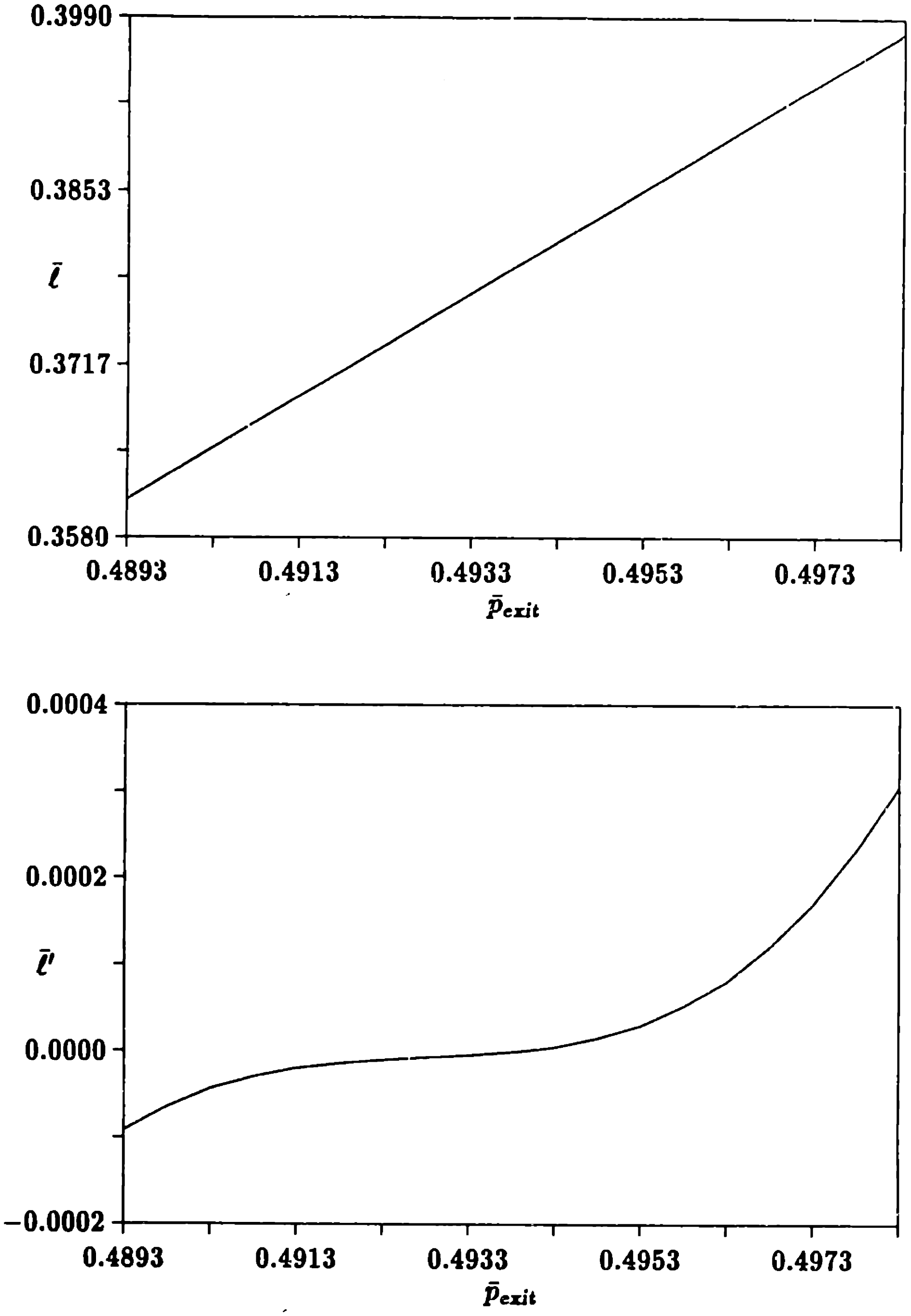

$$\bar{\ell}' = \bar{\ell} - (-1.6161 + 4.0409 \times \bar{p}_{exit})$$

Figure 4.8: Steady lift as a function of exit pressure in the envelope defined by solutions shown in Figure 4.7 for exact solutions and this function after the linear terms are removed.

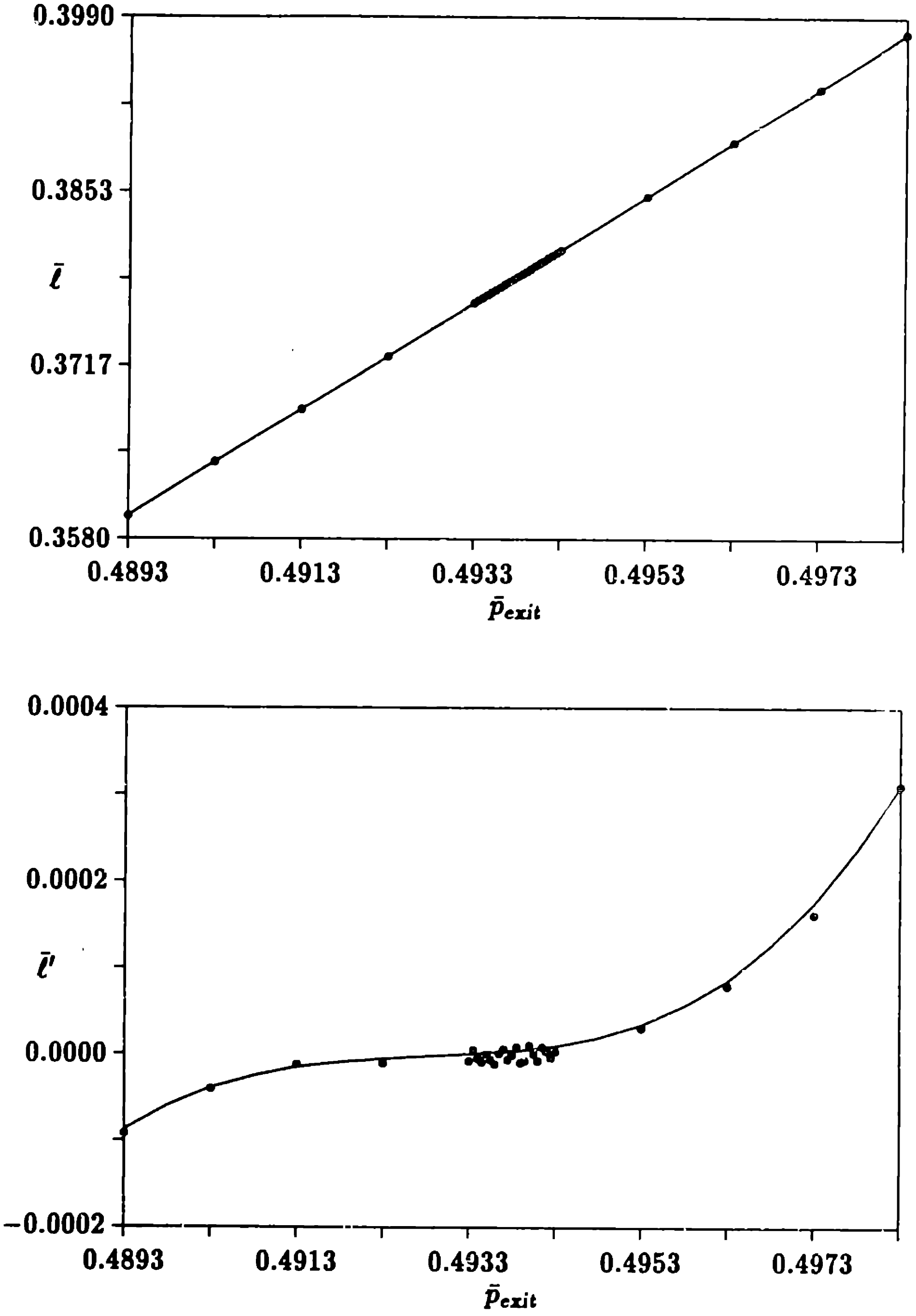

$$\bar{\ell}' = \bar{\ell} - (-1.6161 + 4.0409 \times \bar{p}_{exit})$$

Figure 4.9: Steady lift as a function of exit pressure for the envelope defined by solutions shown in Figure 4.7 for exact solutions and computational solutions, and this function after the linear terms are removed. The computational solution is only sampled at the symbols.

detail in Section 5.1.1). More samples were taken in the center of the domain, illustrated by the greater clustering of the symbols. In this region, the symbols deviate from the exact solution. This is due to the changing shock shape which was seen in the shock-tube problem in Section 4.1.1 and this pattern of deviation from the exact solution should continue through the whole domain. The error due to the changing shock shape in this solution is approximately 0.04%. This computational error represents such a small deviation from the linearity that linearity can be assumed to exist for the computational solution as well as the exact solution.

Again, the effect of changing shock shape in the variable area duct is the same effect illustrated with the constant area duct shock-tube. The errors associated with this changing shock shape are of the same magnitude as the errors found for similar shock-tube problems.

4.3 Conclusions

The effect of discretization on the results presented in Chapter 3 were presented in this chapter. Computationally, a shock profile will have a different shape as the shock moves relative to the grid, since the solution between grid nodes is found by linear interpolation. The changing shock shape in the computational solution introduces errors into the unsteady solution.

When the error in the solution is measured in terms of the integral of a quantity, conservation says the conserved quantities, ρ, ρu and ρE, will have no error. The non-conserved quantities, however, do have errors due to the changing shape of the shock. These errors were shown to be small for the shock-tube, particularly in the integrated pressure, or lift, which is of great interest in fluid mechanics. The error is larger for the flux vector split scheme than for the scheme where artificial viscosity is used to capture the shock. The error in the artificial viscosity schemes decreases as the artificial viscosity is increased. This result was expected since a smoother shock is more likely to retain its shape as it moves, but can be explained in other ways as well. The net result is that these errors are small enough to be considered negligible and we need not be concerned about them in our calculations. This result applies equally to the shock-tube and variable area duct problems and should extend to higher dimensional problems as well.

The results in this chapter are important since they mean it is possible to model the small movement of the shock with a computational scheme. The fact that the error due to a changing discrete shock shape is small implies that the results found in Chapter 3 not only hold analytically, but for a discrete problem as well. At this point, computational schemes which assume the flow field is linear will be formed and results from these schemes will be presented.

Chapter 5

Numerical Scheme

In Chapter 2 the governing equations for a quasi-one-dimensional duct were derived. Two sets of equations, one for the steady state and the other for a linear harmonic perturbation were then formed. In Chapter 3 it was shown that the role of viscosity in the steady solution was to scale the width of the shock and not to determine the location or strength of the shock. In the unsteady solution it was shown that the integrated solution, such as the lift, was linear with the unsteady perturbation imposed on the flowfield, again independent of the level of the viscosity. Since the absolute level of the viscosity only governs the width of the shock, artificial viscosity can be used in the solution to form a shock with a width on the order of a few computational cells. In this chapter, the discrete forms of the governing equations will be found. Two different forms of artificial viscosity as well as flux vector splitting will be used to capture the shocks. A shock fitting scheme is also described, since this represents the zero shock width limit. Finally, a method of solving for the perturbation where the computational grid moves is described.

5.1 Artificial Viscosity Schemes

The computation of the steady state and perturbation solutions decouple. First the steady state solution is found, then the perturbation solution can be calculated using the known steady solution to find the coefficients for the perturbation equation. For the artificial viscosity scheme, the spatial discretization for the steady state will be explained in detail, then the spatial discretization for the perturbation will be given. The two procedures are similar and, in fact, the discrete perturbation equations are a true linearization of the unsteady discrete equations used to find the steady state.

The Runge-Kutta temporal discretization which is used to find both solutions is then described.

5.1.1 Steady State

To develop a finite volume numerical scheme, the computational domain is divided into several control volumes of a size determined by the mesh spacing. Since the discrete equations will be found for these control volumes, the integral form of the governing equations are used instead of the differential form. The unsteady, nonlinear integral Equation (2.17) with no control volume movement is

$$\frac{d}{dt}\int_1^2 Uh\,dx \;=\; -\Big[(Fh)_2 - (Fh)_1\Big] \;+\; \int_1^2 P\,dh. \tag{5.1}$$

A schematic of the computational mesh is given in Figure 5.1, where the node indices go from 1 to J_{max}. The state vector is stored at each of the nodes (represented by dots), and the finite volume discretization involves the neighboring nodes. The control volume for each of the nodes is denoted by the dashed lines in Figure 5.1. When applying Equation (5.1) to the computational control volume, the solution will be assumed to vary linearly between the nodes, so the value at the edge of the control volume is the average of the adjacent nodes.

The spatial discretization will be dealt with first. For now the semi-discrete representation of Equation (5.1) is

$$\begin{aligned}\frac{d}{dt}\Big[\tfrac{1}{2}(h_{J+\frac{1}{2}} + h_{J-\frac{1}{2}})U_J\Delta x_J\Big] \;=&\\ -\Big[h_{J+\frac{1}{2}}F_{J+\frac{1}{2}} - h_{J-\frac{1}{2}}F_{J-\frac{1}{2}}\Big] \;+&\; \tfrac{1}{2}(P_{J+\frac{1}{2}} + P_{J-\frac{1}{2}})(h_{J+\frac{1}{2}} - h_{J-\frac{1}{2}}).\end{aligned} \tag{5.2}$$

For simplicity in writing and understanding of the finite volume discretization, the following have been defined:

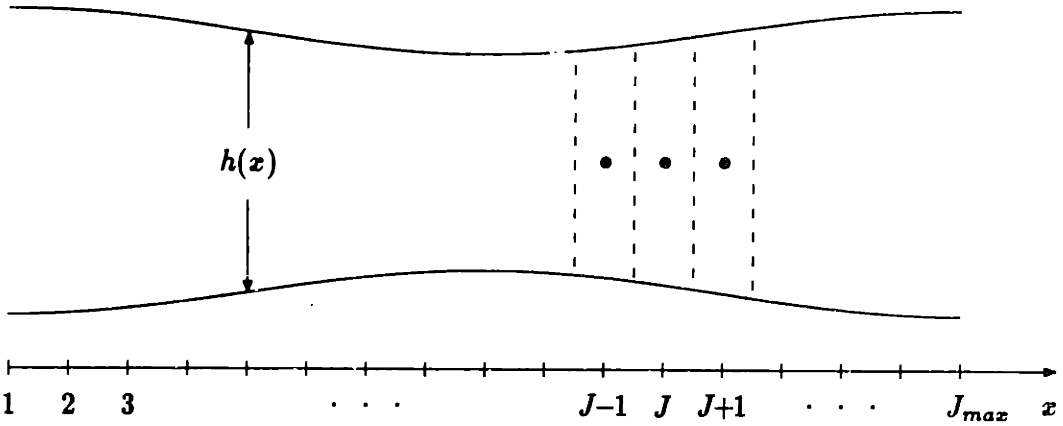

Figure 5.1: Computational mesh for a quasi one-dimensional duct.

$$
\begin{aligned}
&\Delta x_J = \tfrac{1}{2}(x_{J+1} - x_{J-1}), && && \\
&h_{J+\frac{1}{2}} = \tfrac{1}{2}(h_J + h_{J+1}), && F_{J+\frac{1}{2}} = \tfrac{1}{2}(F_J + F_{J+1}), && P_{J+\frac{1}{2}} = \tfrac{1}{2}(P_J + P_{J+1}), \\
&h_{J-\frac{1}{2}} = \tfrac{1}{2}(h_J + h_{J-1}), && F_{J-\frac{1}{2}} = \tfrac{1}{2}(F_J + F_{J-1}), && P_{J-\frac{1}{2}} = \tfrac{1}{2}(P_J + P_{J-1}).
\end{aligned}
$$

The steady state is reached when there is no change in time, or $\frac{\partial}{\partial t} = 0$. The steady solution then satisfies the equation

$$
-\left[h_{J+\frac{1}{2}}\bar{F}_{J+\frac{1}{2}} - h_{J-\frac{1}{2}}\bar{F}_{J-\frac{1}{2}}\right] + \tfrac{1}{2}(\bar{P}_{J+\frac{1}{2}} + \bar{P}_{J-\frac{1}{2}})(h_{J+\frac{1}{2}} - h_{J-\frac{1}{2}}) = 0. \qquad (5.3)
$$

The height of the duct and the mesh spacing are set in the problem definition and are not a function of time, therefore they may be taken outside the time derivative in Equation (5.2). When the equation is rearranged such that all that remains on the left hand side is the time derivative of the state vector, this equation can be written

$$
\left(\frac{\partial U}{\partial t}\right)_J = -R(U_J), \qquad (5.4)
$$

where $R(U_J)$ represents what will be termed the flux residual

$$
\begin{aligned}
R(U_J) \;=\; & \left(\frac{1}{\Delta x_J \frac{1}{2}(h_{J+\frac{1}{2}} + h_{J-\frac{1}{2}})}\right) \times \\
& \left((h_{J+\frac{1}{2}} F_{J+\frac{1}{2}} - h_{J-\frac{1}{2}} F_{J-\frac{1}{2}}) \;-\; \tfrac{1}{2}(P_{J+\frac{1}{2}} + P_{J-\frac{1}{2}})\,(h_{J+\frac{1}{2}} - h_{J-\frac{1}{2}})\right).
\end{aligned}
\tag{5.5}
$$

This discretization is second order accurate.

The temporal discretization of Equation (5.4) will be described in Section 5.1.3.

Second Difference Artificial Viscosity

To capture shocks, a term which looks similar to a viscosity term is added to the equation. This new term will be called artificial viscosity. As a first approximation, the artificial viscosity term will be modeled with a second difference which bears a large resemblance to the true form of viscosity.

$$
\frac{1}{h}\left[\epsilon_2 \frac{\partial}{\partial x}\left(h\left(\tfrac{\Delta x}{\Delta t_{max}}\right)\Delta x \frac{\partial U}{\partial x}\right)\right]
\tag{5.6}
$$

ϵ_2 is the artificial viscosity coefficient which takes values in the range 0.0001 → 0.1 and is held constant. The difference $\Delta x \frac{\partial U}{\partial x}$ is used rather than the derivative $\frac{\partial U}{\partial x}$ to make the smoothing of sawtooth modes independent of the mesh size. The factor $h(\frac{\Delta x}{\Delta t_{max}})$ is necessary to make the artificial viscosity term scale correctly with the flux term, and is appropriately placed to ensure that the scheme will be conservative. The computation these timestep terms is discussed in more detail in Section 5.1.3.

Similar to the discretization of the governing equation, the artificial viscosity term is also discretized

$$
\begin{aligned}
D(U_J) \;=\; & \epsilon_2 \left(\frac{1}{\Delta x_J \frac{1}{2}(h_{J+\frac{1}{2}} + h_{J-\frac{1}{2}})}\right) \times \\
& \left(h_{J+\frac{1}{2}}\left(\tfrac{\Delta x}{\Delta t_{max}}\right)_{J+\frac{1}{2}}(U_{J+1} - U_J) \;-\; h_{J-\frac{1}{2}}\left(\tfrac{\Delta x}{\Delta t_{max}}\right)_{J-\frac{1}{2}}(U_J - U_{J-1})\right).
\end{aligned}
\tag{5.7}
$$

This term has a discretization error $\sim \epsilon_2 \Delta x$, which is to say it is first order accurate. When the artificial viscosity is added to Equation (5.4), the equation becomes

$$\left(\frac{\partial U}{\partial t}\right)_J = -R(U_J) + D(U_J). \tag{5.8}$$

Fourth Difference Artificial Viscosity

In order to have sufficient levels of artificial viscosity near the shock using just second difference artificial viscosity, the smooth regions of the flowfield tend to get more artificial viscosity than is necessary. To remedy this, the second difference artificial viscosity is only turned on in regions where there are shocks and a fourth difference artificial viscosity is used in the rest of the flowfield. It has been found that detecting the second difference of pressure and using this as a switch for the second difference artificial viscosity works well in practice. The fourth difference artificial viscosity is turned off in the shock region, since it over-damps the high frequency nature of the shock. This type of artificial viscosity has the analytical form

$$\frac{1}{h}\left[-\epsilon_4 \frac{\partial}{\partial x}\left((1-S)\,h\left(\tfrac{\Delta x}{\Delta t_{\max}}\right)\Delta x^3 \frac{\partial^3 U}{\partial x^3}\right) + \epsilon_2 \frac{\partial}{\partial x}\left(S\,h\left(\tfrac{\Delta x}{\Delta t_{\max}}\right)\Delta x \frac{\partial U}{\partial x}\right)\right], \tag{5.9}$$

where S is the switch which has a maximum value of 1 in the shock and is zero in smooth regions away from the shock. ϵ_2 and ϵ_4 are the two artificial viscosity coefficients. For this type of artificial viscosity the term defined in the previous section as $D(U_J)$ now becomes

$$\begin{aligned} D(U_J) \;=\; & \left(\frac{1}{\Delta x_J \frac{1}{2}(h_{J+\frac{1}{2}} + h_{J-\frac{1}{2}})}\right) \times \\ & \left[-\epsilon_4 \left((1 - S_{J+\frac{1}{2}})\, h_{J+\frac{1}{2}} \left(\frac{\Delta x}{\Delta t_{\max}}\right)_{J+\frac{1}{2}} (D^2 U_{J+1} - D^2 U_J) \right.\right. \\ & \left. -(1 - S_{J-\frac{1}{2}})\, h_{J-\frac{1}{2}} \left(\frac{\Delta x}{\Delta t_{\max}}\right)_{J-\frac{1}{2}} (D^2 U_J - D^2 U_{J-1}) \right) + \\ & \epsilon_2 \left(S_{J+\frac{1}{2}} h_{J+\frac{1}{2}} \left(\frac{\Delta x}{\Delta t_{\max}}\right)_{J+\frac{1}{2}} (U_{J+1} - U_J) \right. \\ & \left.\left. - S_{J-\frac{1}{2}} h_{J-\frac{1}{2}} \left(\frac{\Delta x}{\Delta t_{\max}}\right)_{J-\frac{1}{2}} (U_J - U_{J-1}) \right)\right] \end{aligned} \tag{5.10}$$

where the numerical second difference is defined as

$$D^2 U_J \;=\; (U_{J+1} - U_J) - (U_J - U_{J-1}) \tag{5.11}$$

This artificial viscosity has an error $\sim \epsilon_4 \Delta x^3$ in regions of the flowfield away from the shock. The switch is given by

$$S_J \;=\; \frac{s_J}{\max(s_J)}, \tag{5.12}$$

where

$$s_J \;=\; \mathrm{abs}\left[\frac{(p_{J+1} - p_J) - (p_J - p_{J-1})}{p_J}\right]. \tag{5.13}$$

Some characteristics of the switch are that it is small in regions where the flowfield is smooth and it is strictly positive so the second difference artificial viscosity is turned on equally in regions of positive and negative curvature. By dividing by $\max(s_J)$, the maximum value of S_J is 1.

5.1.2 Linear Perturbation

In Chapter 2, to find the linear perturbation, the unsteady state vector was assumed to take the form

$$U(x,t) = \bar{U}(x) + \Re\{\widehat{U}(x,t)\, e^{i\omega t}\},$$

for which $\bar{U}(x)$ is the steady state solution found in the previous section, and the governing equation for $\widehat{U}(x,t)$ in integral form with no mesh movement is

$$\frac{d}{dt}\int_1^2 \widehat{U} h\, dx + i\omega \int_1^2 \widehat{U} h\, dx = -\left[(\bar{A}_1 \widehat{U} h)_2 - (\bar{A}_1 \widehat{U} h)_1\right] + \int_1^2 (A_2 \widehat{U})\, dh. \tag{5.14}$$

This equation will be advanced in time until there is no change in time so that eventually $\widehat{U}(x)$ will only be a function of space. The linearization matrices $\bar{A}_1$ and $\bar{A}_2$ are functions of the steady state solution.

$$\bar{A}_1(\bar{U}) = \frac{\partial F(\bar{U})}{\partial \bar{U}} = \begin{bmatrix} 0 & 1 & 0 \\ \frac{1}{2}(\gamma-3)u^2 & (3-\gamma)u & \gamma-1 \\ -\gamma E u + (\gamma-1)u^3 & \gamma E - \frac{3}{2}(\gamma-1)u^2 & \gamma u \end{bmatrix}$$

$$\bar{A}_2(\bar{U}) = \frac{\partial P(\bar{U})}{\partial \bar{U}} = \begin{bmatrix} 0 & 0 & 0 \\ \frac{1}{2}(\gamma-1)u^2 & -(\gamma-1)u & \gamma-1 \\ 0 & 0 & 0 \end{bmatrix}$$

Although the discrete perturbation equation is a discretization of Equation (5.14), it is more appropriate to step back to the discrete form of the time dependent nonlinear Equation (5.2) to find the discrete perturbation equation. This is done to ensure that this equation is a true linearization of the discrete equation for the steady state. The discrete state vector is then set to

$$U_J(t) = \bar{U}_J + \Re\{\widehat{U}_J(t)\, e^{i\omega t}\}, \tag{5.15}$$

from which Equation (5.2) becomes

$$\begin{aligned}
\frac{d}{dt}\left[\tfrac{1}{2}(h_{J+\frac{1}{2}} + h_{J-\frac{1}{2}})\Re\{\widehat{U}_J e^{i\omega t}\}\Delta x_J\right] \;+\; i\omega\,\tfrac{1}{2}(h_{J+\frac{1}{2}} + h_{J-\frac{1}{2}})\Re\{\widehat{U}_J e^{i\omega t}\}\Delta x_J \;=& \\
-\left[h_{J+\frac{1}{2}}(\bar{F}_{J+\frac{1}{2}} + \Re\{(\bar{A}_1\widehat{U})_{J+\frac{1}{2}} e^{i\omega t}\}) - h_{J-\frac{1}{2}}(\bar{F}_{J-\frac{1}{2}} + \Re\{(\bar{A}_1\widehat{U})_{J-\frac{1}{2}} e^{i\omega t}\})\right]& \qquad (5.16) \\
+\tfrac{1}{2}\left[(\bar{P}_{J+\frac{1}{2}} + \Re\{(\bar{A}_2\widehat{U})_{J+\frac{1}{2}} e^{i\omega t}\}) + (\bar{P}_{J-\frac{1}{2}} + \Re\{(\bar{A}_2\widehat{U})_{J-\frac{1}{2}} e^{i\omega t}\})\right](h_{J+\frac{1}{2}} - h_{J-\frac{1}{2}}).&
\end{aligned}$$

After subtracting off the steady state Equation (5.3) and dividing through by $e^{i\omega t}$, the discrete perturbation equation is found. This equation can be written as

$$\left(\frac{\partial\widehat{U}}{\partial t}\right)_J = -R(\widehat{U}_J), \qquad (5.17)$$

where

$$\begin{aligned}
R(\widehat{U}_J) \;=\; i\omega\widehat{U}_J \;+\; \left(\frac{1}{\Delta\bar{x}_J\frac{1}{2}(h_{J+\frac{1}{2}} + h_{J-\frac{1}{2}})}\right) \times& \qquad (5.18) \\
\left((h_{J+\frac{1}{2}}(\bar{A}_1\widehat{U})_{J+\frac{1}{2}} - h_{J-\frac{1}{2}}(\bar{A}_1\widehat{U})_{J-\frac{1}{2}}) \;-\; \tfrac{1}{2}((\bar{A}_2\widehat{U})_{J+\frac{1}{2}} + (\bar{A}_2\widehat{U})_{J-\frac{1}{2}})(h_{J+\frac{1}{2}} - h_{J-\frac{1}{2}})\right).&
\end{aligned}$$

Again for simplicity, the following have been defined:

$$\begin{aligned}
\widehat{U}_{J+\frac{1}{2}} &= \tfrac{1}{2}(\widehat{U}_J + \widehat{U}_{J+1}), \\
\widehat{U}_{J-\frac{1}{2}} &= \tfrac{1}{2}(\widehat{U}_J + \widehat{U}_{J-1}), \\
(\bar{A}_1\widehat{U})_{J+\frac{1}{2}} &= \tfrac{1}{2}((\bar{A}_1\widehat{U})_J + (\bar{A}_1\widehat{U})_{J+1}), \qquad (\bar{A}_2\widehat{U})_{J+\frac{1}{2}} = \tfrac{1}{2}((\bar{A}_2\widehat{U})_J + (\bar{A}_2\widehat{U})_{J+1}), \\
(\bar{A}_1\widehat{U})_{J-\frac{1}{2}} &= \tfrac{1}{2}((\bar{A}_1\widehat{U})_J + (\bar{A}_1\widehat{U})_{J-1}), \qquad (\bar{A}_2\widehat{U})_{J-\frac{1}{2}} = \tfrac{1}{2}((\bar{A}_2\widehat{U})_J + (\bar{A}_2\widehat{U})_{J-1}).
\end{aligned}$$

The temporal discretization of Equation (5.17) will be described in Section 5.1.3.

Second Difference Artificial Viscosity

To find the form of the linearized artificial viscosity term, one follows the same steps which were used to find the discrete linear harmonic equations. First, the form of the state vector for the linear harmonic solution in Equation (5.15) is substituted into the nonlinear form of the second difference artificial viscosity term in Equation (5.7); next the steady state contribution is subtracted off, and finally what remains is divided through by the common term $e^{i\omega t}$. For the form of the second difference artificial viscosity given in Equation (5.6), this procedure produces the discrete artificial viscosity term

$$D(\widehat{U}_J) = \epsilon_2 \left(\frac{1}{\Delta \tilde{x}_J \frac{1}{2}(h_{J+\frac{1}{2}} + h_{J-\frac{1}{2}})} \right) \times \quad (5.19)$$
$$\left(h_{J+\frac{1}{2}} \left(\frac{\Delta x}{\Delta t_{\max}}\right)_{J+\frac{1}{2}} (\widehat{U}_{J+1} - \widehat{U}_J) - h_{J-\frac{1}{2}} \left(\frac{\Delta x}{\Delta t_{\max}}\right)_{J-\frac{1}{2}} (\widehat{U}_J - \widehat{U}_{J-1}) \right).$$

Because the second difference artificial viscosity term is linear, this process is quite simple and produces a numerical artificial viscosity term which is similar to the term for the steady state.

When artificial viscosity is added to Equation (5.17), the equation becomes

$$\left(\frac{\partial \widehat{U}}{\partial t} \right)_J = -R(\widehat{U}_J) + D(\widehat{U}_J). \quad (5.20)$$

Fourth Difference Artificial Viscosity

The fourth difference artificial viscosity term with the switched second difference artificial viscosity is more complicated to linearize than the second difference artificial viscosity term. The fourth difference artificial viscosity term by itself, like the second difference term, is linear so it is easy to linearize. With the addition of the switch, there is a nonlinear term in the equation.

In general, the switch is now written as

$$S_J = \bar{S}_J + \widehat{S}_J. \quad (5.21)$$

The form of the switch given in Equation (5.12) cannot be linearized, but this is certainly not the only form of the switch which could be used. The steady state term $\bar{S}_J$ is

$$\bar{S}_J = \frac{\bar{s}_J}{\max(\bar{s}_J)}, \tag{5.22}$$

where

$$\bar{s}_J = \text{abs}\left[\frac{(\bar{p}_{J+1} - \bar{p}_J) - (\bar{p}_J - \bar{p}_{J-1})}{\bar{p}_J}\right]. \tag{5.23}$$

Since the switch cannot be linearized, the perturbation switch is set to $\widehat{S}_J = 0$. Chapter 6 will discuss the effects on the solutions associated with not linearizing the switch. The equation for the artificial viscosity term, however, will retain the $\widehat{S}_J$ for generality.

The perturbation artificial viscosity term becomes quite complicated. After dropping any higher order contributions, this term is

$$\begin{aligned} D(\widehat{U}_J) = {} & \left(\frac{1}{\Delta\bar{x}_J\frac{1}{2}(h_{J+\frac{1}{2}} + h_{J-\frac{1}{2}})}\right) \times \\ & \Bigg[-\epsilon_4\bigg((1 - \bar{S}_{J+\frac{1}{2}})\, h_{J+\frac{1}{2}} \left(\tfrac{\Delta x}{\Delta t_{\max}}\right)_{J+\frac{1}{2}} (D^2\widehat{U}_{J+1} - D^2\widehat{U}_J) \; - \\ & \quad (1 - \bar{S}_{J-\frac{1}{2}})\, h_{J-\frac{1}{2}} \left(\tfrac{\Delta x}{\Delta t_{\max}}\right)_{J-\frac{1}{2}} (D^2\widehat{U}_J - D^2\widehat{U}_{J-1}) \; + \\ & \quad -\widehat{S}_{J+\frac{1}{2}}\, h_{J+\frac{1}{2}} \left(\tfrac{\Delta x}{\Delta t_{\max}}\right)_{J+\frac{1}{2}} (D^2\bar{U}_{J+1} - D^2\bar{U}_J) \; - \\ & \quad -\widehat{S}_{J-\frac{1}{2}}\, h_{J-\frac{1}{2}} \left(\tfrac{\Delta x}{\Delta t_{\max}}\right)_{J-\frac{1}{2}} (D^2\bar{U}_J - D^2\bar{U}_{J-1})\bigg) \\ & + \epsilon_2\bigg(\bar{S}_{J+\frac{1}{2}} h_{J+\frac{1}{2}} \left(\tfrac{\Delta x}{\Delta t_{\max}}\right)_{J+\frac{1}{2}} (\widehat{U}_{J+1} - \widehat{U}_J) \; - \\ & \quad \bar{S}_{J-\frac{1}{2}} h_{J-\frac{1}{2}} \left(\tfrac{\Delta x}{\Delta t_{\max}}\right)_{J-\frac{1}{2}} (\widehat{U}_J - \widehat{U}_{J-1}) \; + \\ & \quad \widehat{S}_{J+\frac{1}{2}} h_{J+\frac{1}{2}} \left(\tfrac{\Delta x}{\Delta t_{\max}}\right)_{J+\frac{1}{2}} (\bar{U}_{J+1} - \bar{U}_J) \; - \\ & \quad \widehat{S}_{J-\frac{1}{2}} h_{J-\frac{1}{2}} \left(\tfrac{\Delta x}{\Delta t_{\max}}\right)_{J-\frac{1}{2}} (\bar{U}_J - \bar{U}_{J-1})\bigg)\Bigg], \end{aligned} \tag{5.24}$$

where the numerical perturbation second difference is

$$D^2\hat{U}_J = (\hat{U}_{J+1} - \hat{U}_J) - (\hat{U}_J - \hat{U}_{J-1}). \tag{5.25}$$

5.1.3 Temporal Discretization

To model the time derivative for both the steady state and the perturbation, either a four-stage or five-stage Runge-Kutta scheme will be used. For the perturbation, the variables are complex numbers, but otherwise the formulations are the same.

The four-stage scheme presented here is often referred to as "the fourth order Runge-Kutta method" when $R(U) - D(U)$ is a linear function. To reduce the required storage when $R(U) - D(U)$ is nonlinear, this fourth order accuracy in time has been sacrificed. For the nonlinear schemes used here, the interest is in the steady state, so the loss of temporal accuracy is of no concern.

The semi-discrete equations from Equations (5.4) and (5.17) are then modeled by

$$\begin{aligned} U^{(0)} &= U(t_n) \\ U^{(1)} &= U^{(0)} - \alpha_1 \Delta t \left[R(U^{(0)}) - D(U^{(0)}) \right] \\ U^{(2)} &= U^{(0)} - \alpha_2 \Delta t \left[R(U^{(1)}) - D(U^{(1)}) \right] \\ U^{(3)} &= U^{(0)} - \alpha_3 \Delta t \left[R(U^{(2)}) - D(U^{(2)}) \right] \\ U^{(4)} &= U^{(0)} - \alpha_4 \Delta t \left[R(U^{(3)}) - D(U^{(3)}) \right] \\ U(t_{n+1}) &= U^{(4)} \end{aligned} \tag{5.26}$$

where $D(U) = 0$ for the flux vector split scheme and

$$\alpha_1 = \tfrac{1}{4}, \qquad \alpha_2 = \tfrac{1}{3}, \qquad \alpha_3 = \tfrac{1}{2}, \qquad \alpha_4 = 1.$$

There is a limit on the size of Δt which is a function of $R(U)$. Only the results of the stability analysis used to determine Δt are given here, the full analysis is presented in Appendix A. Define Δt_{max} as the characteristic time for information to cross one computational cell:

$$\Delta t_{\max} = \frac{\Delta x}{|u| + c}. \qquad (5.27)$$

The multistep integration scheme given here allows a larger timestep, given by

$$\Delta t = CFL \cdot \Delta t_{\max}, \qquad (5.28)$$

where CFL stands for the Courant-Friedrichs-Lewy number. The stability limit for the steady state equations gives $CFL < 2\sqrt{2}$. The perturbation equation requires $\omega \Delta t + CFL < 2\sqrt{2}$, which when combined with Equation (5.28) gives

$$\Delta t < \frac{2\sqrt{2}\,\Delta t_{\max}}{1 + \omega \Delta t_{\max}}. \qquad (5.29)$$

In practice, $\omega \Delta t_{\max} \ll 1$, so the stability limit for the steady state is used for the perturbation equations as well.

It should be noted that the same value of $\Delta t_{\max}$ must be used in the steady and perturbation solutions to ensure that the linear form of the artificial viscosity is a true linearization of the nonlinear artificial viscosity term, since Equations (5.6) and (5.9) are functions of $(\frac{\Delta x}{\Delta t_{\max}})$.

The five-stage Runge-Kutta scheme is similar to the four-stage scheme, with the major modification, other than the addition of another stage, of holding the dissipation term fixed after the first stage. By not continuously re-computing the dissipation, the computational requirement for the scheme is reduced. The addition of the extra stage and the choice of coefficients make the scheme particularly suited for use with multigrid schemes. Section 7.2 describes the multigrid process and the benefits of this five-stage scheme in detail. The five-stage scheme is then

$$\begin{aligned}
U^{(0)} &= U(t_n) \\
U^{(1)} &= U^{(0)} - \alpha_1 \Delta t \left[R(U^{(0)}) - D(U^{(0)}) \right] \\
U^{(2)} &= U^{(0)} - \alpha_2 \Delta t \left[R(U^{(1)}) - D(U^{(1)}) \right] \\
U^{(3)} &= U^{(0)} - \alpha_3 \Delta t \left[R(U^{(2)}) - D(U^{(1)}) \right] \\
U^{(4)} &= U^{(0)} - \alpha_4 \Delta t \left[R(U^{(3)}) - D(U^{(1)}) \right] \\
U^{(5)} &= U^{(0)} - \alpha_5 \Delta t \left[R(U^{(4)}) - D(U^{(1)}) \right] \\
U(t_{n+1}) &= U^{(5)}
\end{aligned} \tag{5.30}$$

where

$$\alpha_1 = \tfrac{1}{4}, \qquad \alpha_2 = \tfrac{1}{6}, \qquad \alpha_3 = \tfrac{3}{8}, \qquad \alpha_4 = \tfrac{1}{2}, \qquad \alpha_5 = 1.$$

The stability limit for the five-stage scheme is slightly larger than the four-stage scheme, where now $CFL < 4$ for the steady scheme and $\omega\Delta t + CFL < 4$ for the perturbation. In practice, a much lesser value of CFL than is allowed is used, such as $CFL = 3$, to obtain the desired temporal damping effects of this scheme.

5.2 Flux Vector Splitting Schemes

Flux vector split schemes take into account more of the physics in the problem than the artificial viscosity schemes presented in the previous section. They use upwinded differences which impose the knowledge of the information propagation in the flowfield on the numerical scheme. The hope for these schemes is that by using more physics, the schemes will be more robust and have fewer overshoots in the solutions. The particular upwinding scheme described here is van Leer's flux vector splitting [26]. This scheme is essentially the same as the flux vector split scheme described in Chapter 4. Also discussed is the MUSCL (Monotone Upstream-centered Scheme for Conservation Laws) modification to this scheme [2].

The solution procedure for the flux vector split scheme is similar to that used for the artificial viscosity schemes. The time integration is the same Runge-Kutta method described in Section 5.1.3, but the computation of the residual is done differently. For this reason, only the spatial discretization will be described.

5.2.1 Steady State

Equation (5.6) (which is repeated here) still holds for the flux vector split scheme, but the fluxes $F_{J+\frac{1}{2}}$ and $F_{J-\frac{1}{2}}$ are now defined with the direction of the characteristics in mind.

$$\begin{aligned} R(U_J) \;=\; & \left(\frac{1}{\Delta x_J \frac{1}{2}(h_{J+\frac{1}{2}} + h_{J-\frac{1}{2}})}\right) \times \\ & \left((h_{J+\frac{1}{2}} F_{J+\frac{1}{2}} - h_{J-\frac{1}{2}} F_{J-\frac{1}{2}}) \;-\; \tfrac{1}{2}(P_{J+\frac{1}{2}} + P_{J-\frac{1}{2}})\,(h_{J+\frac{1}{2}} - h_{J-\frac{1}{2}})\right). \end{aligned} \tag{5.6}$$

Unlike the artificial viscosity scheme, now

$$F_{J+\frac{1}{2}} = F^{+}(U^{-}_{J+\frac{1}{2}}) + F^{-}(U^{+}_{J+\frac{1}{2}}) \qquad F_{J-\frac{1}{2}} = F^{+}(U^{-}_{J-\frac{1}{2}}) + F^{-}(U^{+}_{J-\frac{1}{2}}).$$

The fluxes F^+ and F^- are the upwinded fluxes which, depending on the local Mach number, are found from

$M > 1$:

$$F^{+} = \begin{bmatrix} \rho u \\ \rho u^2 + p \\ \rho u H \end{bmatrix}, \quad F^{-} = \begin{bmatrix} 0 \\ 0 \\ 0 \end{bmatrix}$$

$M < 1$:

$$F^{\pm} = \begin{bmatrix} f_1^{\pm} \\ f_1^{\pm}\left(\dfrac{c[(\gamma-1)M \pm 2]}{\gamma}\right) \\ f_1^{\pm}\left(\dfrac{c^2[(\gamma-1)M \pm 2]^2}{2(\gamma^2-1)}\right) \end{bmatrix} \qquad \text{where} \quad f_1^{\pm} = \pm\tfrac{1}{4}\,\rho c\,(1 \pm M)^2$$

The state vector for the MUSCL modification to van Leer's original scheme is extrapolated to the cell faces before the evaluation of the fluxes so that

$$U^-_{J+\frac{1}{2}} = U_J + \psi_J \frac{U_J - U_{J-1}}{2} \qquad U^+_{J+\frac{1}{2}} = U_{J+1} + \psi_{J+1} \frac{U_{J+1} - U_{J+2}}{2},$$

where ψ is called the flux limiter. When $\psi = 0$, the scheme reduces to the original first order accurate flux vector split scheme proposed by van Leer, and when $\psi = 1$, the scheme is second-order accurate. The value of ψ can vary throughout the flowfield from $\psi = 0$ to $\psi = 1$. This variation is used to turn off the second-order accurate differencing in the shock so that the added damping from the first order accurate formulation reduces oscillations in the shock region. Although this effect is more noticeable for higher Mach number flows, it is still used here. The form of the flux limiter is similar to the switch used with the fourth difference artificial viscosity to turn on the second difference artificial viscosity in the shock. Since the limiter should be zero in the shock,

$$\psi_J = 1 - S_J, \tag{5.31}$$

where S_J was given in Equation (5.12) as

$$S_J = \frac{s_J}{\max(s_J)}, \tag{5.12}$$

where

$$s_J = \text{abs}\left[\frac{(p_{J+1} - p_J) - (p_J - p_{J-1})}{p_J}\right]. \tag{5.13}$$

5.2.2 Linear Perturbation

As with the steady state, the computational equations used to find the perturbation do not change significantly from the artificial viscosity scheme. Equation (5.19) (which is repeated here) still holds, but the method of computing $(\bar{A}_1\widehat{U})_{J+\frac{1}{2}}$ and $(\bar{A}_1\widehat{U})_{J-\frac{1}{2}}$ is a linearization of the upwinded fluxes used for the steady state solution:

$$R(U_J) = i\omega\tfrac{1}{2}(\widehat{U}_{J+\frac{1}{2}} + \widehat{U}_{J-\frac{1}{2}}) + \left(\frac{1}{\Delta\bar{x}_J\frac{1}{2}(h_{J+\frac{1}{2}} + h_{J-\frac{1}{2}})}\right) \times \tag{5.19}$$

$$\left((h_{J+\frac{1}{2}}(\bar{A}_1\widehat{U})_{J+\frac{1}{2}} - h_{J-\frac{1}{2}}(\bar{A}_1\widehat{U})_{J-\frac{1}{2}}) - \tfrac{1}{2}((\bar{A}_2\widehat{U})_{J+\frac{1}{2}} + (\bar{A}_2\widehat{U})_{J-\frac{1}{2}})(h_{J+\frac{1}{2}} - h_{J-\frac{1}{2}})\right),$$

where now

$$\begin{aligned}(\bar{A}_1\widehat{U})_{J+\frac{1}{2}} &= \bar{A}_1^+(\bar{U}^-_{J+\frac{1}{2}})\,\widehat{U}^-_{J+\frac{1}{2}} + \bar{A}_1^-(\bar{U}^+_{J+\frac{1}{2}})\,\widehat{U}^+_{J+\frac{1}{2}}\\ (\bar{A}_1\widehat{U})_{J-\frac{1}{2}} &= \bar{A}_1^+(\bar{U}^-_{J-\frac{1}{2}})\,\widehat{U}^-_{J-\frac{1}{2}} + \bar{A}_1^-(\bar{U}^+_{J-\frac{1}{2}})\,\widehat{U}^+_{J-\frac{1}{2}}.\end{aligned}$$

$\bar{A}_1^+$ and $\bar{A}_1^-$ are functions of the steady state solution defined by

$$\bar{A}_1^+ = \frac{\partial\bar{F}^+}{\partial\bar{U}} \qquad \bar{A}_1^- = \frac{\partial\bar{F}^-}{\partial\bar{U}},$$

which, just like the steady upwinded fluxes, vary depending on the local Mach number.

$M > 1$:

$$\bar{A}_1^+(\bar{U}) = \begin{bmatrix} 0 & 1 & 0\\ \frac{1}{2}(\gamma-3)u^2 & (3-\gamma)u & \gamma-1\\ -\gamma Eu+(\gamma-1)u^3 & \gamma E-\frac{3}{2}(\gamma-1)u^2 & \gamma u\end{bmatrix}, \quad \bar{A}_1^-(\bar{U}) = \begin{bmatrix} 0 & 0 & 0\\ 0 & 0 & 0\\ 0 & 0 & 0\end{bmatrix}$$

$M < 1$:

The expression for $\bar{A}_1^{\pm}$ when the flow is subsonic is quite complicated. To simplify matters and better define the method for finding these matrices, the process will be split into several steps. Instead of taking the derivative with respect to the state vector directly, the chain rule will be used with the intermediate variables ρ, c and M.

$$\bar{A}_1^{\pm}(\bar{U}) = \begin{bmatrix} \frac{\partial f_1^{\pm}}{\partial\rho} & \frac{\partial f_1^{\pm}}{\partial c} & \frac{\partial f_1^{\pm}}{\partial M}\\ \frac{\partial f_2^{\pm}}{\partial\rho} & \frac{\partial f_2^{\pm}}{\partial c} & \frac{\partial f_2^{\pm}}{\partial M}\\ \frac{\partial f_3^{\pm}}{\partial\rho} & \frac{\partial f_3^{\pm}}{\partial c} & \frac{\partial f_3^{\pm}}{\partial M}\end{bmatrix} \begin{bmatrix} \frac{\partial\rho}{\partial\bar{U}_1} & \frac{\partial\rho}{\partial\bar{U}_2} & \frac{\partial\rho}{\partial\bar{U}_3}\\ \frac{\partial c}{\partial\bar{U}_1} & \frac{\partial c}{\partial\bar{U}_2} & \frac{\partial c}{\partial\bar{U}_3}\\ \frac{\partial M}{\partial\bar{U}_1} & \frac{\partial M}{\partial\bar{U}_2} & \frac{\partial M}{\partial\bar{U}_3}\end{bmatrix}, \tag{5.32}$$

where

$$U = \begin{bmatrix} \rho \\ \rho u \\ \rho E \end{bmatrix} = \begin{bmatrix} U_1 \\ U_2 \\ U_3 \end{bmatrix}.$$

The matrices in Equation (5.32) are then given by

$$\begin{bmatrix} \frac{\partial \rho}{\partial U_1} & \frac{\partial \rho}{\partial U_2} & \frac{\partial \rho}{\partial U_3} \\ \frac{\partial c}{\partial U_1} & \frac{\partial c}{\partial U_2} & \frac{\partial c}{\partial U_3} \\ \frac{\partial M}{\partial U_1} & \frac{\partial M}{\partial U_2} & \frac{\partial M}{\partial U_3} \end{bmatrix} = \begin{bmatrix} 1 & 0 & 0 \\ \frac{\gamma(\gamma-1)}{2c}\left(\frac{-U_3}{U_1^2} + \frac{U_2^2}{U_1^3}\right) & \frac{\gamma(\gamma-1)}{2c}\left(\frac{-U_2}{U_1^2}\right) & \frac{\gamma(\gamma-1)}{2c}\left(\frac{1}{U_1}\right) \\ \frac{-M}{U_1} - \frac{M}{c}\frac{\partial c}{\partial U_1} & \frac{-M}{U_2} - \frac{M}{c}\frac{\partial c}{\partial U_2} & -\frac{M}{c}\frac{\partial c}{\partial U_3} \end{bmatrix},$$

$$\begin{bmatrix} \frac{\partial f_1^\pm}{\partial \rho} & \frac{\partial f_1^\pm}{\partial c} & \frac{\partial f_1^\pm}{\partial M} \\ \frac{\partial f_2^\pm}{\partial \rho} & \frac{\partial f_2^\pm}{\partial c} & \frac{\partial f_2^\pm}{\partial M} \\ \frac{\partial f_3^\pm}{\partial \rho} & \frac{\partial f_3^\pm}{\partial c} & \frac{\partial f_3^\pm}{\partial M} \end{bmatrix} =$$

$$\begin{bmatrix} 1 & 1 & 1 \\ \frac{c[(\gamma-1)M \pm 2]}{\gamma} & \frac{c[(\gamma-1)M \pm 2]}{\gamma} & \frac{c[(\gamma-1)M \pm 2]}{\gamma} \\ \frac{c^2[(\gamma-1)M \pm 2]^2}{2(\gamma^2-1)} & \frac{c^2[(\gamma-1)M \pm 2]^2}{2(\gamma^2-1)} & \frac{c^2[(\gamma-1)M \pm 2]^2}{2(\gamma^2-1)} \end{bmatrix} \begin{bmatrix} \frac{\partial f_1^\pm}{\partial \rho} & 0 & 0 \\ 0 & \frac{\partial f_1^\pm}{\partial c} & 0 \\ 0 & 0 & \frac{\partial f_1^\pm}{\partial M} \end{bmatrix}$$

$$+ \; f_1^\pm \begin{bmatrix} 0 & 0 & 0 \\ 0 & \frac{[(\gamma-1)M \pm 2]}{\gamma} & \frac{c(\gamma-1)}{\gamma} \\ 0 & \frac{c[(\gamma-1)M \pm 2]^2}{(\gamma^2-1)} & \frac{c^2[(\gamma-1)M \pm 2]}{(\gamma+1)} \end{bmatrix},$$

where

$$\frac{\partial f_1^\pm}{\partial \rho} = \frac{f_1^\pm}{\rho}$$

$$\frac{\partial f_1^\pm}{\partial c} = \frac{f_1^\pm}{c}$$

$$\frac{\partial f_1^\pm}{\partial M} = \frac{f_1^\pm}{\pm\frac{1}{2}(1 \pm M)}.$$

As with the steady state, the perturbation state vector is extrapolated to the cell faces before the evaluation of the fluxes, so that

$$\begin{aligned}
\widehat{U}^{-}_{J+\frac{1}{2}} &= \widehat{U}_J + \bar{\psi}_J \tfrac{1}{2}(\widehat{U}_J - \widehat{U}_{J-1}) + \widehat{\psi}_J \tfrac{1}{2}(\bar{U}_J - \bar{U}_{J-1}) \\
\widehat{U}^{+}_{J+\frac{1}{2}} &= \widehat{U}_{J+1} + \bar{\psi}_{J+1} \tfrac{1}{2}(\widehat{U}_{J+1} - \widehat{U}_{J+2}) + \widehat{\psi}_{J+1} \tfrac{1}{2}(\bar{U}_{J+1} - \bar{U}_{J+2}).
\end{aligned}$$

The steady flux limiter $\bar{\psi}$ and the perturbation $\widehat{\psi}$ are both included in this equation. In terms of the switch used for the artificial viscosity scheme, the perturbation flux limiter is now

$$\widehat{\psi}_J = -\widehat{S}_J. \tag{5.33}$$

As mentioned earlier, the switch which is used cannot be linearized. Because of this limitation, to find the perturbation for the artificial viscosity schemes, $\widehat{S}_J = 0$. This will be the approach taken here as well, although the perturbation of the switch has been included in the equations for generality.

5.3 Farfield Boundary Conditions

The farfield boundary conditions are applied at the inlet and outlet boundary nodes. The boundary conditions on hyperbolic equations must correctly close the system of equations. Linear characteristic theory determines the direction of wave motion in and out of the domain, and thus exactly which boundary conditions must be imposed. The following analysis for the steady state boundary conditions is described in more detail in [12, 19, 9]. Since the basis of the analysis is in linearized characteristic theory, the steady state and perturbation boundary conditions are similar.

5.3.1 Steady State

To simplify the analysis, primitive state vector variables U_p are used where

$$U_p = \begin{bmatrix} \rho \\ u \\ p \end{bmatrix}. \tag{5.34}$$

The differential form of the governing equations in terms of these primitive variables will be used to find the boundary conditions. First the equations are linearized.

$$\frac{\partial U_p}{\partial t} + \mathbf{A}\frac{\partial U_p}{\partial x} = 0 \tag{5.35}$$

A is a constant matrix evaluated at some reference state. The reference state for evaluation of the matrix **A** will be the flow on the boundary at the old timestep denoted by the subscript $(\ )_{old}$. The constant matrix **A** is then

$$\mathbf{A} = \begin{bmatrix} u & \rho & 0 \\ 0 & u & \frac{1}{\rho} \\ 0 & \rho c^2 & u \end{bmatrix}_{old}. \tag{5.36}$$

The matrix **A** can be diagonalized by a similarity transformation,

$$\mathbf{T}^{-1}\mathbf{A}\mathbf{T} = \begin{bmatrix} u & 0 & 0 \\ 0 & u+c & 0 \\ 0 & 0 & u-c \end{bmatrix}_{old} = \mathbf{\Lambda}, \tag{5.37}$$

where the matrix **T** is the matrix of right eigenvectors of **A**. Matrix $\mathbf{\Lambda}$ is a diagonal matrix whose elements are the eigenvalues of matrix **A**.

$$\mathbf{T} = \begin{bmatrix} 1 & \rho & -\rho \\ 0 & c & c \\ 0 & \rho c^2 & -\rho c^2 \end{bmatrix}_{old}, \qquad \mathbf{T}^{-1} = \begin{bmatrix} 1 & 0 & \frac{-1}{c^2} \\ 0 & \frac{1}{2c} & \frac{1}{2\rho c^2} \\ 0 & \frac{1}{2c} & \frac{-1}{2\rho c^2} \end{bmatrix}_{old} . \tag{5.38}$$

Multiplication of Equation (5.35) by $\mathbf{T}^{-1}$ produces the equation

$$\frac{\partial \phi}{\partial t} + \mathbf{\Lambda} \frac{\partial \phi}{\partial x} = 0, \tag{5.39}$$

where $\phi = \mathbf{T}^{-1} U_p$. Variation from the values at the old timestep will be considered, therefore for a constant matrix $\mathbf{T}^{-1}$, $\delta\phi = \mathbf{T}^{-1}\delta U_p$. The three equations in the system of Equations (5.39) are now independent. The elements of ϕ are the linearized characteristic variables and the corresponding elements of $\mathbf{\Lambda}$ indicate the direction of the flow of information. For subsonic flow (where $0 < u < c$) the first two characteristics show waves propagating downstream (since the corresponding elements of $\mathbf{\Lambda}$ are positive) and the third propagating upstream (since the third element of $\mathbf{\Lambda}$ is negative). For supersonic flow (where $u > c$) all waves propagate downstream since all elements of $\mathbf{\Lambda}$ are positive.

Subsonic Inlet Boundary

For subsonic flow two pieces of information must be specified at the inlet boundary; here they will be the stagnation pressure, p_o, and the logarithm of the entropy, s.

$$p_o = \rho_o \Big(\frac{\gamma - 1}{2\gamma} u^2 + \frac{p}{\rho} \Big) \tag{5.40}$$

$$s = \log \Big(\frac{p}{\rho^\gamma} \Big), \tag{5.41}$$

where given p_o and $s = \log(\frac{p}{\rho_o^\gamma})$, ρ_o is known.

A third piece of information comes from the interior of the flowfield and will be taken from the values the numerical solver predicts, therefore denoted by the subscript

$(\ )_{pred}$. Let the subscript $(\ )_{spec}$ stand for the value which is specified by the inlet flow conditions. The subscripts $(\ )_{old}$ and $(\ )_{new}$ will stand for the values at the old and new time steps. The amount needed to bring the old values of p_o and s on the boundary to the specified values can be written in terms of a two term Taylor series in ϕ. The constant coefficient of the series can be changed by using the chain rule to contain elements of U_p.

$$\begin{aligned}
(p_o)_{spec} &= (p_o)_{new} \\
&= (p_o)_{old} + \left(\frac{\partial p_o}{\partial \phi}\right)_{old} \delta\phi \\
&= (p_o)_{old} + \left(\frac{\partial p_o}{\partial U_p}\right)_{old} \mathbf{T}\,\delta\phi \\
&= (p_o)_{old} + \begin{bmatrix} 0 & \rho_o u & \frac{\rho_o}{\rho} \end{bmatrix}_{old} \delta\phi
\end{aligned} \tag{5.42}$$

$$s_{spec} = s_{old} + \begin{bmatrix} \frac{-\gamma}{\rho} & 0 & 0 \end{bmatrix}_{old} \delta\phi \tag{5.43}$$

The change in the third characteristic $\delta(\phi_3)$ is equal to the change that the flowfield predicts, $\delta(\phi_3)_{pred}$. Since $\delta\phi = \mathbf{T}^{-1}\delta U_p$, the predicted change in the characteristic variable $\delta(\phi_3)_{pred}$ is

$$\delta(\phi_3)_{pred} = \left(\frac{1}{2c}\right)_{old} \delta u_{pred} - \left(\frac{1}{2\rho c^2}\right)_{old} \delta p_{pred}. \tag{5.44}$$

There are now three Equations (5.42), (5.43) and (5.44) for the change in the characteristic variable ϕ which can be written in matrix form:

$$\begin{bmatrix} (p_o)_{spec} - (p_o)_{old} \\ s_{spec} - s_{old} \\ \delta(\phi_3)_{pred} \end{bmatrix} = \begin{bmatrix} 0 & \rho_o c(u+c) & -\rho c(u+c) \\ \frac{-\gamma}{\rho} & 0 & 0 \\ 0 & 0 & 1 \end{bmatrix}_{old} \begin{bmatrix} \delta(\phi_1) \\ \delta(\phi_2) \\ \delta(\phi_3) \end{bmatrix}. \tag{5.45}$$

Using the relation $\delta U_p = \mathbf{T}\,\delta\phi$, $\delta\phi$ in Equation (5.45) can now be changed back into primitive state vector values U_p.

$$\delta U_p = \begin{bmatrix} \delta(\rho) \\ \delta(u) \\ \delta(p) \end{bmatrix}_{new} = \begin{bmatrix} \frac{\rho}{\rho_o c(u+c)} & \frac{-p}{\gamma} & 0 \\ \frac{1}{\rho_o(u+c)} & 0 & 2c \\ \frac{\rho c}{\rho_o(u+c)} & 0 & 0 \end{bmatrix}_{old} \begin{bmatrix} (p_o)_{spec} - (p_o)_{old} \\ s_{spec} - s_{old} \\ \delta(\phi_3)_{pred} \end{bmatrix} \tag{5.46}$$

To transform the change in the primitive state vector variables δU_p back into the change in the state vector δU, the following transformation is performed.

$$\delta U_{new} = \begin{bmatrix} \delta(\rho) \\ \delta(\rho u) \\ \delta(\rho E) \end{bmatrix}_{new} = \begin{bmatrix} 1 & 0 & 0 \\ u & \rho & 0 \\ \frac{1}{2}u^2 & \rho u & \frac{1}{\gamma-1} \end{bmatrix}_{old} \begin{bmatrix} \delta(\rho) \\ \delta(u) \\ \delta(p) \end{bmatrix}_{new} \tag{5.47}$$

So finally the new value of the state vector at the inlet nodes is

$$U_{new} = U_{old} + \delta U_{new}. \tag{5.48}$$

Subsonic Outlet Boundary

For subsonic flow, the outlet boundary is handled in a similar manner as the inlet boundary, except now only one piece of information must be specified; here static pressure p_{spec} will be used. Once again the amount needed to bring the old value of p to the specified value on the boundary can be written in terms of a two term Taylor series in ϕ.

$$\begin{aligned} p_{spec} &= p_{new} \\ &= p_{old} + \left(\frac{\partial p}{\partial \phi}\right)_{old} \delta\phi \\ &= p_{old} + \left(\frac{\partial p}{\partial U_p}\right)_{old} \mathbf{T}\, \delta\phi \\ &= p_{old} + \begin{bmatrix} 0 & \rho c^2 & \rho c^2 \end{bmatrix}_{old} \delta\phi \end{aligned} \tag{5.49}$$

The changes in the first and second characteristics are equal to the change the flowfield predicts. Again, since $\delta\phi = \mathbf{T}^{-1}\delta U_p$, the predicted change in the characteristic variables $\delta(\phi_1)_{pred}$ and $\delta(\phi_2)_{pred}$ are found to be

$$\delta(\phi_1)_{pred} = \delta\rho_{pred} - \left(\frac{1}{c^2}\right)_{old}\delta p_{pred} \tag{5.50}$$

$$\delta(\phi_2)_{pred} = \left(\frac{1}{2c}\right)_{old}\delta u_{pred} + \left(\frac{1}{2\rho c^2}\right)_{old}\delta p_{pred}. \tag{5.51}$$

As in the subsonic inlet condition, there are now three Equations (5.49), (5.50) and (5.51) for the change in the characteristic variable ϕ.

$$\begin{bmatrix} \delta(\phi_1)_{pred} \\ \delta(\phi_2)_{pred} \\ p_{spec} - p_{old} \end{bmatrix} = \begin{bmatrix} 1 & 0 & 0 \\ 0 & 1 & 0 \\ 0 & \rho c^2 & -\rho c^2 \end{bmatrix}_{old} \begin{bmatrix} \delta(\phi_1) \\ \delta(\phi_2) \\ \delta(\phi_3) \end{bmatrix} \tag{5.52}$$

Using the relation $\delta U_p = \mathbf{T}\,\delta\phi$, $\delta\phi$ in Equation (5.52) can now be changed back into primitive state vector values U_p.

$$\delta U_p = \begin{bmatrix} \delta(\rho) \\ \delta(u) \\ \delta(p) \end{bmatrix}_{new} = \begin{bmatrix} 1 & 0 & \frac{1}{c^2} \\ 0 & 2c & \frac{-1}{\rho c} \\ 0 & 0 & 1 \end{bmatrix}_{old} \begin{bmatrix} \delta(\phi_1)_{pred} \\ \delta(\phi_2)_{pred} \\ p_{spec} - p_{old} \end{bmatrix}. \tag{5.53}$$

The primitive state vector variables, δU_p, are transformed to the state vector, δU, by Equation (5.47) and the update is performed as in Equation (5.48).

Supersonic Inlet Boundary

Since for supersonic flow all waves flow downstream, to implement the inlet boundary condition it is simply necessary to prescribe the flow conditions. The inlet Mach number M_{spec} and the stagnation quantities ρ_o and p_o are all that is needed to find the inlet conditions.

$$\begin{aligned} \rho &= \rho_o\left(1 + \frac{(\gamma-1)}{2} M_{spec}^2\right)^{\frac{-1}{\gamma-1}} \\ p &= p_o\left(1 + \frac{(\gamma-1)}{2} M_{spec}^2\right)^{\frac{-\gamma}{\gamma-1}} \\ u &= M_{spec}\sqrt{\frac{\gamma p}{\rho}} \end{aligned}$$

The state vector is fixed at

$$U = \begin{bmatrix} \rho \\ \rho u \\ \frac{p}{\gamma-1} + \frac{1}{2}u^2\rho \end{bmatrix}_{new} . \tag{5.54}$$

Supersonic Outlet Boundary

For the supersonic outlet all waves flow out of the boundary, so the change in the state vector predicted by the scheme is used here.

$$\delta U_{new} = \delta U_{pred} \tag{5.55}$$

5.3.2 Linear Perturbation

Once again primitive variables are used, but now the state vector has a steady state and a perturbation, $U_p = \bar{U}_p + \Re\{\widehat{U}_p e^{i\omega t}\}$. The steady and perturbation primitive state vectors are

$$\bar{U}_p = \begin{bmatrix} \bar{\rho} \\ \bar{u} \\ \bar{p} \end{bmatrix}, \qquad \widehat{U}_p = \begin{bmatrix} \widehat{\rho} \\ \widehat{u} \\ \widehat{p} \end{bmatrix}. \tag{5.56}$$

Equation (5.35), which is used for the steady state analysis, is already a linear equation, so the equation for the perturbation is clearly

$$\frac{\partial \widehat{U}_p}{\partial t} + \bar{\mathbf{A}} \frac{\partial \widehat{U}_p}{\partial x} = 0. \tag{5.57}$$

Since $\bar{\mathbf{A}}$ is the same matrix given in Equation (5.36), then $\bar{\mathbf{T}}$ and $\bar{\Lambda}$ are the same matrices described in Equations (5.37) and (5.38), and much of the analysis for the steady state carries over directly for the perturbation, except now these matrices are evaluated with the previously calculated steady state solution. The characteristic perturbation is defined by $\widehat{\phi} = \bar{\mathbf{T}}^{-1}\widehat{U}_p$.

Subsonic Inlet Boundary

At the subsonic inlet, the perturbation in the stagnation pressure, $\widehat{p}_o$, and the logarithm of the entropy, $\widehat{s}$ will be specified. These quantities are given by

$$\begin{aligned} \widehat{p}_o &= \bar{\rho}_o\left(\bar{u}\,\widehat{u} + \frac{\widehat{p}}{\bar{\rho}}\right) && (5.58)\\ \widehat{s} &= \frac{-\gamma\,\widehat{\rho}}{\bar{\rho}} + \frac{\widehat{p}}{\bar{p}}. && (5.59) \end{aligned}$$

Again, the specified value for these quantities will be written in terms of a two term Taylor series in $\widehat{\phi}$.

$$\begin{aligned} (\widehat{p}_o)_{spec} &= (\widehat{p}_o)_{new} \\ &= (\widehat{p}_o)_{old} + \left(\frac{\partial \bar{p}_o}{\partial \bar{\phi}}\right)\delta\widehat{\phi} \\ &= (\widehat{p}_o)_{old} + \left(\frac{\partial \bar{p}_o}{\partial \bar{U}_p}\right)\bar{\mathbf{T}}\,\delta\widehat{\phi} \\ &= (\widehat{p}_o)_{old} + \left[\begin{matrix} 0 & \bar{\rho}_o\bar{u} & \frac{\bar{\rho}_o}{\bar{\rho}} \end{matrix}\right]\delta\widehat{\phi} && (5.60) \end{aligned}$$

$$\widehat{s}_{spec} = \widehat{s}_{old} + \left[\begin{matrix} \frac{-\gamma}{\bar{\rho}} & 0 & 0 \end{matrix}\right]\delta\widehat{\phi} \tag{5.61}$$

The change in the third characteristic perturbation $\delta(\widehat{\phi}_3)$ is equal to the change that the flowfield predicts, $\delta(\widehat{\phi}_3)_{pred}$. Since $\delta\widehat{\phi} = \bar{\mathbf{T}}^{-1}\delta\widehat{U}_p$, the predicted change in the characteristic variable $\delta(\widehat{\phi}_3)_{pred}$ is found to be

$$\delta(\widehat{\phi}_3)_{pred} = \left(\frac{1}{2\bar{c}}\right) \delta\widehat{u}_{pred} - \left(\frac{1}{2\bar{\rho}\bar{c}^2}\right) \delta\widehat{p}_{pred}. \tag{5.62}$$

So, as in Equation (5.45), there are now three equations for the change in the characteristic perturbation variable $\widehat{\phi}$:

$$\begin{bmatrix} (\widehat{p}_o)_{spec} - (\widehat{p}_o)_{old} \\ \widehat{s}_{spec} - \widehat{s}_{old} \\ \delta(\widehat{\phi}_3)_{pred} \end{bmatrix} = \begin{bmatrix} 0 & \bar{\rho}_o\bar{c}(\bar{u}+\bar{c}) & -\bar{\rho}\bar{c}(\bar{u}+\bar{c}) \\ \frac{-\gamma}{\bar{\rho}} & 0 & 0 \\ 0 & 0 & 1 \end{bmatrix} \begin{bmatrix} \delta(\widehat{\phi}_1) \\ \delta(\widehat{\phi}_2) \\ \delta(\widehat{\phi}_3) \end{bmatrix}. \tag{5.63}$$

which can now be changed back into primitive perturbation state vector values using the relation $\delta\widehat{U}_p = \bar{\mathbf{T}}\,\delta\widehat{\phi}$.

$$\delta\widehat{U}_p = \begin{bmatrix} \delta(\widehat{\rho}) \\ \delta(\widehat{u}) \\ \delta(\widehat{p}) \end{bmatrix}_{new} = \begin{bmatrix} \frac{\bar{\rho}}{\bar{\rho}_o\bar{c}(\bar{u}+\bar{c})} & \frac{-\bar{p}}{\gamma} & 0 \\ \frac{1}{\bar{\rho}_o(\bar{u}+\bar{c})} & 0 & 2\bar{c} \\ \frac{\bar{\rho}\bar{c}}{\bar{\rho}_o(\bar{u}+\bar{c})} & 0 & 0 \end{bmatrix} \begin{bmatrix} (\widehat{p}_o)_{spec} - (\widehat{p}_o)_{old} \\ \widehat{s}_{spec} - \widehat{s}_{old} \\ \delta(\widehat{\phi}_3)_{pred} \end{bmatrix} \tag{5.64}$$

To transform the change in the primitive perturbation state vector variables $\delta\widehat{U}_p$ back into the change in the perturbation state vector $\delta\widehat{U}$, the following transformation is performed.

$$\delta\widehat{U}_{new} = \begin{bmatrix} \delta(\widehat{\rho}) \\ \delta(\widehat{\rho u})) \\ \delta(\widehat{\rho E}) \end{bmatrix}_{new} = \begin{bmatrix} 1 & 0 & 0 \\ \bar{u} & \bar{\rho} & 0 \\ \frac{1}{2}\bar{u}^2 & \bar{\rho}\bar{u} & \frac{1}{\gamma-1} \end{bmatrix} \begin{bmatrix} \delta(\widehat{\rho}) \\ \delta(\widehat{u}) \\ \delta(\widehat{p}) \end{bmatrix}_{new} \tag{5.65}$$

So finally the new value of the state vector at the inlet node is

$$\widehat{U}_{new} = \widehat{U}_{old} + \delta\widehat{U}_{new}. \tag{5.66}$$

Once again it should be noted that, since the model equation used for the steady state analysis was linear, the perturbation analysis followed along a parallel track. The difference being that instead of linearizing about the previous iteration state vector, here the flow was linearized about the steady state solution.

Subsonic Outlet Boundary

For subsonic flow at the outlet boundary, the pressure perturbation $\widehat{p}_{spec}$ will be specified. Once again the amount needed to bring the old value of $\widehat{p}$ to the specified value on the boundary can be written in terms of a two term Taylor series in $\widehat{\phi}$.

$$\begin{aligned} \widehat{p}_{spec} &= \widehat{p}_{new} \\ &= \widehat{p}_{old} + \left(\frac{\partial \bar{p}}{\partial \bar{\phi}}\right)\delta\widehat{\phi} \\ &= \widehat{p}_{old} + \left(\frac{\partial \bar{p}}{\partial \bar{U}_p}\right)\bar{\mathbf{T}}\,\delta\widehat{\phi} \\ &= \widehat{p}_{old} + \begin{bmatrix} 0 & \bar{\rho}\bar{c}^2 & \bar{\rho}\bar{c}^2 \end{bmatrix}\delta\widehat{\phi} \end{aligned} \tag{5.67}$$

The changes in the first and second characteristic perturbations are equal to the changes the flowfield predicts. Again, since $\delta\widehat{\phi} = \bar{\mathbf{T}}^{-1}\delta\widehat{U}_p$, the predicted change in the characteristic variables $\delta(\widehat{\phi}_1)_{pred}$ and $\delta(\widehat{\phi}_2)_{pred}$ are found to be

$$\delta(\widehat{\phi}_1)_{pred} = \delta\widehat{\rho}_{pred} - \left(\frac{1}{\bar{c}^2}\right)\delta\widehat{p}_{pred} \tag{5.68}$$

$$\delta(\widehat{\phi}_2)_{pred} = \left(\frac{1}{2\bar{c}}\right)\delta\widehat{u}_{pred} + \left(\frac{1}{2\bar{\rho}\bar{c}^2}\right)\delta\widehat{p}_{pred}. \tag{5.69}$$

As in the steady state calculation for the subsonic outlet boundary, there are now three equations for the change in the characteristic perturbation variable $\widehat{\phi}$.

$$\begin{bmatrix} \delta(\widehat{\phi}_1)_{pred} \\ \delta(\widehat{\phi}_2)_{pred} \\ \widehat{p}_{spec} - \widehat{p}_{old} \end{bmatrix} = \begin{bmatrix} 1 & 0 & 0 \\ 0 & 1 & 0 \\ 0 & \bar{\rho}\bar{c}^2 & -\bar{\rho}\bar{c}^2 \end{bmatrix} \begin{bmatrix} \delta(\widehat{\phi}_1) \\ \delta(\widehat{\phi}_2) \\ \delta(\widehat{\phi}_3) \end{bmatrix} \tag{5.70}$$

Using the relation $\delta\widehat{U}_p = \bar{\mathbf{T}}\,\delta\widehat{\phi}$, $\delta\widehat{\phi}$ can now be changed back into primitive state vector values $\widehat{U}_p$.

$$\delta\widehat{U}_p = \begin{bmatrix} \delta(\widehat{\rho}) \\ \delta(\widehat{u}) \\ \delta(\widehat{p}) \end{bmatrix}_{new} = \begin{bmatrix} 1 & 0 & \frac{1}{\bar{c}^2} \\ 0 & 2c & \frac{-1}{\bar{\rho}\bar{c}} \\ 0 & 0 & 1 \end{bmatrix} \begin{bmatrix} \delta(\widehat{\phi}_1)_{pred} \\ \delta(\widehat{\phi}_2)_{pred} \\ \widehat{p}_{spec} - \widehat{p}_{old} \end{bmatrix} \tag{5.71}$$

The primitive state vector variables, $\delta\widehat{U}_p$, are transformed to the state vector, $\delta\widehat{U}$, by Equation (5.65) and the update is performed as in Equation (5.66).

Supersonic Inlet Boundary

Since for supersonic flow all waves flow downstream, the supersonic inlet boundary condition is merely the specification of the perturbation variables at the inlet. The cases which have supersonic inlets shown here do not have a flow perturbation at a supersonic inlet, therefore the state vector perturbation is fixed at

$$\widehat{U} = \begin{bmatrix} 0 \\ 0 \\ 0 \end{bmatrix}_{new} . \tag{5.72}$$

It would be possible, however, to specify another boundary condition for the supersonic inlet.

Supersonic Outlet Boundary

For the supersonic outlet all waves flow out of the boundary, so the change in the perturbation state vector predicted by the scheme is used here.

$$\delta\widehat{U}_{new} = \delta\widehat{U}_{pred} \tag{5.73}$$

5.4 Shock Fit Scheme

In Section 2.4, the jump conditions for the Euler equations were derived for both the steady state and the linear perturbation. These jump conditions can be used as an internal boundary condition in the numerical scheme where the jump condition is explicitly imposed at the shock location. As part of the solution procedure, the grid is moved so that a grid line falls exactly along the shock location. This kind of method is called shock fitting.

The numerical scheme described here which uses shock fitting is a box scheme which uses a two point difference stencil [11]. The solution procedure does not time-march to a steady state, but uses a Newton solver which is very efficient computationally for a one-dimensional scheme.

5.4.1 Steady State

Before describing the Newton solution procedure, the computational equations for different sections of the flowfield will be derived. As well as the general computational cell, there are equations for the shock jump and the inlet/outlet boundary conditions. The set of these equations forms a closed system which can then be solved for the unknown variables.

Interior Domain Cells

As before, the derivation of the computational equations comes from the integral form of the Euler equations, but now the steady Equation (2.24) is used.

$$-\Big[(Fh)_2 - (Fh)_1\Big] + \int_1^2 P\,dh = 0 \tag{2.24}$$

Given an initial guess at the solution, U^n, we wish to find another solution, U^{n+1}, which satisfies Equation (2.24). To do this, the equations are cast into 'delta form' by linearizing about the current solution such that $U^{n+1} = U^n + \Delta U^n$. By keeping only the first two terms in a Taylor expansion

$$F(U^n + \Delta U^n) = F(U^n) + \left(\frac{\partial F(U)}{\partial U}\right)^n \Delta U^n \tag{5.74}$$

$$P(U^n + \Delta U^n) = P(U^n) + \left(\frac{\partial P(U)}{\partial U}\right)^n \Delta U^n, \tag{5.75}$$

where $\frac{\partial F(U)}{\partial U}$ and $\frac{\partial P(U)}{\partial U}$ are the same matrices defined earlier as $\bar{A}_1$ and $\bar{A}_2$.

$$\frac{\partial F(U)}{\partial U} = A_1(U) = \begin{bmatrix} 0 & 1 & 0 \\ \frac{1}{2}(\gamma-3)u^2 & (3-\gamma)u & \gamma-1 \\ -\gamma E u + (\gamma-1)u^3 & \gamma E - \frac{3}{2}(\gamma-1)u^2 & \gamma u \end{bmatrix} \tag{5.76}$$

$$\frac{\partial P(U)}{\partial U} = A_2(U) = \begin{bmatrix} 0 & 0 & 0 \\ \frac{1}{2}(\gamma-1)u^2 & -(\gamma-1)u & \gamma-1 \\ 0 & 0 & 0 \end{bmatrix} \tag{5.77}$$

Making these substitutions, Equation (2.24) then becomes

$$-\Big[(F^n h + A_1^n \Delta U^n h)_2 - (F^n h + A_1^n \Delta U^n h)_1\Big] + \int_1^2 (P^n + A_2^n \Delta U^n)\,dh = 0. \tag{5.78}$$

Now taking the control volume to be one computational cell which goes from $J-1$ to J, where the solution varies linearly in the cell, and moving the known quantities from the current solution to the right hand side of the equation gives

$$\begin{aligned}\Big[-(A_1^n h)_J + \tfrac{1}{2}(A_2^n)_J(h_J - h_{J-1})\Big]\Delta U_J^n \quad &+ \quad \Big[(A_1^n h)_{J-1} + \tfrac{1}{2}(A_2^n)_{J-1}(h_J - h_{J-1})\Big]\Delta U_{J-1}^n \\ &= \Big[(F^n h)_J - (F^n h)_{J-1}\Big] - \tfrac{1}{2}\Big[P_J^n + P_{J-1}^n\Big](h_J - h_{J-1}). \qquad (5.79)\end{aligned}$$

Shock Jump

The shock jump becomes an internal boundary condition for the equations just presented for the internal domain cells. The location of the shock must be part of the computation and the jump across the shock is a function of the flowfield upstream and downstream of the shock. To do this, an additional variable x_s, the shock location, is added to the unknowns which must be found in the solution to the problem. At this location there are two grid nodes, one on either side of the shock but located at the same location, over which the jump conditions are applied. Since the location of the shock is not known, the computational mesh must move to compensate for the movement of the shock. In the method used here, the grid upstream and downstream of the shock re-adjusts after each iteration so the grid spacing on either side of the shock is constant.

The shock jump condition which must hold for the converged steady solution was given in Equation (2.37).

$$[[Fh]] = 0 \qquad (2.37)$$

As with the computational cells upstream and downstream of the shock, Equation (2.37) must be linearized about the current solution to give the jump condition at iteration $n+1$.

$$[[F^{n+1}h]] = [[F^n h]] + [[A_1^n \Delta U^n h]] = 0. \qquad (5.80)$$

The shock location, however, is not known at iteration $n+1$, but an estimate exists at iteration n. To account for this, Equation (5.80) is now linearized about the shock location at iteration n so $x_s^{n+1} = x_s^n + \Delta x_s^n$ to give

$$\left[\left[A_1^n h \Delta U^n + \Delta x_s^n \left(\frac{\partial (Fh)}{\partial x}\right)^n \right]\right] = -[[\, F^n h \,]], \tag{5.81}$$

where $\frac{\partial Fh}{\partial x}$ is found using a one-sided three point difference stencil.

$$\begin{aligned}
\left(\frac{\partial Fh}{\partial x}\right)_J &\approx \frac{(Fh)_{J-2} - 4(Fh)_{J-1} + 3(Fh)_J}{2\Delta x} && \text{ahead of shock} \\
\left(\frac{\partial Fh}{\partial x}\right)_J &\approx \frac{-3(Fh)_J + 4(Fh)_{J+1} - (Fh)_{J+2}}{2\Delta x} && \text{behind shock.}
\end{aligned}$$

Equation (5.81) can be written in a similar form to that given in Equation (5.79).

$$\begin{aligned}
\Big[(A_1^n h)_J\Big]\Delta U_J^n \;+\; \Big[\left(\frac{\partial (Fh)}{\partial x}\right)_J^n - \left(\frac{\partial (Fh)}{\partial x}\right)_{J-1}^n\Big]\Delta x_s^n \;+\; \Big[-(A_1^n h)_{J-1}\Big]\Delta U_{J-1}^n \\
= -(F^n h)_J \;+\; (F^n h)_{J-1},
\end{aligned} \tag{5.82}$$

where the nodes J and $J-1$ are the two nodes at the shock location.

Boundary Conditions

The boundary conditions used here are similar to those used in the shock capturing schemes in that the same quantities are specified at the boundaries, but the implementation is slightly different.

For a subsonic inlet boundary the stagnation pressure p_o, and the logarithm of the entropy s are specified.

$$p_o = \rho_o\left(\frac{\gamma-1}{2\gamma}u^2 + \frac{p}{\rho}\right) \tag{5.83}$$

$$s = \log\left(\frac{p}{\rho^\gamma}\right) \tag{5.84}$$

As with the computational scheme away from the boundary, the boundary condition is cast into 'delta form' so

$$p_o^{n+1} \;=\; p_o^n \;+\; \rho_o\Big[\Big(\frac{(\gamma-3)u^2}{2\rho}\Big)\Delta\rho \;+\; \Big(\frac{(2-\gamma)u}{\rho}\Big)\Delta(\rho u) \;+\; \Big(\frac{\gamma-1}{\rho}\Big)\Delta(\rho E)\Big] \qquad (5.85)$$

$$s^{n+1} \;=\; s^n \;+\; \Big(\frac{-\gamma}{\rho}+\frac{(\gamma-1)u^2}{p}\Big)\Delta\rho \;+\; \Big(\frac{(\gamma-1)u}{p}\Big)\Delta(\rho u) \;+\; \Big(\frac{(\gamma-1)}{p}\Big)\Delta(\rho E), \qquad (5.86)$$

where p_o and s are driven to specified values, so $p_o^{n+1} = (p_o)_{spec}$ and $s^{n+1} = s_{spec}$. In matrix form this becomes

$$\begin{bmatrix} \frac{(\gamma-3)u^2}{2\rho} & \frac{(2-\gamma)u}{\rho} & \frac{\gamma-1}{\rho} \\ \frac{-\gamma}{\rho}+\frac{(\gamma-1)u^2}{p} & \frac{(\gamma-1)u}{p} & \frac{(\gamma-1)}{p} \end{bmatrix} \begin{bmatrix} \Delta\rho \\ \Delta(\rho u) \\ \Delta(\rho E) \end{bmatrix}^n \;=\; \begin{bmatrix} (p_o)_{spec} - (p_o)^n \\ s_{spec} - s^n \end{bmatrix}. \qquad (5.87)$$

For a subsonic outlet boundary, the pressure p is specified. Again, the 'delta form' is used to write the value of p at iteration $n+1$.

$$p^{n+1} \;=\; p^n \;+\; \Big(\tfrac{1}{2}(\gamma-1)u^2\Big)\Delta\rho \;+\; \Big(-(\gamma-1)u\Big)\Delta(\rho u) \;+\; \Big(\gamma-1\Big)\Delta(\rho E), \qquad (5.88)$$

where p is to be driven to a specified value, $p^{n+1} = p_{spec}$. In matrix form this becomes

$$\begin{bmatrix} \tfrac{1}{2}(\gamma-1)u^2 & -(\gamma-1)u & \gamma-1 \end{bmatrix} \begin{bmatrix} \Delta\rho \\ \Delta(\rho u) \\ \Delta(\rho E) \end{bmatrix}^n \;=\; \begin{bmatrix} p_{spec} - p^n \end{bmatrix}. \qquad (5.89)$$

For a supersonic inlet, it is simply necessary to prescribe the flow conditions. Again, the inlet Mach number M_{spec} and stagnation quantities ρ_o and p_o are all that are needed to find the inlet conditions.

$$\rho \;=\; \rho_o\Big(1 \;+\; \frac{(\gamma-1)}{2}\,M_{spec}^2\Big)^{\frac{-1}{\gamma-1}}$$

$$p = p_o\left(1 + \frac{(\gamma-1)}{2} M_{spec}^2\right)^{\frac{-\gamma}{\gamma-1}}$$
$$u = M_{spec}\sqrt{\frac{\gamma p}{\rho}}$$

The state vector is fixed at

$$U^{n+1} = \begin{bmatrix} \rho \\ \rho u \\ \frac{p}{\gamma-1} + \frac{1}{2}u^2\rho \end{bmatrix}_{spec} . \tag{5.90}$$

In the same matrix form given above, this condition is

$$\begin{bmatrix} 1 & 0 & 0 \\ 0 & 1 & 0 \\ 0 & 0 & 1 \end{bmatrix} \begin{bmatrix} \Delta\rho \\ \Delta(\rho u) \\ \Delta(\rho E) \end{bmatrix}^n = \begin{bmatrix} \rho_{spec} - \rho^n \\ (\rho u)_{spec} - (\rho u)^n \\ (\rho E)_{spec} - (\rho E)^n \end{bmatrix} . \tag{5.91}$$

Solution Procedure

What has been derived is a set of equations to find ΔU^n for the boundary conditions, the shock jump and the rest of the flow region. It should be noted that no treatment has been added for a non-shock sonic point. There are methods for treating a sonic point [15, 11], but for the applications presented here this point will simply be avoided. These equations can be written in terms of a matrix equation where a know matrix times an unknown vector of 'delta' quantities is equal to a known vector. Examples of this matrix equation are given in Figure 5.2 for a subsonic case which does not include the shock jump conditions and Figure 5.3 for a transonic case. Notice that for the transonic case the variable Δx_s is part of the matrix equation, but there is still the correct number of equations for unknowns.

To solve these equations for ΔU^n, a direct matrix solver must be used. This is easy in one dimension where the matrix is small and banded, but can require considerable computer resources when extended to two and three dimensions.

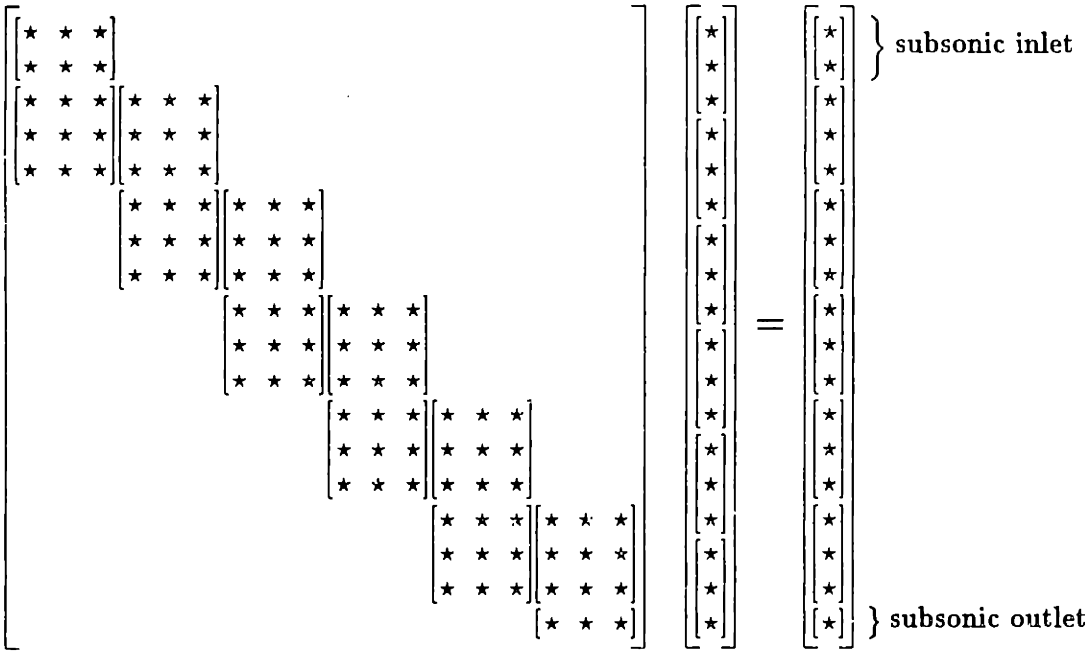

Figure 5.2: Representation of the matrix equation for the direct solver for both subsonic inlet and outlet.

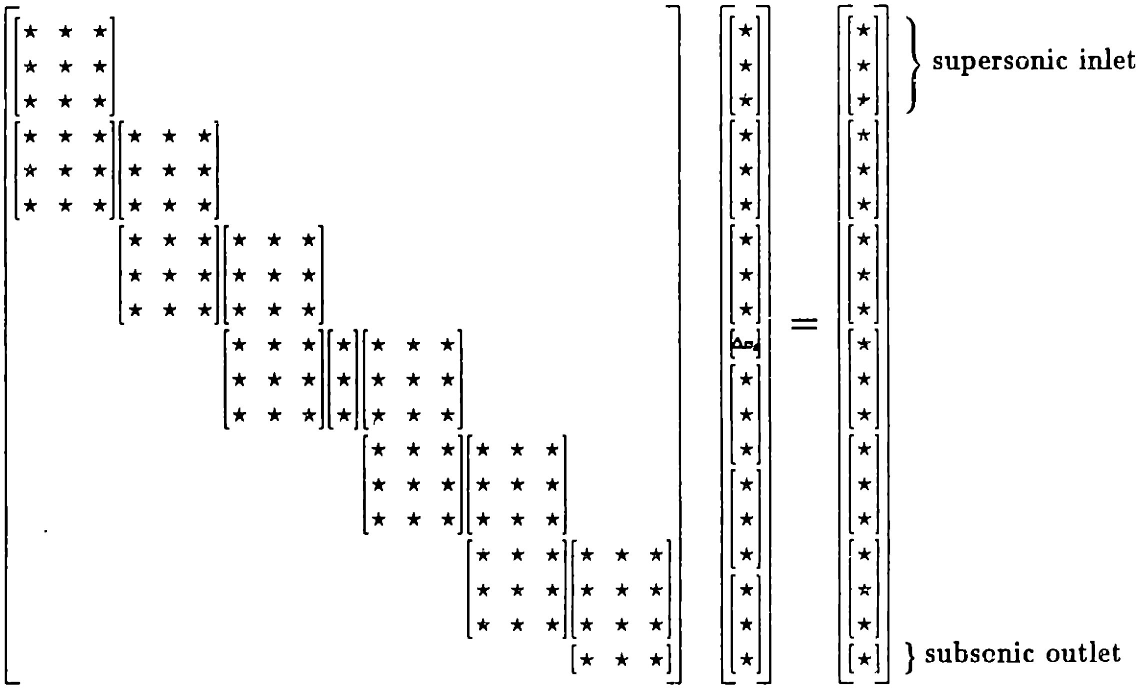

Figure 5.3: Representation of the matrix equation for the direct solver for a supersonic inlet, a shock jump and a subsonic outlet.

Due to linearization effects, one pass to find ΔU^n is not sufficient to find the desired solution, therefore the ΔU^n found from Equation (5.79) is used to update the current solution to U^{n+1}. Now this updated value becomes the current solution and the procedure is repeated until the computed value of ΔU^n is below some tolerance. Convergence generally requires only a few iterations.

5.4.2 Linear Perturbation

The perturbation equations are similar to the steady state equations, but now, since the equation is linear, the solution can be found in one iteration. Again, the equations for each portion of the flowfield are derived in turn.

Interior Domain Cells

The integral form of the perturbation equation comes from Equation (2.31). For a harmonic time dependency this equation becomes

$$i\omega \int_1^2 \widehat{U} h \, dx = -\left[(\bar{A}_1 \widehat{U} h)_2 - (\bar{A}_1 \widehat{U} h)_1\right] + \int_1^2 \bar{A}_2 \widehat{U} \, dh. \qquad (5.92)$$

Again using a control volume of one computational which goes from $J-1$ to J where the solution varies linearly in the cell gives

$$\begin{aligned} &\left[i\omega \tfrac{1}{2} h_J (x_J - x_{J-1}) + (\bar{A}_1 h)_J - \tfrac{1}{2} (\bar{A}_2)_J (h_J - h_{J-1}) \right] \widehat{U}_J + \\ &\left[i\omega \tfrac{1}{2} h_{J-1} (x_J - x_{J-1}) - (\bar{A}_1 h)_{J-1} - \tfrac{1}{2} (\bar{A}_2)_{J-1} (h_J - h_{J-1}) \right] \widehat{U}_{J-1} = 0. \qquad (5.93) \end{aligned}$$

Shock Jump

The steady shock location, $\bar{x}_s$ is already known from the computation of the steady solution. What will be found here is the unsteady perturbation on the shock location due to the unsteadiness in the flowfield, therefore $x_s(t) = \bar{x}_s + \Re\{\hat{x}_s e^{i\omega t}\}$.

The linear shock jump condition which must hold was given in Equation (2.40).

$$\left[\left[A_1\hat{U}h + \hat{x}_s\left(\frac{\partial(\bar{F}h)}{\partial x}\right) - \bar{U}\,h\,i\omega\,\hat{x}_s\right]\right] = 0 \tag{2.40}$$

$\frac{\partial \bar{F}h}{\partial x}$ is found using the same one-sided three point difference stencils given for the steady solution.

Equation (2.40) can be written in a similar form to that given in Equation (5.93).

$$\begin{aligned} \Big[(\bar{A}_1 h)_J\Big]\hat{U}_J \;&+\; \left[\left(\frac{\partial \bar{F}h}{\partial x}\right)^n_J - \left(\frac{\partial \bar{F}h}{\partial x}\right)^n_{J-1} - i\,\omega\Big((\bar{U}h)_J - (\bar{U}h)_{J-1}\Big)\right]\hat{x}_s \\ &+\; \Big[-(\bar{A}_1 h)_{J-1}\Big]\hat{U}_{J-1} \;=\; 0. \end{aligned} \tag{5.94}$$

where the nodes J and $J-1$ are the same two nodes at the shock location from the steady solution.

Boundary Conditions

Again, the boundary conditions used here are similar to those used in the shock capturing schemes. The equations will also look similar to those used for the steady state shock fitting scheme just described, because the Newton solver used involves the same linearization of the nonlinear boundary conditions used to find the perturbation.

For a subsonic inlet boundary, the perturbation stagnation pressure $\hat{p}_o$ and logarithm of the entropy $\hat{s}$ are specified.

$$\hat{p}_o = \bar{\rho}_o\left(\bar{u}\,\hat{u} + \frac{\hat{p}}{\bar{\rho}}\right) \tag{5.95}$$

$$\hat{s} = \frac{-\gamma\,\hat{\rho}}{\bar{\rho}} + \frac{\hat{p}}{\bar{p}} \tag{5.96}$$

Written in terms of the perturbation state vector in matrix form where $(\widehat{p}_o)_{spec}$ and logarithm of the entropy $\widehat{s}_{spec}$ are specified, this becomes

$$\begin{bmatrix} \frac{(\gamma-3)\bar{u}^2}{2\bar{\rho}} & \frac{(2-\gamma)\bar{u}}{\bar{\rho}} & \frac{\gamma-1}{\bar{\rho}} \\ \frac{-\gamma}{\bar{\rho}} + \frac{(\gamma-1)\bar{u}^2}{\bar{p}} & \frac{(\gamma-1)\bar{u}}{\bar{p}} & \frac{(\gamma-1)}{\bar{p}} \end{bmatrix} \begin{bmatrix} \widehat{\rho} \\ (\widehat{\rho u}) \\ (\widehat{\rho E}) \end{bmatrix}^n = \begin{bmatrix} (\widehat{p}_o)_{spec} \\ \widehat{s}_{spec} \end{bmatrix}. \tag{5.97}$$

For a subsonic outlet boundary, the pressure perturbation $\widehat{p}$ is specified to be $\widehat{p}_{spec}$. In terms of the state vector perturbation in matrix form this becomes

$$\begin{bmatrix} \frac{1}{2}(\gamma-1)\,\bar{u}^2 & -(\gamma-1)\,\bar{u} & \gamma-1 \end{bmatrix} \begin{bmatrix} \widehat{\rho} \\ (\widehat{\rho u}) \\ (\widehat{\rho E}) \end{bmatrix}^n = \begin{bmatrix} \widehat{p}_{spec} \end{bmatrix}. \tag{5.98}$$

For a supersonic inlet, the inlet perturbation state vector is fully specified. The cases shown here do not have a flow perturbation at the supersonic inlet, therefore the state vector perturbation is fixed at

$$\widehat{U} = \begin{bmatrix} 0 \\ 0 \\ 0 \end{bmatrix}, \tag{5.99}$$

which in the matrix form used thus far becomes

$$\begin{bmatrix} 1 & 0 & 0 \\ 0 & 1 & 0 \\ 0 & 0 & 1 \end{bmatrix} \begin{bmatrix} \widehat{\rho} \\ (\widehat{\rho u}) \\ (\widehat{\rho E}) \end{bmatrix}^n = \begin{bmatrix} 0 \\ 0 \\ 0 \end{bmatrix}. \tag{5.100}$$

Solution Procedure

As with the solution procedure for the steady state, there is now a set of equations for $\widehat{U}$ for the boundary conditions, the shock jump and the rest of the flow region. These equations can be written in similar matrix equations to those shown in Figures 5.2 and 5.3 for the steady state. Again, the perturbation in the shock location, $\widehat{x}_s$ is part of the matrix equation.

Since the perturbation equation is linear, the resulting matrix equation gives the desired solution in one pass.

5.5 Moving Grid

The computational methods just described in this chapter were for fixed control volumes. Here, the grid will move in the computation of the perturbation solution, a concept which is well accepted for nonlinear calculations. The steady state control volume will be considered fixed, and a prescribed grid movement is added as a perturbation about this fixed steady grid. Since the linear perturbation computation is for a perturbation in the flow variables, this is in keeping with the present computation. There are several reasons why a moving control volume might be desired. The most obvious is the introduction of a moving body, such as the blade in two or three dimensions, which could be implemented through the movement of the grid surrounding the blade. Another reason is to implement a grid movement, which corresponds to a shock movement, with the result that the shock then does not move with respect to the grid. These reasons for the use of grid movement as well as the method of implementing this grid movement in the context of the methods already described will be addressed in this section.

In the past, most linear methods have implemented blade movement through the use of a stationary blade with the desired boundary condition extrapolated back to this stationary point. This amounts to applying a velocity perturbation at the steady blade location. This method involves finding gradients of the steady solution for the extrapolation process. These gradient terms can be difficult to compute accurately, especially in regions such as the leading edge of the blade where there is a large variation in the gradients, and can amplify errors in the steady computation and inject these into the computation of the perturbation. To avoid these difficulties, Whitehead [31] introduced a method for implementing the blade movement by rotating the whole mesh and performing the extrapolation process just mentioned away from the blade where the variation of the gradient of the flowfield is less severe. His results show the rational for using this method. Hall [16, 14] uses a variation on this method which uses a continuously deforming mesh. Although these issues apply to two and three-dimensional problems, the techniques described here for the quasi-one-dimensional duct problem directly extend to the higher dimensional problems.

In Chapters 3 and 4 the importance of keeping a similar shock shape as the shock moves was discussed. The computational shock shape is a function of the shock's location with respect to the grid, as shown in Figure 4.1. Since the computation of the linear perturbation finds a linearization of the fully nonlinear discrete solution, these problems will exist there as well. One method of ensuring that the shock shape will remain the same as the shock moves is to move the grid with the shock. Of course, the shock movement is not known before the computation is begun and its computation must be part of the solution procedure. Given a computation where there is no grid movement, it is possible to estimate the shock movement, $\hat{x}_s$, from

$$\left(\frac{d\bar{U}}{d\bar{x}}\right)_s \hat{x}_s \approx -\hat{U}_s, \tag{5.101}$$

where $(\frac{d\bar{U}}{d\bar{x}})_s$ is the steady state gradient in the shock. This expression merely states that the variable $\hat{U}_s$ represents a translation of the steady shock. This approximate shock movement is then used as the grid movement, $\hat{x}_g$, for a new computation. The solution procedure then becomes:

- set $\hat{x}_g = 0$
- repeat 1-2 times
  - calculate solution $\widehat{U}$
  - find shock movement relative to the grid movement from

    $$\left(\frac{d\bar{U}}{d\bar{x}}\right)_s (\hat{x}_s)_{rel} \approx -(\widehat{U}_s)_{rel}$$

  - set $(\hat{x}_g)_{new} = (\hat{x}_g)_{old} + (\hat{x}_s)_{rel}$

In practice, a region of computational cells which enclose the shock is moved. It is in principle possible to extend this procedure to two and three-dimensional problems. The detection of the shock region becomes more complicated, but is clearly possible.

5.5.1 Computational Procedure

To develop the perturbation equations which include the terms for a moving mesh, the nonlinear Equation (2.17) which includes the effect of a moving control volume will be used as a starting point.

$$\frac{d}{dt}\int_1^2 Uh\,dx = -\Big[(Fh)_2 - (Fh)_1\Big] + \Big[(Uhu_b)_2 - (Uhu_b)_1\Big] + \int_1^2 P\,dh \qquad (2.17)$$

The discrete form of this equation is similar to Equation (5.2), except for the addition of the moving control volume boundary.

$$\begin{aligned} \frac{d}{dt}\left[\tfrac{1}{2}(h_{J+\frac{1}{2}} + h_{J-\frac{1}{2}})U_J\Delta x_J\right] &= -\left[h_{J+\frac{1}{2}}F_{J+\frac{1}{2}} - h_{J-\frac{1}{2}}F_{J-\frac{1}{2}}\right] \\ &+ \left[U_{J+\frac{1}{2}}h_{J+\frac{1}{2}}\dot{x}_{J+\frac{1}{2}} - U_{J-\frac{1}{2}}h_{J-\frac{1}{2}}\dot{x}_{J-\frac{1}{2}}\right] + \tfrac{1}{2}(P_{J+\frac{1}{2}} + P_{J-\frac{1}{2}})(h_{J+\frac{1}{2}} - h_{J-\frac{1}{2}}) \end{aligned} \qquad (5.102)$$

The process of taking this nonlinear discrete equation and forming the linear perturbation equation is similar to the process described in Section 2.3.2, except now there is a perturbation in the node locations as well as a perturbation in the flow variables. As a result of the perturbation in the node locations, there is also a perturbation in the height of the duct which is found from

$$\widehat{h}_J = \left(\frac{d\bar{h}}{d\bar{x}}\right)_J \widehat{x}_J. \tag{5.103}$$

Therefore, adding to the list of substitutions made in Section 2.3.2

$$\begin{aligned} x_J(t) &= \bar{x}_J + \Re\{\widehat{x}_J e^{i\omega t}\} && (5.104) \\ h_J(t) &= \bar{h}_J + \Re\{\widehat{h}_J e^{i\omega t}\}, && (5.105) \end{aligned}$$

and after subtracting off the steady state equation, the perturbation equation for a moving mesh is found. This equation contains Equation (5.19), so the new form of this equation will be written:

$$\left(\frac{\partial \widehat{U}}{\partial t}\right)_J = -R(\widehat{U}_J) - S_R, \tag{5.106}$$

where $R(\widehat{U}_J)$ is given in Equation (5.19) and

$$\begin{aligned} S_R = \left(\frac{1}{\frac{1}{2}(\bar{h}_{J+\frac{1}{2}} + \bar{h}_{J-\frac{1}{2}})\,\Delta\bar{x}_J}\right)\Big(& i\,\omega\,\tfrac{1}{2}(\widehat{h}_{J+\frac{1}{2}} + \widehat{h}_{J-\frac{1}{2}})\,\bar{U}_J\,\Delta\bar{x}_J \\ & + i\,\omega\,\tfrac{1}{2}(\bar{h}_{J+\frac{1}{2}} + \bar{h}_{J-\frac{1}{2}})\,\bar{U}_J\,(\widehat{x}_{J+\frac{1}{2}} - \widehat{x}_{J-\frac{1}{2}}) + \widehat{h}_{J+\frac{1}{2}}\bar{F}_{J+\frac{1}{2}} - \widehat{h}_{J-\frac{1}{2}}\bar{F}_{J-\frac{1}{2}} \\ & - i\,\omega\,(\bar{h}_{J+\frac{1}{2}}\bar{U}_{J+\frac{1}{2}}\widehat{x}_{J+\frac{1}{2}} - \bar{h}_{J-\frac{1}{2}}\bar{U}_{J-\frac{1}{2}}\widehat{x}_{J-\frac{1}{2}}) \\ & - \tfrac{1}{2}(\bar{P}_{J+\frac{1}{2}} + \bar{P}_{J-\frac{1}{2}})\,(\widehat{h}_{J+\frac{1}{2}} - \widehat{h}_{J-\frac{1}{2}})\Big). \end{aligned} \tag{5.107}$$

S_R is a source term, since it is solely a function of the steady state solution and the prescribed grid motion. This source term is found at the beginning of the computation and does not change from one iteration to the next, hence adding little extra computational cost. Equation (5.107) is applicable to both the artificial viscosity and flux vector split schemes, where $\bar{F}_{J+\frac{1}{2}}$ and $\bar{F}_{J-\frac{1}{2}}$ are given in Section 5.2, but the artificial viscosity schemes require a source term from the additional artificial viscosity terms.

After adding Equations (5.104) and (5.105) to the substitution list for the artificial viscosity terms, Equation (5.20) becomes

$$\left(\frac{\partial \widehat{U}}{\partial t}\right)_J = -R(\widehat{U}_J) + D(\widehat{U}_J) - S_R + S_D, \tag{5.108}$$

where for second difference artificial viscosity

$$\begin{aligned} S_D = {} & \epsilon_2 \left(\frac{1}{\Delta\bar{x}_J \frac{1}{2}(\bar{h}_{J+\frac{1}{2}} + \bar{h}_{J-\frac{1}{2}})}\right) \times \\ & \left(\widehat{h}_{J+\frac{1}{2}} \left(\frac{\Delta x}{\Delta t_{\max}}\right)_{J+\frac{1}{2}} (\bar{U}_{J+1} - \bar{U}_J) - \widehat{h}_{J-\frac{1}{2}} \left(\frac{\Delta x}{\Delta t_{\max}}\right)_{J-\frac{1}{2}} (\bar{U}_J - \bar{U}_{J-1})\right), \end{aligned} \tag{5.109}$$

and for fourth difference artificial viscosity where the second difference artificial viscosity is turned on in the shock

$$\begin{aligned} S_D = {} & \left(\frac{1}{\Delta\bar{x}_J \frac{1}{2}(\bar{h}_{J+\frac{1}{2}} + \bar{h}_{J-\frac{1}{2}})}\right) \times \\ & \Bigg[-\epsilon_4 \Bigg((1 - \bar{S}_{J+\frac{1}{2}})\widehat{h}_{J+\frac{1}{2}} \left(\frac{\Delta x}{\Delta t_{\max}}\right)_{J+\frac{1}{2}} (D^2\bar{U}_{J+1} - D^2\bar{U}_J) - \\ & \qquad (1 - \bar{S}_{J-\frac{1}{2}})\widehat{h}_{J-\frac{1}{2}} \left(\frac{\Delta x}{\Delta t_{\max}}\right)_{J-\frac{1}{2}} (D^2\bar{U}_J - D^2\bar{U}_{J-1})\Bigg) \\ & + \epsilon_2 \Bigg(\bar{S}_{J+\frac{1}{2}} \widehat{h}_{J+\frac{1}{2}} \left(\frac{\Delta x}{\Delta t_{\max}}\right)_{J+\frac{1}{2}} (\bar{U}_{J+1} - \bar{U}_J) - \\ & \qquad \bar{S}_{J-\frac{1}{2}} \widehat{h}_{J-\frac{1}{2}} \left(\frac{\Delta x}{\Delta t_{\max}}\right)_{J-\frac{1}{2}} (\bar{U}_J - \bar{U}_{J-1})\Bigg)\Bigg]. \end{aligned} \tag{5.110}$$

Similar source terms can be added to the shock fit scheme described in Section 5.4. Results which include grid movement are given in Section 6.3.

Chapter 6

Results

In Chapter 5, several computational schemes were described. The schemes were designed for a quasi-one-dimensional duct where the height of the duct varies, but the flow variables are constant across the duct. Using these assumptions, a one-dimensional equation which includes some two dimensional effects is found. This chapter presents some results from these schemes for this quasi-one-dimensional duct problem.

The focus of this thesis is on transonic flowfields, but to isolate the effects of the scheme from the effects of the shock, a subsonic case will be examined first. Next, the more interesting transonic cases will be examined. Finally, results which include grid movement in the linear perturbation solution procedure, as described in Section 5.5, will be examined.

6.1 Subsonic Case

A subsonic case is used to illustrate the basic capabilities of the numerical schemes described in Chapter 5. These schemes include a finite volume discretization of the Euler equations with the addition of second or fourth difference artificial viscosity described in Section 5.1. When the fourth difference artificial viscosity was described, there was a switch which caused a change to second difference artificial viscosity in the shock. The cases used here freeze the switch at $S = 0$, so only fourth difference artificial viscosity is used. The flux vector split scheme described in Section 5.2 was designed for transonic flowfields, but it can be used for subsonic flowfields as well. Some subsonic results are shown here using the flux vector split scheme with and without MUSCL upwinding. As with the fourth difference artificial viscosity scheme, when MUSCL upwinding is used there is a switch which turns off the MUSCL upwinding in the shock. For the subsonic cases, the switch which turns off the MUSCL upwinding in the shock is frozen at $S = 0$ so there is only MUSCL upwinding. Throughout, the direct solver scheme which uses shock fitting when the flowfield is transonic (as described in Section 5.4) is used as a baseline solution. This direct solver solution is run using double precision while the other schemes use single precision, unless otherwise indicated. It should be noted that there is also an exact solution for the steady state found from the equations for a varying height isentropic streamtube.

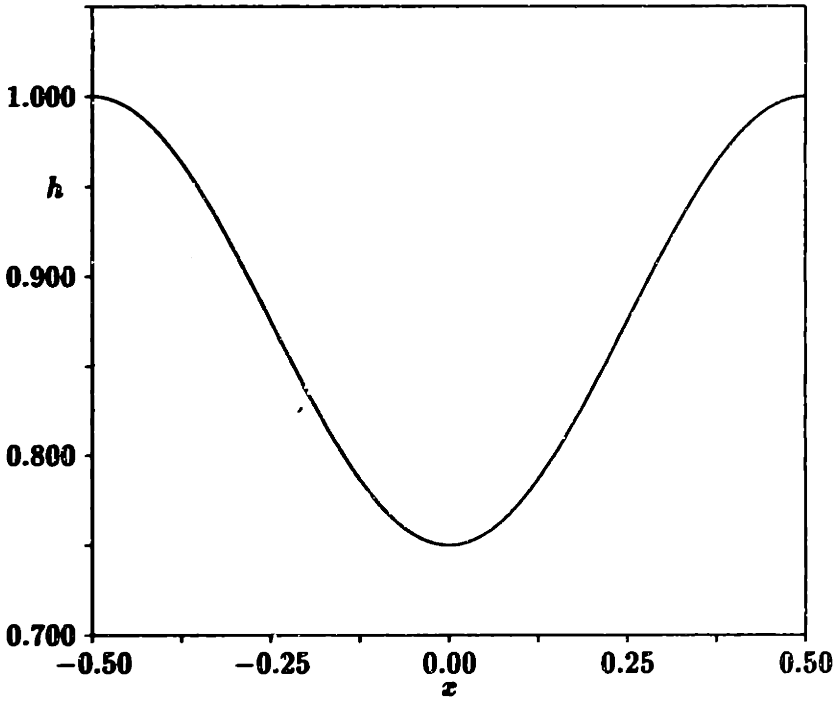

Figure 6.1: Duct height [$h = 1 - 0.25(\cos(\pi x))^2$] used for the subsonic case.

The subsonic case has a unit length duct whose domain is $-0.5 \leq x \leq 0.5$. The height distribution in this domain is given by the function $h = 1 - 0.25(\cos(\pi x))^2$ which is shown in Figure 6.1. The duct has equal inlet and outlet heights and converges smoothly to a throat which is 75% of the inlet height. The case has inlet Mach number $M_{in} = 0.5$. The steady state Mach number distribution is shown in Figure 6.2 and the steady state pressure distribution in Figure 6.3 for 360 cells along the duct and second difference artificial viscosity with coefficient $\epsilon_2 = 0.0005$. These figures also include the solution from the direct solver, but it is hard to tell the difference between the two lines in these plots since they lie almost directly on top of each other. In the unsteady perturbation, the frequency of the unsteadiness is $\omega = 1.729$ introduced through a perturbation in the exit pressure of $\widehat{p} = 0.001$ which is 0.14% of the steady exit pressure. In Figure 6.4, the real and imaginary parts of the complex pressure perturbation are shown, again for the second difference artificial viscosity scheme along with the direct solver. Once again, there is no perceivable difference in the solutions.

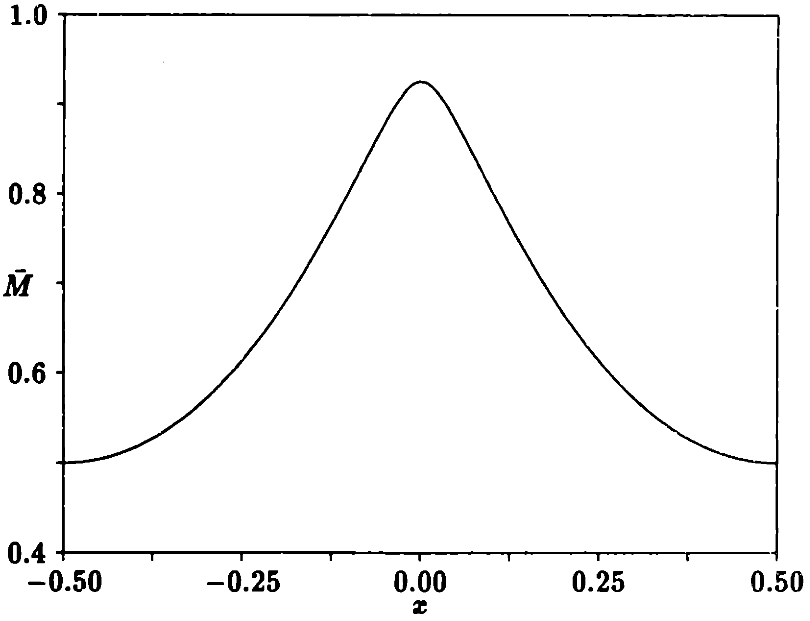

Figure 6.2: Subsonic steady state Mach number, for $\epsilon_2 = 0.0005$ and 360 cells.

The accuracy of the numerical schemes can be addressed with the subsonic to provide a baseline for the transonic case. As with all CFD methods, the more cells in the comptational domain, the more accurate the solution. The question becomes, how many cells are required to achieve some acceptable error in the solution. The resolution in the solutions given here provide errors which are far less than required for engineering accuracy, but the desire is to examine the nature of the scheme itself, not produce engineering solutions. In Figure 6.5 the steady state integrated pressure, which will be called lift, $\bar{l}$, is shown as a function of the number of cells in the domain for two different second difference artificial viscosity coefficients. The solutions have been normalized by the finest resolution direct solver solution with 720 cells, $\bar{l} = 0.534405$, to provide a

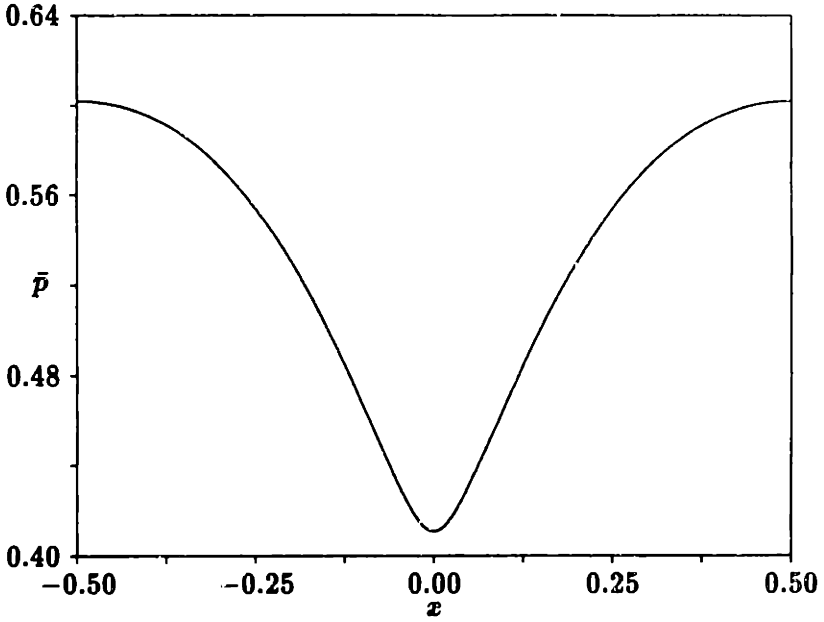

Figure 6.3: Subsonic steady state pressure, for $\epsilon_2 = 0.0005$ and 360 cells.

clearer indication of the error in the solutions. Notice that the error for the resolution shown here is less than 0.06%. The discretization of the flux for the artificial viscosity scheme is second order accurate, which is to say the error $\sim \Delta x^2$, but this accuracy is deteriorated by the addition of second difference artificial viscosity term whose error $\sim \epsilon_2 \Delta x$. This effect can be seen in Figure 6.5 where the introduction of the $O(\Delta x)$ term from the second difference artificial viscosity becomes more apparent with the larger artificial viscosity coefficient. Figure 6.6 shows the same trend for the magnitude and phase of the lift perturbation, $\hat{\ell}$ defined by $\int \hat{p} dx$, again normalized by the shock fit solution with 720 cells, $\hat{\ell} = 0.00027578 \angle 68.391°$.

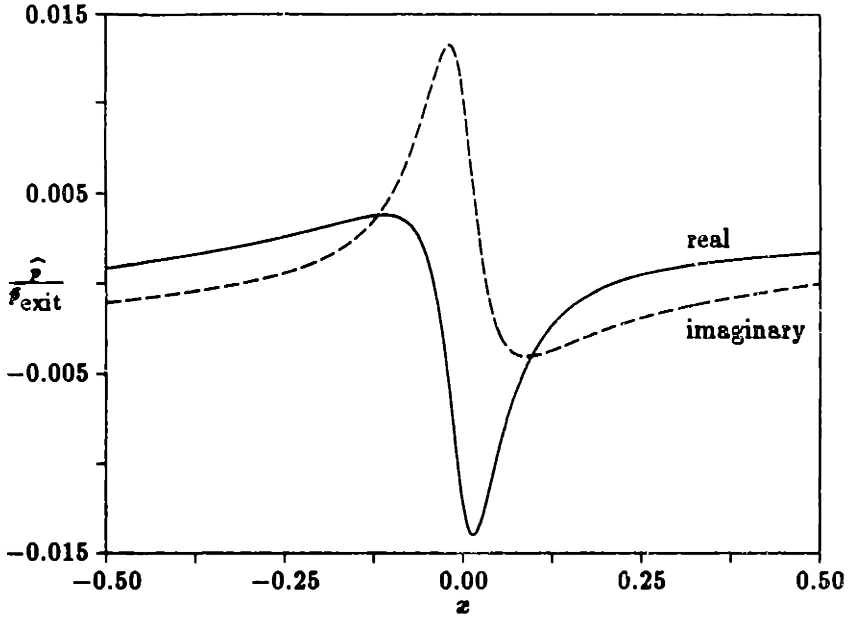

Figure 6.4: Real and imaginary parts of the pressure perturbation with $\omega = 1.729$ for the subsonic case shown in Figures 6.2 and 6.3 where $\epsilon_2 = 0.0005$ in a 360 cell domain.

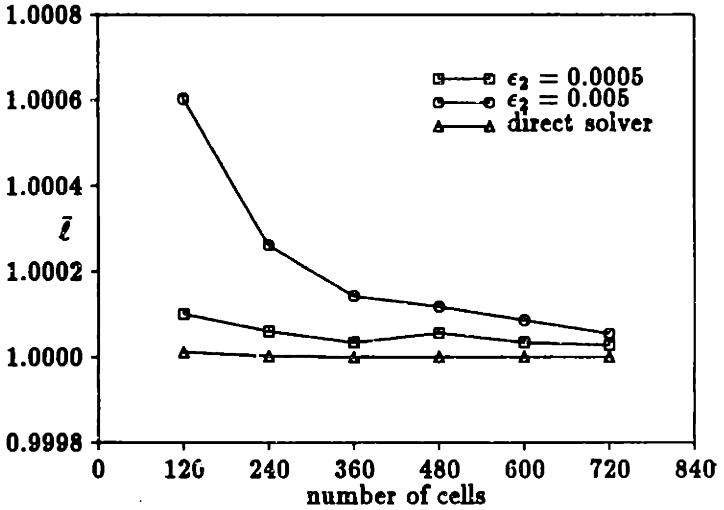

Figure 6.5: Steady state lift vs. the number of cells in the domain, for the subsonic case normalized by $\bar{l} = 0.534405$, for two different second difference artificial viscosity coefficients and the direct solver used for the shock fit scheme.

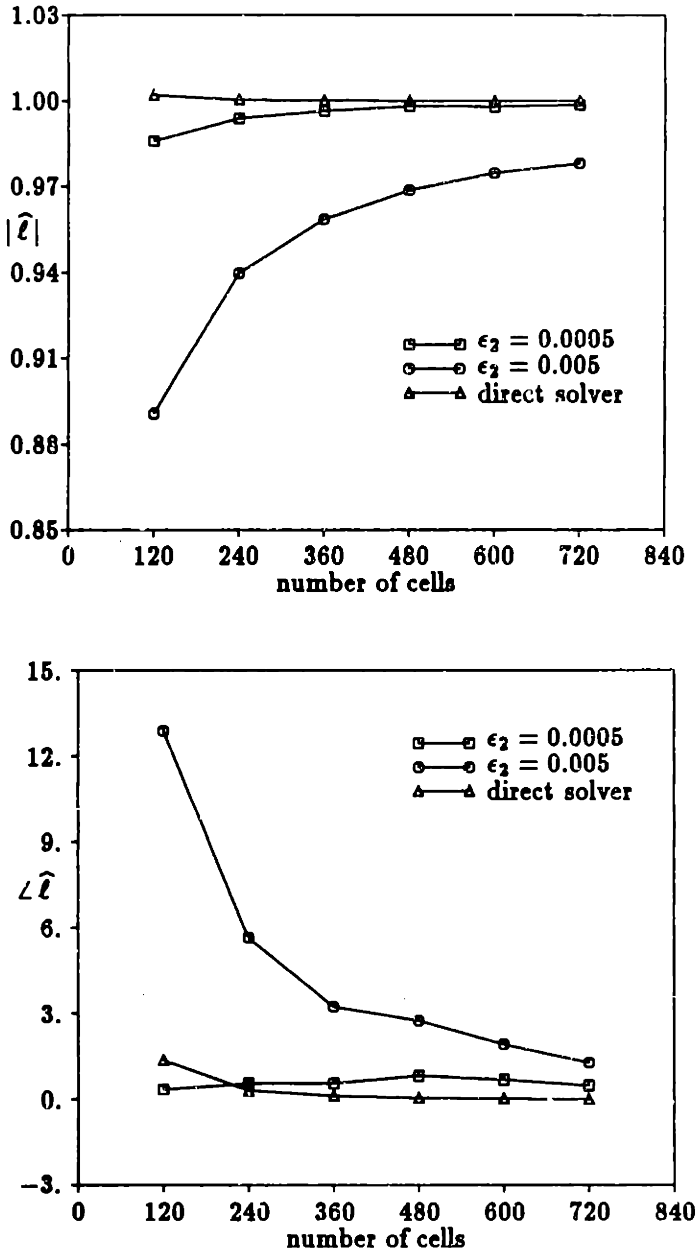

Figure 6.6: Magnitude and phase (in degrees) of lift perturbation vs. the number of cells in the domain, for the subsonic case normalized by $\widehat{\ell} = 0.00027578\ \angle 68.391^\circ$, for two different second difference artificial viscosity coefficients and the direct solver used for the shock fit scheme.

Similar results can be shown when fourth difference artificial viscosity is used instead of second difference artificial viscosity. The solution accuracy should not deteriorate as much now since the error from the fourth difference artificial viscosity $\sim \epsilon_4 \Delta x^3$. Figure 6.7 shows the steady state lift as a function of the number of cells in the domain on the same scale as the corresponding Figure 6.5 for second difference artificial viscosity. Again the solutions have been normalized by the finest resolution direct solver solution with 720 cells, $\bar{l} = 0.534405$. Notice that the error is much smaller now. Figure 6.8 shows similar results for the perturbation, again on the same scale as Figure 6.6 for second difference artificial viscosity and normalized by the shock fit solution with 720 cells, $\hat{l} = 0.00027578 \angle 68.391°$.

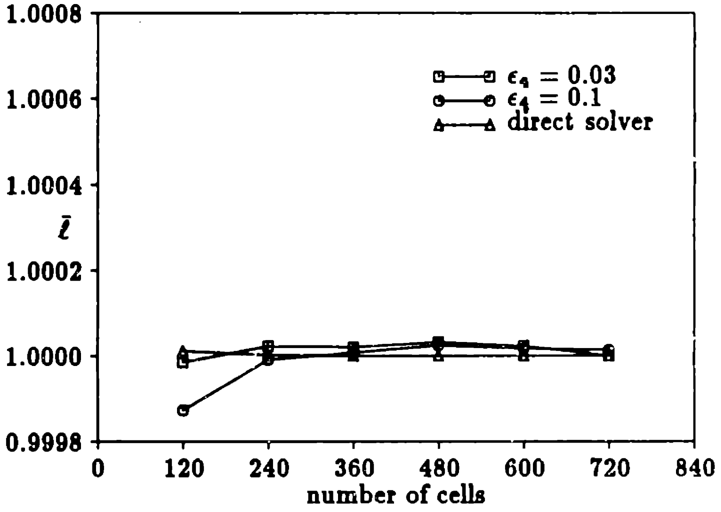

Figure 6.7: Steady state lift vs. the number of cells in the domain, for the subsonic case normalized by $\bar{l} = 0.534405$, for two different fourth difference artificial viscosity coefficients and the direct solver used for the shock fit scheme.

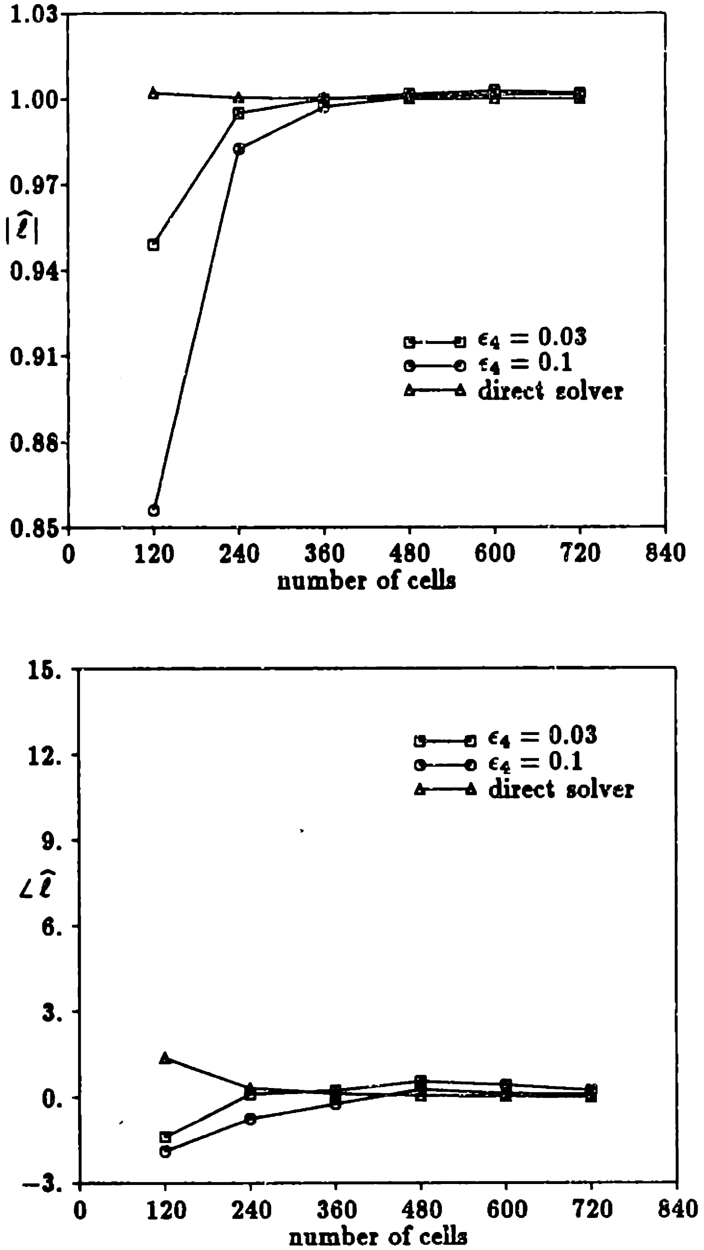

Figure 6.8: Magnitude and phase (in degrees) of lift perturbation vs. the number of cells in the domain, for the subsonic case normalized by $\hat{\ell} = 0.00027578 \angle 68.391^\circ$, for two different fourth difference artificial viscosity coefficients and the direct solver used for the shock fit scheme.

The flux vector split scheme described in Section 5.2 without MUSCL upwinding is actually only first order accurate, or in other words the error $\sim \Delta x$. When the MUSCL upwinding is used, the scheme is increased to second order accurate so the error $\sim \Delta x^2$. In Figure 6.9 the first and second order error for each of the versions of this scheme can easily be seen for the steady state lift. Again, the solutions have been normalized by the finest resolution direct solver solution with 720 cells, $\bar{l} = 0.534405$. Notice that this figure has a different scale from the corresponding artificial viscosity figures. The increased accuracy of the MUSCL upwinding version of the flux vector split scheme is clear from this figure. Figure 6.10 shows the magnitude and phase of the lift perturbation which have errors of corresponding magnitude, again normalized by the shock fit solution with 720 cells, $\hat{l} = 0.00027578 \angle 68.391°$. Notice that the trend, although not the magnitude, of the errors for the first order accurate flux vector split scheme is similar to the trend in the errors when second difference artificial viscosity, which is also first order accurate, is used in Figures 6.5 and 6.6.

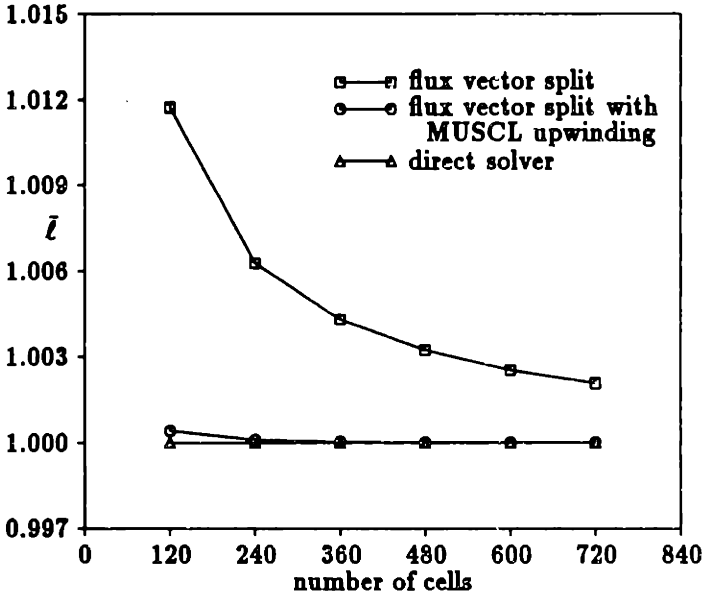

Figure 6.9: Steady state lift vs. the number of cells in the domain, for the subsonic case normalized by $\bar{l} = 0.534405$, for the flux vector split scheme with and without MUSCL upwinding and the direct solver used for the shock fit scheme.

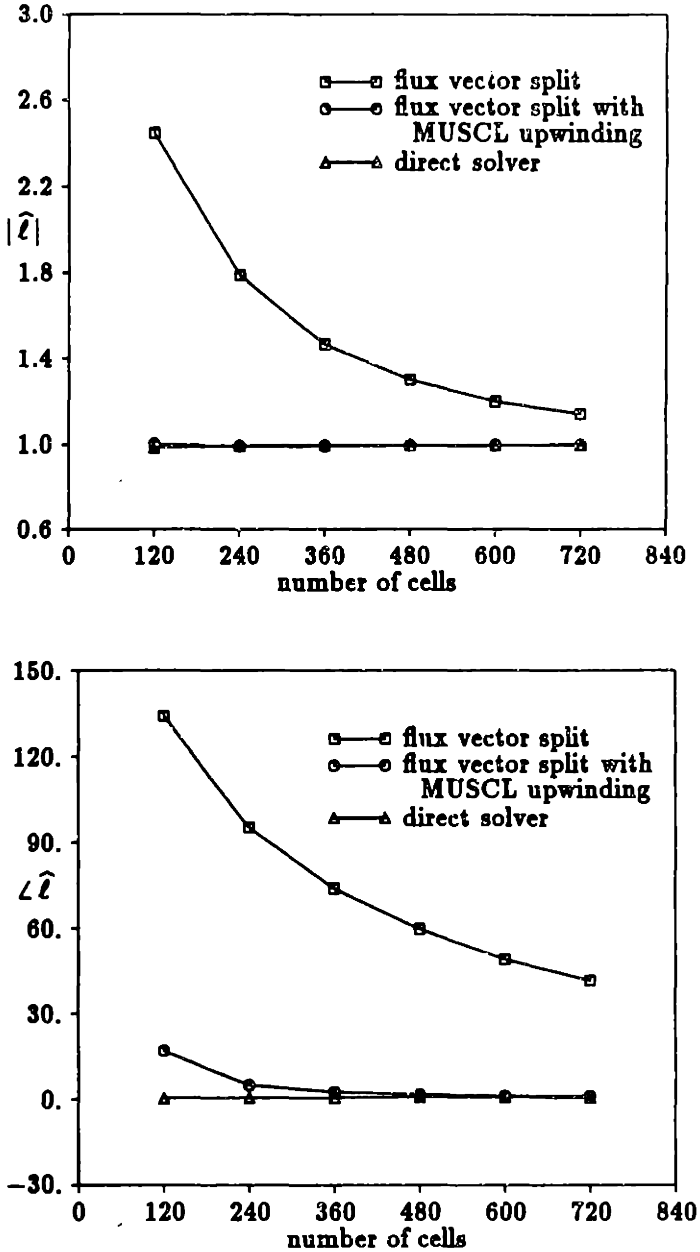

Figure 6.10: Magnitude and phase (in degrees) of lift perturbation vs. the number of cells in the domain, for the subsonic case normalized by $\hat{\ell} = 0.00027578 \angle 68.391^\circ$, for the flux vector split scheme with and without MUSCL upwinding and the direct solver used for the shock fit scheme.

6.2 Transonic Cases

In this section, the transonic cases are presented. These cases use the same numerical schemes used for the subsonic case except now they have some additional method for dealing with the shock region. The artificial viscosity schemes either use only second difference artificial viscosity, or fourth difference artificial viscosity where a switch causes a change to second difference artificial viscosity in the shock. Since the switch used here cannot be linearized, the perturbation equations do not include the linearization of the switch, as discussed in Section 5.1.2. Results for the flux vector split scheme are shown as well where, similar to the artificial viscosity schemes, either MUSCL upwinding is not used at all or it is used in most of the flowfield and turned off in the shock with the use of a switch as described in Section 5.2. Throughout, the scheme which uses shock fitting as described in Section 5.4, is used as a baseline solution.

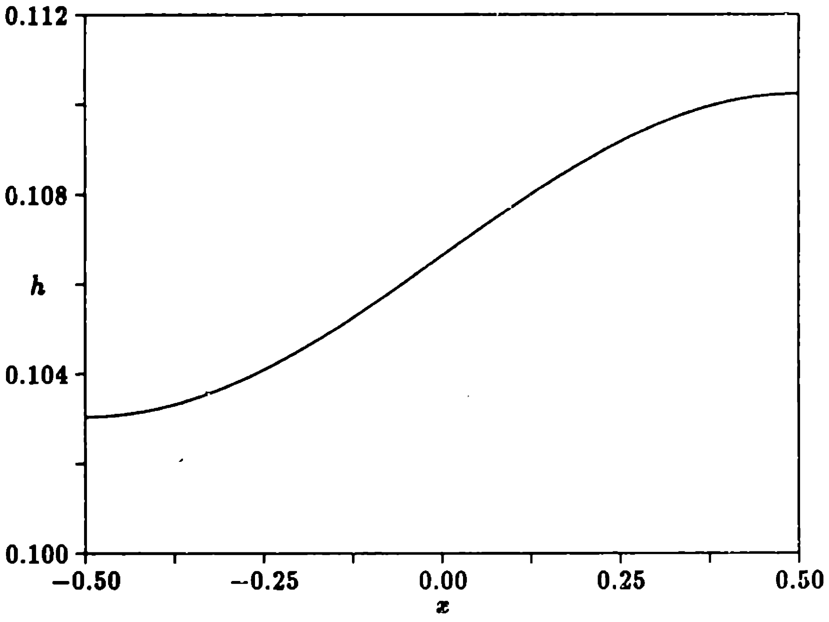

Figure 6.11: Duct height $[h = 0.10663 + 0.00359\sin(\pi x)]$ used for transonic case with $M_{in} = 1.2$.

The first transonic case once again has a one unit long domain in the region $-0.5 \leq x \leq 0.5$, but now the duct is purely diverging and has a height distribution given by the function $h = 0.10663 + 0.00359\sin(\pi x)$ as shown in Figure 6.11. This transonic case has inlet Mach number $M_{in} = 1.2$. The steady state Mach number distribution is shown in Figure 6.12 and the steady state pressure distribution in Figure 6.13 for 360 cells along the duct and second difference artificial viscosity with coefficient $\epsilon_2 = 0.1$. The shock in this case is moderate, having a jump from $M = 1.30$ to $M = 0.78$, which is representative of the strongest shocks appearing in turbomachinery flowfields. These figures also include the solution from the shock fit direct solver which can be seen in the shock region where the artificial viscosity scheme smears the shock. In the unsteady perturbation, the frequency of the unsteadiness is $\omega = 1.729$ introduced through a perturbation in the exit pressure of $\hat{p} = 0.001$ which is 0.22% of the steady exit pressure. In Figure 6.14, the real and imaginary parts of the complex pressure perturbation are shown, again for the second difference artificial viscosity scheme along with the direct solver shock fit scheme. The solution found using the artificial viscosity scheme has a peak in the shock region which does not appear in the shock fit solution. The shock fit solution, however, has an additional piece of information which comes from the shock jump condition, the explicit movement of the shock $\hat{x}_s$. To get the lift due to the moving shock, this shock movement is multiplied by the steady pressure jump across the shock, $-\hat{x}_s[[\bar{p}]]$. The peak in the shock capturing scheme represents this same shock movement and is actually a smeared out delta function, where the delta function is defined by its integral. As the width of the shock gets narrower, the height of the peak gets correspondingly higher to maintain a constant integral over this region which, in the limit of an infinitely thin shock, is $-\hat{x}_s[[\bar{p}]]$, the same extra piece of information from the shock fit scheme which does not have a peak in the solution. Since the shock fit scheme represents this limit of an infinitely thin shock, it becomes a good baseline for comparison. To compare the two schemes, the unsteady lift perturbation, $\hat{\ell}$, which is defined as the integral of the pressure perturbation in the domain, $\int \hat{p}\, dx$, is found for both schemes where, again, the shock fit scheme has the added contribution from the shock movement included in the lift.

As with the subsonic case, the accuracy of the schemes can now be studied. An important point in the justification of using the linear perturbation scheme is whether the shock capturing schemes approach the shock fit scheme with increased resolution. The shock width in the shock capturing schemes is proportional to the cell size, therefore

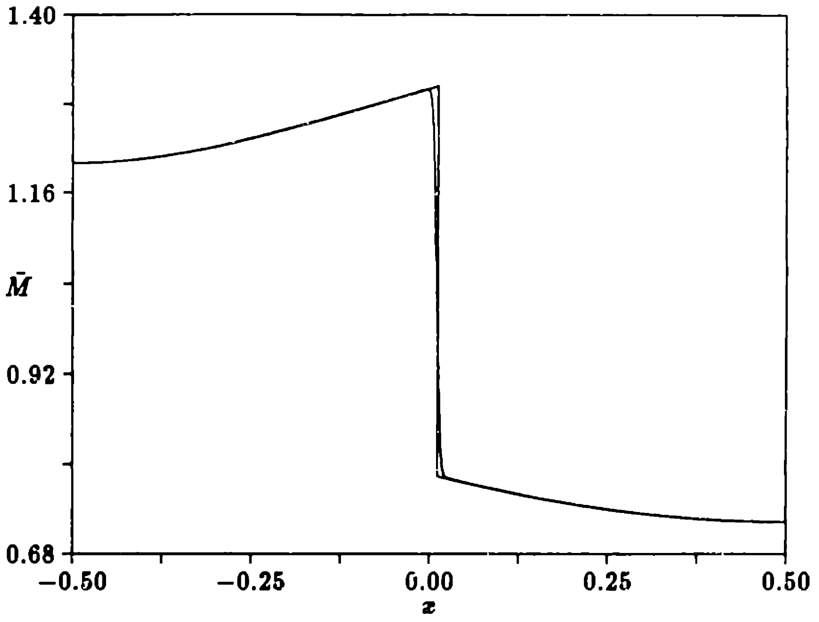

Figure 6.12: Transonic steady state Mach number for case with $M_{in} = 1.2$ for $\epsilon_2 = 0.1$ and 360 cells.

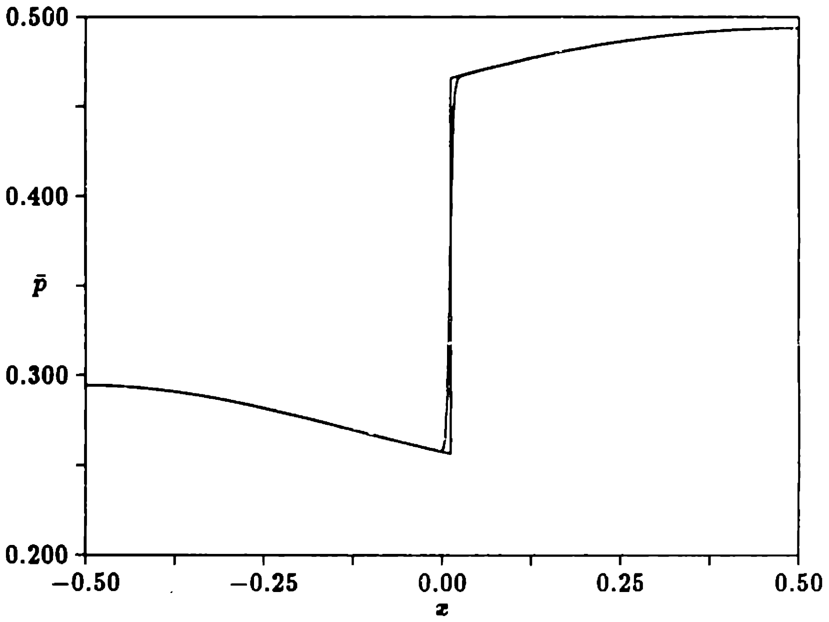

Figure 6.13: Transonic steady state pressure for case with $M_{in} = 1.2$ for $\epsilon_2 = 0.1$ and 360 cells.

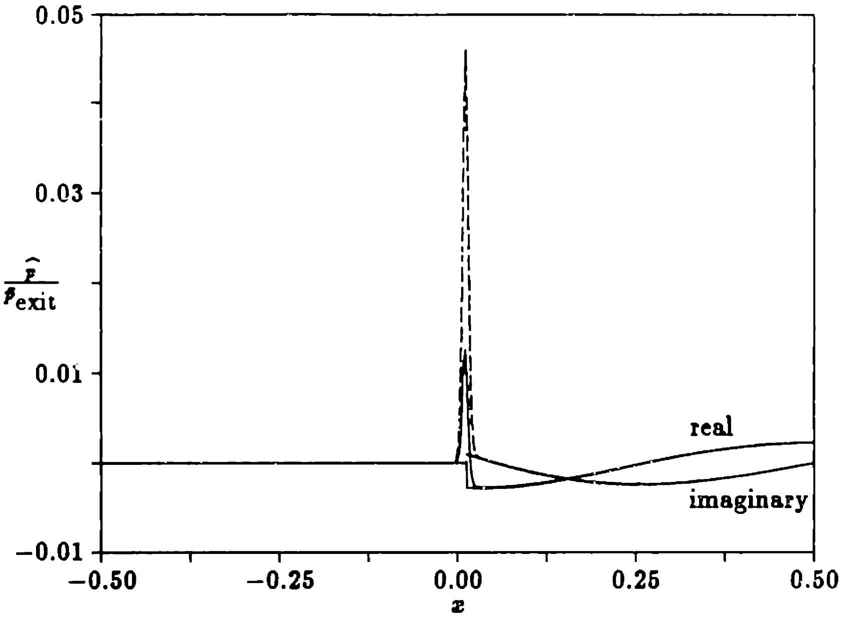

Figure 6.14: Real and imaginary parts of the pressure perturbation with $\omega = 1.729$ for the transonic case with $M_{in} = 1.2$ shown in Figures 6.12 and 6.13 where $\epsilon_2 = 0.10$ in a 360 cell domain.

the limit of $\Delta x \rightarrow 0$ corresponds to the zero shock width shock fit scheme. In Figure 6.15 the steady state lift, $\bar{l}$, is shown as a function of the number of cells in the domain for two different second difference artificial viscosity coefficients. The solutions have been normalized by the finest resolution direct solver solution with 720 cells, $\bar{l} = 0.379319$, so what is actually seen is relative error from this solution. Although the trend in the artificial viscosity scheme is away from the shock fit scheme with increased resolution, the error does not vary by more than 0.015%. Recall that the shock fit scheme was run using double precision and the artificial viscosity schemes were run using single precision, so this trend away from the shock fit scheme is clearly the effect of computer roundoff which dominates the error. Figure 6.16 shows the magnitude and phase of the lift perturbation, again normalized by the shock fit solution with 720 cells, $\hat{l} = 0.00013321 \angle -87.653^\circ$.

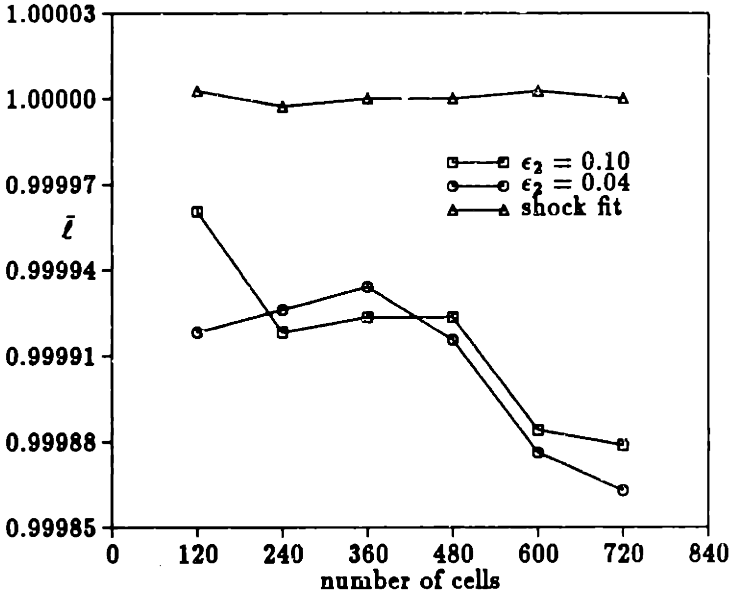

Figure 5.15: Steady state lift vs. the number of cells in the domain, for the transonic case with $M_{\text{in}} = 1.2$ normalized by $\bar{\ell} = 0.379319$, for two different second difference artificial viscosity coefficients and the direct solver shock fit scheme.

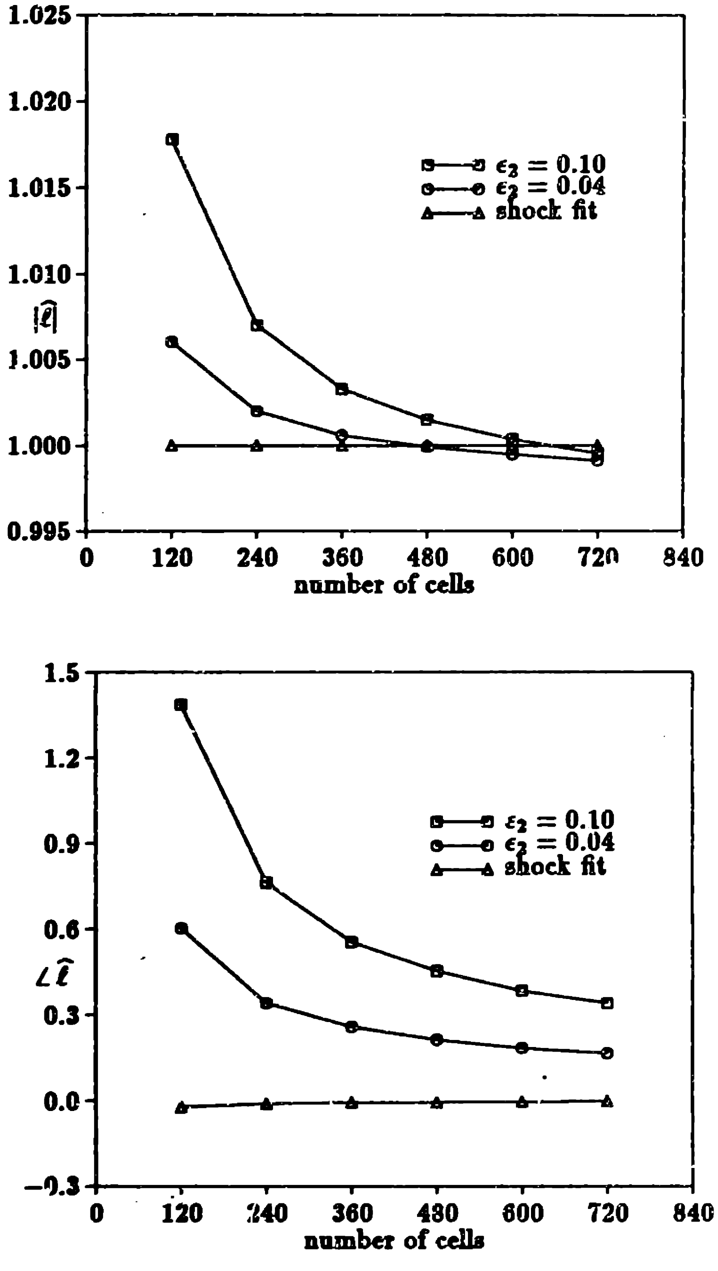

Figure 6.16: Magnitude and phase (in degrees) of lift perturbation vs. the number of cells in the domain, for the transonic case with $M_{in} = 1.2$ normalized by $\hat{\ell} = 0.00013321 \angle -87.653°$, for two different second difference artificial viscosity coefficients and the direct solver shock fit scheme.

The perturbation pressure distribution in Figure 6.17 has the same steady state solution as the case just discussed with second difference artificial viscosity, except now the frequency in the perturbation has been doubled to $\omega = 3.458$. Figure 6.18 shows the effect of changing the resolution in the domain. The solutions have been normalized with the shock fit solution with 720 cells, $\hat{\ell} = 0.00008157 \angle -95.5484^\circ$.

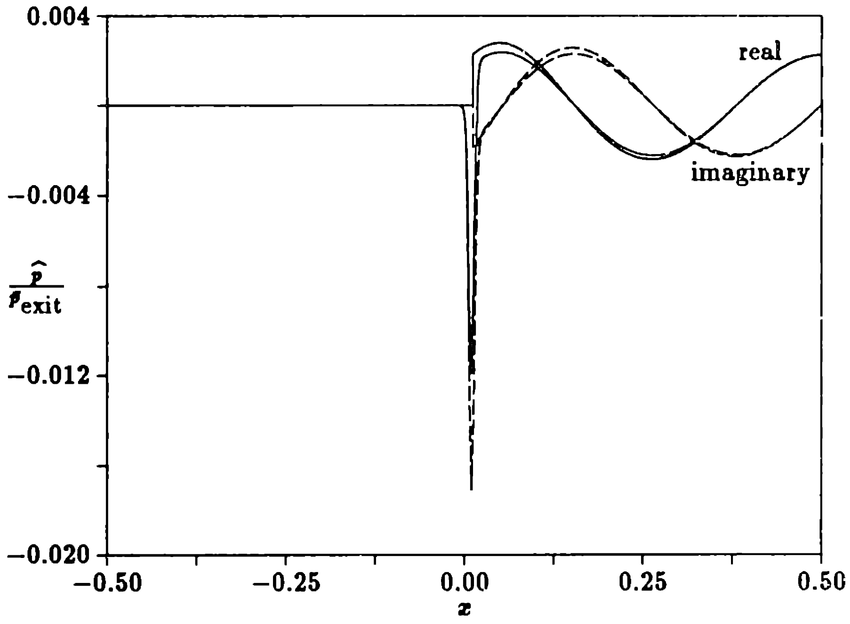

Figure 6.17: Real and imaginary parts of the pressure perturbation with $\omega = 3.458$ for the transonic case with $M_{in} = 1.2$ shown in Figures 6.12 and 6.13 where $\epsilon_2 = 0.10$ in a 360 cell domain.

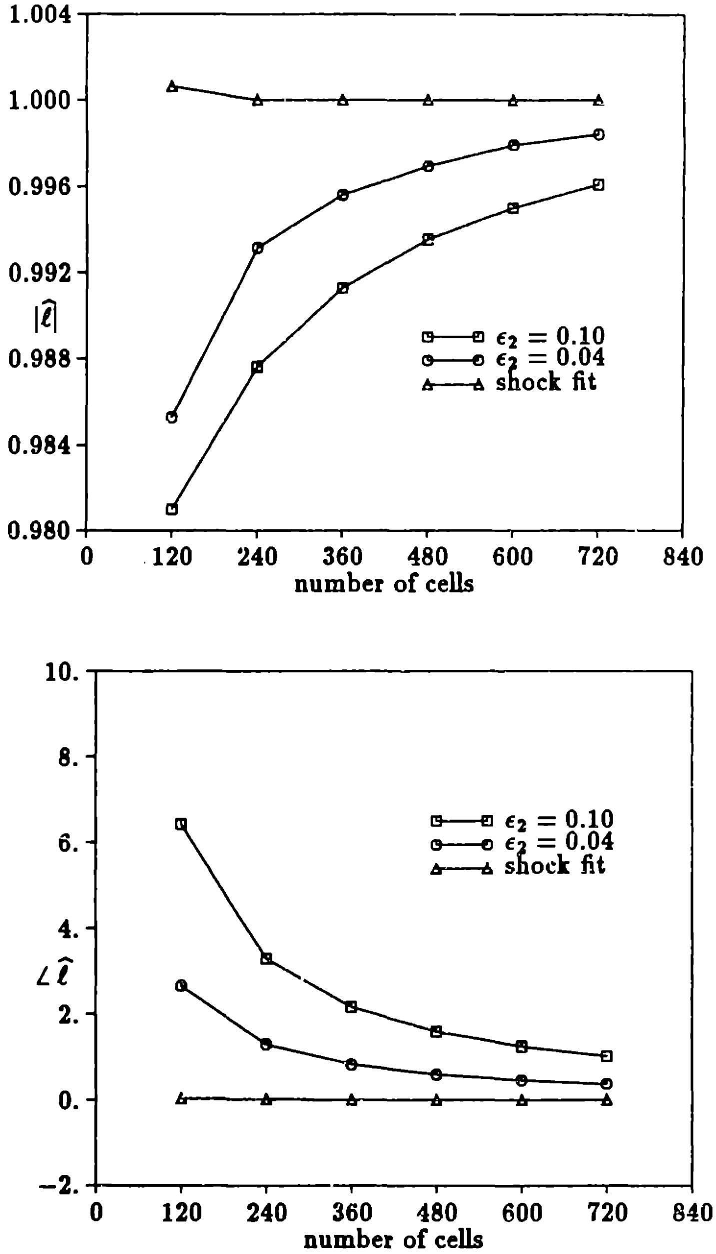

Figure 6.18: Magnitude and phase (in degrees) of lift perturbation vs. the number of cells in the domain, for the transonic case with $M_{\text{in}} = 1.2$ and $\omega = 3.458$ normalized by $\hat{\ell} = 0.000008157 \angle - 95.5484°$, for two different second difference artificial viscosity coefficients and the direct solver shock fit scheme.

Figures 6.19 and 6.20 show the effect of using a mix of second and fourth difference artificial viscosity. In Figure 6.19 the effect of using double and single precision is again illustrated where the shock fit scheme is run in double precision. Once again, the frequency in the perturbation is $\omega = 1.729$. Recall that the switch is not linearized in the perturbation solution, so there will be some error associated with this assumption. This error in the perturbation can be seen in Figure 6.20 where the artificial viscosity solution with the switch seems to asymptote to a constant error. This not only illustrates the errors associated with not linearizing the switch, but more fundamentally it illustrates the errors of an incorrect linearization in deriving the perturbation equations. If the discrete perturbation equations are not a true linearization of the nonlinear discrete equations, there will be an error in the solution. In this case, however, it would be possible to devise an effective switch which could be linearized, or since the errors illustrated here are quite small, they may be acceptable for an engineering application. In the next section it will be shown that by moving the grid with the shock, it is possible to reduce the error associated with not linearizing the switch.

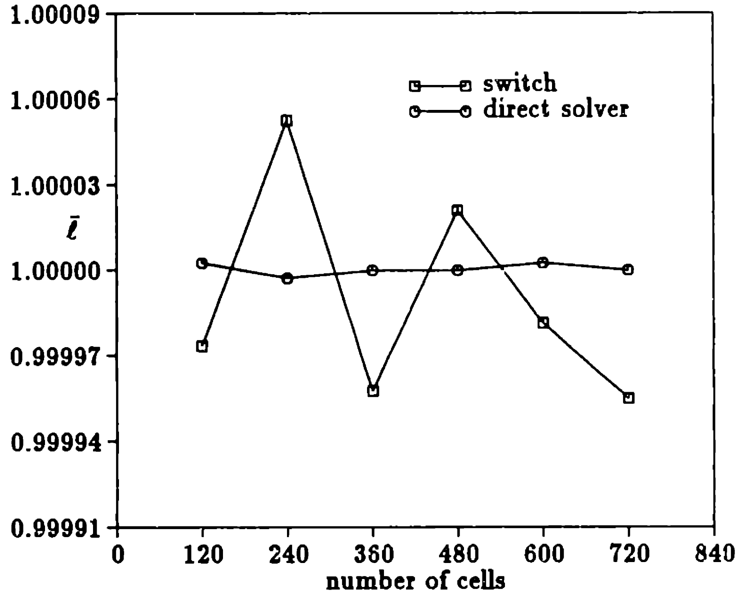

Figure 6.19: Steady state lift vs. the number of cells in the domain, for the transonic case with $M_{in} = 1.2$ normalized by $\bar{l} = 0.379319$, for fourth difference artificial viscosity with $\epsilon_4 = 0.001$ in most of the domain and second difference artificial viscosity with $\epsilon_2 = 0.2$ turned on in the shock by a switch and the direct solver shock fit scheme.

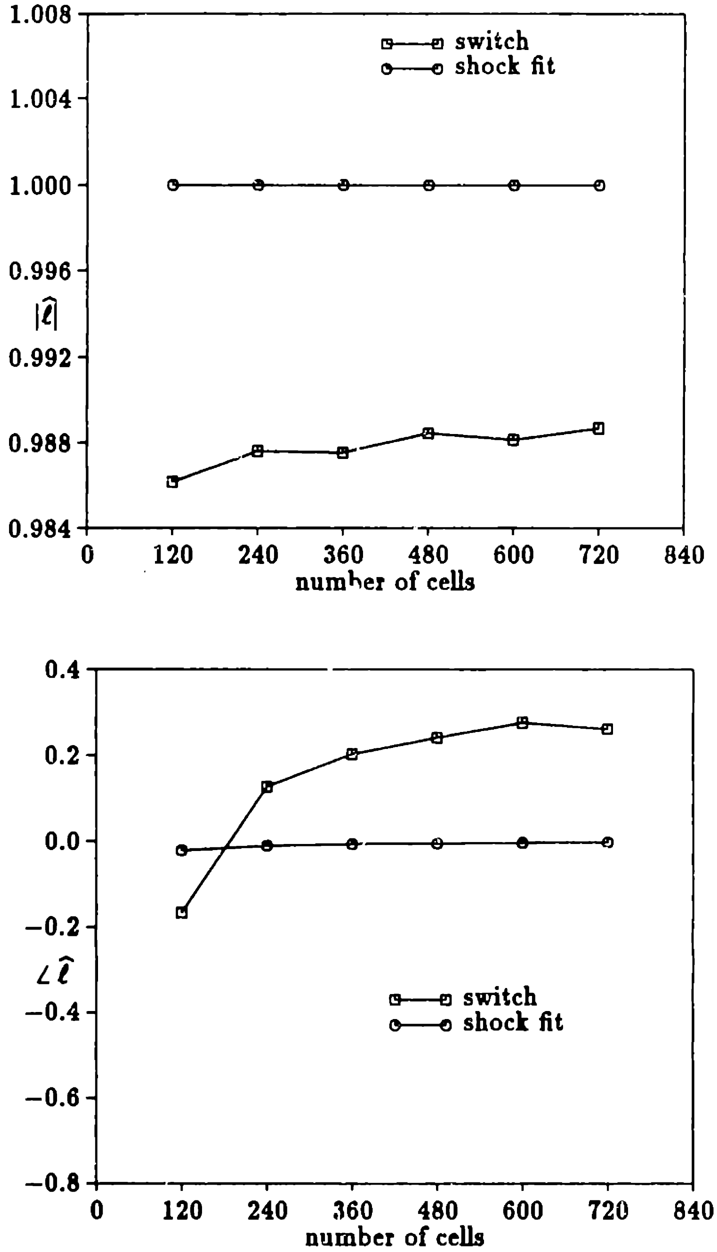

Figure 6.20: Magnitude and phase (in degrees) of lift perturbation vs. the number of cells in the domain, for the transonic case with $M_{in} = 1.2$ normalized by $\hat{\ell} = 0.00013321 \angle - 87.653°$, for fourth difference artificial viscosity with $\epsilon_4 = 0.001$ in most of the domain and second difference artificial viscosity with $\epsilon_2 = 0.2$ turned on in the shock by a switch which has not been linearized and the direct solver shock fit scheme.

Figure 6.21 illustrates the use of the flux vector split scheme on the steady state solution. Again, the results indicate the effect of using double and single precision, since the shock fit scheme is run in double precision, rather than the effect of the schemes themselves. In Figure 6.22 the perturbation is shown as a function of resolution. Here, when MUSCL upwinding is used in a transonic case it is turned off in the shock by a switch which, as for the artificial viscosity scheme, is not linearized in the perturbation scheme. The strange results in Figure 6.22, however, are not due to not linearizing the switch, but a more interesting aspect of the MUSCL flux vector split scheme.

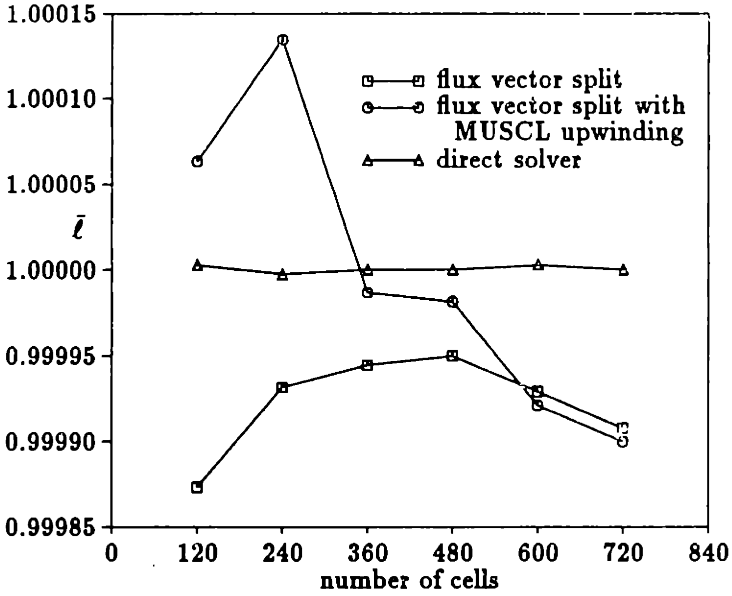

Figure 6.21: Steady state lift vs. the number of cells in the domain, for the transonic case with $M_{in} = 1.2$ normalized by $\bar{\ell} = 0.379319$, with flux vector splitting and the direct solver shock fit scheme.

Similar to the analysis in Section 4.2, eleven different steady state solutions were found using the MUSCL flux vector split scheme where the exit pressure was slightly different for each solution. The same transonic problem used previously in this section is used here where there are 360 cells in the domain, except the exit pressure for these solutions range from $p_{exit} = 0.49345$ to $p_{exit} = 0.4937$ to provide a slight variation in the shock shape. Figure 6.23 shows the Mach number distribution for each of these eleven solutions in the shock region. The solution of interest is highlighted and is distinguished from the rest by having a node near $M = 1$, the break between subsonic and supersonic

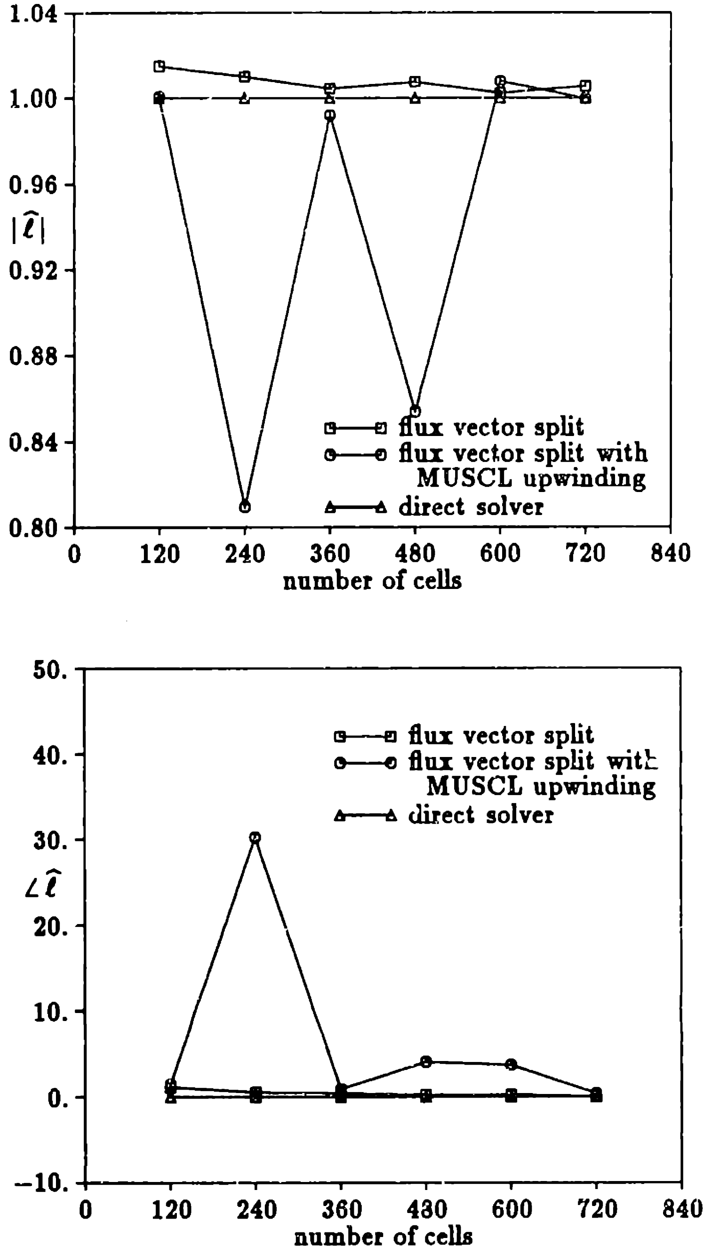

Figure 6.22: Magnitude and phase (in degrees) of lift perturbation vs. the number of cells in the domain, for the transonic case with $M_{in} = 1.2$ normalized by $\hat{\ell} = 0.00013321 \angle -87.653°$, with flux vector splitting and the direct solver shock fit scheme.

flow which are dealt with differently in the flux vector split scheme. These solutions were run using both single and double precision versions of the code. The residual for this solution would not decrease to the levels the other solutions would reach. Figure 6.24 shows the pressure at this $M \approx 1$ node, in a pattern which continues indefinitely, for a double precision solution at the point where the residual would no longer decrease. To show that this behavior is particular to this solution, each of the eleven solutions were examined. Each of the solutions were run in single and double precision to the point where the residual would no longer decrease. At this point the solution was run for an additional 2000 iterations while the code kept track of the maximum and minimum values of pressure at each of the nodes. Figure 6.25 shows the maximum change in pressure over these nodes for each solution. The solution for exit pressure $p_{exit} = 0.49455$ is clearly different from the other solutions and is the same solution whose shock profile had a node near $M = 1$. The value of this variation in the solution is the amplitude of the perturbation seen in Figure 6.24. It is interesting to note that the amplitude of the variation for this solution is the same in single precision and double precision. What this is illustrating is a limit-cycle in the solution. This limit-cycle is only noticed when a node in the shock lies near $M = 1$ and MUSCL upwinding is used with the flux vector split scheme, even though it is turned 'off' in the shock. Actually, the switch does not turn the MUSCL upwinding off completely in the shock region, but merely turns its effect down. Since the solution is in a limit-sycle, a perturbation at any point in this 'converged' state will not cause the solution to return to the initial solution. For this reason the concept of finding a steady state and superimposing a linear perturbation on this steady state no longer holds, and the results shown in Figure 6.22 no longer seem strange. In Figure 6.22 the solutions with 240 and 480 cells in the domain have a shock node near $M = 1$. The next section will show that moving the grid with the shock reduces the effect of the the limit-cycle.

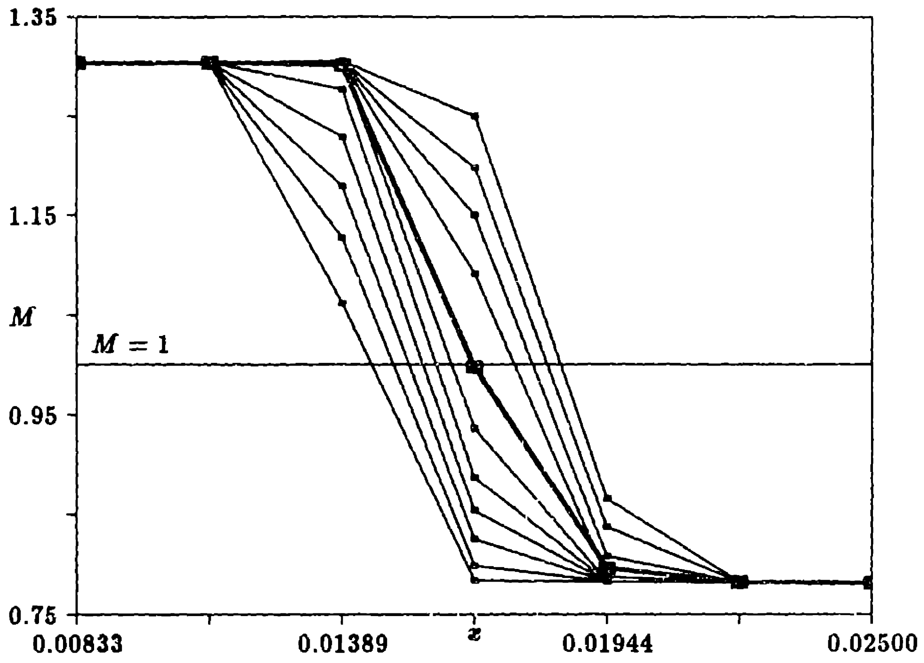

Figure 6.23: Shock profiles for several exit pressures ranging from $p_{exit} = 0.49345$ to $p_{exit} = 0.4937$ by an increment of $\Delta p_{exit} = 0.000025$ where the profile with $p_{exit} = 0.49355$ is highlighted.

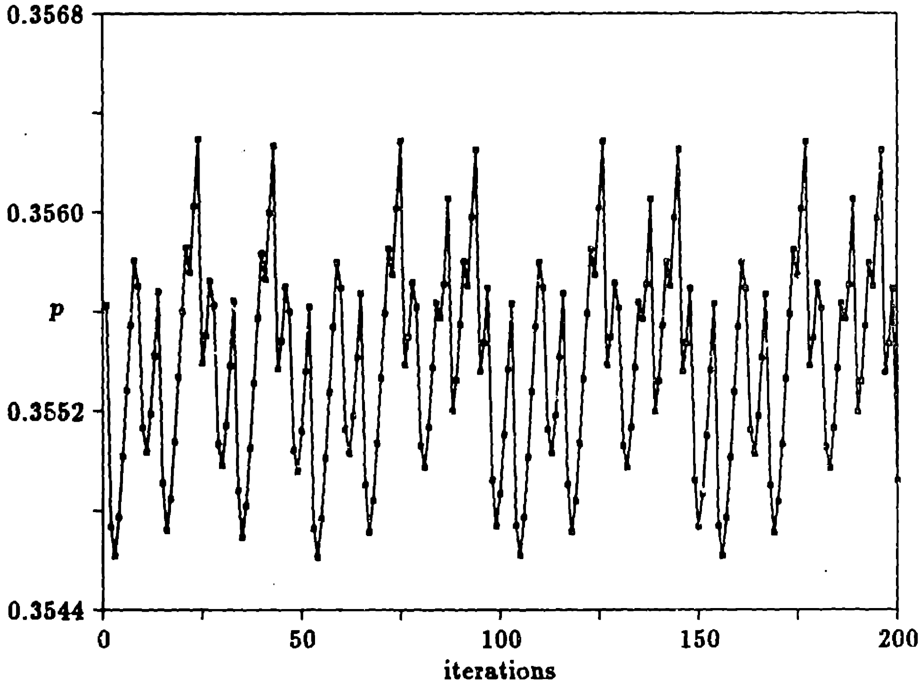

Figure 6.24: Pressure at the shock node for the highlighted shock profile shown in Figure 6.23.

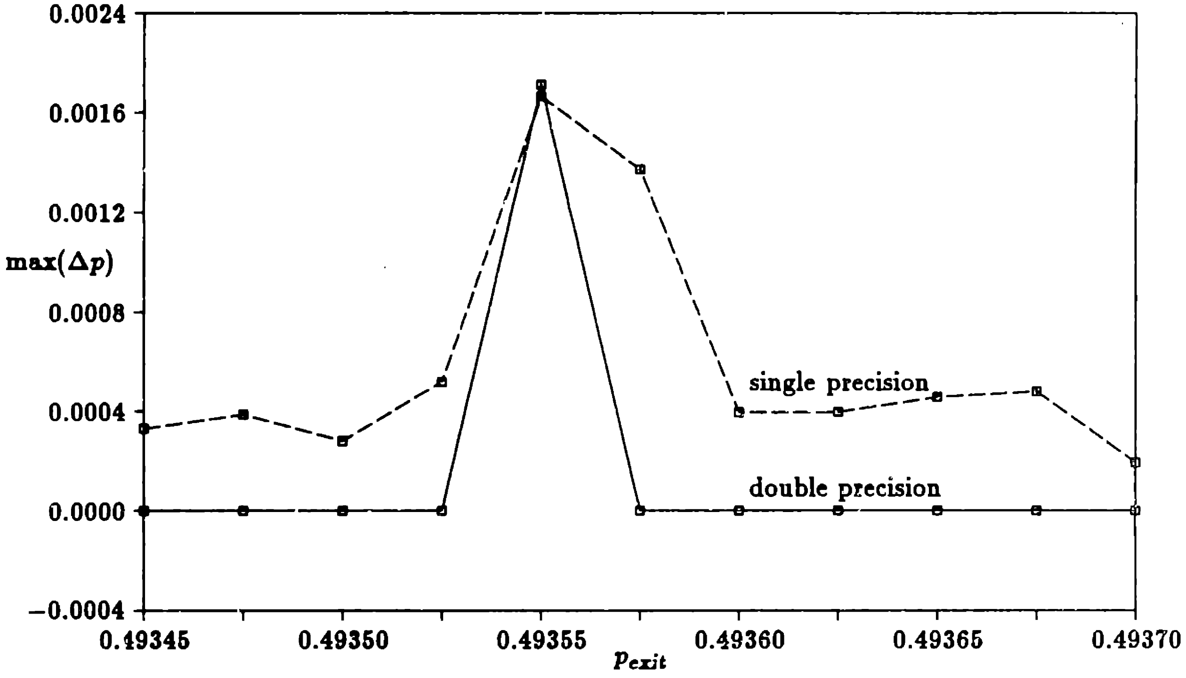

Figure 6.25: Maximum amount by which the pressure changes at a node over 2000 iterations.

A second transonic case was also examined. This case has a smaller shock jump than the first transonic case. The geometry is similar to the diverging duct used in the first case, but now the height distribution of the duct is given by the function $h = 0.10 + 0.000778 \sin(\pi x)$ as shown in Figure 6.26. This case has inlet Mach number $M_{in} = 1.01$. The steady state Mach number distribution is shown in Figure 6.27 and the steady state pressure distribution in Figure 6.28 for 360 cells along the duct and second difference artificial viscosity with coefficient $\epsilon_2 = 0.03$. The shock in this case is moderate, having a jump from $M = 1.10$ to $M = 0.91$, which is representative of a more common shock appearing in turbomachinery flowfields. Once again, these figures include the shock fit direct solver solution as well. In the unsteady perturbation, the frequency of the unsteadiness is $\omega = 1.729$ introduced through a perturbation in the exit pressure of $\hat{p} = 0.001$ which is 0.27% of the steady exit pressure. In Figure 6.29, the real and imaginary parts of the complex pressure perturbation are shown, again for the second difference artificial viscosity scheme along with the direct solver shock fit scheme. As with the previous transonic case, the solution found using the artificial viscosity scheme has a peak in the shock region which does not appear in the shock fit solution which explicitely includes the shock movement.

Again the accuracy of the solution can be studied. In Figure 6.30 the steady state lift, $\bar{\ell}$, is shown as a function of the number of cells in the domain for second difference artificial viscosity coefficient $\epsilon_2 = 0.03$. The solutions have been normalized by the finest resolution direct solver solution with 720 cells, $\bar{\ell} = 0.391436$, so what is actually seen is relative error from this solution. Figure 6.31 shows the magnitude and phase of the lift perturbation, again normalized by the shock fit solution with 720 cells, $\hat{\ell} = 0.00006727 \angle -92.444^\circ$.

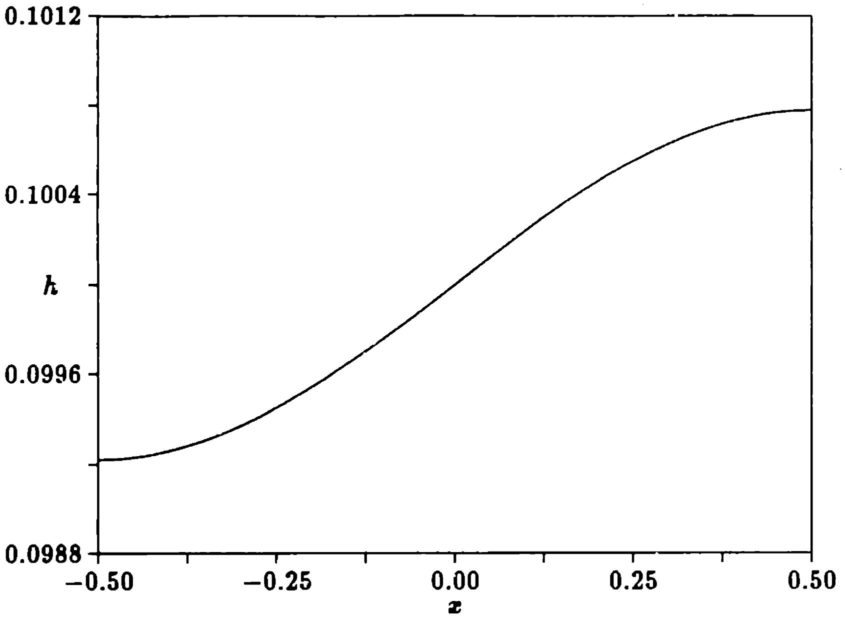

Figure 6.26: Duct height [$h = 0.10 + 0.000778\sin(\pi x)$] used for transonic case with $M_{in} = 1.01$.

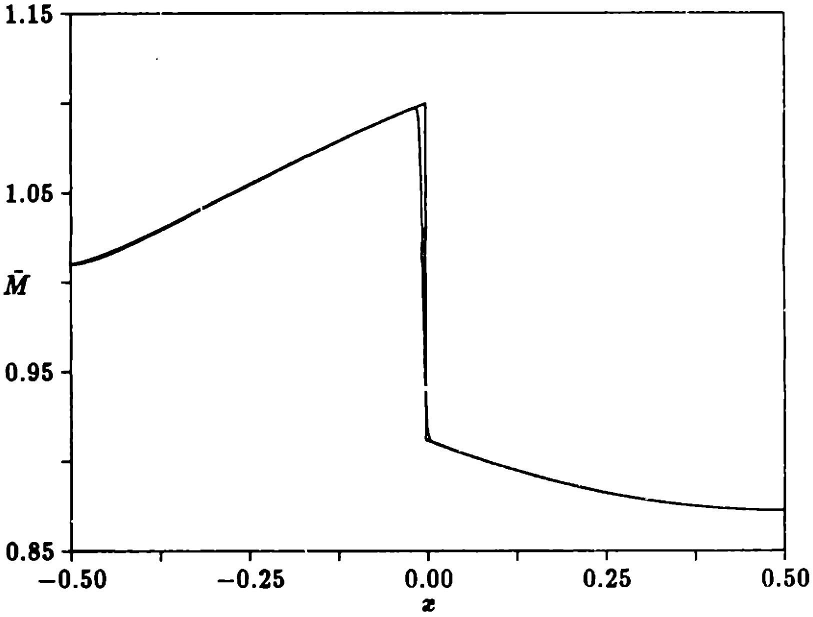

Figure 6.27: Transonic steady state Mach number for case with $M_{in} = 1.01$, with $\epsilon_2 = 0.03$ and 360 cells.

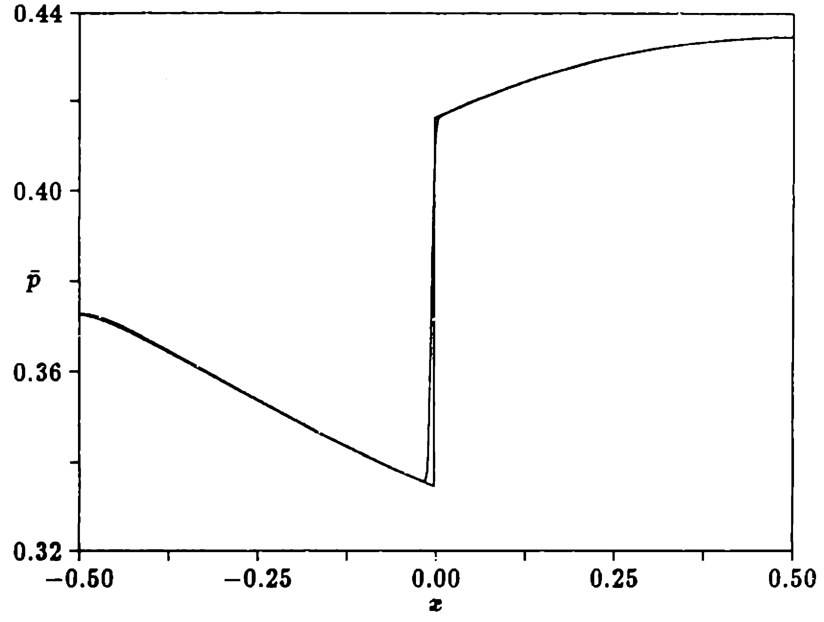

Figure 6.28: Transonic steady state pressure for case with $M_{in} = 1.01$, with $\epsilon_2 = 0.03$ and 360 cells.

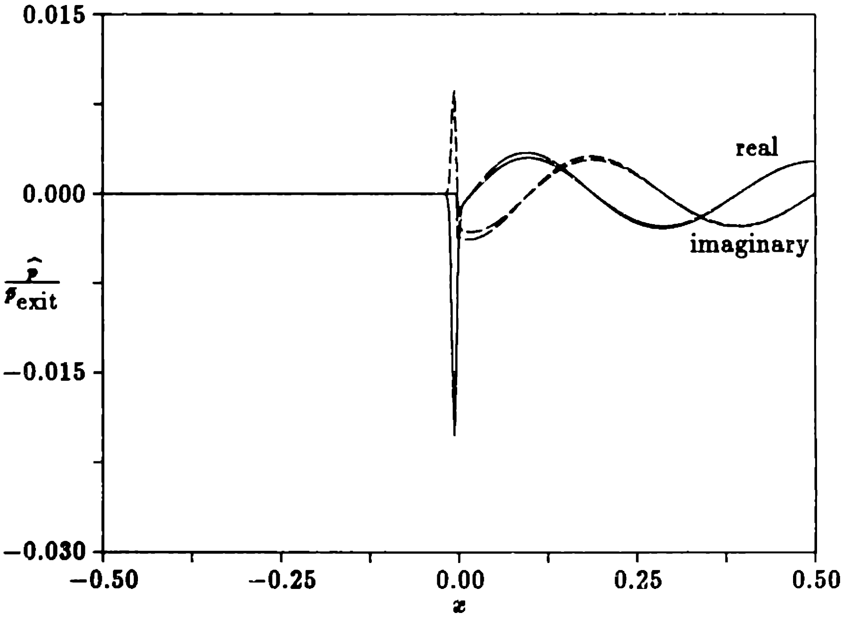

Figure 6.29: Real and imaginary parts of the pressure perturbation with $\omega = 1.729$ for the transonic case with $M_{\text{in}} = 1.01$ shown in Figures 6.27 and 6.28, where $\epsilon_2 = 0.03$ in a 360 cell domain.

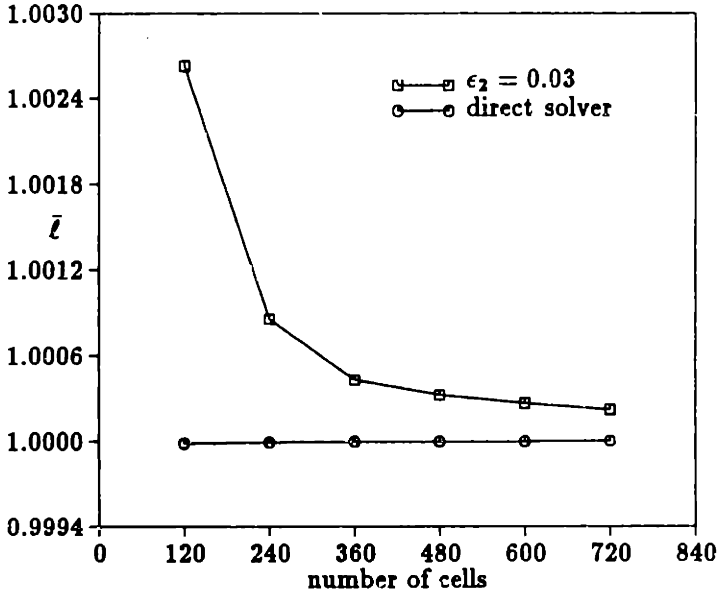

Figure 6.30: Steady state lift vs. the number of cells in the domain, for the transonic case with $M_{in} = 1.01$ normalized by $\bar{\ell} = 0.391436$, for second difference artificial viscosity coefficient $\epsilon_2 = 0.03$ and the direct solver shock fit scheme.

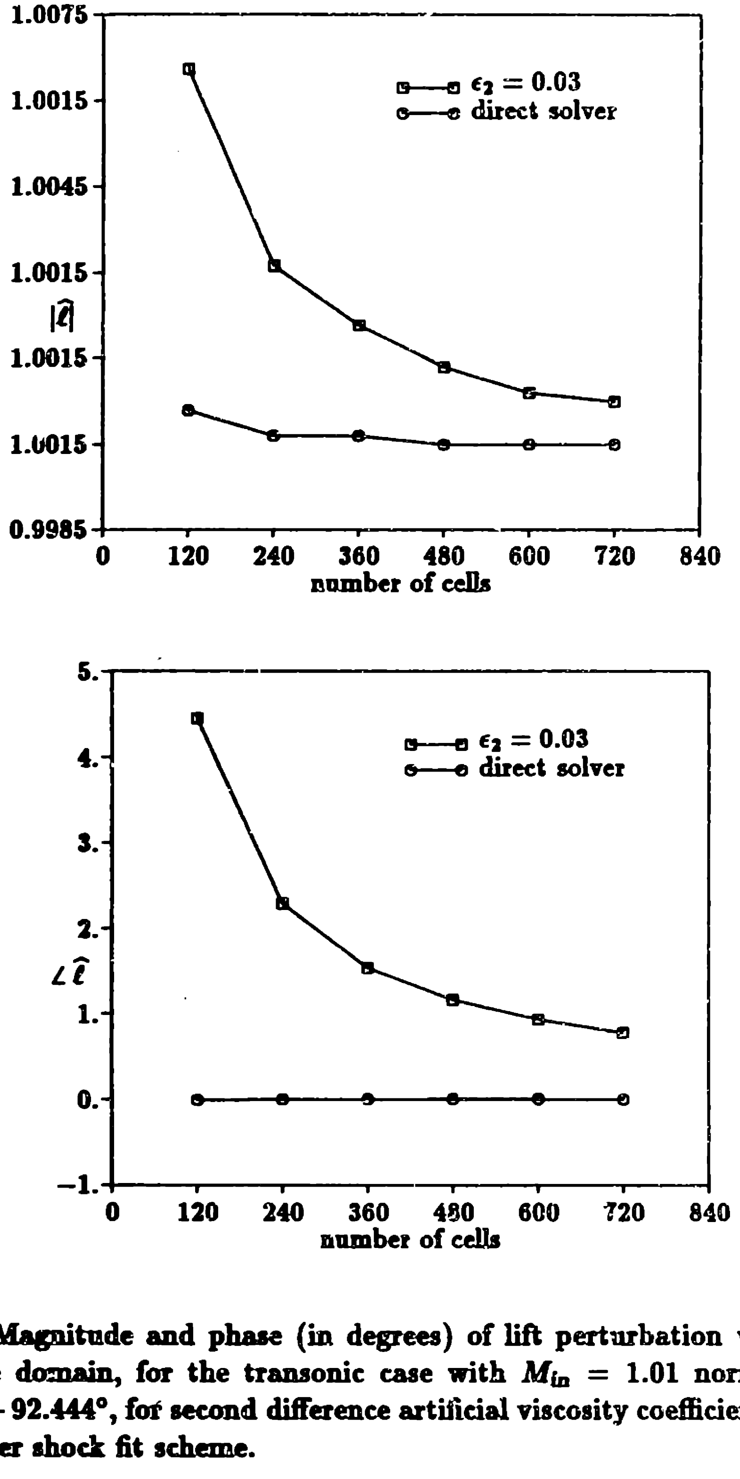

Figure 6.31: Magnitude and phase (in degrees) of lift perturbation vs. the number **of cells in the domain, for the transonic case with M_{in}** = 1.01 normalized by $\widehat{\ell}$ = **0.00006727 $\angle -92.444°$, for second difference artificial viscosity coefficient ϵ_2** = 0.03 and **the direct solver shock fit scheme.**

6.3 Moving Grid

In Section 5.5 the addition of a moving grid was made to the basic numerical schemes used in this work. Although there are many reasons for moving a grid, the primary motivation here was to reduce the error from a changing shock shape due to discretization effects. Other benefits of moving the grid in the shock region were also found, including reducing the effect of not linearizing a switch in the shock region and reducing the effect of the limit-cycle in the MUSCL upwinding flux vector split scheme.

The distribution of the complex perturbation grid movement is the same function of x for all the cases presented here, regardless of the number of cells in the domain. Maintaining this consistency aids in the comparison of results with different resolutions. This distribution is given in Figure 6.32 where the specified value for the grid movement is the value in the center of the domain. The grid movement then tapers off linearly away from this center region.

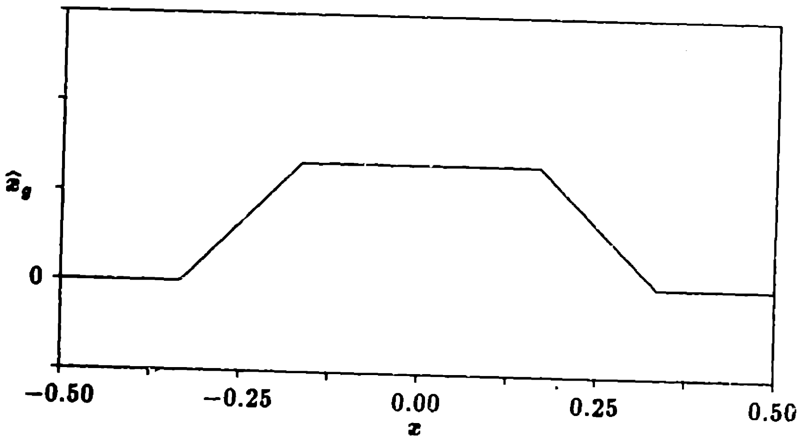

Figure 6.32: Distribution of grid movement function $\hat{x}_g$ along the duct.

6.3.1 Subsonic Case

As before, the subsonic case will be examined first to isolate the effects of the shock from the effects of the scheme. The subsonic case is the same case discussed in Section 6.1.

Figure 6.33 shows the subsonic flow solution for the perturbation with 360 cells in the domain and second difference artificial viscosity coefficient $\epsilon_2 = 0.0005$ with grid movement with $\widehat{x}_g = (-5 \times 10^{-4}, -5 \times 10^{-4})$ and without grid movement. The solution for the perturbation with grid movement is actually the solution on the moving grid, not at the stationary grid locations, therefore the two solutions are connected by the relationship

$$\widehat{p}_{GM} = \widehat{p}_{\text{no GM}} + \widehat{x}_g \left(\frac{d\bar{p}}{d\bar{x}} \right) \qquad (6.1)$$

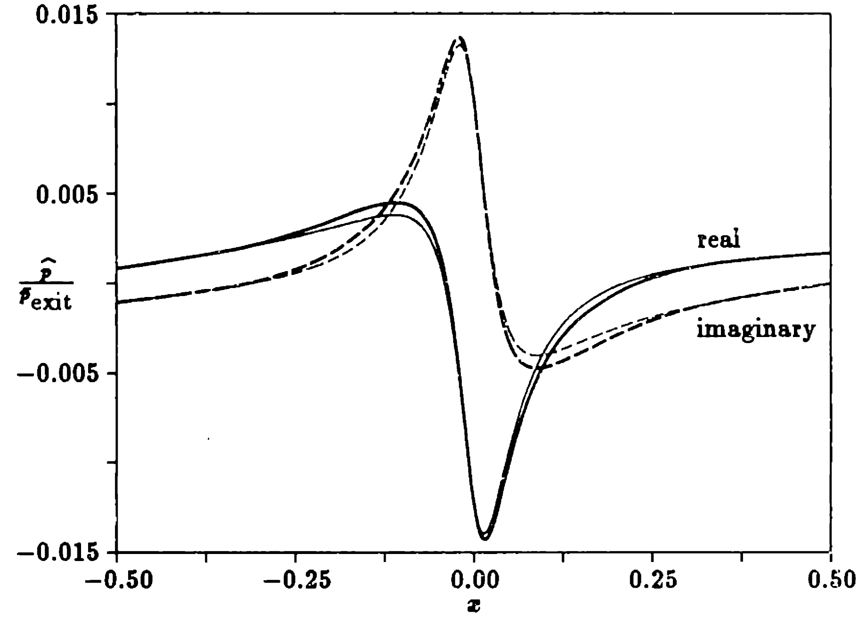

Figure 6.33: Real and imaginary parts of the pressure perturbation with $\omega = 1.729$ for the subsonic case shown in Figures 6.2 and 6.3 where $\epsilon_2 = 0.0005$ in a 360 cell domain with grid movement $\widehat{x}_g = (-5 \times 10^{-4}, -5 \times 10^{-4})$ (dark line) and without grid movement (light line).

To compare the solutions with and without grid movement, Figures 6.34 and 6.35 show the effect of resolution on the perturbation for both second and fourth difference artificial viscosity, as well as for the direct solver used for the shock fit scheme. To calculate the lift perturbation where there is grid movement, the effect of the grid movement must be added so now $\widehat{\ell} = \int \widehat{p} d\bar{x} + \int \bar{p} d\widehat{x}_g$. The results for the subsonic case with and without grid movement are nearly identical.

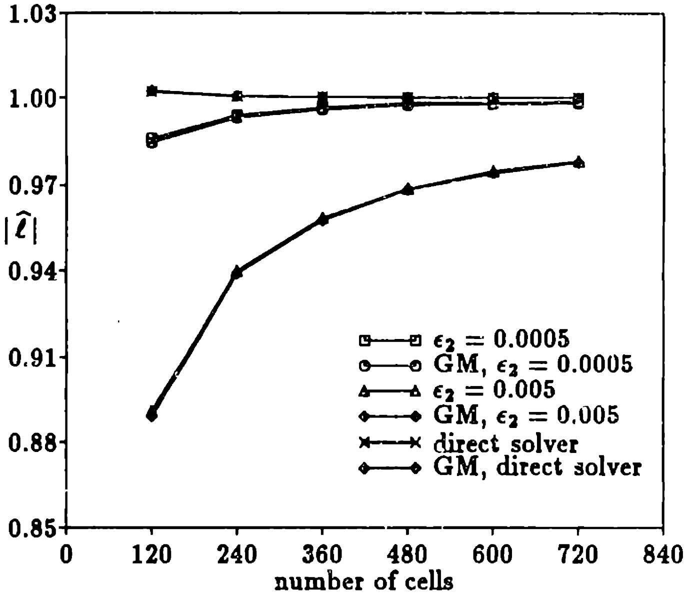

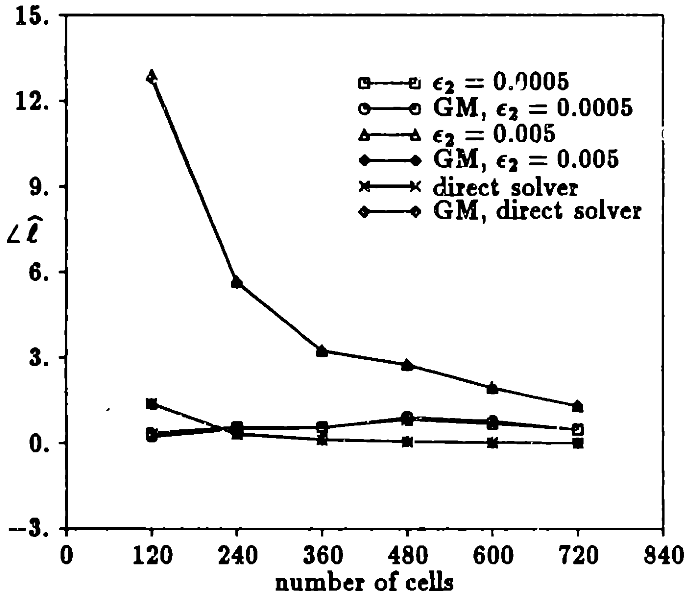

Figure 6.34: Magnitude and phase (in degrees) of lift perturbation vs. the number of cells in the domain, for the subsonic case normalized by $\hat{\ell} = 0.00027578 \angle 68.391°$, for two different second difference artificial viscosity coefficients and the direct solver used for the shock fit scheme. Both grid movement (GM) $\hat{x}_g = (-5 \times 10^{-4}, -5 \times 10^{-4})$ and no grid movement are shown.

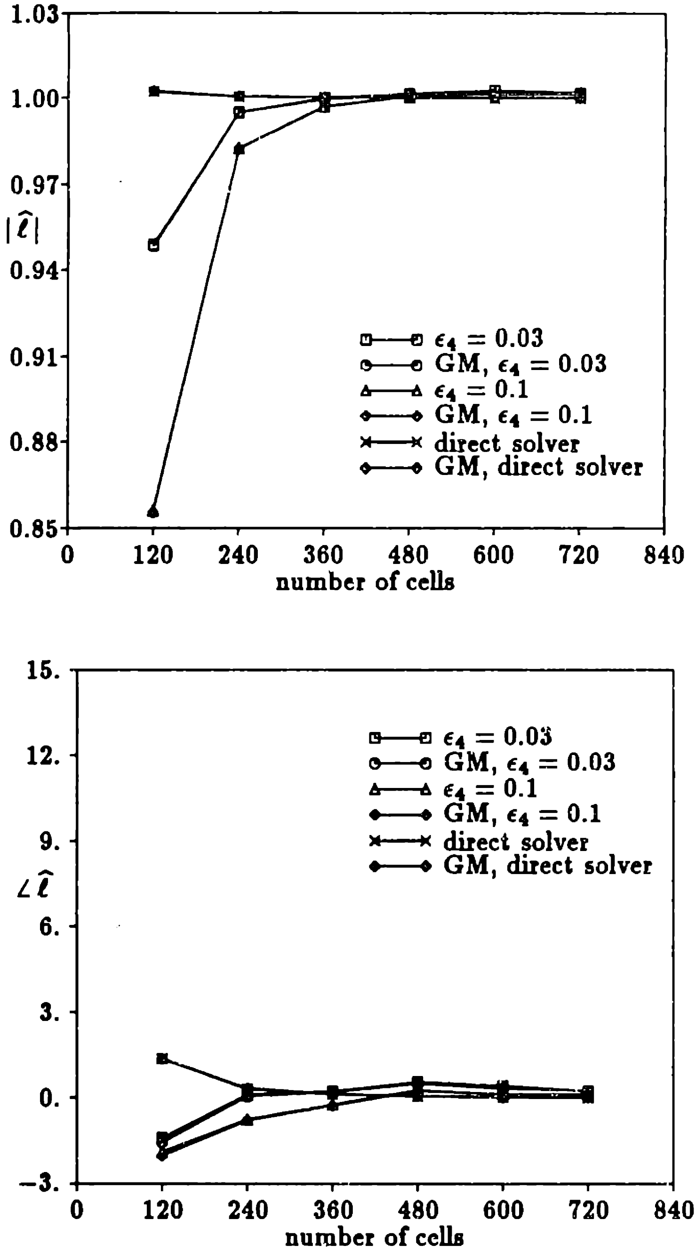

Figure 6.35: Magnitude and phase (in degrees) of lift perturbation vs. the number of cells in the domain, for the subsonic case normalized by $\hat{\ell} = 0.00027578\ \angle 68.391°$, for two different fourth difference artificial viscosity coefficients and the direct solver used for the shock fit scheme. Both grid movement (GM) $\hat{x}_g = (-5 \times 10^{-4}, -5 \times 10^{-4})$ and no grid movement are shown.

6.3.2 Transonic Case

Figure 6.36 shows the solution for the transonic case presented in Section 6.2 for 360 cells in the domain and $\epsilon_2 = 0.10$ with grid movement $\hat{x}_g = (-2 \times 10^{-4}, -7.4 \times 10^{-4})$. Notice that there is no longer a peak in the shock region for the solution. The grid is now moving at approximately the magnitude of the shock movement, so there is very little shock movement relative to the grid which would be represented by the peak. The perturbation in the solution upstream of the shock is solely due to the grid movement in this region since there should otherwise be no perturbation upstream of the shock. Figure 6.37 shows the effect of adding grid movement to the transonic case with second difference artificial viscosity. Again, this is the same transonic case presented in Section 6.2 with the addition of grid movement $\hat{x}_g = (-2 \times 10^{-4}, -7.4 \times 10^{-4})$. For both values of the artificial viscosity coefficient, the magnitude of $\hat{\ell}$ is increased and the phase of $\hat{\ell}$ is decreased when grid movement is added, but the solutions have not changed significantly.

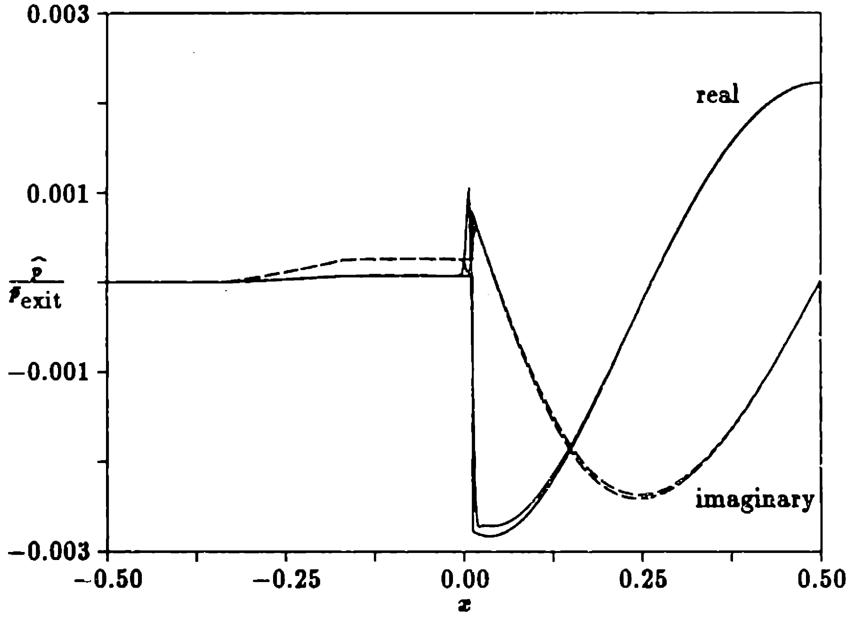

Figure 6.36: Real and imaginary parts of the pressure perturbation with $\omega = 1.729$ for the transonic case with $M_{\text{in}} = 1.2$ shown in Figures 6.12 and 6.13 where $\epsilon_2 = 0.10$ in a 360 cell domain with grid movement $\hat{x}_g = (-2 \times 10^{-4}, -7.4 \times 10^{-4})$.

When a combination of second and fourth difference artificial viscosity are used, where a switch turns on the second difference artificial viscosity in the shock, moving the grid with the shock reduces the effect of not linearizing the switch in the shock region. Figure 6.38, shows this effect quite effectively. Since the moving grid picks up most of the shock movement, the contribution to the lift from the perturbation pressure in the shock region as well as the errors in this contribution are decreased.

Finally, there is the effect of moving the grid with the flux vector split scheme. Since the errors associated with moving a crisp flux vector split shock relative to its grid location is larger than the errors from the artificial viscosity schemes, one would assume the effect of moving the grid would produce the largest benefit with the flux vector split scheme. The effects of this scheme are shown in Figure 6.39. When MUSCL upwinding is not used the scheme is only first order accurate, and this first order accuracy still dominates the errors, so little or no benefit is seen in moving the grid. When MUSCL upwinding is used, two effects can be seen. First, the errors associated with the limit-cycle in the steady solution are dramatically reduced since, again, the bulk of the moving shock effect is captured with the moving grid. Second, the desired reduction in error is seen for the rest of the perturbation solutions which do not have a problem with the steady state solution.

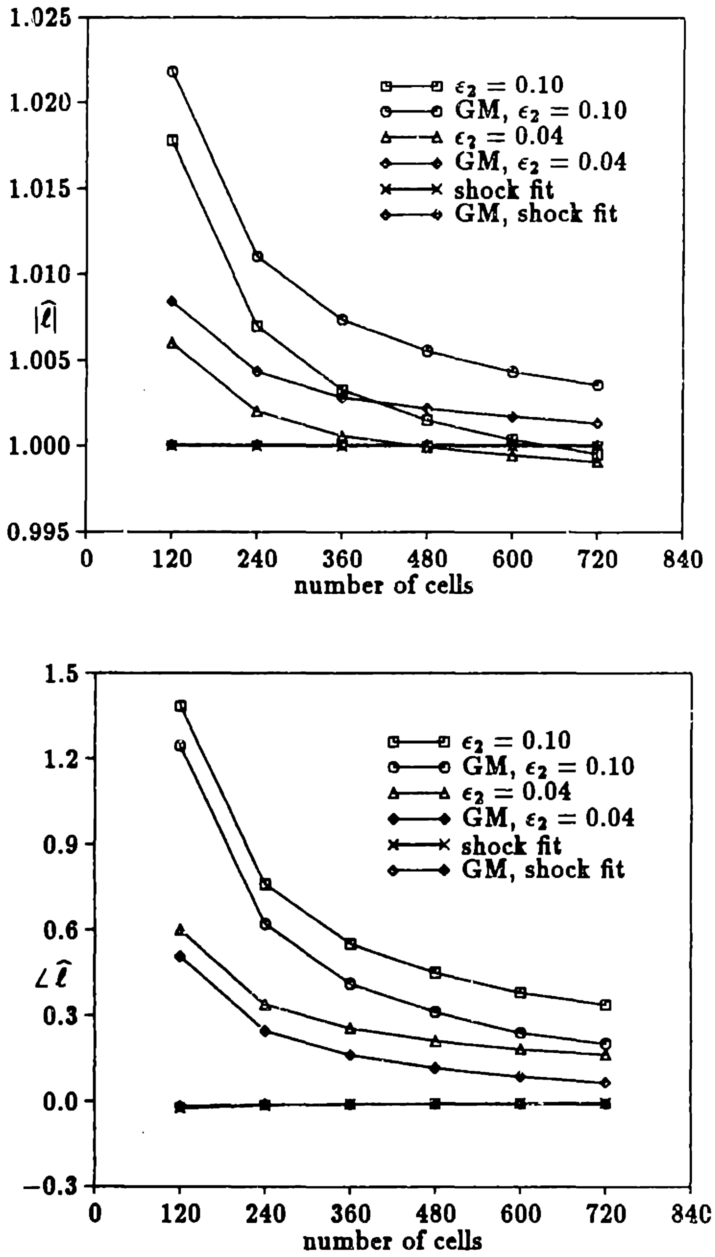

Figure 6.37: Magnitude and phase (in degrees) of lift perturbation vs. the number of cells in the domain, for the transonic case with $M_{in} = 1.2$ normalized by $\hat{\ell} = 0.00013321 \angle -87.653^\circ$, for two different second difference artificial viscosity coefficients and the direct solver used for the shock fit scheme. Both grid movement (GM) $\hat{x}_g = (-2 \times 10^{-4}, -7.4 \times 10^{-4})$ and no grid movement are shown.

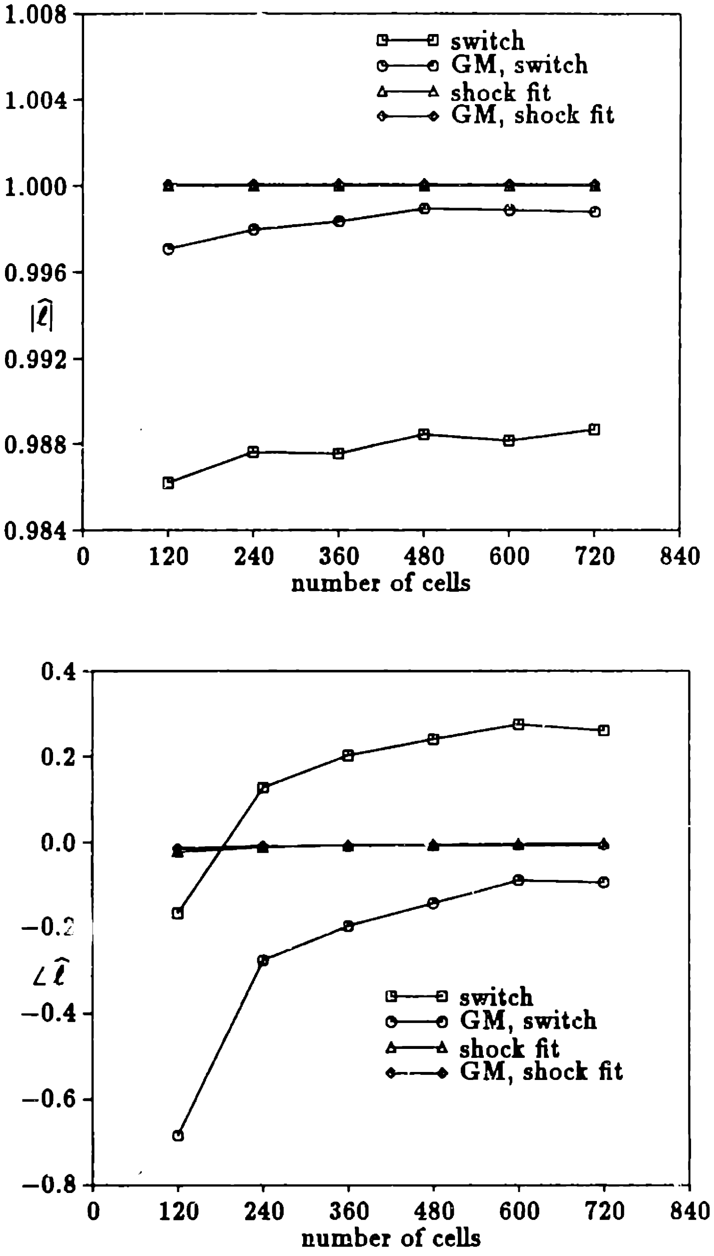

Figure 6.38: Magnitude and phase (in degrees) of lift perturbation vs. the number of cells in the domain, for the transonic case with $M_{in} = 1.2$ normalized by $\hat{\ell} = 0.00013321 \angle - 87.653^\circ$, with fourth difference artificial viscosity $\epsilon_4 = 0.001$ in most of the domain and second difference artificial viscosity with $\epsilon_2 = 0.2$ turned on in the shock by a switch which has not been linearized and the direct solver used for the shock fit scheme. Both grid movement (GM) $\hat{x}_g = (-2 \times 10^{-4}, -7.4 \times 10^{-4})$ and no grid movement are shown.

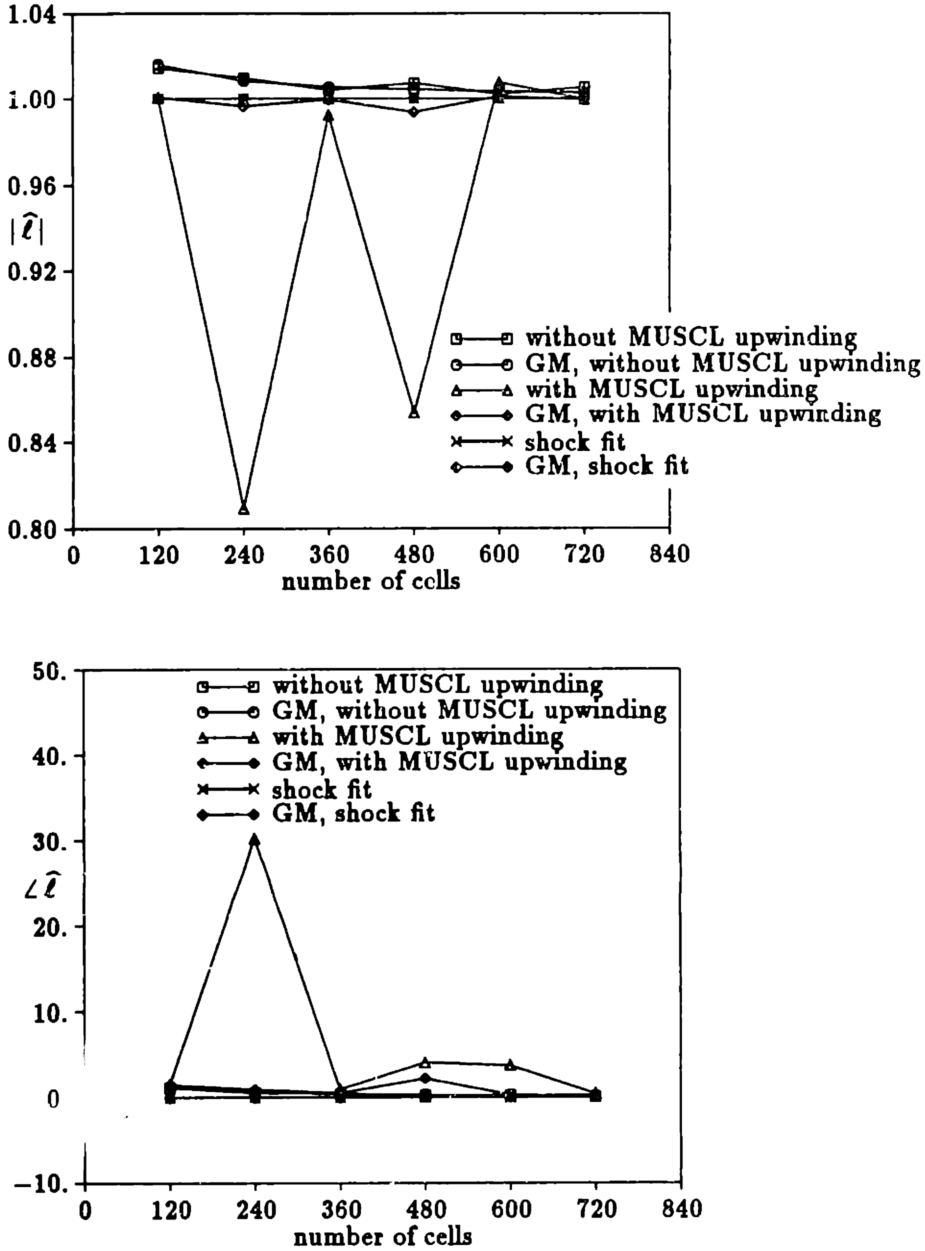

Figure 6.39: Magnitude and phase (in degrees) of lift perturbation vs. the number of cells in the domain, for the transonic case with $M_{in} = 1.2$ normalized by $\hat{\ell} = 0.00013321 \angle - 87.653°$, with flux vector splitting and the Direct solver shock fit scheme. Both grid movement (GM) $\hat{x}_g = (-2 \times 10^{-4}, -7.4 \times 10^{-4})$ and no grid movement are shown.

6.3.3 Conclusions

By moving the grid with the shock, the desire was to decrease the errors associated with a changing shock shape as a discrete shock moves. This effect was indeed seen in the MUSCL upwinding flux vector split scheme where the changing shock shape would be most predominant. Other benefit of moving the grid with the shock were to reduce errors in the shock region associated with the scheme itself. Most importantly, the effect of not linearizing a switch in the shock region was reduced so the complexities associated with incorporating the linearization of a switch in the code can be eliminated as is the need to find a switch which can be linearized. Finally, the effect of a limit-cycle in the shock region of the steady state solution to the MUSCL upwinding flux vector split scheme are also reduced. This result is not as important since the initial limitations in the scheme may make it difficult to find the desired shock movement in the first place.

Chapter 7

Convergence Acceleration Techniques

The solution technique used in this thesis for the shock capturing schemes described in Chapter 5, is to advance a time dependent equation until there is no longer a change in time. At this point the steady state solution or the time independent amplitude of the perturbation solution is found. In this process, the actual time history to the converged solution is not important, merely the converged state itself. There are several methods of convergence acceleration which speed the process of reaching this solution. In general, the idea is to change the path taken to this state, but again the actual time history to convergence is not important to the solution. Here the methods of local timesteps, multigrid and GMRES (Generalized Minimal Residual algorithm) are used. The next three sections describe these methods in detail while the last section in this chapter illustrates the effectiveness of these methods by comparing the computational requirements for each of them.

7.1 Local Timesteps

The concept of local timesteps is the most simple of convergence acceleration techniques and is widely used when advancing a solution in time to the steady state. The computational timestep in Equation (5.27),

$$\Delta t_{\max} = \frac{\Delta x}{|u| + c}, \tag{5.27}$$

can be different for each cell in the computational domain, determined only by the local stability limit for the cell. The true time history of the computation will not be retained, but convergence in each part of the domain will happen at the maximum rate allowed by the stability of the scheme. The benefit of using of local timesteps is most significant when there are large variations in the grid spacing, or when the Mach number variance in the flowfield is large, for example when there is a stagnation point or in the boundary layer of a viscous calculation.

7.2 Multigrid

Multigrid is another method of speeding up the convergence to a steady state. Once again, the time history is not retained, and the goal is to reach a converged state as quickly as possible. The theoretical foundation for multigrid has been well developed for elliptic problems [4], however the theory for the hyperbolic Euler equations used here is less concrete. Nevertheless, the success of multigrid used with the Euler equations is clear. Ni [21, 22, 9] first demonstrated this use of multigrid in 1981. His method was based on the idea of speeding wave propagation through the domain. In 1983 Jameson [18, 22] provided another method of using multigrid which is more closely related to classical multigrid methods.

Multigrid methods are founded on two pieces of information which are true for most time-marching computational schemes.

1. The spatial error in a scheme is proportional to a function of the mesh spacing (generally Δx or Δx^2). Which is to say, the finer the mesh the more accurate the solution.
2. The timestep (Δt) limit given by stability is proportional to the mesh spacing (Δx). This means that the finer the mesh, the more computational time will be required to reach a converged solution.

Since we want accurate solutions, but we do not want to use a lot of computer time to find these solutions, it is usually necessary to make a compromise between accuracy and computer time. The idea behind the multigrid strategy is to get the best of both worlds.

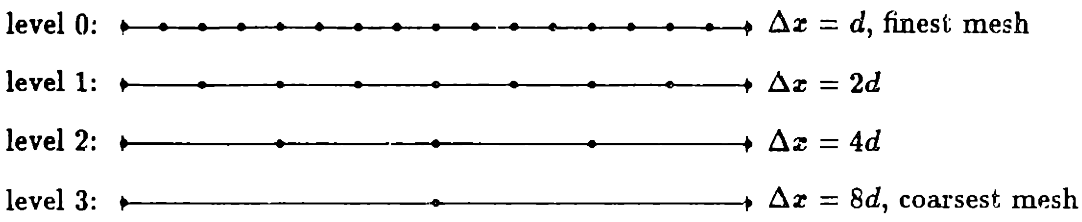

Figure 7.1: Successive grids used for different levels in the multigrid cycle.

A series of meshes is created, as shown in Figure 7.1, and the solution procedure involves computing on all mesh levels. Information is passed between mesh levels to ensure that the effect of the coarser meshes is to drive the fine mesh solution, but by using coarser meshes faster convergence rates are achieved. The result is that the accuracy of the fine mesh can be obtained at the convergence rate of the coarse mesh.

In practice, there are several issues which must be considered in the application of this process to a real problem. The stability of the whole process and appropriate interpolation of the solution and fluxes between the meshes must be considered. Most importantly, the multigrid process must drive the solution to the same solution which would be obtained by only using the fine grid.

To form a set of multigrid meshes, successive nodes are removed from the mesh as shown in Figure 7.1. To help in the description of the multigrid process, each level of the mesh has been given a number. The finest mesh is level 0 and has a mesh spacing $\Delta x = d$. Each successively coarser mesh has an increasing level number and a mesh spacing which is some factor of two times the finest mesh spacing.

The actual multigrid method used here is based on Jameson's method. The timestepping schemes using artificial viscosity described in Section 5.1.1 for the steady state and Section 5.1.2 for the linear perturbation will be used to illustrate this multigrid method. The description of this method applies equally for the steady state or the perturbation. The five-stage Runge-Kutta scheme described in Section 5.1.3 is repeated here with the addition of the function P which provides the means to force the solution to the fine mesh solution.

$$
\begin{aligned}
U^{(0)} &= U(t_n) \\
U^{(1)} &= U^{(0)} - \alpha_1 \Delta t \left[R(U^{(0)}) - D(U^{(0)}) + P \right] \\
U^{(2)} &= U^{(0)} - \alpha_2 \Delta t \left[R(U^{(1)}) - D(U^{(1)}) + P \right] \\
U^{(3)} &= U^{(0)} - \alpha_3 \Delta t \left[R(U^{(2)}) - D(U^{(1)}) + P \right] \\
U^{(4)} &= U^{(0)} - \alpha_4 \Delta t \left[R(U^{(3)}) - D(U^{(1)}) + P \right] \\
U^{(5)} &= U^{(0)} - \alpha_5 \Delta t \left[R(U^{(4)}) - D(U^{(1)}) + P \right] \\
U(t_{n+1}) &= U^{(5)}
\end{aligned}
\tag{7.1}
$$

where

$$\alpha_1 = \tfrac{1}{4}, \qquad \alpha_2 = \tfrac{1}{6}, \qquad \alpha_3 = \tfrac{3}{8}, \qquad \alpha_4 = \tfrac{1}{2}, \qquad \alpha_5 = 1.$$

To describe the multigrid strategy, the two processes of transferring information to a coarser mesh and interpolating back up to a finer mesh will be described.

Transfer: When transferring from a fine mesh level to the next coarser level it is important to not only transfer the solution but the residual. To transfer the solution, direct injection is used. The coarse mesh nodes take the state vector values of their corresponding fine mesh nodes.

$$
\begin{aligned}
U_A &= U_a \\
U_B &= U_b
\end{aligned}
$$

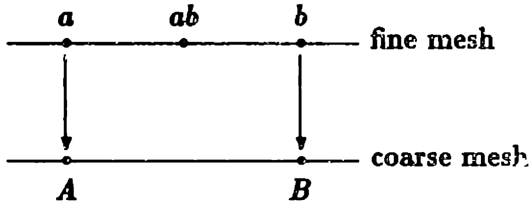

The function P carries the fine mesh residual down to the coarser meshes. This is what drives the solution to the fine mesh level. It is important that the residual transfer be conservative. To do this, the contribution from the fine node between the coarser nodes is split evenly between the neighboring coarse nodes after multiplying by $h\Delta x$, the control volume for the node. $\overline{R}$, $\overline{D}$ and $\overline{P}$ are the values on the coarse mesh after the transfer from the fine mesh.

$$\overline{R}_B = \frac{\frac{1}{2}(Rh\Delta x)_{ab} + (Rh\Delta x)_b + \frac{1}{2}(Rh\Delta x)_{bc}}{(h\Delta x)_B}$$

$$\overline{D}_B = \frac{\frac{1}{2}(Dh\Delta x)_{ab} + (Dh\Delta x)_b + \frac{1}{2}(Dh\Delta x)_{bc}}{(h\Delta x)_B}$$

$$\overline{P}_B = \frac{\frac{1}{2}(Ph\Delta x)_{ab} + (Ph\Delta x)_b + \frac{1}{2}(Ph\Delta x)_{bc}}{(h\Delta x)_B}$$

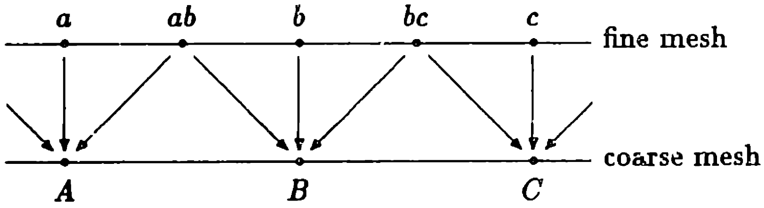

P_B on the coarse mesh is now defined as

$$P_B = \overline{R}_B - \overline{D}_B + \overline{P}_B - (R_B - D_B)$$

where R_B and D_B are evaluated at the transferred coarse mesh state vector U_B. Notice in Equation (7.1) that in the first stage, the term $(R_B - D_B)$ cancels with the same term in P_B and the transferred fine mesh residual drives the scheme. This is what guarantees that in convergence, the fine mesh solution is reached.

Before transferring to a coarser mesh, the change ΔU from the fine mesh iteration is saved. This change will be added to the reference value of the state vector before the multigrid cycle is performed.

Interpolate: When interpolating to a finer mesh, the saved ΔU on the fine mesh is corrected with the ΔU from the coarse mesh solution. The coarse mesh correction ΔU is linearly interpolated between the coarse mesh cells.

$$(\Delta U_{ab})_{\text{new}} = (\Delta U_{ab})_{\text{old}} + \frac{(x_{ab}-x_a)\Delta U_B + (x_b - x_{ab})\Delta U_A}{x_B - x_A}$$

$$(\Delta U_b)_{\text{new}} = (\Delta U_b)_{\text{old}} + \Delta U_B$$

$$(\Delta U_{bc})_{\text{new}} = (\Delta U_{bc})_{\text{old}} + \frac{(x_{bc}-x_b)\Delta U_C + (x_c - x_{bc})\Delta U_B}{x_C - x_B}$$

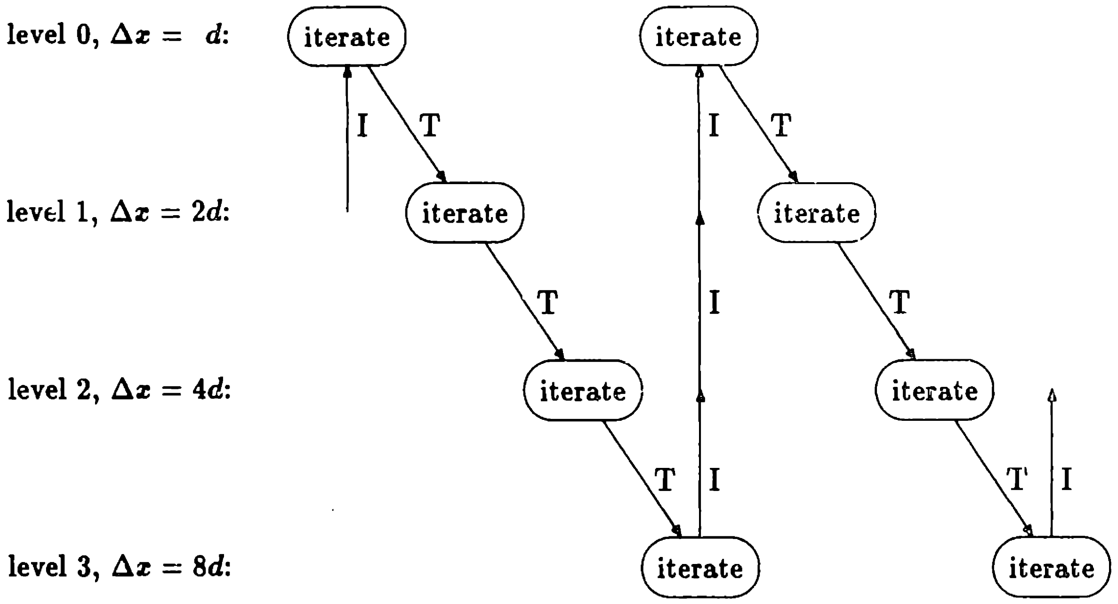

T ≡ solution is transferred to a coarser mesh
I ≡ corrections are interpolated to a finer mesh

Figure 7.2: The multigrid cycle.

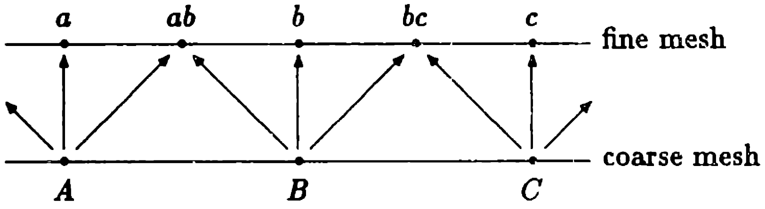

The multigrid cycle starts with an iteration on the finest mesh, level 0. For this level the function P is zero. The solution before this iteration is saved since it serves as a reference for the update in the multigrid cycle. The solution and residual are then transferred to the next coarser mesh while the change from this iteration is stored. This cycle of iterate then transfer to a higher level is repeated until the third level of multigrid, with eight times fewer cells, is reached. The changes in the state vector on the way down are then interpolated back up to the finest mesh level. The reference value of the state vector is then updated. This represents one multigrid cycle and is illustrated in Figure 7.2.

The time-marching methods used to drive the Euler equations to a steady state actually involve the propagation of transient waves through the computational domain. By enforcing the desired boundary conditions, transient waves are driven out of the domain and eventually the steady state is reached. By using successively coarser meshes in the multigrid cycle, the transient waves are both damped and more rapidly driven to the boundaries where they can be expelled from the domain. One set of undesired waves are the high frequency, odd-even mode waves which are introduced in the process of interpolation the corrections back to the fine mesh using linear interpolation. Therefore, one requirement for a good multigrid strategy is that the scheme have the ability to damp high frequency waves. As mentioned in Appendix A, the five-stage Runge-Kutta scheme described in Section 5.1.3 has this ability. Figure A.5 shows the amplification factor for this scheme. The point of interest is $\theta = \pi$ which represents the sawtooth, odd-even mode. At this point the amplification factor is $|g| = 0$ so these waves are damped. This scheme uses a CFL number which is much smaller than the limit for stability. Since the accelerated convergence rate achieved from multigrid is due to the damping of waves through the use of several meshes rather than the timestepping process itself, obtaining the smallest amplification factor for the scheme is more important than obtaining a larger timestep.

Finally, there are a few notes which should be made about the multigrid strategy used here. In particular, the CFL number and the artificial viscosity coefficients are held constant through all levels of the multigrid and local timesteps are used. Results from both subsonic and transonic cases are shown which use different methods of artificial viscosity. When the artificial viscosity used has a fourth difference formulation away from a shock and a second difference turned on in the shock region by a switch, as described in Section 5.1.1, it is important to freeze the switch at the fine mesh level. The solution on the coarse meshes is driven by the fine mesh solution through the introduction of the function P, but while solving on the coarse mesh the solution cannot be 'pulled' away from this solution. Hence the reason for freezing the switch.

7.3 GMRES

GMRES is an acronym for Generalized Minimal Residual Algorithm. The idea is to reduce the dimension of the problem from several thousand down to 20 → 40 and use minimization methods in this reduced space to find the problem solution. The reduced subspace used, called Krylov space, is where the minimization is performed using Givens rotation procedure. While the size of the Krylov space is specified for the linear GMRES, the nonlinear version requires a range for the size of the Krylov space as input, and as part of the computation the size of this space is adjusted based on the need, or lack of need, to increase the number of search directions for the minimization process. An underlying iterative method is used as a preconditioner for the method. The original GMRES algorithm was designed for linear problems and is a leading iterative method for the solution of nonsymmetric systems of linear equations. The nonlinear version of GMRES was developed by Wigton, Yu and Young [32] to solve the nonlinear problems arising in aerodynamics, acoustics, etc. Given a good preconditioner, GMRES can increase convergence significantly. Here, GMRES is used as a packaged program which is distributed by Boeing Computer Services [6, 5].

Only the complex variable version GMRES is used to accelerate convergence of the linear perturbation problem, although in practice a version for real variables could also be used to find the steady state. Although the problem is linear, the nonlinear version of the code was actually used since it proved to be more robust while requiring the same, if not less, computation time. The preconditioner which is used is one multigrid cycle described in Section 7.2. With one multigrid cycle, GMRES required 60% of the total computation time outside the preconditioner cycle, and it was found that using, for example, two multigrid cycles in the preconditioner did not reduce the total time to convergence.

Integrating this version of GMRES into the existing code was very straight forward, making it a fairly easy to add to an existing code. In the schematic shown in Figure 7.3, the preconditioner routine consists of most of the original code. The input to this routine from GMRES is a current value of the state vector and the output is a new, predicted

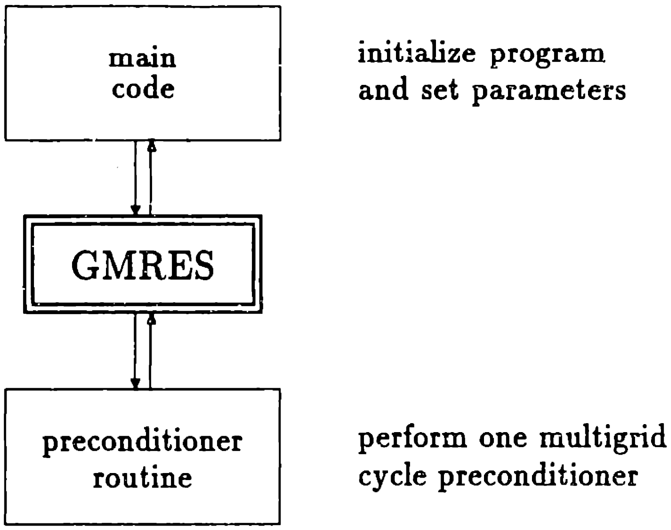

Figure 7.3: Schematic of the code using GMRES.

value for this same state vector. The main code consists of basic startup procedures such as reading parameters and other initialization procedures which would normally be performed before any computation commenced. The inputs to GMRES consist of the range in size of the Krylov space and other tolerance parameters. In effect, GMRES merely splits the original code in two pieces and fits itself in between.

7.4 Results

As before, a subsonic case will be used first to examine the nature of the numerical scheme without a shock. The subsonic case shown in Section 6.1 will be used for this purpose. Figure 6.1 gives the height distribution along the duct for this case, where Figures 6.2 and 6.3 give the steady Mach number and pressure distributions. Figure 6.4 gives the perturbation pressure distribution for this case, where the unsteadiness is introduced though a pressure perturbation at the duct exit with $\omega = 1.729$. The case for which the convergence is examined has only fourth difference artificial viscosity with $\epsilon_4 = 0.04$, uses the five-stage Runge Kutta scheme with $CFL = 3$, and has 240 cells. Figure 7.4 gives the convergence histories when a global timestep, local timesteps, multigrid, and, for the perturbation scheme, GMRES are used. The computational time is given in seconds on a Decstation 5000/200 workstation. For consistency, the error is measured as the logarithm base 10 of the fine grid residual, $R - D$, which is driven to zero. The converged state, when the residual is no longer decreasing, corresponds to the point in the calculation when computer roundoff will not allow the residual to continue to decrease. Each iteration in the perturbation scheme requires approximately twice the computation time as the steady state scheme, mostly due to the use of complex variables. From Figure 7.4 it can be seen that the convergence rate for the steady state is about half that of the perturbation, so in terms of iterations, the schemes converge at the same rate. Notice that for both the steady state and the perturbation, there is not much difference between using local timesteps or a single global timestep. This is because the Mach number variation in the domain is very slight and there is no variation in the cell size. Using multigrid, approximately a factor of 10 speedup can be achieved over using a global timestep. GMRES, however, does not have much effect on convergence. The benefits of using GMRES will be more apparent in the transonic cases.

Figure 7.5 shows the effect of using the five-stage Runge-Kutta scheme over the four-stage Runge-Kutta scheme for this same subsonic case. Since the dissipation is only calculated in the first two stages of the five-stage scheme, it requires only 85%

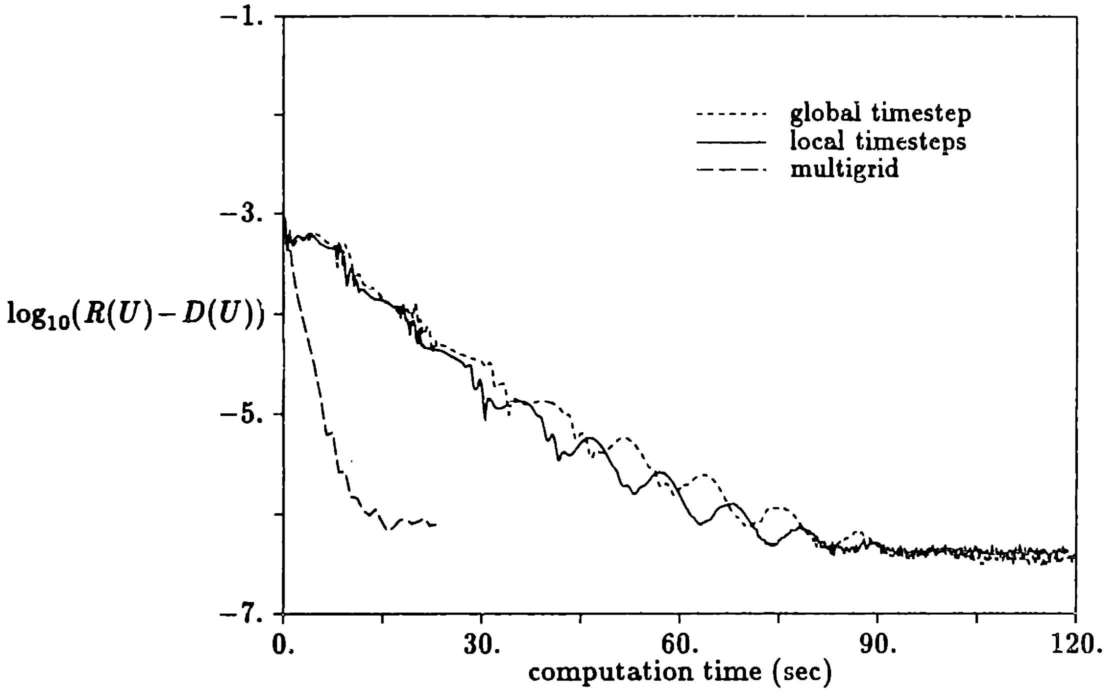

a) steady state

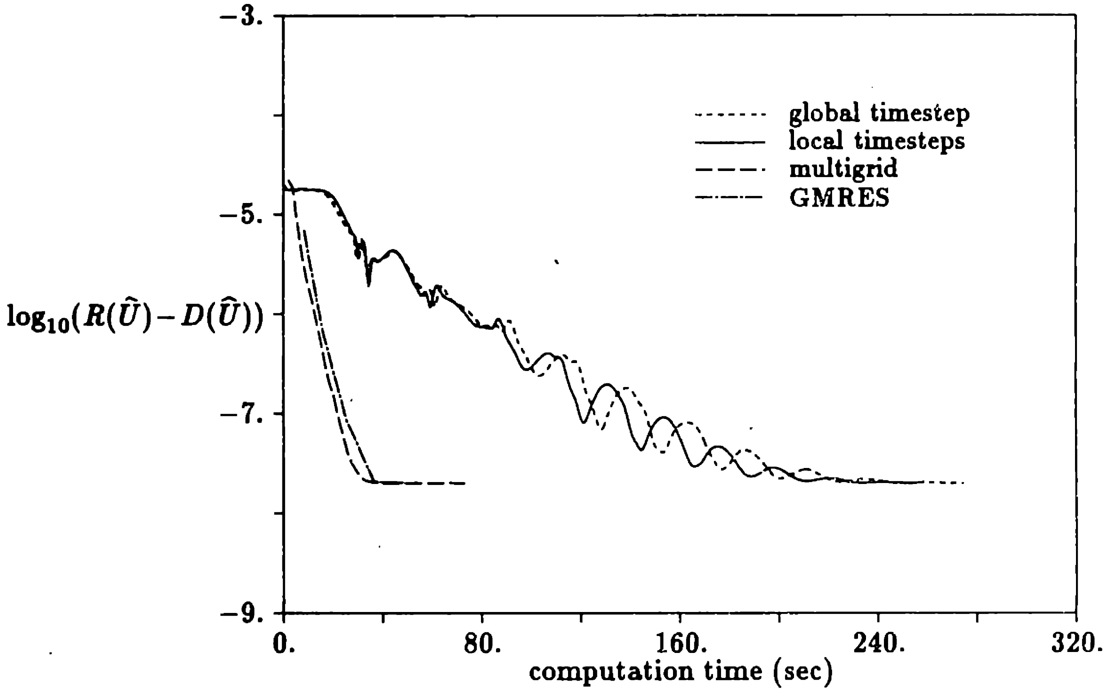

b) perturbation

Figure 7.4: Convergence history for the steady state and perturbation for the subsonic case for only fourth difference artificial viscosity with $\epsilon_4 = 0.04$, 240 cells and CFL=3 for the five-stage Runge-Kutta scheme.

of the computation time of the four-stage scheme per iteration. The motivation for using the five-stage scheme is to provide better damping of undesirable modes which would increase the convergence rate, and since less time is required per iteration and the CFL limit is higher as well, the five-stage scheme, it is more desirable to use than the four-stage scheme.

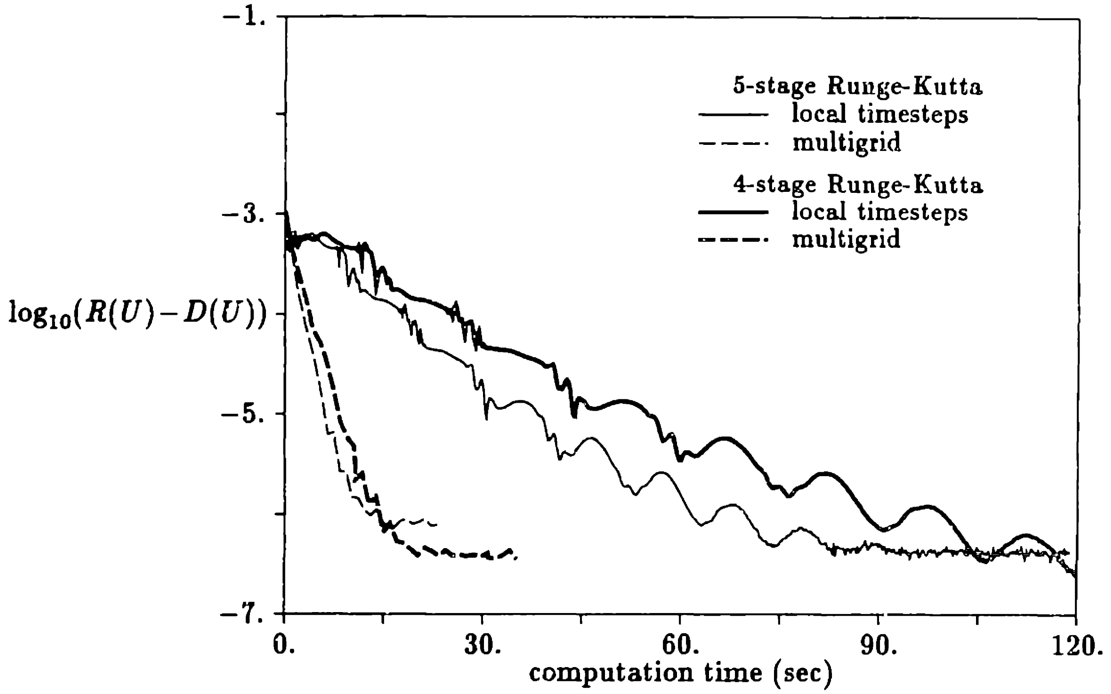

a) steady state

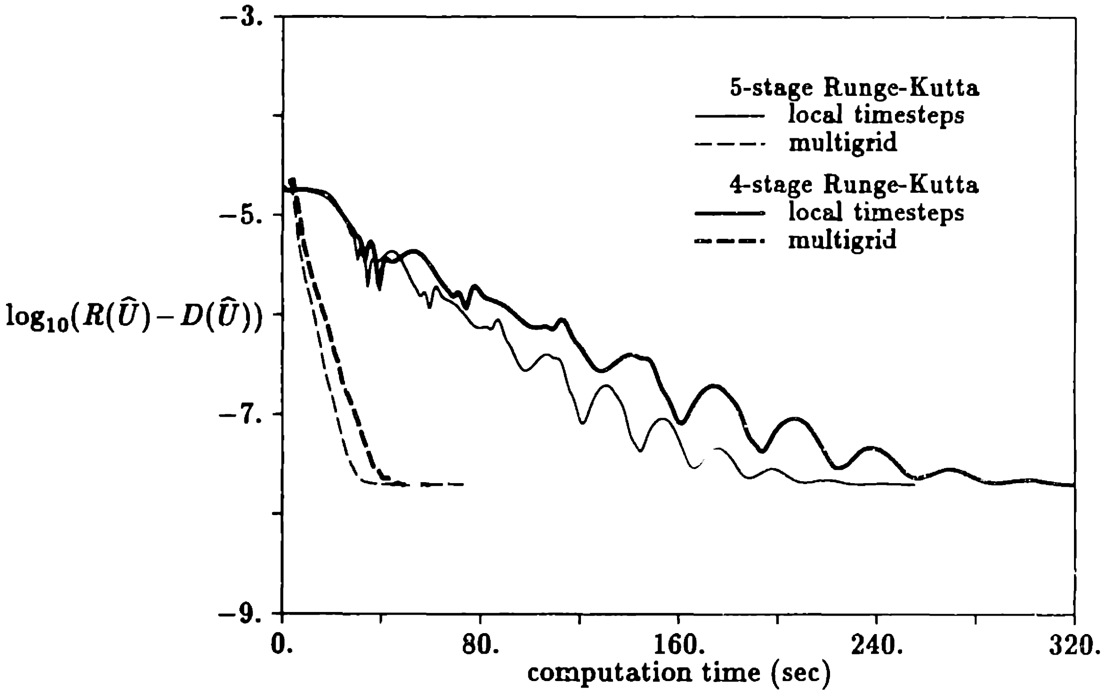

b) perturbation

Figure 7.5: Convergence history for the steady state and perturbation for the subsonic case for only fourth difference artificial viscosity with $\epsilon_4 = 0.04$, 240 cells and CFL=3 for the five-stage Runge-Kutta scheme and CFL=2.5 for the four-stage Runge-Kutta scheme.

The transonic case with inlet Mach number $M_{in} = 1.2$ shown in Section 6.2 will be examined next. Figure 6.11 gives the height distribution along the duct for this case, where Figures 6.12 and 6.13 give the steady Mach number and pressure distributions. Figure 6.14 gives the perturbation pressure distribution, where the unsteadiness is introduced though a pressure perturbation at the duct exit with $\omega = 1.729$. The case shown here has only second difference artificial viscosity with $\epsilon_2 = 0.15$, uses the five-stage Runge Kutta scheme with $CFL = 3$, and has 240 cells. Figure 7.6 gives the convergence history when a global timestep, local timesteps, multigrid, and, for the perturbation scheme, GMRES are used. Again, the computational time is seconds on a Decstation 5000/200 workstation. For consistency, the error is measured as the logarithm base 10 of the fine grid residual. As with the subsonic case, each iteration in the perturbation scheme requires approximately twice the computation time as the steady state scheme. From Figure 7.6 it can be seen that the rate of convergence (although not the time to convergence) in terms of computation time for the perturbation scheme is about twice that of the steady state, so in terms of iterations, the schemes converge at the same rate. Notice that for both the steady state and the perturbation, there is not much difference between using local timesteps or a global timestep. As with the subsonic case, this is because the Mach number variation in the domain is very slight and there is no variation in the cell size. By using multigrid, approximately a factor of 7 speedup for the steady state and a factor of 12 speedup for the perturbation is achieved over using a global timestep. Unlike the subsonic case, there is also a significant speedup when GMRES is used. The explanation for this speedup will be given in the next paragraph.

The increase in computer time required to converge the perturbation over the steady state, as well as the benefit of using GMRES, for the transonic case can be explained by looking at what is actually happening as the computation progresses. Most of the computational domain does not change and reaches the converged state very quickly. However, the amplitude of the peak in the shock region, similar to that shown in Figure 6.14, oscillates about the time independent solution for the perturbation. Figure 7.7 shows the amplitude of the three components of the state vector for the global timestep computation shown in Figure 7.6b. The amplitude of the peak oscillates at a nearly

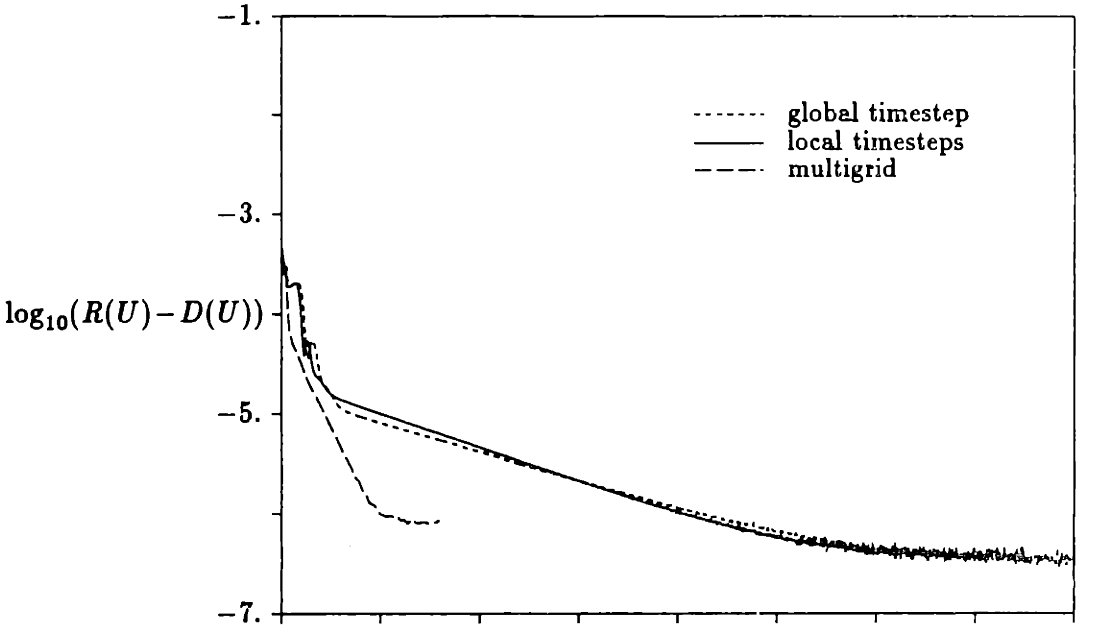

a) steady state

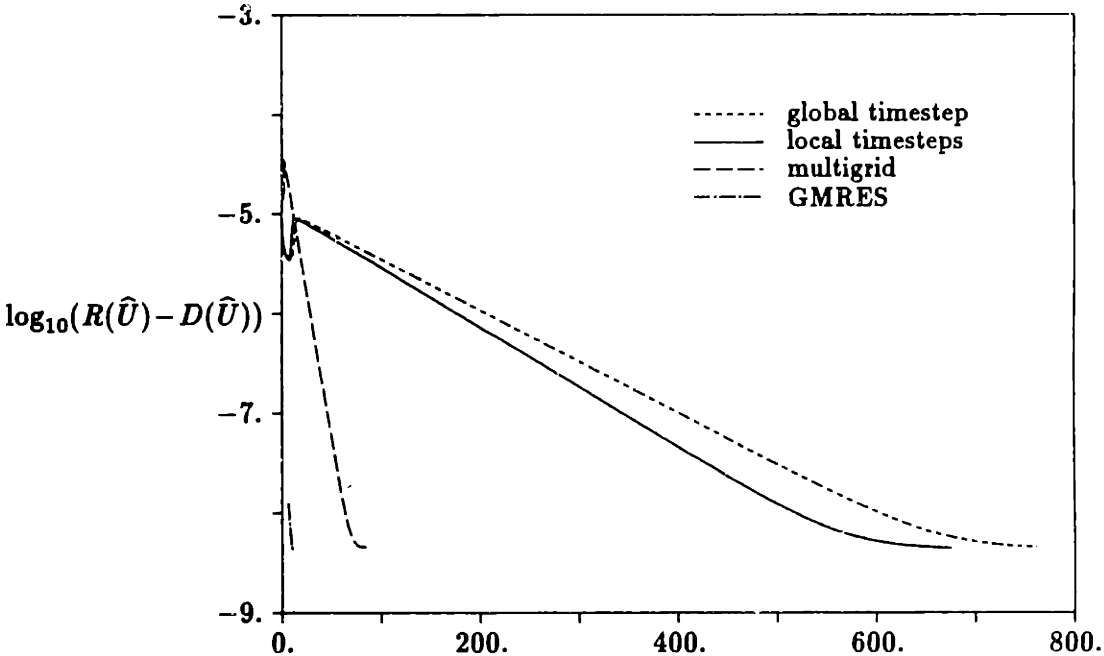

b) perturbation

Figure 7.6: Convergence history for the steady state and perturbation for the transonic case with inlet Mach number $M_{\text{in}} = 1.2$ for only second difference artificial viscosity with $\epsilon_2 = 0.15$, 240 cells and CFL=3 for the five-stage Runge-Kutta scheme.

constant frequency and has a nearly exponential decay to the time independent solution. This is a physical phenomena since the physical time frequency and decay rate do not vary as either the CFL number, artificial viscosity coefficient or the number of cells in the domain are changed, but they do change when a different transonic problem is explored. The frequency of the oscillations is very nearly the frequency imposed on the problem and doubling this input frequency, doubles the oscillation frequency as well. The peak in the solution around the shock region is a smeared delta function which represents the movement of the shock times the steady strength of the shock, so physically the change in the solution represents the movement of the shock. This quantity is exhibiting the behavior which is seen in an equation of the form

$$\frac{\partial y}{\partial t} = C_1 y + C_2, \tag{7.2}$$

where C_1 and C_2 are complex numbers, which is solved to give

$$y = e^{C_1 t} - \frac{C_2}{C_1}, \tag{7.3}$$

where $\Re\{C_1\}$ gives the decay rate and $\Im\{C_1\}$ gives the frequency of oscillation as seen in Figure 7.7. $-\frac{C_2}{C_1}$ is the time independent solution which is eventually reached. By analyzing the plots in Figure 7.7 it can be seen that they exhibit almost exactly a solution of the form in Equation (7.3). Since the frequency of oscillation in Figure 7.7 are the input oscillations represented by a term $e^{i\omega t}$, physically only an exponential decay is represented by this phenomena. The minimization in GMRES takes this predictable behavior and finds the solution for the converged state, hence the large increase in convergence rate achieved with GMRES. Since the decay is represented by a single mode, a simple method which performs the same task as GMRES, by predicting this mode and setting the solution to the converged state, could be implemented. This physical convergence mode will exist in higher dimensional problems as well, where the decay rate will vary along the shock, therefore some method for increasing the convergence could be devised for these problems as well.

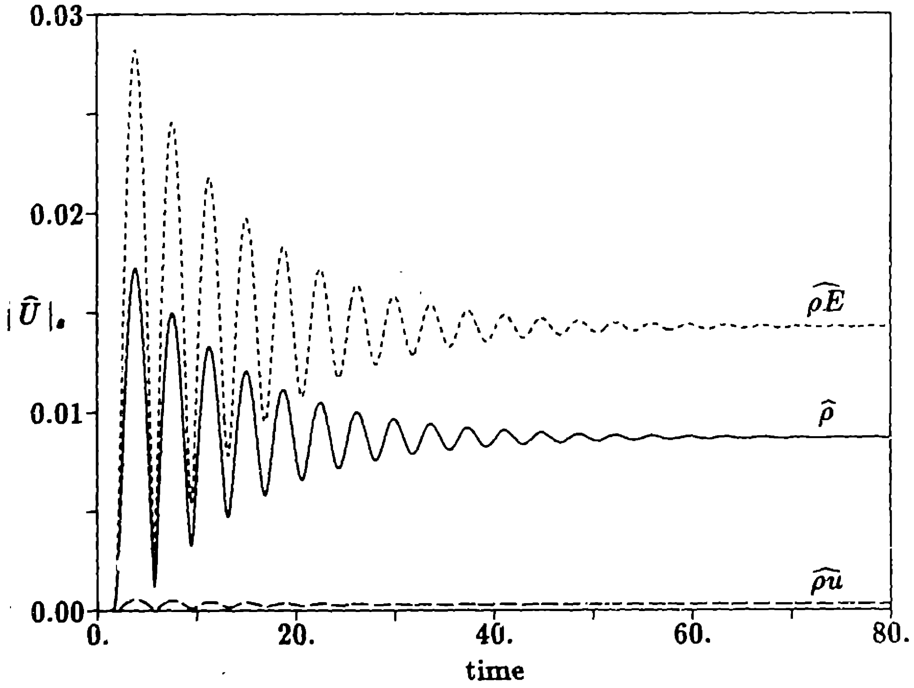

Figure 7.7: Magnitude of the perturbation state vector for the shock node (node number 123) vs. time for the same case shown in Figure 7.6 with 240 cells and CFL=3 for the five-stage Runge-Kutta scheme.

The last case is the same transonic case just discussed, except a different method of shock capturing is used. Here, fourth difference artificial viscosity with $\epsilon_4 = 0.04$ is used in most of the domain except in the shock region where the second difference artificial viscosity with $\epsilon_2 = 0.15$ is turned on by a switch. As discussed in Section 6.3, the switch is not linearized in this case and there is no grid movement for the case given here. The convergence histories for this case shown in Figure 7.8 are similar to those given in Figure 7.6, so the effect of the switch does not have a large effect on the convergence characteristics of the scheme.

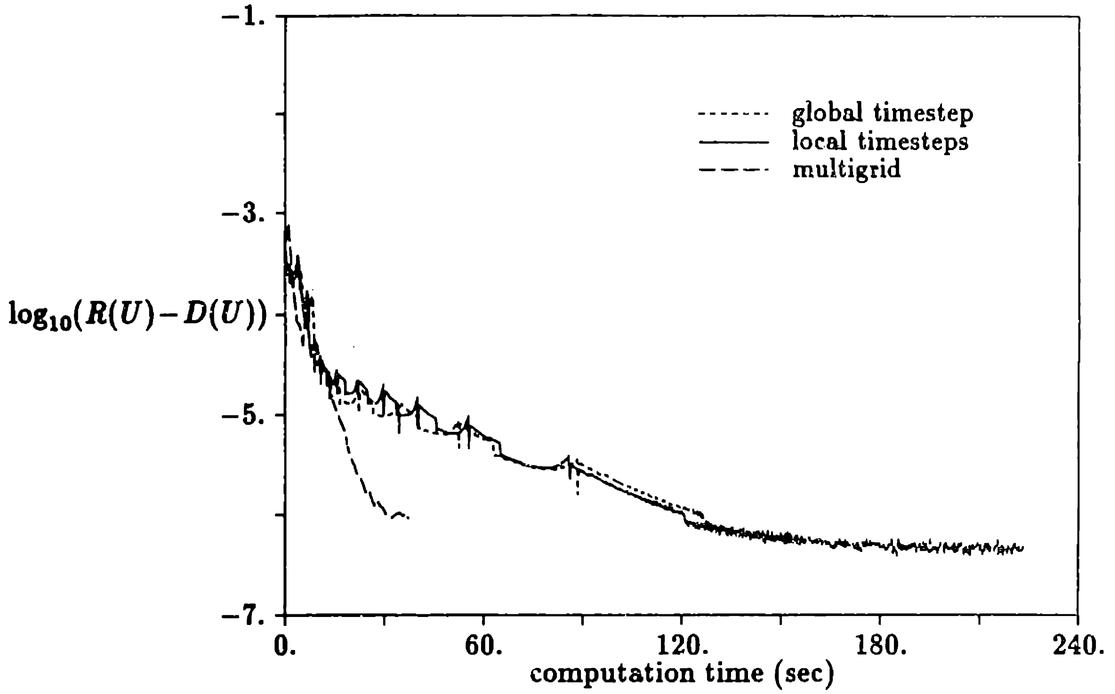

a) steady state

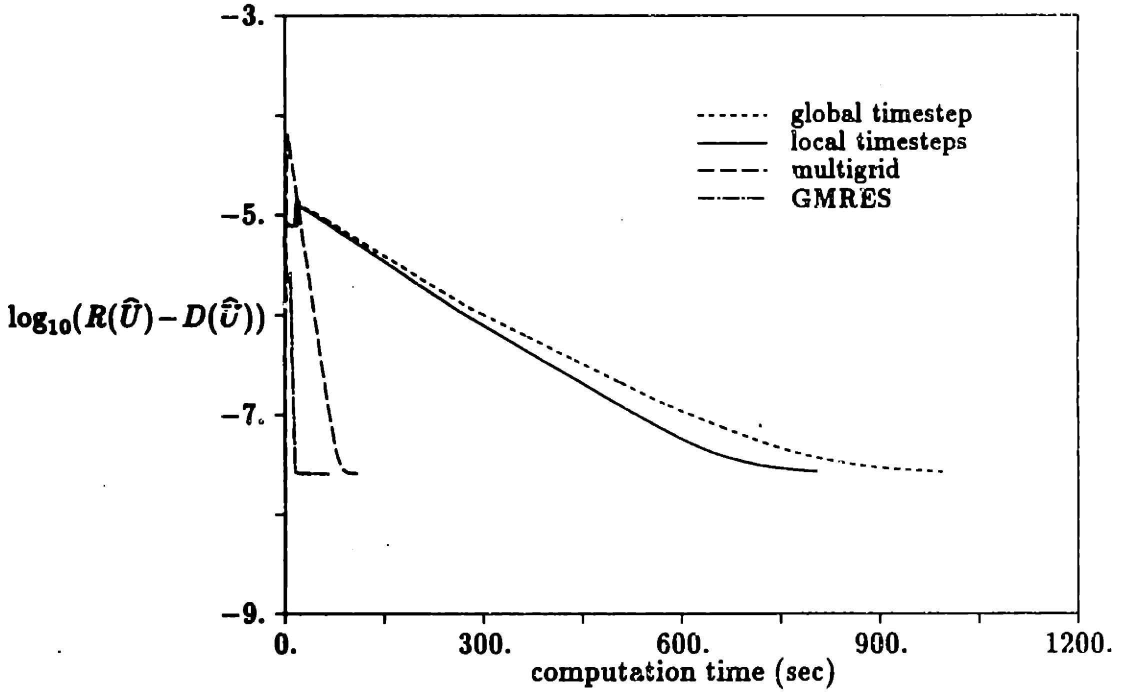

b) perturbation

Figure 7.8: Convergence history for the steady state and perturbation for the transonic case with inlet Mach number $M_{\text{in}} = 1.2$ for mixed second difference artificial viscosity with $\epsilon_2 = 0.15$ in the shock and fourth difference artificial viscosity with $\epsilon_4 = 0.04$ in the rest of the domain, 240 cells and CFL=3 for the five-stage Runge-Kutta scheme.

Chapter 8

Concluding Remarks

The focus of this work is on the fundamental issues associated with the use of the linear perturbation Euler equations with shock capturing in the computation of unsteady transonic flowfields. As a justification for this method, an analytical discussion of the Navier-Stokes equations and the effect of discretization on a moving shock was presented. Based on this discussion, several numerical schemes were developed and computational results using these schemes were presented. One of the major motivations for the use of the linear perturbation equations is the reduction in computational resources required for these schemes over full nonlinear calculations. One linear calculation can require well over a factor of ten less computation time than the nonlinear calculation. Since reduced computation time is an issue, convergence acceleration techniques were also explored. What will follow is an expanded summary of the important findings presented in this work and a discussion of future work which would be based on the research presented here.

8.1 Summary

There is nothing new about the use of perturbation methods. For several years the linear perturbation potential equations have been used to compute unsteady flowfields. In these methods the steady state solution is first found and the unsteadiness is introduced into the flowfield as a linear perturbation on this steady solution. The perturbation normally has a single frequency dependency, since linearity allows a full solution to be composed of the superposition of several frequencies. Ni was the first to present a linear perturbation method for the Euler equations, but this method was limited to shock free flowfields. In 1987, Hall used the Euler equations for transonic flowfields with shock fitting, but there are limitations to all shock fitting schemes, especially in three dimensional flow. Shock capturing has been long accepted for use with both steady and unsteady flowfields, but many researchers have convinced themselves that shock capturing with the linear perturbation equations was infeasible for all but the weakest shocks. This work provides the first justification for the use of shock capturing with the linearized Euler equations.

The analysis began in Chapter 3. For a steady transonic flowfield it is easy to show that the location and strength of the shock are not functions of the viscosity and that the viscosity merely governs the width of the shock. In a true flowfield, however, the width of the shock is on the order of a few mean free paths, which would be unrealistic to model computationally. This nearly zero width shock motivates the use of shock fitting which explicitly sets the shock width to zero. Knowing that the magnitude of the viscosity can be changed without affecting the location and strength of the shock allows for the use of artificial viscosity, a function which simulates the true viscosity terms but allows for a shock with a width on the order of a few computational cells. This method is called shock capturing, since the existence and location of the shock becomes part of the computation, as for the true viscosity, and has been accepted for steady problems for several years. The challenge here was to show that artificial viscosity could be used for the linear perturbation equations as well. Like the argument for its use with the steady equations, the analysis involved the use of the Navier-Stokes equations. It was shown that if the unsteadiness in the flowfield has reduced frequency on the order of the Reynolds number or less, the unsteady shock shape is a quasi-steady function of the flow upstream and downstream of the shock and, like the steady case, the level of the viscosity only governs the width of the shock. With this information it was then found that the perturbation of the integral of the flow solution is a linear function of the perturbation imposed on the flowfield, again independent of the level of the viscosity. This result follows from showing that the leading order contribution to the integrated solution in the shock region is purely due to a translation of the shock. This information is used to justify the use of artificial viscosity with the perturbation equations which represent a linear viscous solution, where any other integrated solution can then be found by linear scaling.

The next question which needed to be asked was, what is the effect of discretization on this analysis? This question was addressed in Chapter 4. The major computational issue is associated with the changing discrete shock shape as the shock moves relative to the mesh. This changing shock shape comes about since in the discrete flowfield, the solution is known at several nodes in the flowfield and linear interpolation is used to find the solution between these nodes. This is an important issue, since part of the analysis previously described required that the shock maintain a similar shape as it moved, and this must hold for the computational solution as well. A constant area duct, or shock-tube, was used to concentrate on the effects of the moving shock. It was found that the error associated with the changing shock shape on the integrated solution was quite small. The more smeared the shock, the smaller the error, so the flux vector split scheme which put only two nodes in the shock produced the largest errors. It was concluded that computational errors associated with the problem were again small and the concept of finding a linear perturbation solution with shock capturing could still be considered valid.

Based on this analysis, several computational schemes were developed in Chapter 5 to solve for the steady state and the amplitude of the linear perturbation. As discussed earlier, the linear perturbation has an imposed harmonic time dependency, so the perturbation amplitude is not a function of time. In the solution method, the time dependency was left in the equations for the steady state as well as the equations for the amplitude of the harmonic perturbation and the solution was advanced until there was no change in time and the time independent steady state or perturbation amplitude were reached. These schemes were based on the Euler equations and in the shock region use shock capturing with either artificial viscosity or flux vector splitting. For comparison purposes, a direct solver shock fitting scheme was developed as well. The computational geometry was a quasi-one-dimensional duct which simplified the problem while at the same time allowing the relevant computational issues to be addressed. A method which adds a perturbation grid movement to the perturbation equations was also described. This method allows the shock to move with the grid with the aim that this will reduce the errors associated with the changing shock shape of a discrete moving shock.

As with all CFD methods, there is always a question of how many cells are necessary to achieve a desired level of accuracy. For example, it may be acceptable to have a 1% error in the solution, so for that particular problem the question becomes, how many cells are necessary to achieve this level of accuracy? In Chapter 6 the goal of studying the effect of grid resolution was to show that the computational methods were mathematically rigorous and that, in the limit of an infinite number of cells in the domain, the solution approaches some appropriate limiting solution. In the shock capturing schemes, the shock width is proportional to the size of the computational cells, so in the limiting case the shock width will go to zero. The limiting solution for these schemes is then comparable to the shock fit scheme which has zero shock width, so this becomes a good comparison for the schemes. When only second difference artificial viscosity was used, the effect of the first order accuracy of this scheme dominated the results. When second difference artificial viscosity was only used in the shock region and switched to fourth difference artificial viscosity, which made the scheme second order accurate, in the rest of the flowfield, the error was reduced. This scheme has a constant error in the perturbation associated with not linearizing the switch which can be seen in the perturbation results, but this error is quite small and was then eliminated by moving the grid with the shock. Flux vector splitting produced some interesting results. To make the scheme second order accurate, MUSCL upwinding was added to the scheme, but this kept particular steady solutions from converging by putting them into a limit cycle. Since this behavior is inconsistent with the assumptions made in the method, the results for the perturbation for this special case had a very large error. For the solutions which did not have a limit cycle in the steady solution, the desired effect moving the mesh with the shock to reduce the errors associated with a changing shock shape were clearly evident. The flux vector split case produces two point shocks, so this is the case where the most advantage was expected as well. All in all, the results confirmed what the analysis had shown, that accurate solutions could be found using shock capturing to find the linear perturbation. Similar results are expected for higher dimensional problems.

The major motivation for using perturbation schemes is to reduce the computational cost of finding unsteady flow solutions. For this reason, several convergence acceleration techniques were examined in Chapter 7 for use with the schemes presented here. Since the computational schemes involved advancing an unsteady equation in pseudo-time until the solution became time independent, the actual time history to convergence is unimportant. All the convergence acceleration techniques used here took advantage of this point by changing the path taken to convergence. Timesteps based on local stability restrictions have been used for several years to increase the rate of convergence. For the problems examined here, local timesteps only provided a small acceleration of convergence since the Mach number variation in the problems was small and the cell sizes were constant. However, when there is a large Mach number variation in the flowfield and a large range of cell sizes, local timesteps can provide a considerable savings of computational time. The use of multigrid, however, did provide a large savings in computational time by speeding convergence by a factor of seven to twelve, depending on the problem. GMRES was the last method of convergence acceleration examined. This method provides a minimization process which was particularly useful for finding the perturbation solution for the transonic cases. These cases show an oscillation of the solution in the shock region which has a particularly slow decay rate which was greatly increased by the use of GMRES.

8.2 Future Work

All the discussion in this thesis was in the context of a one-dimensional or quasi-one-dimensional duct. This provided an excellent arena to examine analytical and computational issues associated with unsteady shock motion, which is essentially a quasi-one-dimensional phenomena. All the issues which were discussed here are easily extended to two and three dimensions where the important physical problems are defined. This is clearly one of the next paths to follow in this research, and in fact the development of a three-dimensional scheme by Giles [13] is currently under way. In these higher dimensional problems, the computational savings associated with time-marching to a time independent solution for the steady state and perturbation over a direct solver will be more apparent.

The computational cost associated with solving the nonlinear unsteady viscous equations in two and and especially three dimensions is so prohibitive that these methods are hardly ever used. There is no roadblock to extending the schemes described here to include viscous effects other than those associated with the shock region, since these viscous terms are already linear. The computational savings would be comparable to the savings associated with the solution of the perturbation Euler equations and could make the computation of unsteady viscous flowfields more accessible.

Preliminary work by Hall [15, 17] found that linear perturbation methods can be valid up to levels where the perturbation was 10% of the steady flowfield. More studies must be performed to more rigorously define a region within which flowfields are linear. Both experimental and numerical data could be used in these studies. Preliminary results do show that acceptable levels of perturbation can be quite large, making linear methods applicable to inlet distortion problems and stator/rotor interaction problems, as well as flutter problems where the interest is in the small perturbation of the regime, and perturbation methods are clearly valid.

Bibliography

[1] E. Acton and S. G. Newton. *AGARD manual on Aeroelasticity in Axial-Flow Turbomachines, AGARDograph No. 298*, chapter 6, Numerical Methods for Unsteady Transonic Flow. Vol. 1, Unsteady Turbomachinery Aerodynamics, AGARD, 1987.

[2] W. K. Anderson, J. L. Thomas, and B. Van Leer. "Comparison of Finite Volume Flux Vector Splittings for the Euler Equations." *AIAA Journal*, 24(9):1453–1460, September 1985.

[3] R. L. Bisplinghoff, H. Ashley, and R. L. Halfman. *Aeroelasticity.* Addison-Wesley Publishing Company, Cambridge, MA, 1955.

[4] A. Brandt. "Multilevel Adaptive Computations in Fluid Dynamics." *AIAA Journal*, 18(10):1165–1172, October 1980.

[5] R. H. Burkhart and D. P. Young. *Documentation for GMRES Acceleration and Optimization Codes.* Technical Report ETA-TR-89R1, Boeing Computer Services, Engineering & Scientific Services Division, G-6500, M/ 7L-21, P.O. Box 24346, Seattle, Washington 98124-0346, June 1988.

[6] R. H. Burkhart and D. P. Young. *GMRES Acceleration and Optimization Codes.* Technical Report ETA-TR-88, Boeing Computer Services, Engineering & Scientific Services Division, G-6500, M/S 7L-21, P.O. Box 24346, Seattle, Washington 98124-0346, May 1988.

[7] J. R. Caspar and J. M. Verdon. "Numerical Treatment of Unsteady Subsonic Flow Past an Oscillating Cascade." *AIAA Journal*, 19(12):1531–1539, December 1981.

[8] G. Dahlquist and Å. Björck. *Numerical Methods.* Prentice-Hall, 1974. Translated by Ned Anderson.

[9] J. F. Dannenhoffer III. *Grid Adaptation for Complex Two-Dimensional Transonic Flows.* ScD thesis, Massachusetts Institute of Technology, August 1987.

[10] E. H. Dowell, H. C. Curtis Jr., R. H. Scanlan, and F. Sisto. *A Modern Course in Aeroelasticity.* Kluwer Academic, second revised and enlarged edition, 1989.

[11] M. B. Giles. *Solution of 1-D Euler Equations Using a Box Method.* Technical Report CFDL-TR-84-1, Massachusetts Institute of Technology, February 1984.

[12] M. B. Giles. *UNSFLO: A Numerical Method for Unsteady Inviscid Flow in Turbomachinery.* Technical Report CFDL-TR-86-6, Massachusetts Institute of Technology, December 1986.

[13] M. Giles. personal communication 1991.

[14] K. C. Hall. *A Deforming Grid Variational Principle and Finite Element Method for Computing Unsteady Small Disturbance Flows in Cascades.* January 1992.

[15] K. C. Hall. *A Linearized Euler Analysis of Unsteady Flows in Turbomachinery.* PhD thesis, Massachusetts Institute of Technology, May 1987.

[16] K. C. Hall and W. S. Clark. *Prediction of Unsteady Aerodynamic Loads in Cascades Using the Linearized Euler Equations on Deforming Grids.* Paper AIAA-91-3378, June 1991.

[17] K. C. Hall and E. F. Crawley. "Calculation of Unsteady Flows in Turbomachinery Using the Linearized Euler Equations." In *Fourth Symposium on Unsteady Aerodynamics and Aeroelasticity of Turbomachines and Propellers*, Aachen, West Germany, September 1987.

[18] A. Jameson. "Solution of the Euler Equations by a Multigrid Method." *Applied Math. and Computation*, 13:327–356, June 1983.

[19] D. R. Lindquist. *A Comparison of Numerical Schemes on Triangular and Quadrilateral Meshes.* Master's thesis, Massachusetts Institute of Technology, May 1988.

[20] E. Murman. personal communication, June 1991.

[21] R.-H. Ni. *A Multiple-Grid Scheme for Solving the Euler Equations.* AIAA 181-025R, June 1981.

[22] R.-H. Ni. *Multigrid Convergence Acceleration Techniques for Explicit Euler Solvers and Applications to Navier-Stokes Calculations.* Technical Report Lecture Series 1986-02, von Kármán Institute for Fluid Dynamics, January 1986.

[23] R.-H. Ni. *Nonstationary Aerodynamics of Arbitrary Cascades in Compressible Flow.* PhD thesis, Stevens Institute of Technology, June 1974.

[24] R.-H. Ni and F. Sisto. "Numerical Computation of Nonstationary Aerodynamics of Flat Plate Cascades in Compressible Flow." *Transactions of the ASME: Journal of Engineering for Power*, 98:165–170, April 1976.

[25] T. W. Roberts. "The behavior of flux difference splitting schemes near slowly moving shock waves." In K. W. Morton and M. J. Baines, editors, *Numerical Methods for Fluid Dynamics III*, pp. 442–448, Oxford Science Publications, March 1988.

[26] B. van Leer. *Flux-vector Spitting for the Euler Equations.* Technical Report 82-30, I.C.A.S.E., 1982.

[27] M. VanDyke. *Perturbation Methods in Fluid Mechanics.* Parabolic Press, annotated edition, 1975.

[28] J. M. Verdon and J. R. Caspar. "A Linearized Unsteady Aerodynamic Analysis for Transonic Flows." *Journal of Fluid Mechanics*, 149:403–429, 1984.

[29] J. M. Verdon and J. R. Caspar. "Subsonic Flow Past an Osciliating Cascade With Finite Mean Flow Deflection." *AIAA Journal*, 18(5):540–548, May 1980.

[30] D. S. Whitehead. *AGARD manual on Aeroelasticity in Axial-Flow Turbomachines, AGARDograph No. 298*, chapter 3, Classical Two-Dimensional Methods. Vol. 1, Unsteady Turbomachinery Aerodynamics, AGARD, 1987.

[31] D. S. Whitehead. *The Calculation of Steady and Unsteady Transonic Flow in Cascades.* Technical Report CUED/A-Turbo/TR 118, Cambridge University Engineering Department, February 1982.

[32] L. Wigton, N. J. Yu, and D. P. Young. *GMRES Acceleration of Computational Fluid Dynamics Codes.* Paper AIAA-85-1494, June 1985.

Appendix A

Stability Analysis

The temporal stability of a particular scheme can be studied by considering a model linear scalar equation. When analyzing time-marching to find the steady solution, the wave equation is used.

$$\frac{\partial u}{\partial t} + a\frac{\partial u}{\partial x} = 0 \tag{A.1}$$

When time-marching to find the linear perturbation there is an added term which must be considered, so now the model equation becomes

$$\frac{\partial u}{\partial t} + i\omega u + a\frac{\partial u}{\partial x} = 0. \tag{A.2}$$

The numerical stability analysis considers whether Fourier modes in the solution amplify or decay as the solution procedure progresses. In particular, the transient computational modes must decay so the solution can converge.

A.1 Steady State

First consider the discretization of Equation (A.1) which represents the equation used to find the steady state solution. Since a Runge-Kutta scheme is used, the discretization in time is separated from the discretization in space. In general, the governing equation can be written as

$$\left(\frac{du}{dt}\right)_J = -R_J, \tag{A.3}$$

where R_J represents some spatial discretization. In particular, for the equation used here where central differencing is used, R_J from Equation (A.1) is

$$R_J = a\,\frac{u_{J+1} - u_{J-1}}{2\Delta x}. \tag{A.4}$$

The temporal discretization at node J is now performed using a four-stage Runge-Kutta time-marching scheme. Given some function $R(u)$, this scheme can be written as

$$\begin{aligned} u^{(0)} &= u(t_n) \\ u^{(1)} &= u^{(0)} - \tfrac{1}{4}\,\Delta t\, R(u^{(0)}) \\ u^{(2)} &= u^{(0)} - \tfrac{1}{3}\,\Delta t\, R(u^{(1)}) \\ u^{(3)} &= u^{(0)} - \tfrac{1}{2}\,\Delta t\, R(u^{(2)}) \\ u^{(4)} &= u^{(0)} - \quad \Delta t\, R(u^{(3)}) \\ u(t_{n+1}) &= u^{(4)} \end{aligned} \tag{A.5}$$

Since the interest is in the amplification or decay of discrete modes, the equation is cast in Fourier space by setting $u_J = \bar{u}_k e^{i(J\theta_k)}$ where $\theta_k = k\Delta x$. From now on the subscript k in θ_k and $\bar{u}_k$ will be implied. Let $z\,\bar{u}$ be the transform of the spatial discretization $-\Delta t\, R_J$, so in Fourier space, Equation (A.5) is

$$\begin{aligned}
\bar{u}^{(0)} &= \bar{u}(t_n) \\
\bar{u}^{(1)} &= \bar{u}^{(0)} + \tfrac{1}{4}\, z\, \bar{u}^{(0)} \\
\bar{u}^{(2)} &= \bar{u}^{(0)} + \tfrac{1}{3}\, z\, \bar{u}^{(1)} \\
\bar{u}^{(3)} &= \bar{u}^{(0)} + \tfrac{1}{2}\, z\, \bar{u}^{(2)} \\
\bar{u}^{(4)} &= \bar{u}^{(0)} + \quad z\, \bar{u}^{(3)} \\
\bar{u}(t_{n+1}) &= \bar{u}^{(4)}
\end{aligned} \tag{A.6}$$

Putting the steps of the multi-stage scheme together gives

$$\begin{aligned}
\bar{u}(t_{n+1}) &= \bar{u}(t_n)\,(1 + z + \tfrac{1}{2}z^2 + \tfrac{1}{6}z^3 + \tfrac{1}{24}z^4) \\
&= \bar{u}(t_n)\, g(z),
\end{aligned} \tag{A.7}$$

where $g(z)$ is the amplification factor. If $|g(z)| < 1$, then the Fourier modes decay from time t_n to t_{n+1} and the scheme is stable. In Figure A.1, contours of $|g(z)|$ are shown for $|g(z)| \leq 1$ as a function of the complex variable z. These contours were formed using a contour generation program where the function $|g(z)|$ was evaluated in a discretized domain.

The stability of a particular scheme depends on the value of z for that scheme. For the scheme in question, R_J is given in Equation (A.4) and the Fourier transform of $\Delta t\, R_J$ is found by replacing u_J by $\bar{u}e^{i(J\theta)}$. After some algebra this gives

$$z = -i\,\lambda\,\sin\theta, \tag{A.8}$$

where $\lambda = \frac{a\Delta t}{\Delta x}$ is the CFL number. For $0 \leq \theta < 2\pi$, the value of z for this scheme can be plotted along with the stability contours shown in Figure A.1 This is shown in Figure A.2 for $\lambda = 2\sqrt{2}$. If $\lambda > 2\sqrt{2}$ then the solid line will go outside the contour $|g(z)| = 1$, which defines the stability boundary, and the scheme is unstable, hence this represents the limit on λ for stability.

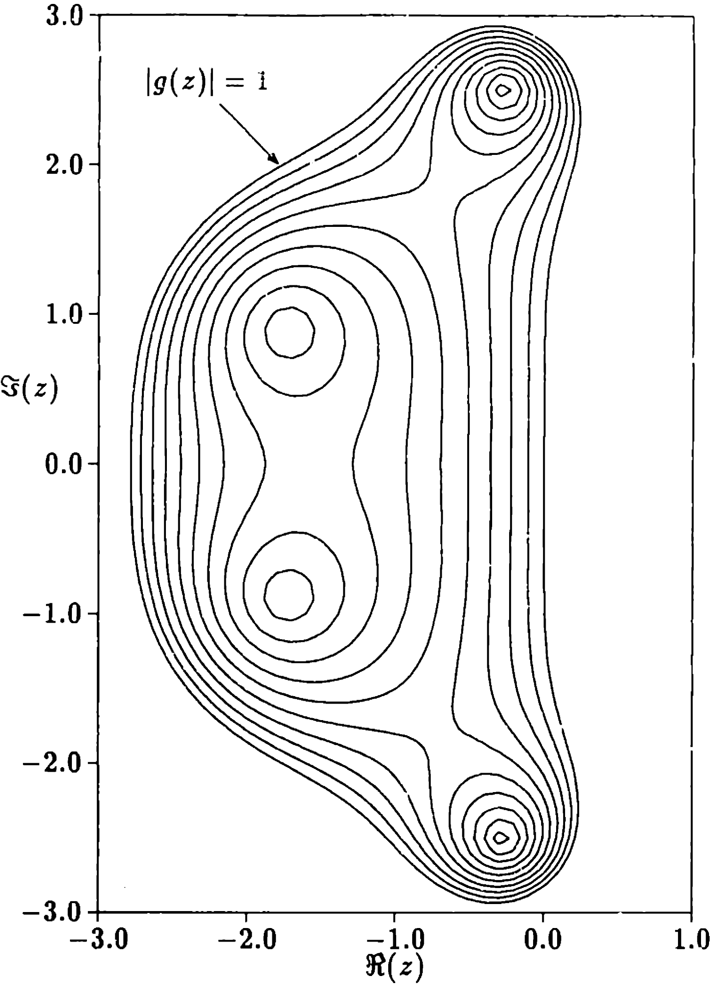

Figure A.1: Contours of $|g(z)|$ for the four-stage Runge-Kutta time-marching scheme.

Three particular values of θ will be examined to gain more insight into the information in Figure A.2.

$\theta = 0$: In this case, very long wavelengths are considered. Upon evaluation, $z = 0$ which gives $g(z) = 1$. $\theta = 0$ can be interpreted as the case where $\Delta x \to 0$ since $\theta = k\Delta x$, which implies that $\Delta t \to 0$ at the same rate for a bounded λ. In this limit of $\Delta t \to 0$ the solution must not advance in one iteration, or in other words $g(z) = 1$. Since this is true, this result confirms that the scheme is consistent, and since it is also stable then in the limit of $\Delta x \to 0$ the difference equation → the differential equation.

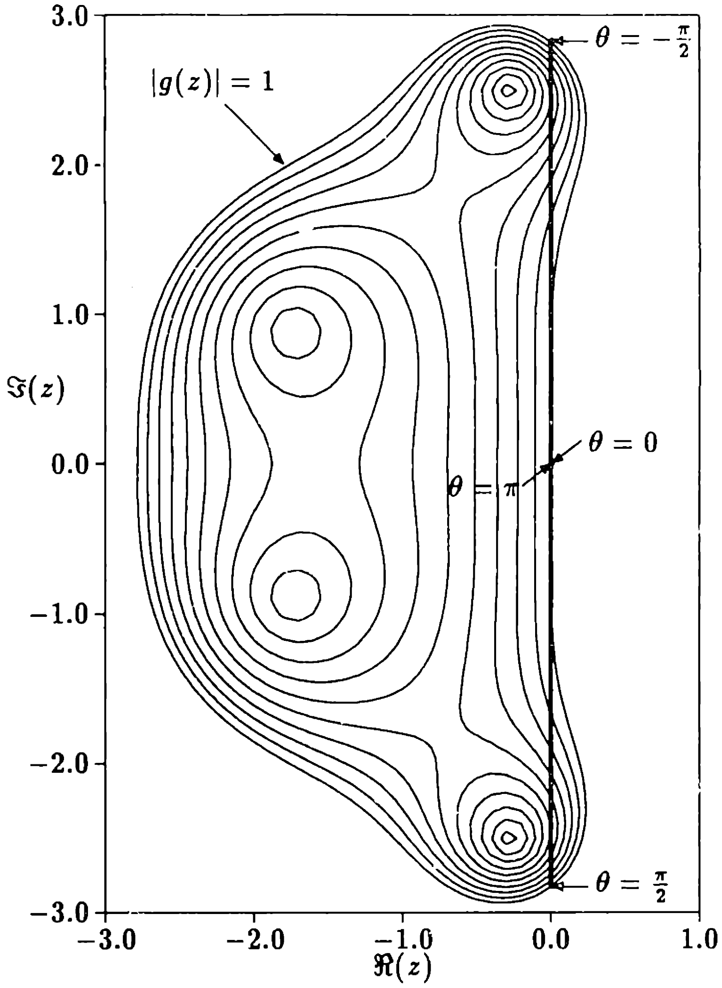

Figure A.2: Contours of $|g(z)|$ for the four-stage Runge-Kutta time-marching scheme and $z = -i\,\lambda\,\sin\theta$ (solid line) for $\lambda = 2\sqrt{2}$.

$\theta = \pm\frac{\pi}{2}$: This case gives $z = \mp i\,\lambda$. Since z is purely imaginary, the maximum value of λ for z to remain inside the $|g(z)| \leq 1$ contours is $\lambda = 2\sqrt{2}$. This gives the stability limit for the scheme, $\lambda \leq 2\sqrt{2}$.

$\theta = \pi$: This is the sawtooth mode, or in other words the wavelength is $2\Delta x$. For this case $z = 0$ and $|g(z)| = 1$. Since $|g(z)| = 1$, these sawtooth modes are not damped by the scheme, and they must be damped for the scheme to be stable. For this reason some damping must be added to the scheme for stability.

Now consider a new scheme where damping is added to the governing equations. Two forms of damping will be considered by adding a dissipative term to Equation (A.1).

$$1)\quad \frac{\partial u}{\partial t} + a\frac{\partial u}{\partial x} = \nu\Delta x\frac{\partial^2 u}{\partial x^2} \qquad \text{second difference damping}$$

$$R_J = a\frac{u_{J+1} - u_{J-1}}{2\Delta x} - \nu\frac{u_{J+1} - 2u_J + u_{J-1}}{\Delta x}$$

$$z = -i\,\lambda\,\sin\theta - \frac{\nu\lambda}{a}2\,(1 - \cos\theta)$$

$$2)\quad \frac{\partial u}{\partial t} + a\frac{\partial u}{\partial x} = -\nu\Delta x^3\frac{\partial^4 u}{\partial x^4} \qquad \text{fourth difference damping}$$

$$R_J = a\frac{u_{J+1} - u_{J-1}}{2\Delta x} + \nu\frac{u_{J+2} - 4u_{J+1} + 6u_J - 4u_{J-1} + u_{J-2}}{\Delta x}$$

$$z = -i\,\lambda\,\sin\theta - \frac{\nu\lambda}{a}4\,(1 - \cos\theta)^2$$

Figure A.3 shows the effect of adding damping to the scheme. Notice that now for $\theta = \pi$, $|g(z)| \neq 1$ and there is some damping of the sawtooth modes. To maintain stability, λ has been reduced from $2\sqrt{2}$ to 2.5 to keep the contour of z inside the $|g(z)| \leq 1$ domain. The change made by adding the damping terms is important to the stability characteristics of the scheme.

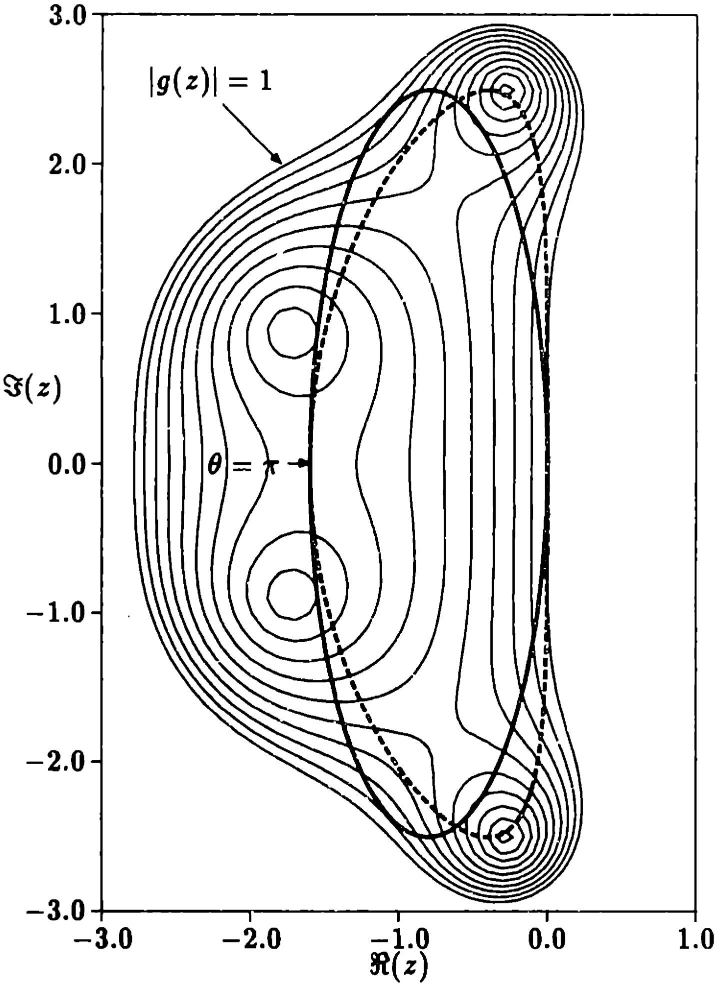

Figure A.3: Contours of $|g(z)|$ for the four-stage Runge-Kutta time-marching scheme for $\lambda = 2.5$ and $z = -i\lambda\sin\theta - \frac{\nu\lambda}{a}2(1-\cos\theta)$ with $\frac{\nu}{a} = 0.16$ (solid line) and $z = -i\lambda\sin\theta - \frac{\nu\lambda}{a}4(1-\cos\theta)^2$ with $\frac{\nu}{a} = 0.04$ (dashed line).

Now consider another scheme which has the same spatial discretization, but a slightly different temporal discretization. A five-stage Runge-Kutta scheme where the damping term is held constant after the first two stages is now analyzed. The contribution to the residual from the flux term and the diffusion term are now separated into $R(u)$ and $D(u)$ respectively.

$$\begin{aligned}
u^{(0)} &= u(t_n) \\
u^{(1)} &= u^{(0)} - \tfrac{1}{4}\,\Delta t\left(R(u^{(0)}) - D(u^{(0)})\right) \\
u^{(2)} &= u^{(0)} - \tfrac{1}{6}\,\Delta t\left(R(u^{(1)}) - D(u^{(1)})\right) \\
u^{(3)} &= u^{(0)} - \tfrac{3}{8}\,\Delta t\left(R(u^{(2)}) - D(u^{(1)})\right) \\
u^{(4)} &= u^{(0)} - \tfrac{1}{2}\,\Delta t\left(R(u^{(3)}) - D(u^{(1)})\right) \\
u^{(5)} &= u^{(0)} - \Delta t\left(R(u^{(4)}) - D(u^{(1)})\right) \\
u(t_{n+1}) &= u^{(5)}
\end{aligned} \tag{A.9}$$

As before, $z\,\bar{u}$ is the Fourier transform of the spatial discretization $-\Delta t\,(R_J - D_J)$, but since $R(u)$ and $D(u)$ are not always evaluated at the same value of u, it is not possible to lump them together and deal with the problem as before. But, in consideration of the Fourier transforms of $\Delta t\, D_J$ and $\Delta t\, R_J$ from before, it is clear that they contribute purely real and purely imaginary parts to z respectively. This allows the definition of

$$z = x - i\,y,$$

where

$i\,y$ is the Fourier operator for $R(u)$

x is the Fourier operator for $D(u)$,

so in Fourier space, Equation (A.9) is

$$
\begin{aligned}
\bar{u}^{(0)} &= \bar{u}(t_n) \\
\bar{u}^{(1)} &= \bar{u}^{(0)} + \tfrac{1}{4}\,(x\,\bar{u}^{(0)} - i\,y\,\bar{u}^{(0)}) \\
\bar{u}^{(2)} &= \bar{u}^{(0)} + \tfrac{1}{6}\,(x\,\bar{u}^{(1)} - i\,y\,\bar{u}^{(1)}) \\
\bar{u}^{(3)} &= \bar{u}^{(0)} + \tfrac{3}{8}\,(x\,\bar{u}^{(1)} - i\,y\,\bar{u}^{(2)}) \\
\bar{u}^{(4)} &= \bar{u}^{(0)} + \tfrac{1}{2}\,(x\,\bar{u}^{(1)} - i\,y\,\bar{u}^{(3)}) \\
\bar{u}^{(5)} &= \bar{u}^{(0)} + \quad (x\,\bar{u}^{(1)} - i\,y\,\bar{u}^{(4)}) \\
\bar{u}(t_{n+1}) &= \bar{u}^{(5)}
\end{aligned}
\tag{A.10}
$$

Putting the steps of the multi-stage scheme together and performing a lot of algebra gives

$$
\begin{aligned}
g(z) = \frac{\bar{u}(t_{n+1})}{\bar{u}(t_n)} &= 1 + (x - i\,y)(1 - \tfrac{1}{2}\,i\,y\,(1 - \tfrac{3}{8}\,i\,y\,(1 - \tfrac{1}{6}\,i\,y\,(1 - \tfrac{1}{4}\,i\,y)))) \\
&\quad \tfrac{1}{4}x(x - i\,y)(1 - \tfrac{1}{2}\,i\,y\,(1 - \tfrac{3}{8}\,i\,y\,(1 - \tfrac{1}{6}\,i\,y)))
\end{aligned}
\tag{A.11}
$$

where $g(z)$ is again the amplification factor. In Figure A.4, contours of this $|g(z)|$ are shown for $|g(z)| \leq 1$ as a function of the complex variable z. Also shown are the traces of z with the two forms of dissipation discussed previously. The stability limit for this scheme is increased to $\lambda \leq 4$, but for this plot $\lambda = 3$.

The reason for using the five-stage scheme can be seen in Figure A.5. When the value of the amplification factor is plotted along the line for z shown in Figures A.3 and A.4 where fourth difference dissipation is added to the scheme, the actual value of the amplification factor for the scheme can be seen. The point of interest is $\theta = \pi$ which, as discussed earlier, represents the odd-even oscillation mode of the scheme. The five-stage scheme has $|g| = 0$, or in other words it critically damps this mode. This is highly desirable for the multigrid method discussed in Section 7.2. It is not possible with the four-stage scheme to reduce the amplification factor to zero for this mode.

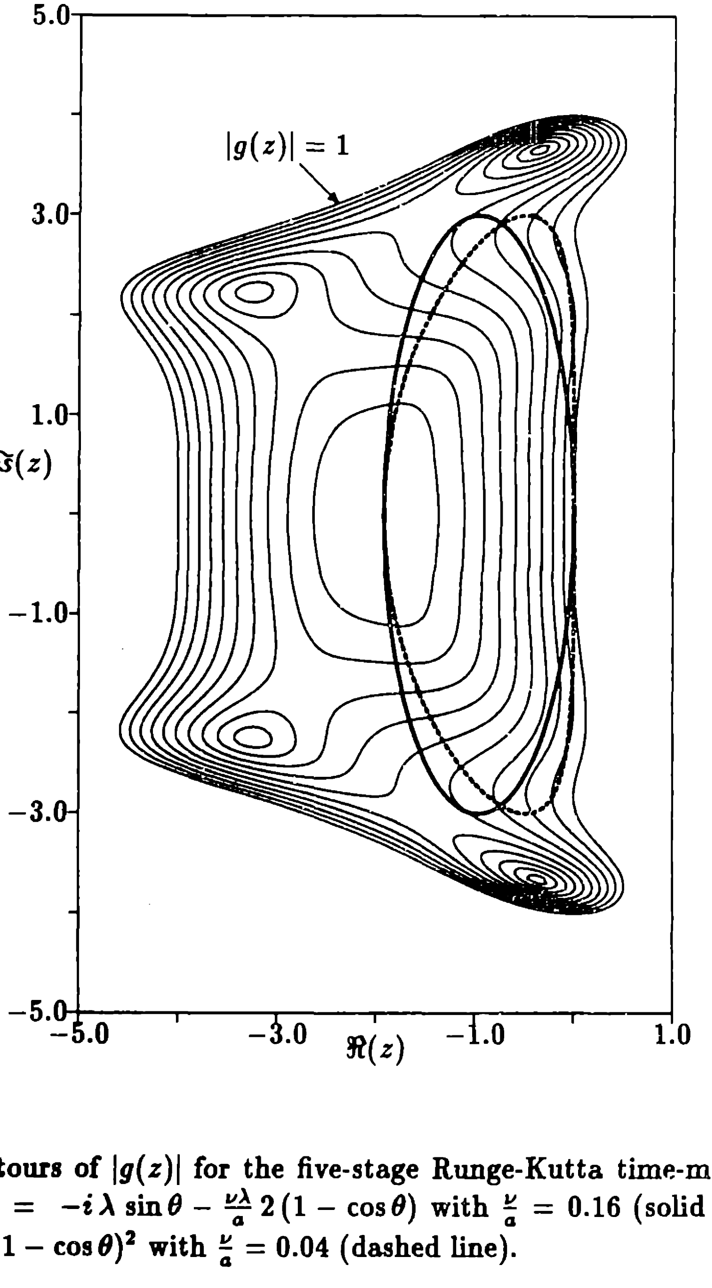

Figure A.4: Contours of $|g(z)|$ for the five-stage Runge-Kutta time-marching scheme for $\lambda = 3$ and $z = -i\,\lambda\,\sin\theta - \frac{\nu\lambda}{a}\,2\,(1-\cos\theta)$ with $\frac{\nu}{a} = 0.16$ (solid line) and $z = -i\,\lambda\,\sin\theta - \frac{\nu\lambda}{a}\,4\,(1-\cos\theta)^2$ with $\frac{\nu}{a} = 0.04$ (dashed line).

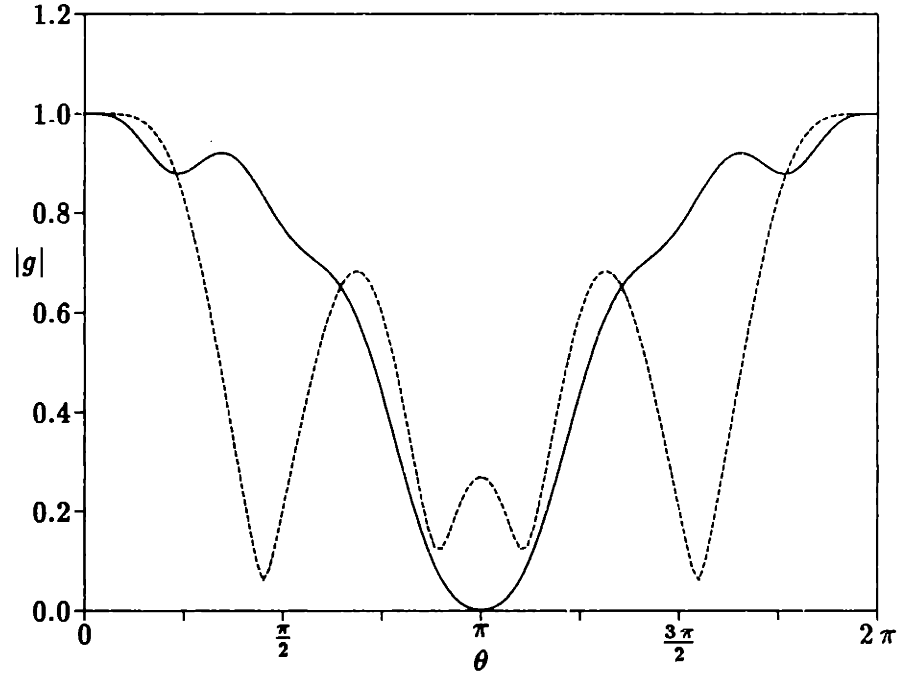

Figure A.5: Amplification factor $|g|$ with fourth difference dissipation $\frac{\nu}{a} = 0.04$ for the four-stage scheme with $\lambda = 2.5$ (dashed line) and the five-stage scheme with $\lambda = 3$ (solid line).

A.2 Linear Perturbation

The analysis for the perturbation Equation (A.2) is similar to the analysis in the previous section, except now R_J is slightly different.

$$R_J \;=\; i\omega u_J \;+\; a\,\frac{u_{J+1} - u_{J-1}}{2\Delta x} \tag{A.12}$$

When the dissipation terms are added to Equation (A.12), the relevant equations become

1) $$\frac{\partial u}{\partial t} + i\omega u + a\frac{\partial u}{\partial x} = \nu\Delta x\frac{\partial^2 u}{\partial x^2} \qquad \text{second difference damping}$$

$$R_J = i\omega u_J + a\frac{u_{J+1} - u_{J-1}}{2\Delta x} - \nu\frac{u_{J+1} - 2u_J + u_{J-1}}{\Delta x}$$

$$z = i\omega\Delta t - i\lambda\sin\theta - \frac{\nu\lambda}{a}2\,(1 - \cos\theta)$$

2) $$\frac{\partial u}{\partial t} + i\omega u + a\frac{\partial u}{\partial x} = -\nu\Delta x^3\frac{\partial^4 u}{\partial x^4} \qquad \text{fourth difference damping}$$

$$R_J = i\omega u_J + a\frac{u_{J+1} - u_{J-1}}{2\Delta x} + \nu\frac{u_{J+2} - 4u_{J+1} + 6u_J - 4u_{J-1} + u_{J-2}}{\Delta x}$$

$$z = i\omega\Delta t - i\lambda\sin\theta - \frac{\nu\lambda}{a}4\,(1 - \cos\theta)^2$$

The effect of the new term in the perturbation equation is to shift the curves in Figure A.3 and A.4 along the imaginary axis by an amount $\omega\Delta t$. Figure A.6 shows this effect for the four-stage Runge-Kutta scheme. This changes the stability limit slightly so now this scheme is stable for $\omega\,\Delta t + \lambda \leq 2\sqrt{2}$ and the five-stage scheme is stable for $\omega\,\Delta t + \lambda \leq 4$ when there is no artificial viscosity.

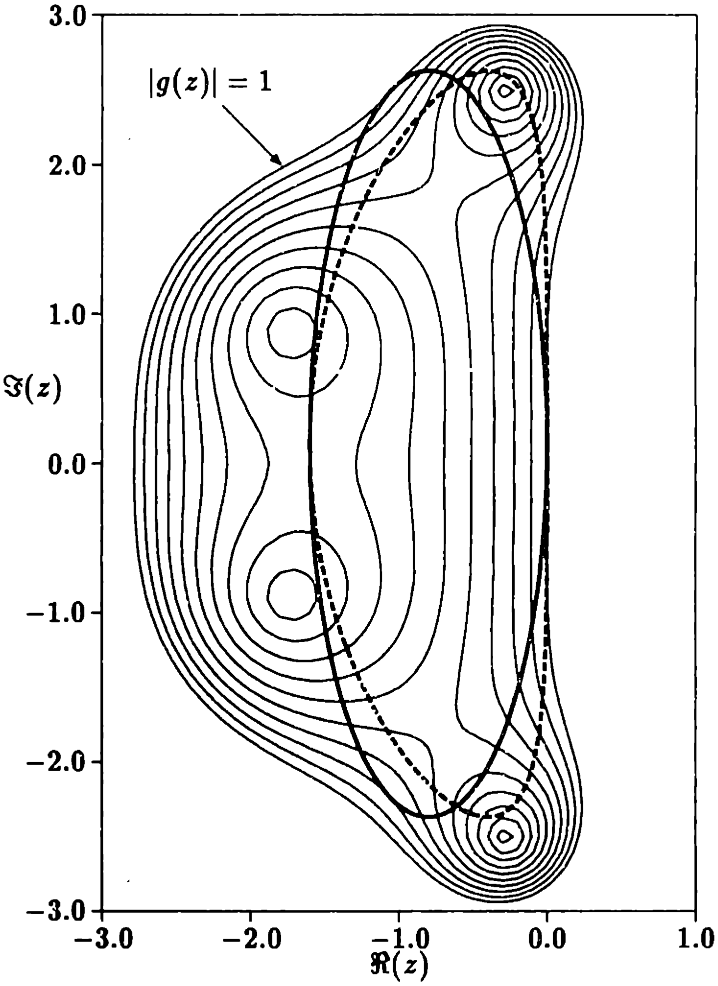

Figure A.6: Contours of $|g(z)|$ for the four-stage Runge-Kutta time-marching scheme for $\lambda = 2.5$ and $\omega\,\Delta t = 0.1$ and $z = i\omega\Delta t - i\,\lambda\,\sin\theta - \frac{\nu\lambda}{a}\,2\,(1-\cos\theta)$ with $\frac{\nu}{a} = 0.16$ (solid line) and $z = i\omega\Delta t - i\,\lambda\,\sin\theta - \frac{\nu\lambda}{a}\,4\,(1-\cos\theta)^2$ with $\frac{\nu}{a} = 0.04$ (dashed line).

A.3 Conclusions

The steady and perturbation equations have different bounds for stability. These bounds were found in the previous two sections.

	4-stage Runge-Kutta	5-stage Runge-Kutta
steady equation	$\lambda \leq 2\sqrt{2}$	$\lambda \leq 4$
perturbation equation	$\omega \Delta t + \lambda \leq 2\sqrt{2}$	$\omega \Delta t + \lambda \leq 4$

Section 5.1.3 talks about the use of these stability limits in conjunction with the nonlinear and linear perturbation Euler equations.